UNIVERSIDADE ESTADUAL DE CAMPINAS

Instituto de Física "Gleb Wataghin"

RODRIGO TREVISAN MASSERA

DOSIMETRY IN CONTEMPORARY X-RAY BREAST IMAGING MODALITIES BY MONTE CARLO SIMULATION

DOSIMETRIA EM MODALIDADES CONTEMPORÂNEAS DE IMAGEAMENTO DA MAMA POR RAIOS X VIA SIMULAÇÃO MONTE CARLO

CAMPINAS

2022

RODRIGO TREVISAN MASSERA

DOSIMETRY IN CONTEMPORARY X-RAY BREAST IMAGING MODALITIES BY
MONTE CARLO SIMULATION

DOSIMETRIA EM MODALIDADES CONTEMPORÂNEAS DE IMAGEAMENTO DA
MAMA POR RAIOS X VIA SIMULAÇÃO MONTE CARLO

Tese apresentada ao Instituto de Física "Gleb Wataghin" da Universidade Estadual de Campinas como parte dos requisitos exigidos para a obtenção do título de Doutor em Ciências, na área de Física Aplicada.

Thesis presented to the "Gleb Wataghin" Institute of Physics of the University of Campinas in partial fulfillment of the requirements for the degree of Doctor in Sciences, in the area of Applied Physics.

Supervisor/Orientador: PROFª. DRª. ALESSANDRA TOMAL

ESTE TRABALHO CORRESPONDE À VERSÃO FINAL DA TESE DEFENDIDA PELO ALUNO RODRIGO TREVISAN MASSERA, E ORIENTADA PELA PROFª. DRª. ALESSANDRA TOMAL

CAMPINAS
2022

Ficha catalográfica
Universidade Estadual de Campinas
Biblioteca do Instituto de Física Gleb Wataghin
Lucimeire de Oliveira Silva da Rocha - CRB 8/9174

M384d   Massera, Rodrigo Trevisan, 1992-
     Dosimetry in contemporary X-ray breast imaging modalities by Monte Carlo
    simulation / Rodrigo Trevisan Massera. – Campinas, SP : [s.n.], 2022.

     Orientador: Alessandra Tomal.
     Tese (doutorado) – Universidade Estadual de Campinas, Instituto de Física
    Gleb Wataghin.

     1. Mamas - Radiografia. 2. Método de Monte Carlo. 3. Aprendizado de
    máquina. 4. Aprendizado profundo. 5. Radiação - Dosimetria. I. Tomal,
    Alessandra, 1983-. II. Universidade Estadual de Campinas. Instituto de Física
    Gleb Wataghin. III. Título.

MEMBROS DA COMISSÃO JULGADORA DA TESE DE DOUTORADO DO ALUNO RODRIGO TREVISAN MASSERA - RA 164177 APRESENTADA E APROVADA AO INSTITUTO DE FÍSICA "GLEB WATAGHIN", DA UNIVERSIDADE ESTADUAL DE CAMPINAS, EM 10/03/2022.

COMISSÃO JULGADORA:

- Profa. Dra. Alessandra Tomal - Presidente e Orientadora (IFGW/UNICAMP)

- Prof. Dr. Mario Antonio Bernal Rodriguez (IFGW/UNICAMP)

- Prof. Dr. Romis Ribeiro de Faissol Attux (DCA/FEEC/UNICAMP)

- Dr. Marcelo Andrade da Costa Vieira (EESC/USP)

- Dr. Andreu Badal Soler (U. S. Food and Drug Administration)

OBS.: Ata da defesa com as respectivas assinaturas dos membros encontra-se no SIGA/Sistema de Fluxo de Dissertação/Tese e na Secretaria do Programa da Unidade.

CAMPINAS

2022

Acknowledgments

This work was only possible thanks to the wonderful people that helped me during my doctorate. First, my supervisor, Professor Doctor Alessandra Tomal, who since my master's, guided me through these academic years. I would also like to thank Professor Doctor Rowan Thomson, my supervisor during my stay in Carleton University, and all my CLRP colleges, for their hospitality and providing this unique opportunity of being part of their research group. Professor Doctor José M. Fernández-Varea, for collaborating in one of the articles and providing essential insights. My research colleagues from GFRMd, IFGW at University of Campinas, that participated in the (virtual) meetings providing ideas for the project. My friend Hitalo, who, since the beginning of our master's, contributed with important discussions. I would also like to thank University of Campinas for providing a thriving environment for research and education, with all professors that ministered the courses that I attended and the professors that participated in examining committees related to my doctorate, and the staff that helped me always when I most needed. My family, Cássio, Cláudia and Giovanna, thanks for supporting me for all those years. Renata, for reviewing countless texts, and helping me during my anxiety episodes. Fábio, for assistance in some technical aspects of this work, and my dearest friends of DDG.

Resumo

O câncer de mama é o tipo de câncer de maior incidência e o maior responsável pela mortalidade entre as mulheres em todo o mundo, sendo a detecção precoce importante na redução do índice de mortalidade desta doença. As modalidades de diagnóstico por imagem empregadas no rastreamento do câncer de mama utilizam radiação ionizante, logo estudos de dosimetria são essenciais para estimativa de risco e controle de qualidade, devido a elevada radiossensibilidade do tecido glandular presente na mama. Este trabalho tem como objetivo principal a análise detalhada da influência de parâmetros físicos e geométricos na dosimetria em imageamento da mama por raios X por simulação Monte Carlo (MC), desde a escala macroscópica com a dose glandular média até a escala microscópica, com a distribuição da energia específica em células. O impacto da escolha de seções de choque para o efeito fotoelétrico e seu efeito em dosimetria em mamografia nas simulações MC foi analisado e os resultados indicaram que pode haver, em alguns casos, uma diferença significativa nos valores das grandezas dosimétricas calculadas, especialmente para baixas energias, da ordem de aproximadamente 2%. A aplicação de técnicas de aprendizado de máquina, mais especificamente redes neurais, foi proposta para o cálculo da dose glandular normalizada em mamografia, com um erro da ordem da incerteza estatística dos resultados da simulação, podendo ser uma técnica complementar a métodos tradicionalmente utilizados, como tabelas e equações paramétricas, especificamente quando uma ampla quantidade de parâmetros é considerada. Outra aplicação de aprendizado de máquina, neste caso aprendizado profundo, foi analisada para a estimativa da densidade mamária em imagens de mamografia simuladas para *phantoms* gerados computacionalmente, e uma possível aplicação para dosimetria foi analisada. O código MC-GPU, desenvolvido para simulações MC em unidades de processamento gráfico, foi validado em comparação com outros códigos MC para diversas técnicas de imageamento da mama. Adicionalmente, o código foi adaptado para gerar arquivos de espaço de fase, possibilitando simulações em nível multiescala. Com essa adaptação, foi realizado um estudo de dosimetria em multiescala para as diversas técnicas de imageamento e comparou-se a distribuição da dose em tecido glandular no interior da mama, assim como a distribuição da energia específica depositada no núcleo e citoplasma celulares. Em conclusão, este trabalho abordou diferentes tópicos em dosimetria da mama, incluindo um estudo da influência de diversos parâmetros na estimativa da dose em escala macroscópica, e a incerteza sistemática resultante da simulação MC. Adicionalmente, mostrou-se que o uso de técnicas de aprendizado de máquina para dosimetria da mama é promissor para a estimativa da dose glandular média e densidade mamária. Finalmente, foi mostrado que simulações em nível multiescala são capazes de realizar estudos mais completos da deposição de energia na mama.

Palavras-chave: Mamas - Radiografia; Método de Monte Carlo; Aprendizado de máquina; Aprendizado profundo; Radiação - Dosimetria.

Abstract

Breast cancer is the type of cancer with the highest incidence and responsible for the highest mortality among women around the world, being the early detection important for reducing the mortality rate of this disease. The diagnostic imaging modalities employed in breast cancer screening use ionizing radiation, thus dosimetry studies are essential for risk assessment and quality control, due to the high radiosensitivity of glandular tissue present in the breast. The main objective of this work is a detailed analysis of the influence of physical and geometrical parameters in x-ray breast imaging dosimetry by Monte Carlo (MC) simulations, from the macroscopic scales, with the mean glandular dose, to the microscopic scale with the specific energy distribution in cells. The impact of the photoelectric cross-sections on mammography dosimetry in MC simulation was analyzed and the results indicate that it could have, in some cases, a significant difference in the calculated dosimetric quantities values, especially for low energies, being in the order of approximately 2% for a mammography spectrum. The application of machine learning techniques, more specifically neural networks, was proposed for normalized glandular dose calculation in mammography, with errors in the order of the statistical uncertainties from the simulation results, which could be a complementary technique to traditional used methods, such as tables and parametric equations, specifically when a large number of parameters is considered. Another machine learning application, in this case deep learning, was analyzed for breast density estimation in simulated mammography images for computer generated phantoms, and a possible dosimetry application was analyzed. The MC-GPU code, developed for MC simulations in graphics processing units, was validated in comparison with other MC codes for different breast imaging techniques. In addition, the code was adapted to generate phase space files, allowing multiscale simulations. With this adaptation, a multiscale dosimetry study was performed for different breast imaging modalities and the dose distribution in glandular tissue inside the breast was compared, along with the specific energy behavior inside the cell nucleus and cytoplasm. In conclusion, this work addressed distinct breast dosimetry topics, including a study about the influence of a plethora of parameters in the dose estimation at macroscopic scales, and the systematic uncertainty obtained from MC simulation. Additionally, it was shown that the use of machine learning techniques for breast dosimetry is promising for mean glandular dose and breast density estimation. Finally, it was shown that multiscale simulations are capable of producing more complete studies about energy deposition in the breast.

Keywords: Breast - Radiography; Monte Carlo method; Machine learning; Deep learning; Radiation dosimetry

List of Abbreviations

2D two-dimensional

3D three-dimensional

AI artificial inteligence

ANN artificial neural networks

CC craniocaudal

CEDM contrast enhanced digital mammography

CPU central processing unit

CR computed radiography

DBCT dedicated breast computed tomography

DBT digital breast tomosynthesis

DL deep learning

DgN normalized glandular dose

GPU graphics processing unit

MC Monte Carlo

MGD mean glandular dose

ML machine learning

MLO mediolateral oblique

VBD volumetric breast density

VGF volumetric glandular fraction

Contents

Chapter 1

Introduction

1.1 Breast cancer and breast imaging

Breast cancer is the most common type of cancer among women around the world, and it is also responsible for the highest mortality rate in the female population [1, 2]. In Brazil, it was estimated that 59700 new female breast cancer cases occurred in 2019 [3].

Evidences have shown that early diagnosis, combined with effective treatment [4] and screening programs [5], are responsible for the decline in breast cancer mortality observed in the past decades. However, while the early diagnosis is focused on symptomatic patients, screening programs target an entire population to detect asymptomatic, very early-stage cancers [4, 6]. Mammography is currently the main, and depending on the country the only, imaging modality employed in breast cancer screening programs. As an example, in Brazil, the Ministry of Health recommends that women from 50 to 69 years undergo mammography screening every two years [7]. Therefore, a large population is submitted periodically to mammography examinations. Over 4.6 million mammography examinations were performed in Brazil through public health care in 2018 [3].

Digital mammography is an imaging modality that uses low-energy x-rays (typically with an average energy ranging from approximately 16 to 20 keV) and high spatial-resolution digital detectors (with pixel size in the order of 50 to $100\,\mu m$) [8]. Photons, produced by an x-ray tube, exit from an aperture which is collimated towards the detector. The breast is located a few centimeters above the detector, and is compressed limiting unwanted patient movement during the image acquisition. Moreover, the compression reduces tissue superposition and scattering, providing a better image quality [9]. As the photon travels through the breast tissues, it can be absorbed, scattered or transmitted without interactions. In mammography, the scattered photons carry no usable information and are often removed using an antiscatter grid [10]. Since the breast tissues present distinct attenuation coefficients, dictated by their respective elemental compositions and densities, the probability of photon transmission is dependent on the distance traveled in each tissue. The photons, transmitted through the breast and

reaching the detector, have a high probability of interacting and transferring most (or totally) of their energy to secondary particles (i.e. electrons) due to the detector material composition (usually elements of high atomic number are employed). Additional processes are responsible for converting this transferred energy directly or indirectly, considering digital radiography (DR) and computed radiology (CR) detectors, to a digital signal for subsequent processing, and forming a digital image [8].

Despite its excellent spatial resolution, digital mammography is known to present lower sensitivity for dense breasts [11] due to low contrast between malignant and healthy tissues. In addition, the generated images are two-dimensional (2D) projections of a three-dimensional (3D) breast, and tissue superposition could be a limitation to accurately detect lesions [12]. Digital breast tomosynthesis (DBT) is an x-ray breast imaging modality with a geometry similar to mammography, but in this case, the tube rotates in a limited angular range (from an interval varying from 15 to 50 degrees) and a series of 2D projections are acquired. Afterwards, the projections are combined to reconstruct a pseudo 3D image of the breast [12]. Due to its advantages, there is an ongoing interest in using DBT as a breast cancer screening tool [13, 14]. Another x-ray imaging technique of the breast is the contrast enhanced digital mammography (CEDM). This technique uses a contrast agent (a medium that contains iodine) that is injected in the patient to enhance image contrast [15]. The images are acquired using the dual-energy mode or the temporal subtraction mode [15]. CEDM was tested as a screening modality for women with high risk of developing breast cancer being superior compared to conventional digital mammography [16].

The previously cited imaging modalities provide 2D or pseudo-3D images of the breast, and consequently, lack a true 3D spatial information. Dedicated breast CT (DBCT) on the other hand, is an imaging technique capable of producing real 3D image reconstructions of breast tissues, offering a superior contrast compared to digital mammography and DBT [17]. In addition, in DBCT the breast is pendant and uncompressed. The images generated with DBCT have allowed studies of the breast anatomy, such as the breast adipose and glandular fraction composition [18], breast volume [19] and skin thickness [20, 21]. Additionally, there is the possibility to employ a contrast agent in DBCT to generate 4D breast CT images [22].

1.2   Breast dosimetry and Monte Carlo simulation

The Monte Carlo (MC) method is a well-established application to simulate stochastic processes using random sampling [23]. MC simulations have being employed to model the process of radiation transport through matter, including photons, electrons, and positrons from a few eV up to GeV [24, 25]. X-ray breast imaging simulations with MC is a common topic in the literature, covering dosimetry [26–30] and image quality [31–33], considering one or both aspects simultaneously. In particular, breast dosimetry is an important topic since ionizing radiation (x-rays) is used in all imaging techniques mentioned in section 1.1, and the breast

is a radiosensitive organ, having one of the highest tissue weighting factor values defined by the International Commission on Radiological Protection (ICRP) among other human body tissues [34]. Additionally, since mammography is employed in screening programs, women are exposed to ionizing radiation several times during their lifetime, contributing to the importance of dosimetry studies of x-ray breast imaging and risk assessment [35, 36].

The evolution of breast dosimetry spans decades and is explained with details in the literature [36]. The current paradigm is focused on the glandular tissue, because it corresponds to the most radiosensitive tissue in the breast. A common quantity employed in breast dosimetry is the mean glandular dose (MGD), which is defined as the ratio between energy absorbed in glandular tissue and its mass. However, it is not possible to obtain the MGD directly, and to circumvent this limitation, conversion factors are employed. These conversion factors, often named Normalized Glandular Dose (DgN), are in most cases obtained with MC simulations [26, 27, 29, 30, 36–38]. Briefly explaining, the MGD is calculated by multiplying the measured air kerma by the adequate DgN, since this conversion factor is dependent on a series of parameters including the breast thickness and composition, x-ray beam quality and geometry of acquisition.

Since the DgN values are obtained from MC simulations, they are directly affected by the computational modeling of this problem (e.g. geometry and physics descriptions). In addition, some parameters are unknown and assumptions must be made, or some approximations and simplifications are necessary due to the computational restraints. For example, the tissue layer that surrounds the breast was previously modeled as a 5 mm thick adipose tissue layer [30] or a 4 mm thick skin [26]. However, with the development of DBCT, more recent studies indicated that, in reality, the shielding layer was thinner, being approximately 1.45 mm skin [20]. Another topic is breast composition and the fraction of glandular tissue. In the past, a standard breast model of a homogeneous mixture of 50% glandular tissue and 50% adipose tissue, by mass, was considered in dosimetry studies. Nowadays, recent findings indicate that the proportion of glandular tissue is considerably lower than the previous standard model [18], being on average, closer to 20%. Although the homogeneous tissue approximation is acceptable in some scenarios [36], it does not reflect the heterogeneous distribution found in real breasts. Heterogeneous breast models, some built from real breasts using DBCT data, presented systematically lower MGD values compared to homogeneous models in the order of 30% [39, 40]. Thus, currently there is a general interest in studying more realistic breast models for breast dosimetry, but the generation of these models is not trivial. To facilitate the implementation of heterogeneous models, a possibility is to sample the glandular distribution inside the breast from fitted equations obtained from a large sample of real breasts [41, 42]. Another approach is to generate anthropomorphic breast phantoms with computer algorithms [43].

Despite the importance of the MGD in breast dosimetry, this quantity does not take into account the dose distribution inside the breast. The glandular dose distribution profile can vary significantly across modalities [44], mainly due to geometry differences and x-ray beam energy. Sechopoulos et al. [45] have shown that the glandular dose in mammography could

vary from approximately 0.15 to 4 times the MGD, while for DBCT it varied from 0.65 to 1.4 times the MGD. Multiscale Monte Carlo simulations could bring new findings in breast dosimetry, since it provides information about the energy deposition at distinct length scales, from the breast as a whole (MGD), the glandular dose distribution and the specific energy distribution in cells. Oliver and Thomson have shown that, besides the variation found in the glandular dose distribution in mammography, there is also the specific energy distribution for the nuclei in cells, whose mean value tends to be higher than the respective scored glandular dose [46]. In addition, the effects of the damage in cells due to exposure of ionizing radiation in mammography examination was explored in the literature [47]. Considering the variations observed in the energy deposition inside the breast, multiscale dosimetry studies could bring additional information to better understand the relation between the energy deposition at different scales, and establish microscopic dose levels and the respective correlations with risk.

1.3 Machine learning and breast imaging

Certain problems are difficult, or extremely time consuming, to solve using a specifically tailored algorithm for that purpose, for example, image classification and segmentation tasks, and text translation. Instead, it is advantageous to actually use machine learning (ML) algorithms that are capable of learning how to solve the desired task by providing examples [48]. However, some machine learning models usually require manually feature preparation and extraction. Deep learning (DL), on the other hand, is a paradigm of machine learning algorithms, composed of many layers of artificial neural networks, capable of extracting and processing abstract features, which substitutes the feature engineering steps present in some ML models, allowing to solve complex problems [49]. Both ML and DL models have their advantages and disadvantages, consequently the choice is based on the characteristics of the problem to solve, and the data availability (ML algorithms usually require smaller samples to train) [50]. ML and DL can be used at different tasks regarding health care [51], including medical imaging classification and segmentation [52], image quality control [53], and cancer research [54].

In the last years, the applications of ML and DL in x-ray breast imaging were also deeply explored under different scenarios. Deep learning models were trained for breast lesion detection in mammography, surpassing the performance of more traditional methods such as Computer Aided Detection (CADe) and Computer Aided Diagnosis (CADx), and being at the same level of an average radiologist [55]. Deep convolutional generative adversarial networks (DCGANs), a type of architecture of DL, was successfully implemented to generate lesions for mammography images to correct imbalanced datasets [56]. The spatial resolution of breast phantom images can be increased using convolutional neural networks (CNN) [57], another type of DL model. DL was also applied for mammography image quality control [58], and digital breast tomosynthesis image reconstruction [59].

A particular application of ML and DL related to breast imaging is the breast density

estimation. Dense breasts have a higher risk of breast cancer, and a lower sensitivity of mammography exams [60]. Breast density is related to the fraction of glandular tissue that composes the breast, and it can be estimated using area-based or volumetric-based algorithms [61]. ML techniques were successfully employed to estimate breast density for mammography images based on area [62]. Meanwhile, DL was used for volumetric breast density (VBD) estimation using mammography [63] and digital breast tomosynthesis images [64]. An advantage of VBD is that the glandularity can be estimated and employed in dosimetric models for a more accurate dose calculation [61].

Besides the glandularity, other parameters are considered to obtain the DgN values, e.g. breast size (thickness), x-ray beam energy, system geometry, among others. Taking into account the possible parameter space, traditional methods of distributing the conversion factors such as tables or parametric equations could be impractical. An alternative format is to employ ML techniques to estimate the DgN values, with the data obtained using Monte Carlo simulations. Regarding breast dosimetry, ML and DL models could contribute for the prediction of more accurate dose values, and are promising techniques in the medical imaging field.

1.4   Developments in breast dosimetry

This section discusses the possible developments that could be achieved in breast dosimetry, based on Sections 1.1, 1.2 and 1.3.

Breast dosimetry is an essential field for risk assessment and quality control, as highlighted in the previous sections. However, since it is a complex topic and in constant evolution, there is still availability for more developments. In this context, the joint Task Group (282) of the American Association of Physicists in Medicine (AAPM) and the European Federation of Organizations for Medical Physics (EFOMP) are developing a new universal breast model for breast dosimetry [65]. Monte Carlo simulations are the current state-of-the art method to obtain the DgN values, that in turn, are employed for DGM calculations. The results obtained in the simulations are derived from the physics and geometric parameters employed in the MC simulations, thus it is important to study the relation of the selected parameters in the simulations and their impact in the final results. For example, the thickness of the skin layer that surrounds the breast, or the choice of the cross-sections used in the calculations of the photon interactions in the simulations. Another important topic in breast dosimetry is the implementation of more realistic breast models, that mimic a glandular tissue distribution similar to what is found in real breasts, in contrast to the simplified homogeneous breast models.

ML and DL algorithms were successfully employed in medical imaging, including lesion detection in breast imaging. Considering this, an interesting topic for breast dosimetry is the application of ML and DL for dose estimation in the breast. For example, DL could be used to determine the volumetric breast density and glandularity, which in turn is a parameter for DgN and MGD calculations. Afterwards, ML algorithms could be employed for DgN calcu-

lations, considering several parameters that can be varied in Monte Carlo simulations to cover distinct breast characteristics, geometry factors and x-ray spectra.

Although MGD is the main quantity employed in breast dosimetry for risk estimation, the effects of the ionizing radiation in biological tissues occur at microscopic scales. Different breast imaging modalities employ distinct x-ray spectra, and consequently, this could also affect the dose distribution inside the breast, even for the same MGD. Therefore, mulstiscale Monte Carlo simulations could contribute for a better understanding of breast dosimetry, because it is possible to study the energy deposition in the breast at different scale lengths, i.e. from the whole breast (MGD), to cells (specific energy distributions).

1.5 Main and specific objectives

In light of the topics presented in the previous sections, and given the importance and complexity of breast dosimetry, one of the main objective of this work was to perform a comprehensive study of breast dosimetry employing Monte Carlo simulations. More specifically, to study the breast dosimetry at different length scales, from the traditional MGD values, to the glandular dose distribution and, finally, the specific energy distribution in cells. However, to perform this type of study, intermediate specific objectives were established, described as follow:

- To study the systematic uncertainty derived from different photoelectric cross sections present in Monte Carlo codes for breast dosimetry.

- To use a ML approach to calculate MGD and DgN values obtained from Monte Carlo simulations, and to compare its feasibility in contrast to more traditional methods found in the literature.

- To develop a DL framework for volumetric breast density estimation for antropomorphic virtual phantoms, and to assess the impact of the glandularity prediction in dosimetry.

- To implement and validate a pipeline for multiscale Monte Carlo simulations in breast dosimetry, capable of performing a full dose simulation in a reasonable time for limited hardware resources.

1.6 Main contributions

This section summarizes the main contributions derived from this thesis, divided per chapter.

As described in Chapter 2, it was found that the photoelectric cross sections between older (pre 2014, without the renormalization) and new (after 2014, with renormalization)

PENELOPE versions provide distinct results for mammography dosimetry under different simulation conditions. Thus, it is important to account for this systematic uncertainty related to the dosimetric quantities obtained using MC simulations due to the photoelectric cross section databases.

Since the variety of parameters that can be altered when calculating DgN values for homogeneous breast in a MC simulation is practically inexhaustible, there must be a compromise to select only a few of them when publishing the results in the traditional formats (tables or fitted equations). In Chapter 3 it was shown that ANN could be an alternative format, and is capable of dealing a significant number of parameters at the same time when predicting DgN values for mammography.

The impossibility of extracting the ground truth breast density directly from mammography images poses a significant challenge of designing algorithms for this purpose, requiring, in most cases, a second imaging modality to extract the ground truth values in order to validate the algorithms. In Chapter 4, it was developed a deep learning framework to predict volumetric breast density from simulated mammography images using virtual anthropomorphic phantoms. The advantage of this case is that the the training and validation process are facilitated because the ground truth is directly obtained from the virtual anthropomorphic phantoms.

The MC-GPU code was adapted to generate phase space files, as described in Chapter 5, optimizing the process of multiscale MC simulations. In addition, the code was validated against other MC codes for dosimetry in x-ray breast imaging. Using phase space files, multiscale MC simulations were performed as described in Chapters 6 and 7. It was found that the behavior of the energy deposition within the breast varies significantly at different length scales. In addition, for the same MGD value, distinct imaging modalities yields different glandular dose distribution profiles and specific energy distribution at cell scales.

1.7   Thesis organization

This work is divided into the following chapters, structured as published or to be submitted articles, that contain specific topics of study and they are briefly explained in this section.

- Chapter 2 consists of the impact of the photoelectric cross section databases in MC simulations for breast dosimetry, and to quantify the differences in mammography.

- Chapter 3 shows an implementation of artificial neural networks for breast dosimetry for homogeneous phantoms.

- Chapter 4 is an implementation of a deep learning framework for breast density estimation in virtual phantoms and a possible use in breast dosimetry.

- Chapter 5 shows an application of phase space files implemented in MC-GPU, and compares breast dosimetry results with other MC codes based on CPU. In addition, the potential optimization in performance is assessed when combining two MC codes for multiscale simulations.

- Chapters 6 and 7 are dedicated to multiscale MC simulations in breast dosimetry at different length scales: from the breast as a whole, sub-millimetric voxels and cells.

- Chapters 8 and 9 synthesize the overall discussions and conclusions, respectively.

The references for Chapters 1 and 8 are at the end of this thesis. Meanwhile, for Chapters 3, 4, 5, 6 and 7, the references are at the end of each respective article.

Chapter 2

Photoelectric cross section and systematic uncertainty in mammography

ACCEPTED MANUSCRIPT

Impact of photoelectric cross section data on systematic uncertainties for Monte Carlo breast dosimetry in mammography

Impact of photoelectric cross section data on systematic uncertainties for Monte Carlo breast dosimetry in mammography

Rodrigo T Massera[1], José M Fernández-Varea[2], Alessandra Tomal[1]

[1] Instituto de Física "Gleb Wataghin", Universidade Estadual de Campinas, 13083-859, Campinas, Brazil

[2] Facultat de Física (FQA and ICC), Universitat de Barcelona. Diagonal 645, ES-08028 Barcelona, Catalonia, Spain

Abstract

Monte Carlo (MC) simulations are employed extensively in breast dosimetry studies. In the energy interval of interest in mammography energy deposition is predominantly caused by the photoelectric effect, and the corresponding cross sections used by the MC codes to model this interaction process have a direct influence on the simulation results. The present work compares two photoelectric cross section databases in order to estimate the systematic uncertainty, related to breast dosimetry, introduced by the choice of cross sections for photoabsorption. The databases with and without the so-called normalization screening correction are denoted as "renormalized" or "unnormalized", respectively. The simulations were performed with the PENELOPE/penEasy code system, for a geometry resembling a mammography examination. The Mean Glandular Dose (MGD), incident air kerma (K_{air}), Normalized Glandular Dose (DgN) and Glandular Depth Dose (GDD(z)) were scored, for homogeneous breast phantoms, using both databases. The AAPM Report TG-195 case 3 was replicated, and the results were included. Moreover, cases with heterogeneous and anthropomorphic breast phantoms were also addressed. The results simulated with the unnormalized cross sections are in better overall agreement with the TG-195 data than those from the renormalized cross sections; for MGD the largest discrepancies are 0.13(6)% and 0.74(5)%, respectively. The MGD, K_{air} and DgN values simulated with the two databases show differences that diminish as the photon energy increase from approximately 10%/3%/6.8% at 8.25 keV down to 1.5%/1.7%/0.4% at 48.75 keV, respectively. For polyenergetic spectra, deviations up to 2.5% were observed. The disagreement between the GDDs simulated with the analyzed databases increases with depth, ranging from -1% near the breast entrance to 4% near the bottom. Thus, the choice of photoelectric cross section database affects the MC simulation results of breast dosimetry and adds a non-negligible systematic uncertainty to the dosimetric quantities used in mammography.

Key-words: Mammography; dosimetry; Monte Carlo simulation; photoelectric absorption; normalization screening correction; systematic uncertainty

1

1. Introduction

Monte Carlo (MC) simulation plays an important role in breast dosimetry (Dance and Sechopoulos 2016). During the last three decades, this computational technique has been used extensively to estimate the energy imparted to the breast in mammographic examinations (Dance 1990, Wu *et al* 1991, Dance *et al* 1999, Boone 1999, 2002, Sechopoulos *et al* 2006, Cunha *et al* 2010, Nosratieh *et al* 2015, Sarno *et al* 2016, 2018). Besides other reasons, the possibility to calculate with MC simulations the Mean Glandular Dose (MGD), which is the main quantity in the dosimetry of the breast, has certainly contributed to the growing importance of MC methods. As an example, the current protocols of breast dosimetry in Europe and the USA rely on conversion factors based on MC data (Wu *et al* 1991, 1994, Dance 1990, Dance *et al* 2000, 2009, Boone 1999, 2002, Nosratieh *et al* 2015). However, the MC results depend on how the modelling of the problem is made.

A few publications have investigated the effect of various parameters employed in the MC simulations and how they affect the calculated MGD (Zoetelief and Jansen 1995, Fedon *et al* 2015, Arce *et al* 2021). These include, among others, the composition of breast tissues, the breast shape, the distribution of tissues inside the breast, and the input x-ray spectra and the photon interaction cross sections. Furthermore, the implementation of realistic breast models derived from real patients has increased the complexity of MC simulations for breast dosimetry (Sechopoulos *et al* 2012, Hernandez *et al* 2015). Several MC codes are nowadays available to conduct breast dosimetry studies, e.g. MCNP or MCNPX (Werner *et al* 2018), Geant4 (Allison *et al* 2016), EGSnrc (Kawrakow *et al* 2017), PENELOPE (Salvat 2019) and some bespoke codes like SIERRA (Boone 2002) among others (Dance 1990, Cunha *et al* 2010), and it is of great interest to compare the results provided by them. Indeed, this was the main purpose of the Report of the AAPM Task Group 195 (Sechopoulos *et al* 2015), hereafter denoted as TG-195.

The dosimetric quantities like MGD estimated by means of MC simulation are usually reported with the corresponding type A statistical uncertainties because this technique is used to simulate stochastic phenomena (Aguirre *et al* 2016). However, a complete uncertainty budget associated to the MC simulations for the determination of MGD should also include the contribution of type B uncertainties due to the presence of systematic errors. As discussed in a recent review by Dance and Sechopoulos (2016), there are systematic uncertainties in the MGD estimation that originate from the computational models used in the simulations, which can be related to: composition and mass density of the breast tissues, simplified breast models, and different protocols based on distinct breast models.

A key ingredient of the MC simulations, especially relevant when mammography is concerned, is the database of photon-atom interaction cross sections that is incorporated in the chosen MC code. The probability density functions derived from the database are used by the MC code routines to simulate photon transport in matter. Hence, the MC results are directly correlated with the selected integrated and differential cross sections (Hubbell 2006). In the energy range of interest in mammography, between 5 and 50 keV, there is a high probability of photoelectric absorption, which is the predominant interaction mechanism below around 25 keV and is responsible for the largest contribution to energy deposition in the complete energy interval. Thus, special attention should be

paid to the cross sections picked for this interaction process. However, the cross section libraries incorporated in the existing MC codes are not standardized, and some codes have different cross section libraries available (Fedon *et al* 2015, Kawrakow *et al* 2017). For example, in the latest versions of PENELOPE (2014, 2018), the earlier database of photoelectric cross sections was replaced with a new one (Salvat 2019). Since previous validation regarding dosimetry in mammography tasks were made with an older PENELOPE version (Sechopoulos *et al* 2015), it is desirable to estimate the impact that this change could have on the calculated MGD.

The aim of the present article is to investigate the systematic (type B) uncertainties arising from the choice of photoelectric cross-section data for dosimetry in the energy interval of concern in mammography. At this low energy range, type B uncertainties due to the choice of photoelectric cross-sections could be significant regarding absorbed dose values (Valdes-Cortez *et al* 2021). The current cross sections for the photoelectric effect are based on the values tabulated in the LLNL Evaluated Photon Data Library EPDL97 (Cullen *et al* 1997). On the other hand, the photoelectric cross sections in PENELOPE versions 2014 and 2018 apply Pratt's normalization screening correction (Pratt 1960, Scofield 1973, Sabbatucci and Salvat 2016 and references therein). The dosimetric quantities relevant to mammography calculated with these two databases were compared for many photon energies and breast characteristics. Finally, both sets of results were compared to those published in TG-195 (Sechopoulos *et al* 2015).

2. Materials and methods

2.1. Photoelectric cross sections

In the photoelectric effect, the target atom absorbs the incident photon and one of the bound electrons is ejected to a free state. This process is only possible for atomic (sub)shells whose binding energy is smaller than the energy of the impinging photon. Various databases of photoelectric cross sections have been published over the past decades, and some of them have been adopted in general-purpose MC codes. The interested reader may consult the review by Hubbell (Hubbell 2006) for a thorough account of this topic.

Regarding comprehensive tabulations of photoelectric cross sections, arguably the most important step forward was made by Scofield in 1973 (Scofield 1973). He treated the relativistic photon-atom interaction Hamiltonian as a 1st-order perturbation, carrying out a full multipole expansion of the quantum-mechanical operator responsible for one-photon absorption. The target atom was described using self-consistent Dirac-Hartree-Fock-Slater wave functions. Scofield's cross sections, which encompass all occupied (sub)shells of atoms with Z = 1-101 and energies between 1 keV and 1.5 MeV, were subsequently introduced in the XCOM program (Berger *et al* 2010) and the EPDL97 database (Cullen *et al* 1997). Moreover, these data are currently implemented in essentially all modern general-purpose MC codes and they are accessible at the website of the National Institute of Standards and Technology (NIST) (Seltzer 1993).

It would be desirable to calculate the photoabsorption cross sections starting from multi-configuration Dirac-Fock wave functions, which are more accurate than Dirac-Hartree-Fock-Slater wave functions. Unfortunately, the required self-consistent scheme involves a non-local potential

that is different for each atomic (sub)shell, rendering the numerical work much more difficult. To circumvent this problem, Scofield (1973) explored the so-called normalization screening approximation proposed by Pratt (1960), a simpler method that compensates for the use of the Dirac-Hartree-Fock-Slater wave functions by means of a multiplicative correction factor that only depends on the radial wave functions near the origin (Sabbatucci and Salvat 2016). However, this approach was not pursued further.

Recently, Sabbatucci and Salvat (2016) revisited the calculation of the atomic photoeffect, reviewing the theoretical formalisms and the associated numerical aspects. Besides, they wrote the computer code PHOTACS that they employed to produce a database using the same conventional 1st-order perturbation theory adopted by Scofield, but on a much denser photon energy grid, which is essentially equivalent to the data in the EPDL97 (Cullen *et al* 1997). PHOTACS was also utilized to prepare another tabulation based on the normalization screening approximation. We will refer to these databases as "renormalized" or "unnormalized" depending on whether they incorporate or not the normalization screening correction, respectively.

The International Commission on Radiation Units and Measurements has so far (ICRU 2016) not issued a recommendation on which photoelectric cross sections should be preferred. But, based on all the information available, the Report to the Consultative Committee for Ionizing Radiation CCRI(I) (McEwen *et al* 2017) endorsed the renormalized cross sections.

2.2. Monte Carlo simulations

The present simulations were done using the PENELOPE general-purpose MC code (v. 2018) (Salvat 2019) with the steering main program penEasy (v. 2019) (Sempau *et al* 2011). A Python script was written to automate the management of the very large number of files and simulations. More details about the MC code for the simulation of photon transport in the mammographic energy range are given in our earlier articles (Massera and Tomal 2018, 2020). The cutoff photon energy was set to 1 keV. Photoelectrons and Compton recoil electrons, as well as Auger electrons emitted in the subsequent atomic relaxation, were assumed to be locally absorbed (Sechopoulos *et al* 2015) because the range of electrons in breast tissues (< 50 μm) is much smaller than the dimensions of the simulated bodies ($\geq$ 0.5 mm) described in the following.

The geometric model mimics a mammographic examination in cranio-caudal view, and it was based on case 3 in TG-195 (Sechopoulos *et al* 2015), being described in more detail in previous works (Massera and Tomal 2018, Trevisan Massera and Tomal 2020) and illustrated in Figure 1. The x-ray source has a punctual focal spot, which is located 66 cm above the detector. A block (rectangular cuboid) of water (30 × 30 × 17 cm³) represents the patient's chest. The compression and support paddles are made of PMMA with dimensions 26 × 14 × 0.2 cm³. The scoring plane is located 1.5 cm under the breast, the detector and antiscatter grid were not simulated. The x-ray beam is collimated by the four detector edges. The world is composed by air.

The breast was modeled as a semi-circular cylinder with 10 cm radius and a thickness of 2 cm, 5 cm or 8 cm. The breast was composed by a 20:80 homogeneous mixture by mass of glandular and adipose tissues, respectively, which represents a glandularity of 20%. An external 1.45-mm-thick

4

skin layer (Huang *et al* 2008) enclosed the breast tissues. The skin thickness was increased to 2 mm when the simulation results had to be compared with TG-195.
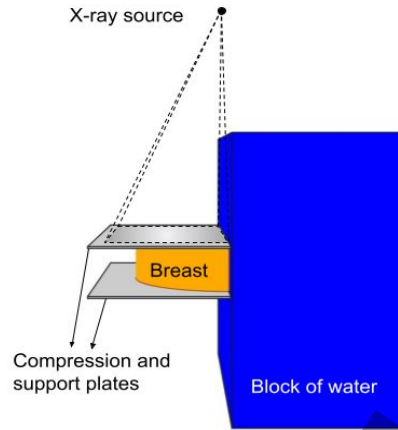

Figure 1. Simulated geometry (not to scale) employed for the comparisons with TG-195. The other simulations presented in this work adapted slightly this geometry as described in the text.

Monoenergetic and polyenergetic x-ray beams were addressed. The monoenergetic beams varied from 8.25 to 48.75 keV in 0.5 keV steps. Besides the reference Mo/(300 µm Mo) 30 kV spectrum adopted in TG-195, we also used polyenergetic spectra W/(0.05 mm Rh) 22-28 kV; W/(0.05 mm Rh) 26-32 kV, W/(0.05 mm Ag) 28-34 kV for the 2 cm, 5 cm and 8 cm breast thicknesses, respectively. Furthermore, the combination of W/(0.3 mm Cu) 45-49 kV was considered for the 5 cm breast to encompass contrast-enhanced digital mammography spectra. These combinations were motivated by the common exposure parameter conditions encountered in clinical practice (Nosratieh *et al* 2015).

The present study is divided in three parts. The first one replicates most of the case 3 conditions described in TG-195 (Sechopoulos *et al* 2015), which is devoted to mammography. Here, the simulations were ran comparing the aforementioned cross section databases, for the 0° and 15° projections. The second part compares the influence of the photoelectric cross section databases over a plethora of x-ray beams and the three breast thicknesses, but only for the 0° projection. Finally, the third part investigates the MGD variation for heterogeneous and anthropomorphic breast phantoms.

2.3. Input data

The polyenergetic x-ray spectra were generated from the model developed by Hernandez *et al* (Hernandez *et al* 2017), using the MASMICS and TASMICS programs for molybdenum and tungsten anodes, respectively. The adipose, glandular and skin tissue compositions and mass densities were taken from Hammerstein *et al* (Hammerstein *et al* 1979). The composition and mass density of the other materials was retrieved from the NIST website (Berger *et al* 2010).

The mass attenuation coefficients of all materials were extracted directly from PENELOPE's database (Salvat 2019). Regarding the physics models for photon transport, the PENELOPE code

5

employs Rayleigh scattering cross sections from the EPDL97 (Cullen *et al* 1997), which are based on the form-factor approximation with anomalous form factors. For the simulation of Compton scattering, PENELOPE uses cross sections obtained from the relativistic impulse approximation (Ribberfors 1975, 1976), which accounts for binding effects and Doppler energy broadening (Wang *et al* 2020 and references therein). On the other hand, PENELOPE versions 2014 and 2018 incorporate Sabbatucci and Salvat's renormalized photoelectric cross sections, but PENELOPE version 2018 (Salvat 2019) offers as an option to replace them with the unnormalized photoelectric cross sections. The simulations reported below were done with both the unnormalized and the renormalized databases.

2.4. Dosimetric quantities and validation

The dosimetric quantities of interest in mammography, namely incident air kerma (K_{air}), MGD and normalized glandular dose (DgN) were calculated as described next.

For the K_{air} calculations, an air cylinder (2 cm radius, 0.2 mm height, 4 cm away from the chest wall) was added, mimicking an ionization chamber. The compression plate was defined in the geometry, being located 40 cm above the air cylinder, but without the breast. Since the simulations exclude electron transport (Andreo 2019), the electrons created in the volume of interest deposit their kinetic energy within it. The interaction forcing variance-reduction technique was activated (forcing factor of 10^3) to shorten the simulation time needed to reach the desired statistical (type A) relative uncertainty (≈0.15%, 1 standard deviation). The tally *TallyKermaCalc* in penEasy (Massera and Tomal 2018) delivered the mean energy per photon transferred to the air volume.

In turn, the MGD was obtained following the geometry proposed in TG-195 (Sechopoulos *et al* 2015). In this case, the breast was modeled as described in section 2.1. The energy deposited in the glandular tissue was determined weighting the energy deposited in the homogeneous breast mixture (interaction-by-interaction) by the relative contribution of the mass energy-absorption coefficients (Seltzer 1993, Berger *et al* 2010) of the glandular tissue to the adipose/glandular mixture (*G*-factor), as proposed by Boone (1999). The energy deposited in the glandular tissue was evaluated, interaction-by-interaction (Wilkinson and Heggie 2000, Sechopoulos *et al* 2015), which is a well-established simulation method to account for the variation of local photon energy in breast dosimetry (Boone 1999, Wilkinson and Heggie 2000, Sechopoulos *et al* 2015, Sarno *et al* 2017). This quantity was estimated resorting to the tally *TallyEnergyDepositionGland* in penEasy (Massera and Tomal 2018). The MGD was computed from the energy deposited in the glandular tissue divididied by the corresponding mass of glandular tissue within the breast. Finally, the DgN is defined as the ratio

$$DgN = \frac{MGD}{K_{air}} \tag{1}$$

where the MGD and K_{air} values were obtained with the same incident x-ray beam, following the geometry explained above, in two independent simulations (Massera and Tomal 2018, 2020).

The glandular depth-dose distribution, GDD(z), in the breast was simulated by slicing the homogeneous mixture within the breast in 10 equally-thick layers. The glandular dose was calculated for each layer as a function of the depth z, starting from the breast upper entrance.

The simulation results were validated following the TG-195 case 3 (Sechopoulos *et al* 2015), which consisted of various test types, as briefly outlined here (we encourage the reader to consult the original publication for more details). (Ia) Energy deposited in the breast (not included in this study) and (Ib) MGD calculation for monoenergetic and polyenergetic x-ray beams. (Ic) Energy deposited in 7 cubic volumes of interest (VOIs, $2 \times 2 \times 1$ cm³) inside the breast. Energy from (IIa) primary and (IIb) scattered x-rays incident on a 2×2 cm² scoring plane 1.5 cm below the support plate. (IIIa) and (IIIb), similar to (IIa) and (IIb), respectively, but with a pencil beam. To simplify the visualization of the trends, the mean results from the MC codes presented in TG-195 were considered. For the TG-195 related comparisons, 4 simulations with independent random-number sequences (Badal and Sempau 2006) consisting of 4×10^8 primary photons were performed in order to estimate the statistical (type A) uncertainty (batch method, for practical reasons). The final results were calculated from the mean and standard deviation of the simulation outputs (Sechopoulos *et al* 2018). Typical simulation times were around 30 min (processor Intel Core™ i7 7700 CPU @ 3.6 GHz). For the MGD and K_{air} simulations, the statistical uncertainties were kept below 0.2% (1 standard deviation, history-by-history method). Figure 2 summarizes the breast models employed in this work and the respective section.
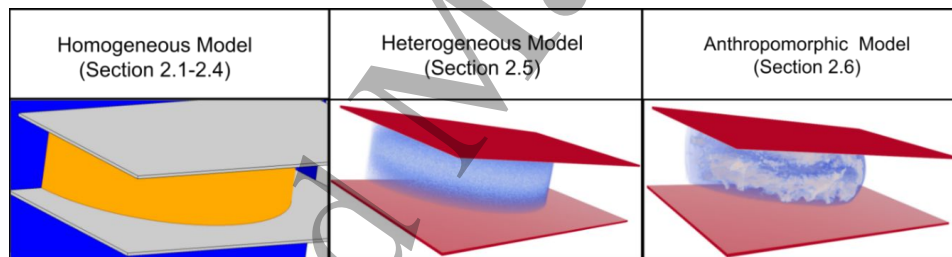
Figure 2. Breast models used in this work with the respective section.

2.5. Simplified heterogeneous models

To address the relation between the glandular tissue distribution inside the breast and the photoelectric cross section databases, simplified heterogeneous models were developed with voxels of 0.5 mm side length. The geometry is similar from section 2.2, except the block of water which is absent. The phantoms have a semi-cylindrical cross section (10 cm radius) including a 1.5 mm skin thickness layer. The central volume consists of a random distribution of glandular and adipose tissues. The random sampling started with the nominal glandular volume percentage, then the central breast region was divided into semi-cylindrical slices (Z direction), one for each voxel layer in depth. Afterwards, the number of glandular voxels for each slice was determined, based on the nominal glandular content, by random sampling from a normal distribution with mean C and standard deviation SD (Tucciariello *et al* 2021). With the number of glandular voxels in a specific layer, their location was sampled from a uniform distribution (X and Y coordinates). The remaining

7

voxels were regarded as adipose tissue. In this study, three values of C were included: ⅓, ½ and ⅔ the breast thickness, representing "lower", "middle" and "upper" glandular tissue distributions, where the SD was fixed at ⅙ of the breast thickness for all cases. This is a simplified model that enables the comparison between distinct glandular tissue distributions over depth, a more realistic case is covered in the upcoming section (Hernandez *et al* 2015, Fedon *et al* 2021). Three breast thickness (and x-ray spectra) were dealt with: 2 cm (W/Rh 25 kV), 5 cm (W/Rh 28 kV) and 8 cm (W/Ag 32 kV), with three glandular volume percentages: 1%, 20% and 40%, totaling 27 combinations. The number of simulated primary photon histories was 10^9. Unlike in the case of the homogeneous models, the glandular dose for heterogeneous models was determined only for the voxels composed by glandular tissue and obtained without the *G* factor.

For the 5 cm breast, 20% glandular volume percentage and lower/upper distributions, we also scored the photon energy spectra in glandular voxels at three depths: 1 cm, 2.5 cm and 4 cm.

2.6. Anthropomorphic models

The case of anthropomorphic breast phantoms was considered to quantify the impact of the tissue distribution inside the breast. The heterogeneous breast models were generated with the BreastPhantom software (Graff 2016) from a modified pipeline included in the VICTRE clinical virtual trial (Badano *et al* 2018, Sharma *et al* 2019). One of the modifications was a script to transform the phantom data to the penEasy voxel format. A total of five breast models were studied with a glandular weight percentage (breast glandularity) varying from approximately 22.9% to 23.5%. These small variations are attributed to the random tissue sampling by the algorithm when a computational breast with glandular volume percentage of 20% is generated. The skin thickness was set to 1.5 mm, and a voxel resolution of 0.5 mm was selected. Moreover, generated tissues that were neither glandular, skin nor adipose were classified as adipose. The five models were compressed until they reached a thickness of 5 cm using the BreastCompress program (Sharma *et al* 2019) and cropped to remove uncompressed tissues, mainly muscle (BreastCrop program) (Sharma *et al* 2019). The average (standard deviation) for the compressed breast models volumes were 628(5) cm³, and presented an averaged area (volume divided by height) of 126(1) cm². 8 simulations were done for each model (batch method uncertainty, while maintaining the same voxel distribution for each model), using the unnormalized and renormalized photoelectric cross sections. Each simulation involved 2×10^{10} photon histories with their initial energies sampled from a Mo/Mo 30 kV spectrum. Like section 2.5, the glandular dose was determined directly (without the G factor).

3. Results and discussion

3.1. Comparison of mass attenuation and mass energy-absorption coefficients

The mass attenuation (μ/ρ) and mass energy-absorption (μ_{en}/ρ) coefficients of the analyzed photon-atom cross-section databases are compared in Figure 3 for the energy range of interest in mammography. The μ_{en}/ρ coefficients were calculated with the *mutren* routine from PENELOPE

(Salvat 2019). The relative differences between the results obtained with the renormalized and unnormalized photoelectric cross sections are plotted following the convention

$$\text{Rel. diff.} = \frac{\text{renormalized} - \text{unnormalized}}{\text{unnormalized}} \times 100\% \qquad (2)$$
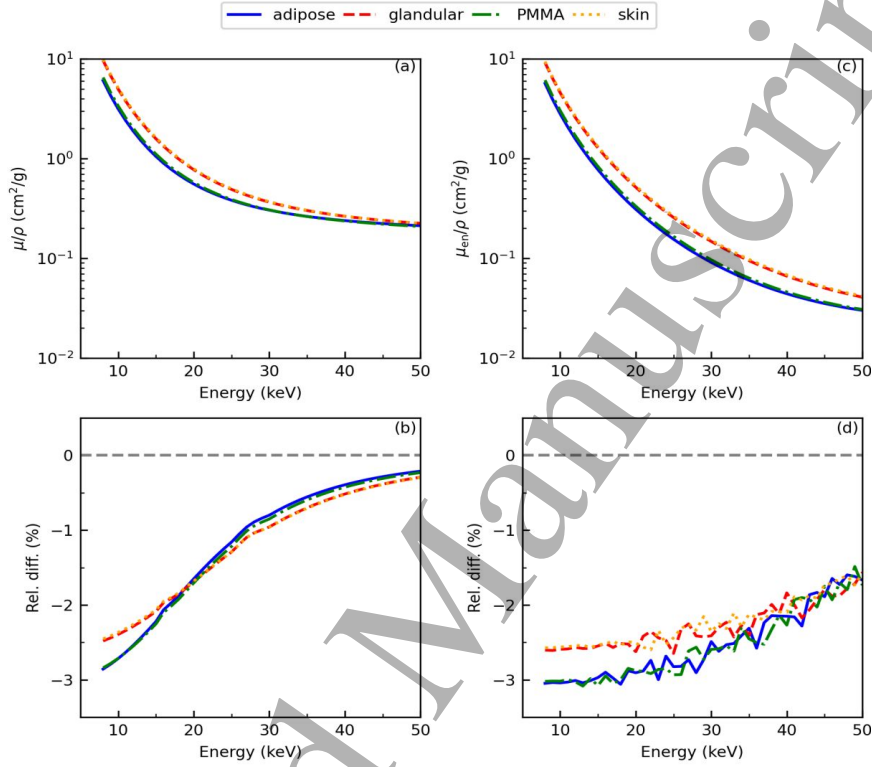

Figure 3. (a) Mass attenuation and (c) mass energy-absorption coefficients for the indicated tissues, taken from the unnormalized cross section database. (b)/(d) Corresponding relative differences, equation (2), between the simulation results of the renormalized and unnormalized databases for the same materials.

In both cases (Figures 3a and 3c), the values decrease monotonously with energy, which is expected given the low equivalent atomic number of the considered materials. The relative difference for μ/ρ between the databases (Figure 3b) decreases with energy because the probability of Compton interactions increases and becomes dominant above several tens of keV. However, in the case of μ_{en}/ρ (Figure 3d) the relative differences stay rather constant because the photoelectric effect is the main interaction mechanism that contributes to energy deposition, despite being less likely to occur for higher energies (Andreo *et al* 2017). It is interesting to note that the adipose/PMMA and skin/glandular curves are clearly distinguishable. This pattern can be understood recalling the elemental compositions of these materials: adipose tissue and PMMA have Carbon as the main constituent element (fraction by weight), while Oxygen is the main constituent of glandular tissue and skin. In addition, the fluctuations observed in Figure 3d can be traced to the uncertainty of the μ_{en}/ρ values (default values of 0.1%) which is comparable to the difference between the μ_{en}/ρ for the unnormalized and renormalized cross section databases.

9

3.2.   Validation and AAPM TG-195

When comparing the results of this work, for both unnormalized and renormalized photoelectric cross sections, and those reported in TG-195, the relative differences were computed as

$$\text{Rel. diff.} = \frac{This\ work\ -\ TG195}{TG195} \times 100\% \qquad (3)$$

Figure 4 shows the relative differences of MGD obtained with the renormalized and unnormalized photoelectric cross sections with respect to the TG-195 results in test Ib (Sechopoulos *et al* 2015) for 0° and 15° projections. In order to keep a clear view, test Ia was not included in the figure because it follows a similar trend as test Ib. The results for the unnormalized cross sections are closer to TG-195 than the renormalized ones, with maximum deviations of 0.13(6)% and 0.74(5)%, respectively. This was expected because, to our knowledge, all MC codes utilized in TG-195 implement Scofield's unnormalized photoelectric cross sections. The small deviations between the relative differences in MGD for the 0° and 15° projections can be explained by the higher variation of the MGD values provided by the MC codes of TG-195 for the large-angle projections.
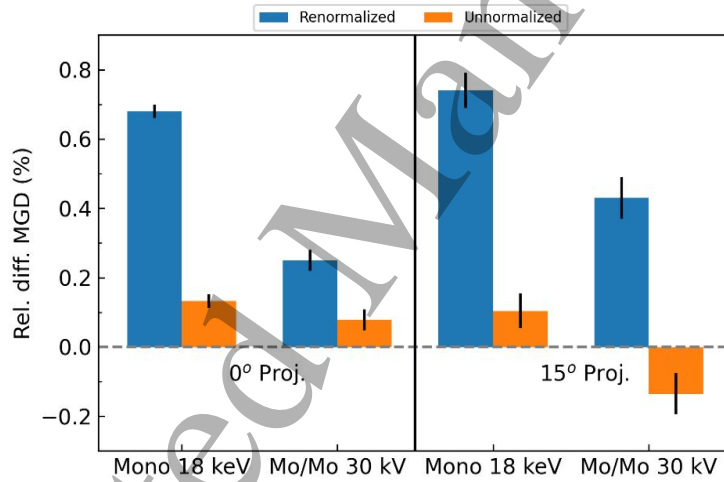
Figure 4. Relative difference between the MGD values computed with the renormalized and unnormalized cross sections for the photoelectric effect compared with the mean results from TG-195 (Sechopoulos et al 2015). Values computed for monoenergetic and polyenergetic beams, for both 0° and 15° projections. Breast: 5 cm thick, 20% glandular fraction.

The boxplots in Figure 5 summarize the relative differences between the mean results from TG-195 and the simulated results of the tests Ic, II and III for the energy incident in a scoring plane, as described in TG-195 case 3, considering the two photoelectric cross section databases. For each test, it comprises the monoenergetic and polyenergetic spectra for the 0° and 15° projections. The results for each test (Ic, II a and b, and III a and b) were condensed and expressed in a boxplot graph format to facilitate the visualization. As can be observed in Figure 5, the data distributions ensuing from the simulations carried out with the analyzed databases clearly differ, being the differences smaller when the unnormalized photoelectric cross-section are used. Again, this tendency can be ascribed to the cross sections in the MC codes employed in TG-195. For instance, PENELOPE version 2006

was used in TG-195, while the renormalized cross sections were implemented starting with version 2014. The results obtained with the renormalized cross sections were in general higher than the TG-195 due to the lower mass attenuation coefficients (see Figure 3). The unnormalized results tend to be lower than the TG-195 for the tests II and III (Figures 5(b) and (c), respectively), with differences up to 5% (test III). Although the higher deviations compared to the other tests, the unnormalized values are still in better agreement with TG-195 than the normalized ones.
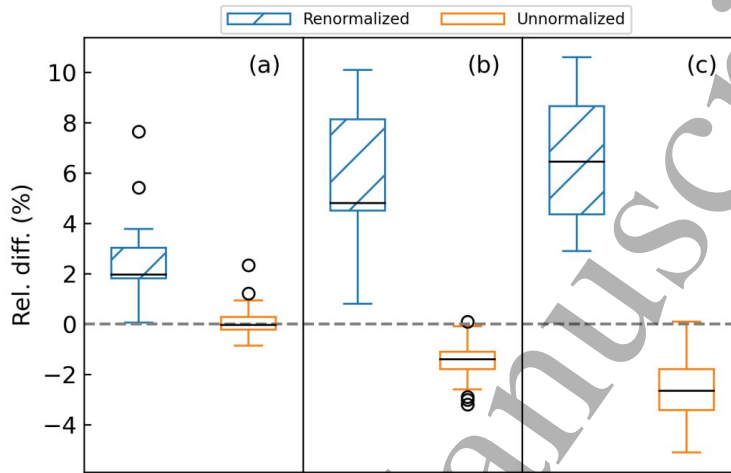

Figure 5. Relative differences between -TG-195 mean results for each test (explained further) across the different Monte Carlo codes and renormalized (hatched, red) and unnormalized (open, blue) photoelectric cross sections. (a) Test Ic: energy deposited in the VOIs inside the breast. (b) Test II: energy fluence for regions of interest under the support plate. (c) Test III: similar to (b) but with a pencil beam. Center line: median, lower and upper box edges: first and third quartile, whiskers: 1.5 times the interquartile range, and circles are outliers.

3.3. Mean glandular dose and incident air kerma

Figure 6a shows the MGD values for breasts with a 20% glandular fraction and thicknesses of 2 cm, 5 cm and 8 cm as a function of photon energy for monoenergetic x-rays. Figure 6c displays K_{air} for a 5 cm breast as a function of photon energy. The dependence of the incident air kerma (K_{air}) on photon energy follows a similar trend for the other breast thicknesses, but their values are corrected by the inverse-square law to account for the beam divergence. These results were obtained using the unnormalized photoelectric cross sections. Figure 6b and 6d present the relative differences between the results of MGD and K_{air}, respectively, calculated with the renormalized and unnormalized photoelectric cross sections. In both figures, data above (below) the dashed horizontal line indicate MGD or K_{air} values higher (lower) for renormalized cross sections. The MGD and K_{air} are higher for the renormalized cross sections at low energies up to approximately 12-20 keV, when the unnormalized values become higher. This behaviour is explained by Figure 3. The relative difference for μ_{en}/ρ between the databases decreases with energy, whereas for μ/ρ it remains almost constant.
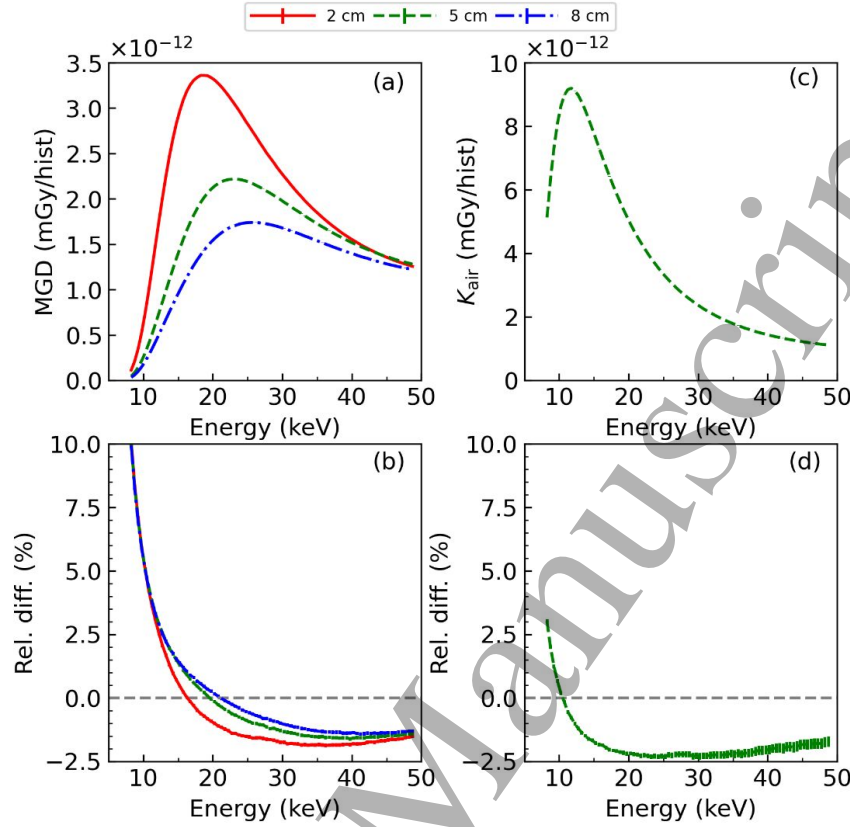
Figure 6. (a) MGD values for breasts of the indicated thicknesses simulated with the unnormalized photoelectric cross sections. (c) K_{air} calculated for the 5 cm breast. The relative differences for the analyzed photoelectric cross section databases are plotted for MGD (b) and K_{air} (d).

3.4. Normalized glandular dose

As already mentioned, the DgN was calculated by the ratio MGD/K_{air}, and it is shown in Figure 7a for monoenergetic x-rays and three breast thicknesses. Figure 7b depicts the relative differences of renormalized vs unnormalized cross sections, equation (2). The trend is a combination of the results from Figure 6b and 6d, i.e. the ratio of the MGD and K_{air} differences. The renormalized DgN values are systematically higher than the unnormalized ones from 8.25 keV to 48.75 keV. Since DgN is the ratio between MGD and K_{air}, the pattern observed in Figure 7b can be understood recalling the discussion in section 3.3.

Figure 7. (a) DgN computed using the unnormalized photoelectric cross section database for monoenergetic photon beams and three breast thicknesses (20% glandular fraction). (b) Relative differences between the DgN calculated with the renormalized and unnormalized photoelectric cross sections, as a function of photon energy.

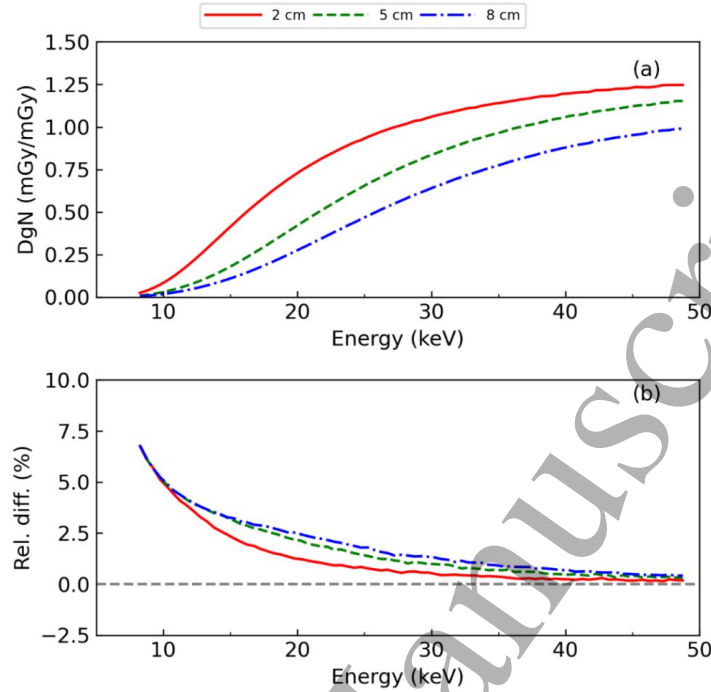The DgN values for polyenergetic spectra simulated with the unnormalized photoelectric cross sections are displayed in Figure 8a for various x-ray spectra and three breast thicknesses. Figure 8b plots the relative difference of the DgN results simulated using the two photoelectric cross section databases. From Figure 8a it is evident that DgN depends on the breast thickness and the incident x-ray spectrum (anode/filter combination and tube potential). The DgN values computed with the two databases vary from ≈0.5% for the high-energy beams employed in contrast-enhanced mammography to ≈2.5% for conventional mammography. This is a consequence of the integration of the monoenergetic DgN over the x-ray spectra because the largest relative differences happen for low-energy photons (see Figure 7). This systematic uncertainty on the DgN estimation introduced by the selection of cross section database is, in principle, below the threshold established by the IAEA Report TRS 457 (IAEA 2007), where uncertainties up to 7% are tolerated in some conditions. However, as pointed out by Dance and Sechopoulos (2016), there are other sources of systematic uncertainty in breast dosimetry that should be evaluated as well, such as the elemental composition of breast tissues and the adopted breast models. Even for a specific breast thickness, the systematic uncertainties could vary depending on the imaging modality owing to the differences in the respective x-ray spectra.

It is worth mentioning that another important source of systematic errors associated to MC-based breast dosimetry data is the limited and old information on breast tissue composition, which affects significantly the MGD estimation. However, its impact on the systematic uncertainty from

13

the photoelectric cross sections may not be important because the variation between the unnormalized and renormalized databases is modified only slightly by the composition for low atomic number materials in the mammographic energy range.
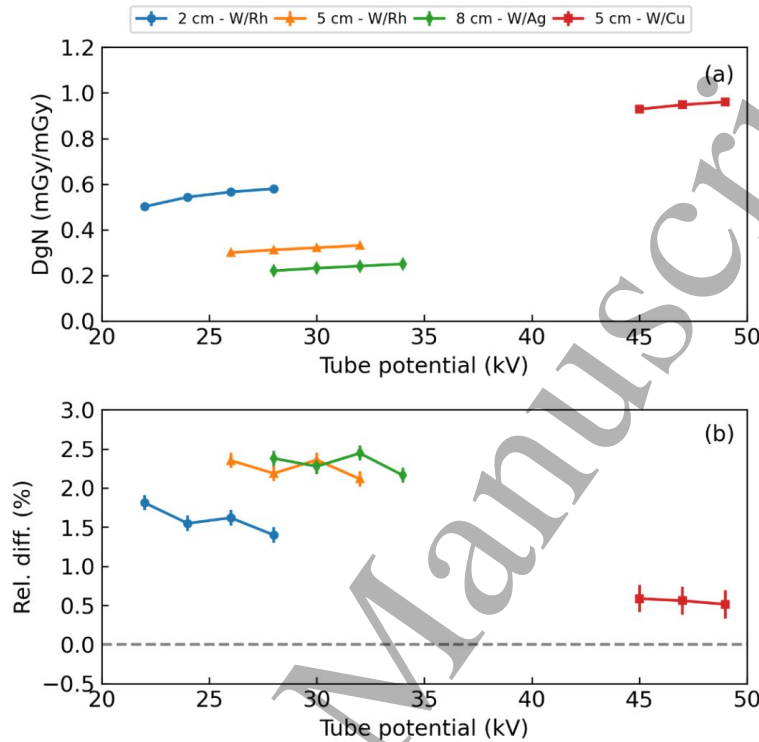
Figure 8. (a) DgN values calculated with the unnormalized photoelectric cross sections for the indicated x-ray spectra and breast thicknesses. (b) DgN relative difference between the renormalized and unnormalized photoelectric cross sections, matching the spectra and thicknesses from (a). In most cases, the error bars are not visible because they are smaller than the symbols.

3.5.   Glandular depth dose

Figure 9a shows the glandular depth-dose distribution, GDD(z), simulated with the unnormalized photoelectric cross sections. Each bin corresponds to a depth interval. The results were computed for a polyenergetic beam, with a Mo/ Mo Anode/Filter combination and 30 kV tube potential. This combination represents the average beam quality used for imaging a breast with this thickness (Sechopoulos *et al* 2015). As anticipated, GDD(z) decreases with depth z due to photon attenuation through the breast tissues. The corresponding relative difference between the renormalized and unnormalized photoelectric cross sections, equation (2), is plotted in Figure 9b. The differences between the cross sections over the MGD varies with the breast depth, being higher for the unnormalized near the breast entrance and changing progressively as the depth increases. At the bottom of the breast, the variations can be as high as 4%. This is expected from the mass attenuation coefficients of the two databases (Figure 3): since μ/ρ for the renormalized cross sections is lower, photons have a higher probability to interact at larger depths in the breast as

14

compared to the unnormalized cross sections. The results for thicker breast were not included because a similar Rel. diff. GDD behaviour was observed between 8 cm and 5 cm breasts, this is mainly due to the more energetic spectrum employed for thicker breasts. These findings highlight that, together with the thickness of the breast, the x-ray spectrum is an important factor to dictate the differences for the GDD between the cross-section databases.
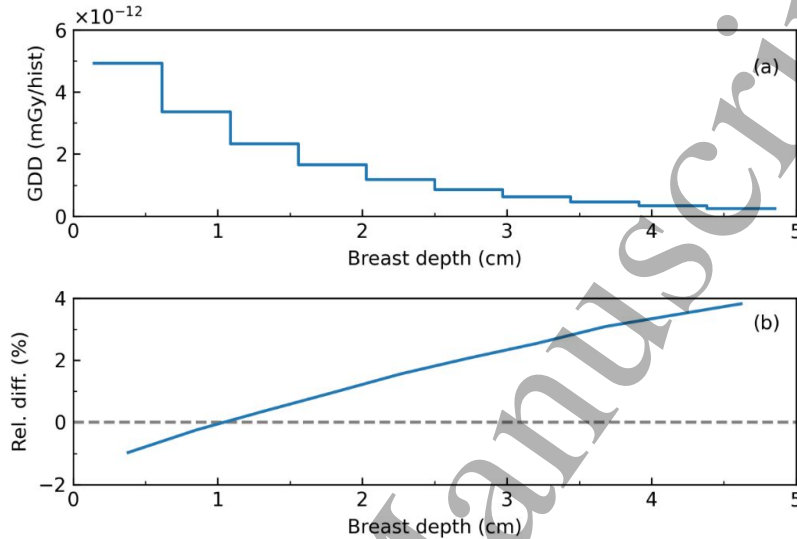

Figure 9. (a) GDD(z) obtained with the unnormalized photoelectric cross sections. (b) Relative differences for glandular depth dose values as function of the breast depth computed between the two photoelectric cross section databases. Breast: 5 cm thick, 20% glandular fraction.

3.6.   Glandular dose in simplified heterogeneous models

Table 1 summarizes the relative differences for the mean glandular dose, obtained with the simplified heterogeneous breast models, between the normalized and unnormalized cross section databases. The results indicate that the breast glandular content provides a minor impact over the MGD differences compared to the tissue distribution inside the breast. The highest discrepancies occur for thicker breasts when most of the glandular tissue is located towards the bottom of the breast (up to 1.85(2)%).

Figure 10 compares the energy spectrum of the x-ray beam at various depths for a 5 cm 20% glandular volume breast, considering two glandular tissue distributions: concentrated either at the top of the breast or towards the bottom. For both configurations, the x-ray beam hardening is evident as the depth increases. Additionally, Figures 10d and 10h reveal that the disagreement between the scored spectra for the analyzed cross section databases grows with depth, explaining the results contained in Table 1, where the largest deviations for the MGD occur when most of the glandular tissue is located towards the bottom of the breast. The relative difference between the recorded spectra decreases with higher energies, and this is due to the attenuation coefficients values (as discussed in section 3.1 and shown in Figure 3b). The uncertainty changes with depth owing to the number of glandular voxels in that particular location.

15

Table 1. MGD relative differences between the unnormalized and renormalized cross section databases for various breast thickness, glandular volume percentages and glandular tissue distributions.

Breast thickness	Glandular volume percentage (%)	Glandular distribution center	Rel. diff.
2 cm	1	Lower	-0.06(9)%
		Middle	-0.47(8)%
		Upper	-0.86(7)%
	20	Lower	0.02(2)%
		Middle	-0.38(2)%
		Upper	-0.80(2)%
	40	Lower	0.04(1)%
		Middle	-0.36(1)%
		Upper	-0.75(1)%
5 cm	1	Lower	1.49(9)%
		Middle	0.70(7)%
		Upper	-0.13(5)%
	20	Lower	1.43(2)%
		Middle	0.71(2)%
		Upper	0.00(1)%
	40	Lower	1.48(1)%
		Middle	0.76(1)%
		Upper	0.05(1)%
8 cm	1	Lower	1.76(9)%
		Middle	0.95(7)%
		Upper	0.18(5)%
	20	Lower	1.85(2)%
		Middle	1.00(1)%
		Upper	0.20(1)%
	40	Lower	1.82(2)%
		Middle	1.01(1)%
		Upper	0.23(1)%

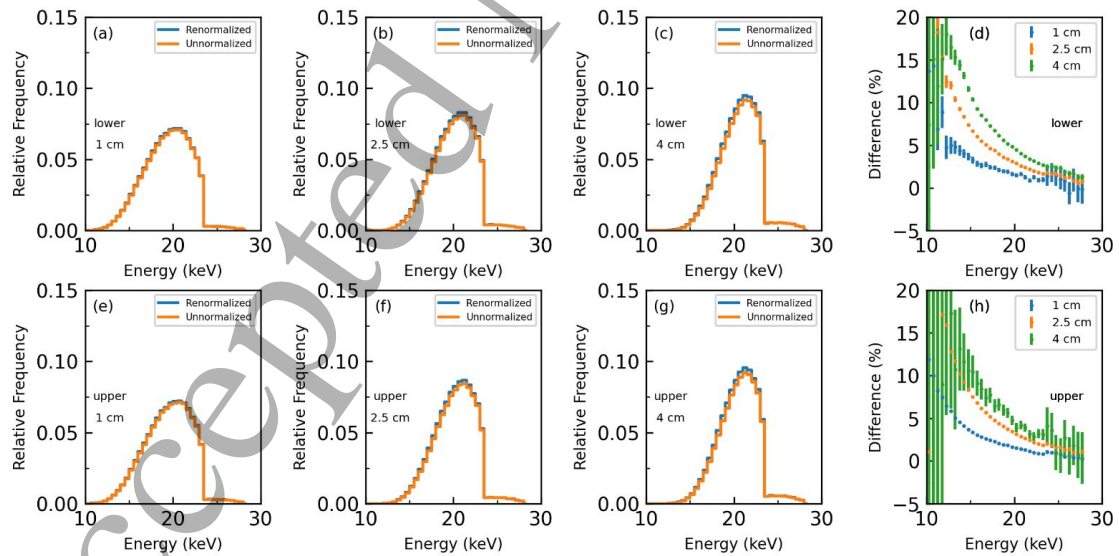*Figure 10. (a)-(c) and (e)-(g) scored photon spectrum in glandular tissue for renormalized and unnormalized cross sections, at different depths for a 5 cm thick 20% glandular volume breast. Figures (a)-(d) and (e)-(h) show, respectively, the results when the glandular tissue is located towards the bottom and surface of the breast. Figures (d) and (h) compare the relative differences in frequency for each energy bin.*

16

3.7.   Mean glandular dose and anthropomorphic breast models

Table**Error! Reference source not found.** 2 displays the differences, calculated with equation (2), for the MGD between the two cross section databases for the five anthropomorphic phantoms, represented by a slight variation of glandular fraction resulting from the phantom model. A non-negligible variation between the relative MGD difference for the renormalized and unnormalized cross sections is found in each case, although all models have a similar glandular fraction, the same compressed breast thickness, and they were irradiated with the same x-ray spectrum. The statistical uncertainties were around 0.001%. The origin of this behaviour might be the glandular tissue distribution inside the breast. The heterogeneous models present some regions of high glandular content while other regions are predominantly adipose tissue (Huang *et al* 2011, Hernandez *et al* 2015, Sechopoulos *et al* 2012). As discussed in section 3.5, the relative glandular dose difference for the two cross section databases varies with depth. Therefore, the glandular dose distribution inside the breast, especially in depth, could be one explanation for the MGD difference between the cross-section models.

Table 2. Relative differences for the MGD across five anthropomorphic breast phantoms (with slight variation on glandular mass proportions) between the renormalized and unnormalized cross sections.

Breast Model	Glandularity (%)	Rel. diff.
1	23.5	0.789(1)%
2	23.3	0.813(1)%
3	23.1	0.824(1)%
4	23.0	0.761(1)%
5	22.9	0.680(1)%

4. Conclusions

The photoelectric effect is the photon-atom interaction mechanism responsible for most of the energy deposition by mammography x-ray beams. Consequently, the dosimetry results in the MC simulations are sensitive to the employed database for this interaction process. The present work demonstrates that the adoption of the newer renormalized photoelectric cross sections, which apply the normalization screening correction, has a significant impact on the simulated MGD and DgN. In addition, a comparison was made with the TG-195 values obtained with MC codes that implement the unnormalized cross sections. Hence, there is a considerable systematic uncertainty for low-energy beams, mainly present in the mammography energy interval. This effect is smaller for techniques that use x-rays beams of higher energy, such as contrast-enhanced mammography and breast CT. Moreover, the effects as a function of the depth in the breast as well as the anthropomorphic phantoms were also addressed. It is important to remark that the aim of our investigation was not to endorse one of the databases, but rather to quantify the possible differences they bring about when applied to breast dosimetry. Consequently, the discrepancies brought about by the selection of photoelectric cross-sections should be considered in the interpretation of the simulation results, specifically regarding the systematic uncertainties, in the dosimetry, risk assessment and optimization studies recommended by the international guidelines.

Unfortunately, it is not possible to encompass all the conclusions of this work in a single result due to the large variety of parameters and quantities (e.g. x-ray spectrum, breast characteristics, MGD, K_{air}, DgN, etc.) involved. However, since the DgN and MGD are the most used quantities in breast dosimetry studies, our results highlight that for conventional x-ray spectra employed in mammography differences of up to 2.5% appear in the DgN values calculated with the renormalized and unnormalized databases. The present simulations were carried out with the PENELOPE MC code, but similar findings are anticipated if other codes were employed that offer (or might offer in the future) to choose between renormalized and unnormalized photoelectric cross sections.

Acknowledgements

References

Aguirre E, David M, deAlmeida C E and Bernal M A 2016 Impact of photon cross section uncertainties on Monte Carlo-determined depth-dose distributions *Phys. Med.* **32** 1065–71. DOI:10.1016/j.ejmp.2016.08.002

Allison J, Amako K, Apostolakis J, Arce P, Asai M, Aso T, Bagli E, Bagulya A, Banerjee S, Barrand G, Beck B R, Bogdanov A G, Brandt D, Brown J M C, Burkhardt H, Canal P, Cano-Ott D, Chauvie S, Cho K, Cirrone G A P, Cooperman G, Cortés-Giraldo M A, Cosmo G, Cuttone G, Depaola G, Desorgher L, Dong X, Dotti A, Elvira V D, Folger G, Francis Z, Galoyan A, Garnier L, Gayer M, Genser K L, Grichine V M, Guatelli S, Guèye P, Gumplinger P, Howard A S, Hřivnáčová I, Hwang S, Incerti S, Ivanchenko A, Ivanchenko V N, Jones F W, Jun S Y, Kaitaniemi P, Karakatsanis N, Karamitros M, Kelsey M, Kimura A, Koi T, Kurashige H, Lechner A, Lee S B, Longo F, Maire M, Mancusi D, Mantero A, Mendoza E, Morgan B, Murakami K, Nikitina T, Pandola L, Paprocki P, Perl J, Petrović I, Pia M G, Pokorski W, Quesada J M, Raine M, Reis M A, Ribon A, Ristić Fira A, Romano F, Russo G, Santin G, Sasaki T, Sawkey D, Shin J I, Strakovsky I I, Taborda A, Tanaka S, Tomé B, Toshito T, Tran H N, Truscott P R, Urban L, Uzhinsky V, Verbeke J M, Verderi M, Wendt B L, Wenzel H, Wright D H, Wright D M, Yamashita T, Yarba J, et al 2016 Recent developments in Geant4 *Nucl. Instruments Methods Phys. Res. Sect. A Accel. Spectrometers, Detect. Assoc. Equip.* **835** 186–225. DOI:10.1016/j.nima.2016.06.125

Andreo P 2019 Data for the dosimetry of low- and medium-energy kV x rays *Phys. Med. Biol.* **64** 205019. DOI:10.1088/1361-6560/ab421d

Andreo P, Burns D T, Nahum A E, Seuntjens J and Attix F H 2017 *Fundamentals of Ionizing Radiation Dosimetry* (John Wiley & Sons)

Arce P, Bolst D, Bordage M-C, Brown J M C, Cirrone P, Cortés-Giraldo M A, Cutajar D, Cuttone G, Desorgher L, Dondero P, Dotti A, Faddegon B, Fedon C, Guatelli S, Incerti S, Ivanchenko V, Konstantinov D, Kyriakou I, Latyshev G, Le A, Mancini-Terracciano C, Maire M, Mantero A, Novak M, Omachi C, Pandola L, Perales A, Perrot Y, Petringa G, Quesada J M, Ramos-Méndez J, Romano F, Rosenfeld A B, Sarmiento L G, Sakata D, Sasaki T, Sechopoulos I, Simpson E C, Toshito T and Wright D H 2021 Report on G4-Med, a Geant4 benchmarking system for medical physics applications developed by the Geant4 Medical Simulation Benchmarking Group *Med. Phys.* **48** 19–56.

18

DOI:https://doi.org/10.1002/mp.14226

Badal A and Sempau J 2006 A package of Linux scripts for the parallelization of Monte Carlo simulations *Comput. Phys. Commun.* **175** 440–50. DOI:10.1016/J.CPC.2006.05.009

Badano A, Graff C G, Badal A, Sharma D, Zeng R, Samuelson F W, Glick S J and Myers K J 2018 Evaluation of digital breast tomosynthesis as replacement of full-field digital mammography using an in silico imaging trial *JAMA Netw. Open* **1** e185474. DOI:10.1001/jamanetworkopen.2018.5474

Berger M J, Hubbell J H, Seltzer S M, Chang J, Coursey J S, Sukumar R, Zucker D S and Olsen K 2010 Tables of X-Ray Mass XCOM: Photon Cross Sections Database. National Institute of Standards and Technology (NIST)

Boone J M 1999 Glandular Breast Dose for Monoenergetic and High-Energy X-ray Beams: Monte Carlo Assessment *Radiology* **213** 23–37. DOI:10.1148/radiology.213.1.r99oc3923

Boone J M 2002 Normalized glandular dose (DgN) coefficients for arbitrary x-ray spectra in mammography: Computer-fit values of Monte Carlo derived data *Med. Phys.* **29** 869–75. DOI:10.1118/1.1472499

Cullen D E, Hubbell J H and Kissel L 1997 *EPDL97: the evaluated photo data library `97 version Report UCRL 50400* vol 6, rev 5 (Livermore, CA). DOI:10.2172/295438

Cunha D M, Tomal A and Poletti M E 2010 Evaluation of scatter-to-primary ratio, grid performance and normalized average glandular dose in mammography by Monte Carlo simulation including interference and energy broadening effects *Phys. Med. Biol.* **55** 4335–59. DOI:10.1088/0031-9155/55/15/010

Dance D R 1990 Monte-Carlo calculation of conversion factors for the estimation of mean glandular breast dose *Phys. Med. Biol.* **35** 1211–20. DOI:10.1088/0031-9155/35/9/002

Dance D R and Sechopoulos I 2016 Dosimetry in x-ray-based breast imaging *Phys. Med. Biol.* **61** R271–304. DOI:10.1088/0031-9155/61/19/R271

Dance D R, Skinner C L and Alm Carlsson G 1999 Breast dosimetry *Appl. Radiat. Isot.* **50** 185–203. DOI:10.1016/S0969-8043(98)00047-5

Dance D R, Skinner C L, Young K C, Beckett J R and Kotre C J 2000 Additional factors for the estimation of mean glandular breast dose using the UK mammography dosimetry protocol *Phys. Med. Biol.* **45** 3225–40. DOI:10.1088/0031-9155/45/11/308

Dance D R, Young K C and van Engen R E 2009 Further factors for the estimation of mean glandular dose using the United Kingdom, European and IAEA breast dosimetry protocols *Phys. Med. Biol.* **54** 4361–72. DOI:10.1088/0031-9155/54/14/002

Fedon C, Caballo M, García E, Diaz O, Boone J M, Dance D R and Sechopoulos I 2021 Fibroglandular tissue distribution in the breast during mammography and tomosynthesis based on breast CT data: A patient-based characterization of the breast parenchyma *Med. Phys.* **48** 1436–47. DOI:10.1002/mp.14716

Fedon C, Longo F, Mettivier G and Longo R 2015 GEANT4 for breast dosimetry: parameters optimization study *Phys. Med. Biol.* **60** N311–23. DOI:10.1088/0031-9155/60/16/N311

Graff C G 2016 A new, open-source, multi-modality digital breast phantom *Medical Imaging 2016: Physics of Medical Imaging* vol 9783, ed D Kontos, T G Flohr and J Y Lo (SPIE) p 978309. DOI:10.1117/12.2216312

Hammerstein R G, Miller D W, White D R, Masterson M E, Woodard H Q and Laughlin J S 1979 Absorbed Radiation Dose in Mammography *Radiology* **130** 485–91. DOI:10.1148/130.2.485

Hernandez A M, Seibert J A and Boone J M 2015 Breast dose in mammography is about 30% lower when realistic heterogeneous glandular distributions are considered *Med. Phys.* **42** 6337–48.

DOI:10.1118/1.4931966

Hernandez A M, Seibert J A, Nosratieh A and Boone J M 2017 Generation and analysis of clinically relevant breast imaging x-ray spectra *Med. Phys.* **44** 2148–60. DOI:10.1002/mp.12222

Huang S-Y, Boone J M, Yang K, Kwan A L C and Packard N J 2008 The effect of skin thickness determined using breast CT on mammographic dosimetry *Med. Phys.* **35** 1199–206. DOI:10.1118/1.2841938

Huang S-Y, Boone J M, Yang K, Packard N J, McKenney S E, Prionas N D, Lindfors K K and Yaffe M J 2011 The characterization of breast anatomical metrics using dedicated breast CT *Med. Phys.* **38** 2180–91. DOI:10.1118/1.3567147

Hubbell J H 2006 Review and history of photon cross section calculations *Phys. Med. Biol.* **51** R245--R262. DOI:10.1088/0031-9155/51/13/r15

IAEA 2007 *Dosimetry in Diagnostic Radiology: An International Code of Practice Reports Series No. 457* (Vienna: IAEA)

ICRU 2016 Key Data for Ionizing-Radiation Dosimetry: Measurement Standards and Applications (ICRU Report 90) *J. Int. Comm. Radiat. Units Meas.* **14** NP-NP. DOI:10.1093/jicru/ndw043

Kawrakow I, Mainegra-Hing E, Rogers D W O, Tessier F and Walters B R B 2017 The EGSnrc code system: Monte Carlo simulation of electron and photon transport, Technical Report PIRS-701 *Natl. Res. Counc. Canada*

Massera R T and Tomal A 2018 Skin models and their impact on mean glandular dose in mammography *Phys. Med.* **51** 38–47. DOI:10.1016/j.ejmp.2018.04.009

McEwen M, Burns D, Darienzo M, de Pooter J, Pinto M and Rapp B 2017 *private communication*

Nosratieh A, Hernandez A, Shen S Z, Yaffe M J, Seibert J A and Boone J M 2015 Mean glandular dose coefficients (D(g)N) for x-ray spectra used in contemporary breast imaging systems. *Phys. Med. Biol.* **60** 7179–90. DOI:10.1088/0031-9155/60/18/7179

Pratt R H 1960 Atomic Photoelectric effect at high energies *Phys. Rev.* **117** 1017–28. DOI:10.1103/PhysRev.117.1017

Ribberfors R 1976 Erratum: Relationship of the relativistic Compton cross section to the momentum distribution of bound electron states *Phys. Rev. B* **13** 950–950. DOI:10.1103/PhysRevB.13.950

Ribberfors R 1975 Relationship of the relativistic Compton cross section to the momentum distribution of bound electron states *Phys. Rev. B* **12** 2067–74. DOI:10.1103/PhysRevB.12.2067

Sabbatucci L and Salvat F 2016 Theory and calculation of the atomic photoeffect *Radiat. Phys. Chem.* **121** 122–40. DOI:10.1016/j.radphyschem.2015.10.021

Salvat F 2019 *PENELOPE-2018: A Code System for Monte Carlo Simulations of Electron and Photon Transport* (Issy-les-Mounlineaux, OECD/NEA)

Sarno A, Mettivier G, Di Lillo F and Russo P 2017 A Monte Carlo study of monoenergetic and polyenergetic normalized glandular dose (DgN) coefficients in mammography *Phys. Med. Biol.* **62** 306–25. DOI:10.1088/1361-6560/62/1/306

Sarno A, Mettivier G, Di Lillo F and Russo P 2016 Monte Carlo evaluation of normalized glandular dose coefficients in mammography *Proceedings of the 13th International Workshop on Breast Imaging - Volume 9699* (Springer-Verlag) pp 190–6. DOI:10.1007/978-3-319-41546-8_25

Sarno A, Mettivier G, Di Lillo F, Tucciariello R M, Bliznakova K and Russo P 2018 Normalized glandular dose coefficients in mammography, digital breast tomosynthesis and dedicated breast CT *Phys. Med.* **55** 142–8. DOI:10.1016/j.ejmp.2018.09.002

Scofield J H 1973 *Theoretical photoionization cross sections from 1 to 1500 keV. Report UCRL 51326*

(Livermore, CA). DOI:10.2172/4545040

Sechopoulos I, Ali E S M, Badal A, Badano A, Boone J M, Kyprianou I S, Mainegra-Hing E, McMillan K L, McNitt-Gray M F, Rogers D W O, Samei E and Turner A C 2015 Monte Carlo reference data sets for imaging research: Executive summary of the report of AAPM Research Committee Task Group 195 *Med. Phys.* **42** 5679–91. DOI:10.1118/1.4928676

Sechopoulos I, Bliznakova K, Qin X, Fei B and Feng S S J 2012 Characterization of the homogeneous tissue mixture approximation in breast imaging dosimetry *Med. Phys.* **39** 5050–9. DOI:10.1118/1.4737025

Sechopoulos I, Rogers D W O, Bazalova-Carter M, Bolch W E, Heath E C, McNitt-Gray M F, Sempau J and Williamson J F 2018 RECORDS: improved Reporting of montE CarlO RaDiation transport Studies: Report of the AAPM Research Committee Task Group 268 *Med. Phys.* **45** e1–5. DOI:10.1002/mp.12702

Sechopoulos I, Suryanarayanan S, Vedantham S, D'Orsi C and Karellas A 2006 Computation of the glandular radiation dose in digital tomosynthesis of the breast *Med. Phys.* **34** 221–32. DOI:10.1118/1.2400836

Seltzer S M 1993 Calculation of Photon Mass Energy-Transfer and Mass Energy-Absorption Coefficients *Radiat. Res.* **136** 147–70. DOI:10.2307/3578607

Sempau J, Badal A and Brualla L 2011 A PENELOPE -based system for the automated Monte Carlo simulation of clinacs and voxelized geometries-application to far-from-axis fields *Med. Phys.* **38** 5887–95. DOI:10.1118/1.3643029

Sharma D, Graff C G, Badal A, Zeng R, Sawant P, Sengupta A, Dahal E and Badano A 2019 Technical Note: In silico imaging tools from the VICTRE clinical trial *Med. Phys.* **46** 3924–8. DOI:10.1002/mp.13674

Trevisan Massera R and Tomal A 2020 Estimation of glandular dose in mammography based on artificial neural networks *Phys. Med. Biol.* **65** 095009. DOI:10.1088/1361-6560/ab7a6d

Tucciariello R, Barca P, Sarto D, Lamastra R, Mettivier G, Retico A, Russo P, Sarno A, Traino A and Fantacci M 2021 Voxelized Breast Phantoms for Dosimetry in Mammography *Proceedings of the 14th International Joint Conference on Biomedical Engineering Systems and Technologies - Volume 3: BIOINFORMATICS,* (SciTePress) pp 154–61. DOI:10.5220/0010322901540161

Valdes-Cortez C, Mansour I, Rivard M J, Ballester F, Mainegra-Hing E, Thomson R M and Vijande J 2021 A study of Type B uncertainties associated with the photoelectric effect in low-energy Monte Carlo simulations (accepted manuscript) *Phys. Med. Biol.*

Wang X J, Miguel B, Seuntjens J and Fernández-Varea J M 2020 On the relativistic impulse approximation for the calculation of Compton scattering cross sections and photon interaction coefficients used in kV dosimetry *Phys. Med. Biol.* **65** 125010. DOI:10.1088/1361-6560/ab8108

Werner C J, Bull J S, Solomon C J, Brown F B, McKinney G W, Rising M E, Dixon D A, Martz R L, Hughes H G, Cox L J, Zukaitis A J, Armstrong J C, Forster R A and Casswell L 2018 *MCNP Version 6.2 Release Notes* (Los Alamos, NM (United States)). DOI:10.2172/1419730

Wilkinson L and Heggie J C P 2000 Glandular breast dose: potential errors Radiology (electronic letter in response to: Boone J M 1999 Glandular breast dose for monoenergetic and high-energy x-ray beams: Monte Carlo assessment *Radiology* **213** 23–37

Wu X, Barnes G T and Tucker D M 1991 Spectral dependence of glandular tissue dose in screen-film mammography. *Radiology* **179** 143–8. DOI:10.1148/radiology.179.1.2006265

Wu X, Gingold E L, Barnes G T and Tucker D M 1994 Normalized average glandular dose in molybdenum target-rhodium filter and rhodium target-rhodium filter mammography. *Radiology* **193** 83–9. DOI:10.1148/radiology.193.1.8090926

Zoetelief J and Jansen J T M 1995 Calculation of Air Kerma to Average Glandular Tissue Dose Conversion Factors for Mammography *Radiat. Prot. Dosimetry* **57** 397–400.

1
2
3
4
5
6
7
8
9
10
11
12
13
14
15
16
17
18
19
20
21
22
23
24
25
26
27
28
29
30
31
32
33
34
35
36
37
38
39
40
41
42
43
44
45
46
47
48
49
50
51
52
53
54
55
56
57
58
59
60

Chapter 3

Glandular dose in mammography with ANN

ACCEPTED MANUSCRIPT

Estimation of glandular dose in mammography based on artificial neural networks

To cite this article before publication: Rodrigo Trevisan Massera *et al* 2020 *Phys. Med. Biol.* in press https://doi.org/10.1088/1361-6560/ab7a6d

1

Estimation of glandular dose in mammography based on Artificial Neural Networks

Rodrigo Trevisan Massera, Alessandra Tomal

Instituto de Física "Gleb Wataghin", Universidade Estadual de Campinas, 13083-859, Campinas, Brazil

Address correspondence to A.T. (e-mail: atomal@ifi.unicamp.br.)

Declarations of interest: none

2

ABSTRACT

This work proposes to use Artificial Neural Networks (ANN) for the regression of dosimetric quantities employed in mammography. The data were generated by Monte Carlo simulations using a modified and validated version of PENELOPE (v. 2014) + penEasy (v. 2015) code. A breast model of homogeneous mixture of adipose and glandular tissue was adopted. The ANN were constructed with Keras and scikit-learn libraries for Mean Glandular Dose (MGD) and air kerma (K_{air}) regressions, respectively. In total, seven parameters were considered, including the incident photon energies (from 8.25 to 48.75 keV), the breast geometry, breast glandularity and K_{air} acquisition geometry. Two ensembles of 5 ANN networks each were formed to calculate MGD and K_{air}. The Normalized Glandular Dose coefficients (DgN) are calculated by the ratio of the ensembles outputs for MGD and K_{air}. Polyenergetic DgN values were calculated weighting monoenergetic values by the spectra bin probabilities. The results indicated a very good ANN prediction performance when compared to the validation data, with median errors on the order of the average simulation uncertainties (≈0.2%). Moreover, the predicted DgN values compared with works previously published were in good agreement, with mean(maximum) differences up to 2.2(9.4)%. Therefore, it was showed that ANN could be a complementary or alternative technique to tables, parametric equations and polynomial fits to estimate DgN values obtained via MC simulations.

Key words: Mammography; Dosimetry; Glandular Dose; Monte Carlo; Machine Learning; Neural Networks

3

1. Introduction

The exposure of the breast to ionizing radiation in mammography and other advanced breast imaging techniques has led the development of several dosimetric protocols among the years (Dance *et al* 1999, Dance and Sechopoulos 2016). Nowadays, the mean glandular dose (*MGD*) is the standard quantity for dosimetric studies in breast imaging, being employed in quality controls and risk assessment routines (Dance and Sechopoulos 2016). The *MGD* can be derived by the product of the air kerma (K_{air}), which is usually obtained experimentally, and conversion factors, calculated via Monte Carlo simulations (Wu *et al* 1991, 1994, Dance 1990, Boone 1999). These conversion factors, called Normalized Glandular Dose (*DgN*), are dependent on several parameters, including the exposure geometry, beam quality and breast characteristics (Boone 1999). Additionally, the *DgN* values for a given group of parameters are usually published in tables (Wu *et al* 1991, Boone 1999, Nosratieh *et al* 2015, Dance 1990, Dance *et al* 2000, 2009), or can be computed using parametric equations (Sobol and Wu 1997, Dance 1990) or fit equations (Boone 2002, Sarno *et al* 2019). From these approaches, *DgN* values can be directly calculated without the necessity of reperforming the simulations.

The anode/filter combination, tube potential and half-value layer are factors that strongly influences the incident x-ray spectra and, consequently, the *DgN* values (Wu *et al* 1991). Therefore, the published *DgN* values need to cover a variety of mammography x-ray spectra. The polyenergetic *DgN* can be directly obtained simulating a polyenergetic mammography spectra or can be calculated via monoenergetic *DgN* weighted by the spectra probabilities (Boone 2002). The *DgN* values also depends on the breast characteristics, dictated by breast composition (Wu *et al* 1991, Boone 1999, Dance 1990, Sarno *et al* 2019), thickness (Wu *et al* 1991, Boone 1999, Dance 1990, Sarno *et al* 2019), radius (Boone 2002), and thickness of the skin layer (Boone 1999, Massera and Tomal 2018, Huang *et al* 2008). Although recent studies showed an overall overestimation of the dose compared to anthropomorphic breast models (Sechopoulos *et al* 2012, Hernandez *et al* 2015), the homogeneous adipose-glandular mixture model is still used for model comparison studies, and quality control routines (Dance and Sechopoulos 2016). Additionally, the geometry for air kerma estimation must be considered because it also influences the *DgN* values (Dance *et al* 2009, Sarno *et al* 2017b), as showed by the effect of the compression paddle to the ionization chamber distance (Dance *et al* 2009).

The *DgN* values published in previous works relies from the previous cited parameters implemented in the *MGD* and K_{air} simulations. Considering the possible combinations derived from the parameters, this becomes a high-dimensional problem. In practice, only a limited number of parameters and specific values ranges were studied. For example, fixing the breast radius and skin thickness to a constant value (Boone 2002). Another difficult arises on how to represent the *DgN* results, as tables, parametric equations or other methods. If the number of parameters combinations is high, it could be impractical to share it in table form. Or if the results are in parametric equations, it could be difficult to add more parameters in future works without remodeling the previously published equations. Moreover, in some cases, interpolations and extrapolations are implemented to calculate *DgN* values, respectively, between or outside published intervals. Care must be taken with these approaches since they can introduce significant deviations (Wilkinson and Heggie 2000, Sobol and Wu 1997). Consequently, a method that could handle efficiently a large number of parameters is desirable, with interpolations errors as low as possible.

Recently, machine learning techniques have been used for different applications on medical physics (Litjens *et al* 2017). These applications includes mammography and related imaging techniques (Lee and Nishikawa 2018, Ma *et al* 2019, Samala *et al* 2017, Caballo *et al* 2018b, Sechopoulos and Mann 2020). Among its capabilities, machine learning algorithms have been used for automated

segmentation of the breast tissues and aiding in the detection of malignant lesions. More specifically, Artificial Neural Networks, a type of machine learning algorithm, was used to estimate the *MGD* for W/Rh spectra with varying breast thicknesses and compositions (Erguzel *et al* 2018). One drawback that difficulties the ANN in some applications is the lack of data for training, validation and testing. On the other hand, for the homogeneous breast geometry, it is now possible to generate a large enough database with Monte Carlo simulations in a reasonable amount of time due to the advance of computer hardware and computation parallelism. Therefore, the ANN and other Machine Learning techniques were successfully employed in different complex tasks in the medical physics area, including mammography.

This work proposes the use ANN to estimate the Normalized Glandular Doses coefficients for homogeneous breasts models considering different parameters as inputs: x-ray beam energy, breast thickness and radius, glandularity, skin thickness, adipose shielding thickness and compression plate ionization chamber distance. For this, a modified and validated PENELOPE + penEasy Monte Carlo code was employed with a Python script for automatization of the simulation setup and output storage. Afterwards, ANN were trained with the simulation results for *MGD*, K_{air} for *DgN* predictions.

2. Materials and methods

2.1.1 Monte Carlo Code

The PENELOPE code (version 2014) (Salvat 2015) with a modified and validated penEasy extension (v. 2015) (Sempau *et al* 2011), as a main program was employed. Moreover, a Python script was written to automatize the simulations. More details about the code and validations can be seen on the reference (Massera and Tomal 2018). For each evaluated parameter (beam energy, breast characteristics and irradiation geometry), two independent simulations were performed in order to determine the *MGD* and the K_{air}. Only photons were simulated, with a cutoff energy of 1 keV. The electrons were considered locally deposited. The simulations were stopped when one of the following conditions were achieved: the statistical uncertainties were on the order of 0.5% (considering 2 standard deviations); the maximum number of simulated particles or the maximum simulation time were reached. Following all these conditions, the uncertainties were never higher than 1%, as commented in Section 3.1. The average simulation speed was in the order of $\approx 10^5$ histories per second per thread, requiring a few minutes to complete, considering the three used personal computers (processor, base clock in GHz, cores/threads): (i) AMD Ryzen 1700X (@3.6 GHz, 8/16), (ii) AMD Ryzen 2700 (@3.2 GHz, 8/16), (iii) Intel Core i7 7700 (@3.6 GHz, 4/8). For the *MGD* simulation, the uncertainty was estimated with the history-by-history method and for the K_{air} with the batch method (4 identical simulations with independent seeds) (Badal and Sempau 2006, Sechopoulos *et al* 2018). The breast glandular, adipose and skin tissue compositions were extracted from Hammerstein et al. (Hammerstein *et al* 1979), while the other material compositions were taken from NIST databased (Berger *et al* 2010). The cross sections were computed by the PENELOPE MC code (Salvat 2015).

2.1.2 Geometry

The simulated geometry was based on a planar mammography examination, representing a craniocaudal (CC) projection (Sechopoulos *et al* 2015). The included features depend on the output quantity of the simulation (*MGD* or K_{air}). The geometry is described as follow: a point source collimated within 4 edges of an ideal detector with 30 x 24 cm² area. The source emits monoenergetic photons from 8.25 to 48.75 keV (0.5 step), and the heel effect was not considered. For the *MGD* calculations, it was included: a block of water (30 x 17 x 30 cm³) which mimics the patient body; the

compression and support plates (PMMA, 30 x 24 x 0.2 cm³). The source distance to detector is 66 cm and the source distance to the breast support plate is 64.5 cm. The breast is located between the plates and is shaped as a semicylinder with varying radius and thickness. The inner section of the breast is composed of a homogeneous mixture of glandular and adipose tissues in different weight fractions (glandularity, f_g). A layer of skin or adipose tissue from 0 to 5 mm thick surrounds the mixture, except the contact area between the breast and the body. We also included the combination of 1.45 mm skin plus 2 mm adipose (Sarno *et al* 2017a). For the K_{air} calculations, only the compression plate was present, and an air cylinder (2 cm radius, 0.2 mm in height) was included, simulating an ionization chamber. The top of the air-cylinder was in all the cases aligned with the breast entrance plane. The compression plate was raised to a distance (called Compression plate - Ion chamber distance - CPCD) that ranged from 0 to 40 cm to the top of the air cylinder. In the simulations, the world is filled with air. Figure 1 shows the out of scale geometry for both cases.
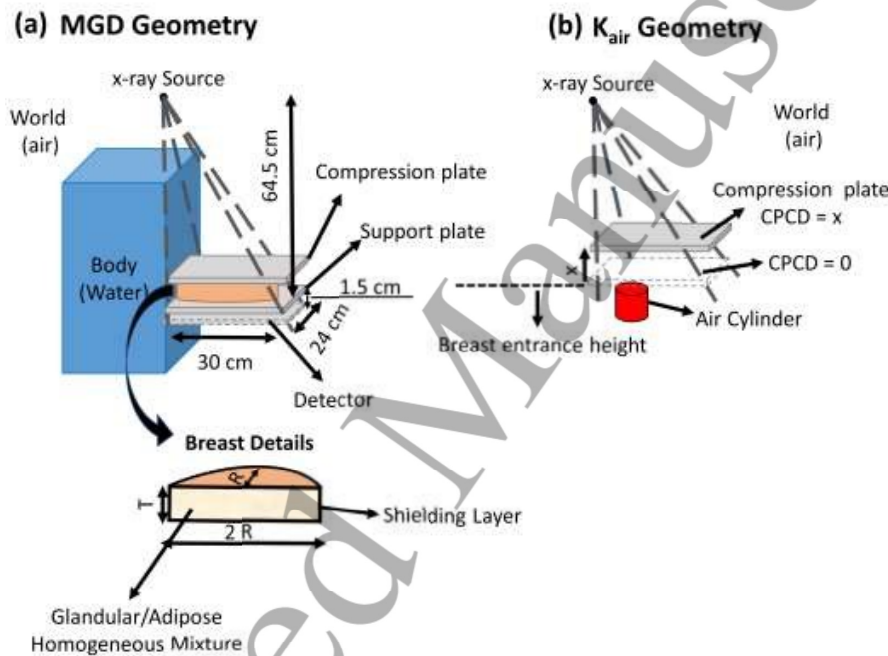
Figure 1. Illustration of the simulated geometries (out of scale) for calculating the quantities: (a) *MGD* and (b) K_{air}.

Table 1 shows the summary of the parameters used in the simulations and, when applied, where the information was retrieved. The first batch of simulations were performed with a fixed spaced parameter grid. Afterwards, new simulations were performed at low energies, where the ANN training proved to be more difficult to converge, the maximum interval value between the parameters is described in table 1.

6

Table 1. Summary of the parameters considered in the simulations, the value range when applicable.

Parameter	Description	Value-range if applicable (maximum interval between values)	MGD, K_{air} or both
SDD (source detector distance)	Distance from x-ray source to the detector	66 cm	Both
Field size	X-ray field size at the detector	24 x 30 cm	Both
Photon energy beam	Initial photon energy	8.25 – 48.75 keV (0.5 keV)	Both
Breast thickness	The height of the compressed breast	2 – 11 cm (1 cm)	Both
Breast radius	The radius of the compressed breast	6 – 12 cm (2 cm)	MGD
Breast glandularity (f_g)	The glandular mass fraction of the homogeneous mixture	0 – 1 (0.3)	MGD
Breast skin thickness	The skin layer that surrounds the homogeneous mixture	0 – 5 mm *also used 1.45 mm skin + 2 mm adipose (Sarno *et al* 2017a) (1)	MGD
Breast adipose shielding thickness	The adipose layer that surrounds the homogeneous mixture	0 - 5mm *also used 1.45 mm skin + 2 mm adipose (1)	MGD
Compression plate-ionization chamber distance (CPCD)	Distance from the top of the air cylinder to the bottom of the compression plate	0 – 40 cm (10 cm)	K_{air}

2.1.3 Mean Glandular Dose and Air Kerma Computations

The energy deposited in glandular tissue (E_{gland}) was determined by weighting the energy deposited in the homogeneous breast mixture (E_{dep}), interaction-by-interaction (Wilkinson and Heggie 2001), by the *G* factor, as described in equation (1) (Boone 1999).

$$E_{gland} = \sum_i E_{dep}^i \times G(E) \; ; \; G(E) = \frac{f_g (\mu_{en}(E)/\rho)_g}{f_g (\mu_{en}(E)/\rho)_g + (1-f_g)(\mu_{en}(E)/\rho)_a} \tag{1}$$

Where E_{dep}^i is the energy deposited in the homogeneous mixture per interaction *i* obtained via MC simulation, $\mu_{en}(E)/\rho$ is the mass absorption coefficient for glandular (*g*) and adipose (*a*) tissues; f_g is the glandular fraction.

The *MGD* was calculated by equation (2).

$$MGD = \frac{E_{gland}}{N \times \frac{1}{2} \times \pi \times (R - t_s)^2 \times (t - 2 t_s) \times \rho_{homo} \times f_g} \; (mGy/photon) \tag{2}$$

Where R and t are the breast radius and thickness, respectively; t_s is the skin plus adipose shielding thickness; ρ_{homo} is the homogeneous mixture density and N the total number of histories simulated.

The K_{air} was calculated by the ratio between the total energy transferred to the charged particles in the air cylinder and its mass. Finally, the Normalized Glandular Dose (*DgN*) was calculated with the ratio *MGD/ K_{air}*. The *DgN* for polyenergetic beams were obtained by averaging the monoenergetic *MGD* and K_{air} with the respective probability spectra (Boone 2002, Sarno *et al* 2019) according to equation (3).

$$DgN_{poly} = \frac{\sum_{Emin}^{Emax} \phi(E)MGD(E)}{\sum_{Emin}^{Emax} \phi(E)K_{air}(E)} \quad (3)$$

Where ϕ is the spectra fluence in a given energy bin (E) equal to 0.5 keV. The raw spectra were obtained from MASMICS, TASMICS and RASMICS programs (Hernandez *et al* 2017), and filtered afterwards with NIST-XCOM attenuation coefficient data (Berger *et al* 2010). A variance reduction technique named Interaction Forcing (Sempau *et al* 2011) with a value of 1000 was used for the K_{air} simulations to speed-up the data acquisition without biasing the results.

2.2.1 Artificial Neural Networks Implementation

Python (v. 3) scripts were developed to train and test the Artificial Neural Networks (ANN) for the regression of *MGD* and K_{air}. For the *MGD*, the ANN were constructed with Keras (v. 2.2.4) (Chollet and Others 2015) library plus TensorFlow (v. 1.12) (Abadi *et al* 2016) as backend. Keras was chosen since it is a well stablished library for Neural Networks implementations and allows the use of GPU for a faster training. For the K_{air}, the selected library was scikit-learn (0.21.1) (Pedregosa *et al* 2011), another well documented library with machine learning implementations, but does not support GPU training. However, the K_{air} ANN were quite simple and can be trained relatively fast in a CPU. Moreover, scikit-learn provides preprocessing and data selection tools to facilitate the ANN implementations. For *MGD* and K_{air}, feed-forward ANN were employed using Keras Dense layers and scikit-learn MLPRegressor, respectively. Table 2 describes the features and regression quantities considered in the ANN.

Table 2. Summary of the features used for training the ANN.

ANN Type & Regression Quantity	*MGD*	K_{air}
Photon Energy	1. Monoenergetic	1. Monoenergetic
Breast Characteristics	2. Breast thickness	2. Breast thickness
	3. Breast radius	
	4. Breast composition	
	5. Skin thickness	
	6. Adipose thickness	
Irradiation Geometry		3. CPCD

2.2.2 Training, Validation and Test Processes

The ANN consists of a set of neurons, more particularly in this case the Multi-Layer Perceptron (MLP), divided in three types of layers (Murtagh 1991). The artificial neuron is a mathematical function capable of tensor operations. It receives inputs (x), with adjustable weights (α), and applies an activation function f, to return a value f(αx). The first layer is the input, the neurons in this layer are responsible to receive the parameters of the problem in question, named features, and to propagate to another layers. In this case, the MGD or K_{air} features used for training the respective ANN, as detailed in Table 2. The middle, known as hidden layers (there could be one or more) are responsible for the learning process: they receive the information from the previous layer and by applying the weights, the information is modified and passed to the next layer. Finally, the output layer converges the information from the intermediate layers to form the output (label), in this case, the MGD or K_{air} numerical values. The ANN architecture implemented in this work is the fully-connected feed-forward neural network, i.e. each neuron from the previous layer are connected to the subsequent layer, and the information passes within one direction, starting from the input and ending in the output. The ANN usually starts with neurons with randomly assigned weights. The learning process consists of updating those weights in each interaction ("batch"), via

backpropagation (LeCun 1988), to minimize the differences between the label in the dataset, and the output value calculated by the ANN. For this, it is crucial to separate the dataset between the training, validation and test samples. The training sample is used to update the weights of the ANN in each interaction, until the error reaches a certain threshold, or the maximum number of interactions is surpassed. The validation samples guarantee that there is no overfitting during the training phase, and they are presented after each epoch to verify the ANN performance. Finally, the test samples are presented only after the ANN is fully trained and ensembled, and they are used to verify the generality of the ANN to novel data. Following all those steps, it is necessary to guarantee the optimal performance of the ANN. For this, the ANN hyperparameters must be tailored for each specific problem. For example, finding the best activation functions, best number of neurons and hidden layer, batch size, error metric, learning algorithm, which will be discussed in section 3.2.

From the total data acquired with MC simulations (4,181 for K_{air} and 262,222 for MGD) as described in section 2.1, 80% were randomly selected for training and validating, while the remaining 20% were dedicated for testing. Before the ANN training, data preprocessing was applied on the simulation results as following: for both MGD and K_{air} the features where scaled between 0 to 1 (from scikit-learn $MinMax$ and $Standard$ transform, respectively). Moreover, for the MGD and K_{air}, the labels were divided by the minimum value ($MinNorm$). The optimal hyperparameters were found using a search grid and selecting the models that produced the smallest errors for the training, validation and testing steps. For this, the absolute percentage error (APE) was considered as a performance metric and is calculated by equation (4).

$$APE = 100 \times \frac{|y_{label} - y_{ANN}|}{y_{label}} \ (\%) \qquad (4)$$

Where $y_{label/ANN}$ is the *ith* element for the label or ANN regression value. For evaluating the performance of the ANN, we considered the following metrics for the dataset: (1) mean APE; (2) median APE; (3) 70% and (4) 90% percentiles APE, which is the average of the highest APEs in those intervals; (5) maximum APE; (6) 100 outliers APE, which is the average APE of the 100 highest errors. A geometric mean ($\overline{APE}_g$) was calculated to encompass the 6 previous metrics, which is given by equation (5).

$$\overline{APE}g = \left(\prod_{i=1}^{6} APE_i\right)^{1/6} \qquad (5)$$

Where APE_i represents each one of the six APE metrics previous defined. To account for the test and validation data, the final metric was calculated by equation (6).

$$\varphi = \overline{APE}_g(validation) + 2 \times \overline{APE}_g(test) \qquad (6)$$

The metric φ is employed to select the best performing ANN for a given set of hyperparameters selected from the original hyperparameters grid. Once the hyperparameters were defined, a 5 k-fold cross validation was performed in the 80% of the training data yielding two ANN ensembles of 5 trained networks, one for MGD and other for K_{air}. During the ensemble training, the labels were sampled by a normal distribution, centered at the label value with a standard deviation equal to it uncertainty. This ensured a variation of the data during the k-fold training, incorporating the label uncertainty acquired using Monte Carlo simulations. Figure 2 illustrate the scheme implemented in this work.
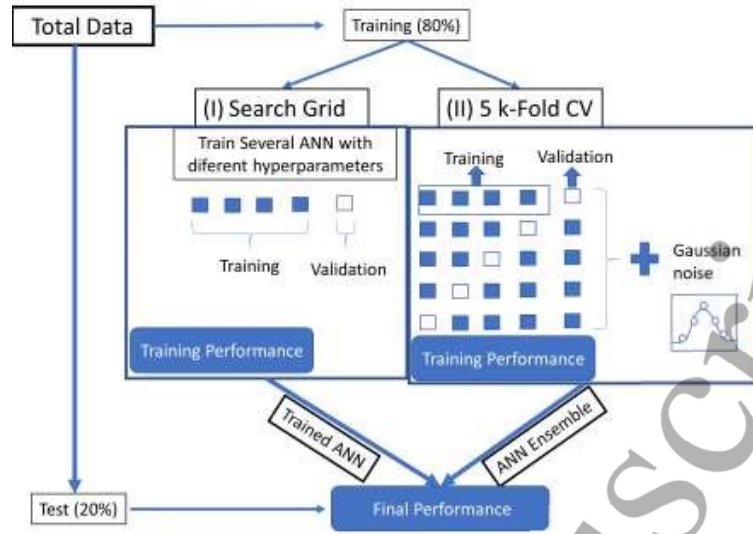
Figure 2. ANN framework implemented in this work for training and validation.

The results expressed in this work, if not explicitly indicated, corresponds to the mean and standard-deviation output of the ensembles. This method allows an approximate estimation of the ANN uncertainty over the predicted values. Besides, the early-stopping technique was implemented for the *MGD* training (patience=5, i.e. maximum number of consecutive tries without improvement) to prevent overfitting.

To calculate the relative *DgN* values between samples, the convention of equation (7) was used.

$$Rel.\ Dif. = 100 \times \frac{|DgN_{sample} - DgN_{control}|}{DgN_{control}}\ (\%) \tag{7}$$

3. Results

3.1 Simulation Results

Figure 3 summarize the results of the simulations for *MGD* and K_{air} for all parameters evaluated, which are described in table 2. In figure 3(a), the histograms are normalized to have area equal to one. In general, the *MGD* presented values below 2×10^{-12} mGy/history, in contrast to K_{air} values, with values up to 6×10^{-12} mGy/history. *The MGD* and K_{air} distributions are attributed to the influence of the parameters, including the beam energy, the geometric and breast thickness, radius and composition. The label distribution was analyzed before the machine learning process to verify if there are any discontinuities in the dataset or unbalanced data distribution that could bias the ANN training. In this study, as shown in 3(a), both *MGD* and K_{air} have a continuous and relatively even distributed values. Therefore, no correction technique was applied in the datasets. Figure 3(b) shows the uncertainty distribution of the simulated MGD and K_{air} values. The errors derived from the simulation are below 1% for both cases, with a median of 0.21% and 0.22% for *MGD* and K_{air}, respectively, as indicated with a horizontal bar inside the boxes. The boxes lower and upper limits represent the first and third quartiles. Moreover, as indicated in figure 3(b) the whiskers represent the 99% intervals and shows that the uncertainties were below 0.4% and 0.7% for *MGD* and K_{air}, respectively. The simulation uncertainty could be one of the indicators to benchmark the ANN performance. It is expected that during training, the ANN prediction errors are in the order of the

simulation uncertainties. If the prediction errors are much smaller than the uncertainties, it could suggest an overfitting behavior, i.e. the ANN is learning the error pattern and not the actual desired values.
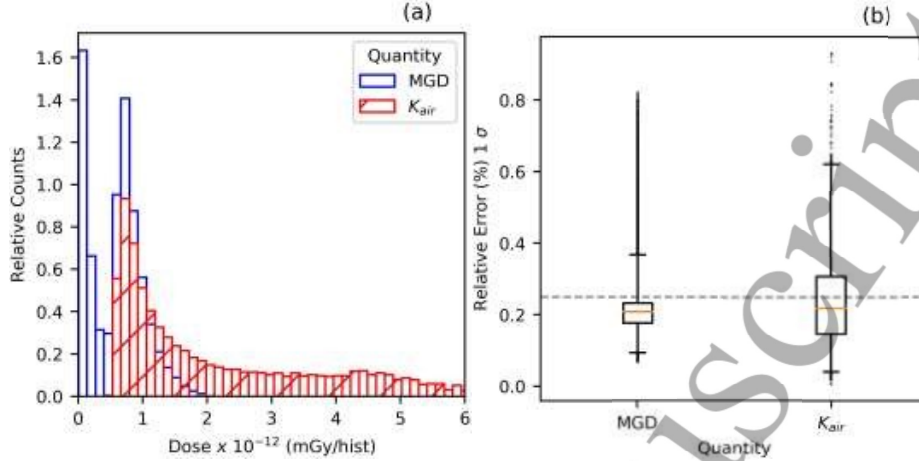
Figure 3. (a) Value distribution for *MGD* and *K$_{air}$*. (b) Boxplot of the uncertainty distribution for *MGD* and *K$_{air}$*, centerline: median, lower and upper box edges: first and third quartiles. Whiskers: 1% and 99% percentiles. The dashed line indicates the 0.25% uncertainty value. Circles: outliers.

3.2 Optimal ANN hyperparameters

Table 3 summarizes the optimal hyperparameters for the *MGD* and *K$_{air}$* ANN obtained after a thoughtful search in the hyperparameters grid and using the metric determined by equation (6). Appendix A1 contains an explanation of each hyperparameter, meanwhile appendix A2 shows the influence of different ANN hyperparameters over the training performance. It is observed that the parameters are different for each ANN type. In general, the ANN for *MGD* regression were more complex, as expected due to the higher number of parameters and bigger dataset.

Table 3. Optimal parameters found for the ANN after the search grid.

	MGD	*K$_{air}$*
Parameter Name	**Value**	**Value**
Number of Neurons	500	20
Number of Hidden Layers	3	2
Activation Function	RELU	TanH
Feature Scaler	MinMax	Standard
Label Scaler	MinNorm	MinNorm
Loss Function	MAPE	MSE
Optimizer	ADAM	Lbfgs
Learning Rate	10^{-3}	N/A
Decay	10^{-4}	N/A
Activity Regularizer	L2: 10^{-4}	L2: 10^{-5}
Batch Size	250	N/A
Max Epochs	500	N/A
Tolerance	N/A	10^{-5}
Max Iteration	N/A	10^{3}

Figure 4 shows the error distribution for training and validation processes for (a) *MGD* and (b) *K_{air}*. However, the performance of the ANN could vary due the selected training and validation sample populations and the initial random activation weights. Considering this, the process was repeated at least 40 times with independent seeds, measuring the mean and standard deviation of the population results, which are described in table 4. The maxima errors - mean(std) - obtained were 5(1)% and 3(1)% for *MGD* ANN validation and test, respectively. Although most of the highest errors belong to lower energies (below 8.75 keV) which represents the lowest *DgN* contribution for polyenergetic mammography spectra. Observing the whiskers in figure 4, the 1% to 99% intervals are contained within a relative error below 2% for *MGD* and 1% for *K_{air}*. The errors of the testing process were slightly below the validation errors, indicating that the use of 5 ANNs as an ensemble could predict unknown values more precisely than an individual ANN. Moreover, the ensemble was less prone to outlier errors, as seen in table 4.

Figure 4. Boxplot of the relative error distributions for the ANN validation and testing processes for (a) *MGD* and (b) *K_{air}*, respectively. Centerline: median, lower and upper box edges: first and third quartiles. Whiskers: 1% and 99% percentiles. Circles: outliers. Results obtained with the addiction of normal sampled noise.

Table 4. Relative percent prediction errors (in %) for the ANN regressors, for validation and testing processes. Results are shown as mean (standard deviation) over 40 measurements with independent seeds. The outliers represent the average of the 100 highest APE values. Results obtained with the addiction of normal sampled noise.

ANN Type	Validation				Test			
	Median	Std. Dev.	Outliers	Max.Error	Median	Std. Dev.	Outliers	Max.Error
MGD	0.23(1)	0.27(2)	3.1(6)	5(1)	0.16(1)	0.17(1)	1.3(2)	3(1)
K_{air}	0.15(1)	0.21(3)	0.9(1)	1.7(4)	0.15(1)	0.18(3)	0.6(1)	1.6(2)

3.3 The additional noise influence over training and testing

We compared the ANN performance without and with the addition of the gaussian noise over the training data. The results for the median APE are shown in figure 5 for (a) *MGD* and (b) *K_{air}*, respectively, for the other metrics (not shown) there was a similar trend. As expected, the inclusion of the noise provided an increase in the validation and test errors, in the order of 0.02% for the median, since there is a penalty proportionally with the simulation uncertainty. This method provides

a penalization for the training reducing the likelihood of overfitting. Moreover, it propagates the data uncertainty over the ensemble, allowing a more accurate error estimation when the ANN is trained.
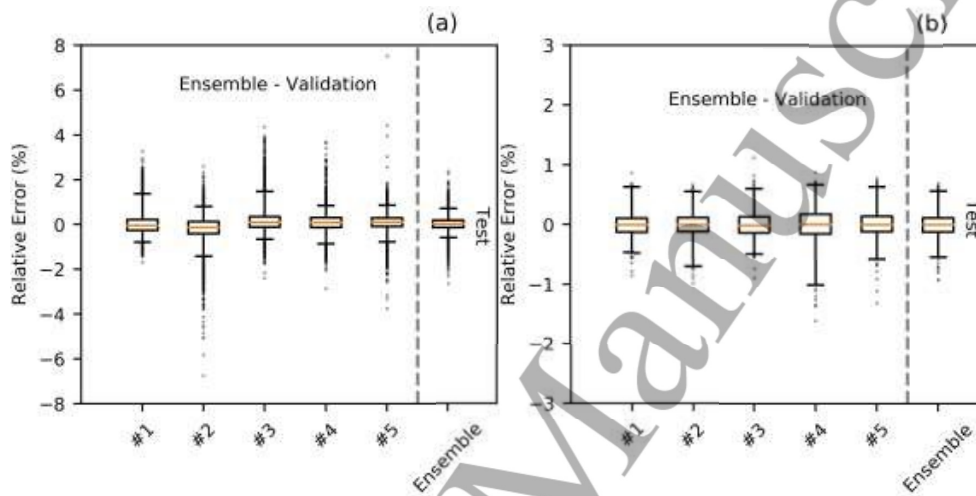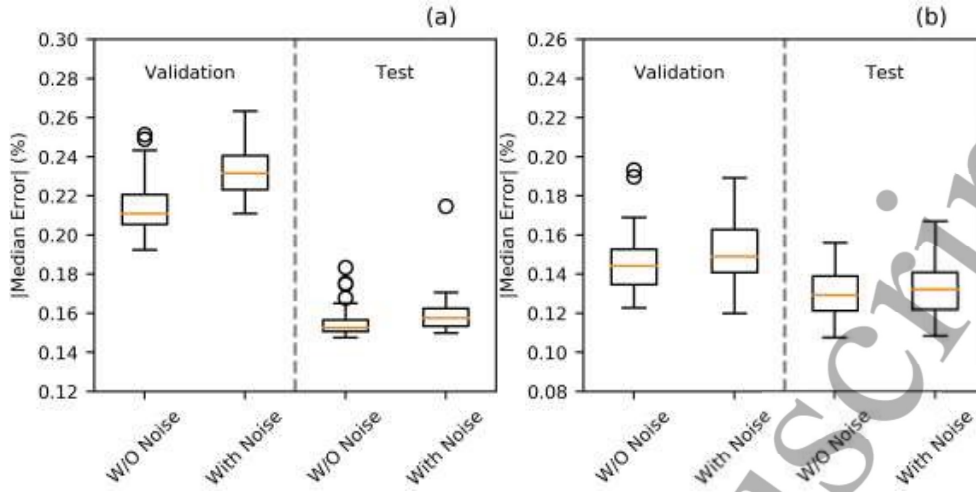

Figure 5. Boxplot of the relative error distributions of the median for the ANN validation and testing processes for (a) *MGD* and (b) *K$_{air}$*, respectively. Centerline: median, lower and upper box edges: first and third quartiles. Whiskers: 1% and 99% percentiles. Circles: outliers.

3.4 ANN regressions for monoenergetic energies

Figure 6 shows the relative *DgN* as function of the breast (a) radius and (b) thickness for different photon energies. The relative *DgN* represents the *DgN* values normalized by the leftmost value of each curve. On the right of each curve the conversion factor for computing the absolute values of *DgN* is provided. The *DgN* is almost independent of the breast radius for photons with energies of 20 keV. On the other hand, for lower and higher energies the *DgN* has a variation up to 10% with the breast radius. As expected, the *DgN* decreases with breast thickness due to the photon exponential attenuation and glandular volume increasing (Cunha *et al* 2010).
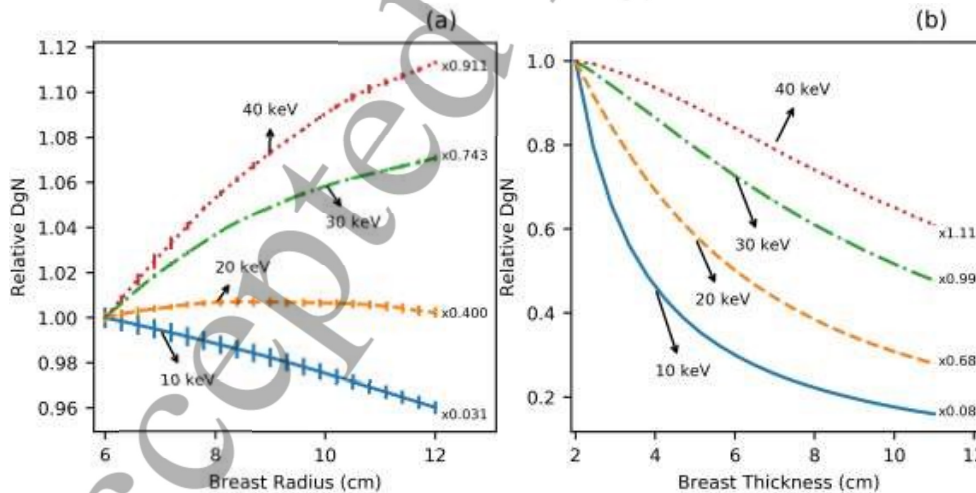
Figure 6. Relative *DgN* as function of breast (a) radius and (b) thickness for different photon energies, normalized by the value for the lowest (a) breast radius and (b) thickness. Therefore, the absolute *DgN* values can be obtained by multiplying the relative values by the number on the right of each curve. The Relative *DgN* values were calculated for the following parameters: (a) Breast 5 cm thick, 20% glandular; (b) Breast 10 cm radius, 20% glandular. CPCD = 0 cm.

The *DgN* variation with the breast model in terms of skin and adipose thickness is shown in figure 7, considering as reference (a) 1.45 mm skin and (b) 0 mm adipose, respectively. The predicted values for 5 mm skin are in good agreement with the work of Sarno et al. (Sarno *et al* 2017a) as shown in figure 7(a), with differences smaller than 1.8%. In figure 7(b), the *DgN* is lower as the adipose thickness increases for energies below 25 keV, for higher energies the *DgN* increases slightly with the adipose thickness. The contribution of the thickness of the breast shielding layer over the *DgN* values becomes less important as the incident photon energy increases.
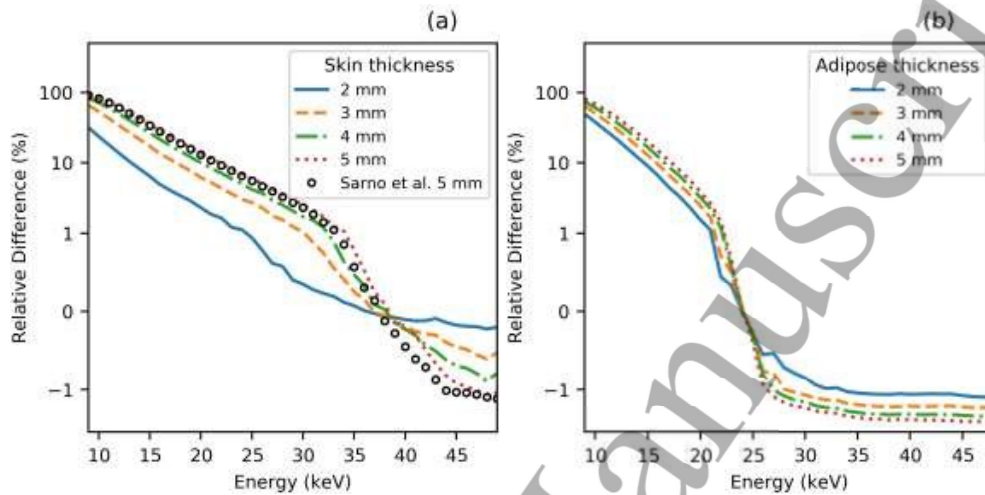
Figure 7. (a) Relative *DgN* differences as function of the photon energy for various skin thickness. Reference skin thickness: 1.45 mm. Values from Sarno et al. (Sarno *et al* 2017a) were also included for comparison. (b) Relative *DgN* differences as function of the energy for various adipose thickness. Reference adipose thickness: 0 mm. Both cases: 5 cm breast, 20% glandular. Graphs are in symbolic logarithm scale, with a linear interval between -1% to 1%.

The *DgN* as function of the breast glandularity is shown in figure 8(a), where *DgN* values are lower for denser breasts. This behavior is more evident for lower photon energies. Figure 8(b) shows the relation between *DgN* and CPCD, with the *DgN* increasing with increasing CPCD. This behavior is explained by the lower number of scattered photons from the compression plate that can reach the ionization chamber. In figure 8(b), this effect is dependent on the energy, since the cross section of the incoherent scattering increases with increasing energy for the mammographic energy range. In both cases, the relative *DgN* represents the *DgN* values normalized by the leftmost value of each curve.
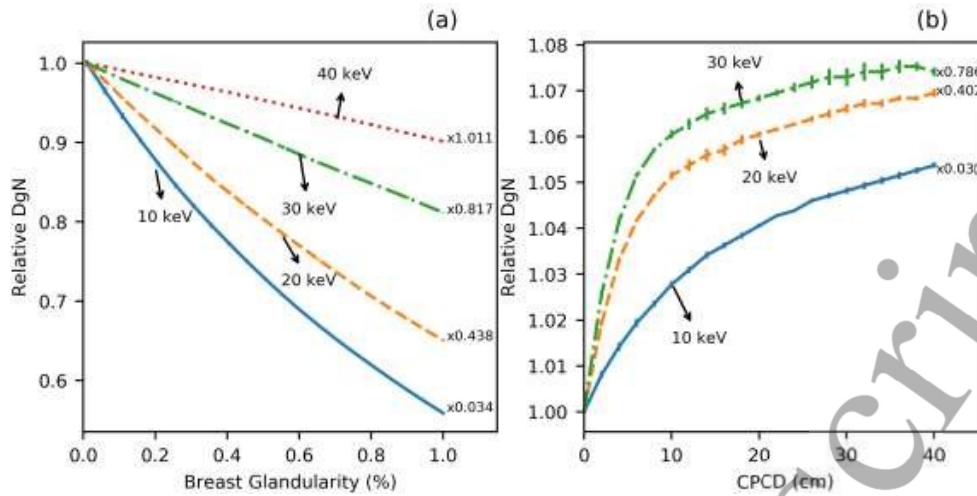
Figure 8. Relative *DgN* for different photon energies as function of: (a) the breast glandularity, and (b) the CPCD. Therefore, the absolute *DgN* values can be obtained by multiplying the relative values by the number on the right of each curve. Both cases: 5 cm breast, 1.45 mm skin thickness.

3.5 Implementation for Polyenergetic Spectra

The ANN performance was investigated over polyenergetic spectra, employing the weighting described in section 2. For this, the ANN input parameters were matched as close as possible from the works of Nosratieh et al. (Nosratieh *et al* 2015) and Dance et al. (Dance 1990, Dance *et al* 2000, 2009) in order to generate values for comparison. The comparison between the results of this work with the reference values is showed in figure 9. A good agreement was achieved for both cases with mean (maxima) differences of 1.7(3.5)% and 2.2(9.4)% for Nosratieh et al. and Dance et al. (Nosratieh *et al* 2015, Dance 1990, Dance *et al* 2000, 2009), respectively.
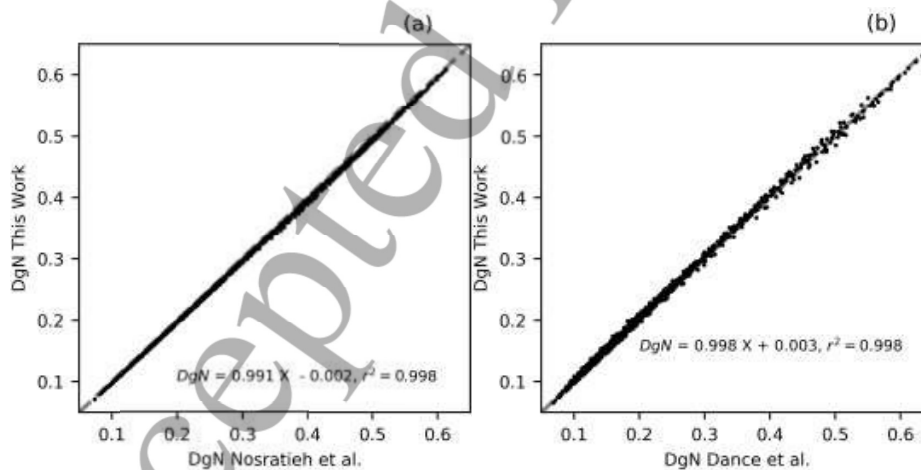
Figure 9. Comparison of the ANN calculated *DgN* with the works of (a) Nosratieh et al. (Nosratieh *et al* 2015) and (b) Dance et al. (Dance 1990, Dance *et al* 2000, 2009).

The influence of each parameter over the *DgN* was evaluated using a random sampling on the parameter space. For each variable, 1000 *DgN* samples were selected as the control group. Afterwards, these values were compared with new ones randomly sampled. For this, we calculated

the relative difference between the *DgN* values from the control group and the newly sampled values (equation 7). This process was repeated 4 times for each variable to calculate the mean and standard deviation of the variations. Figure 10 shows the relative *DgN* difference of the samples compared to control data obtained with this procedure as function of the sorted parameter.
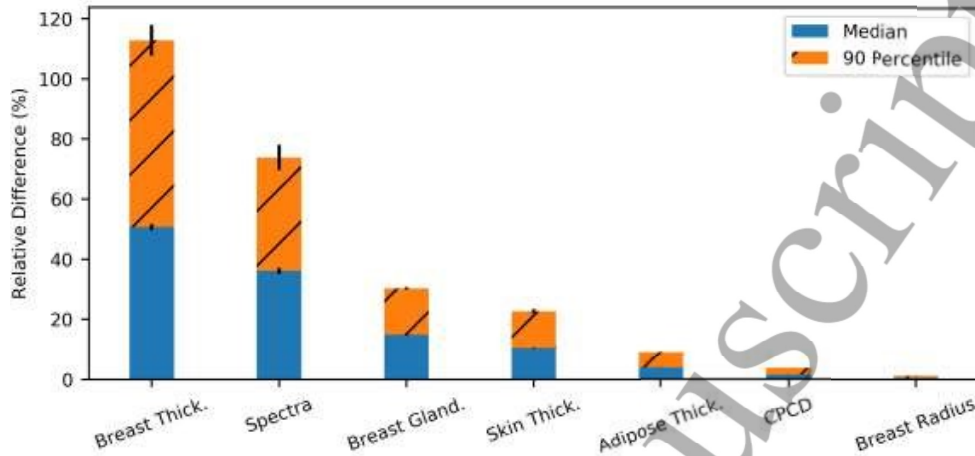
Figure 10. *DgN* relative difference between the control and sampled groups following the convention used in equation (7), for each parameter the intervals of the median and 90 percentile are displayed and sorted from the highest (left) to lowest (right) in the "X" axis. The error bars describe the standard variations after 4 repetitions.

3.6 Graphical Interface Implementations

A Python script was written using the Jupyter (Kluyver *et al* 2016) package to provide a graphical user interface for achieve the *DgN* estimations via ANN. Figure 11 shows an example of the ANN implementation in this environment, where the user can select the values for each variable and the program returns the *DgN* values in the desired energy range. The program works for monoenergetic and polyenergetic spectra produced by different anode/filter combinations. Moreover, the code can be modified to include other anode and filter materials.
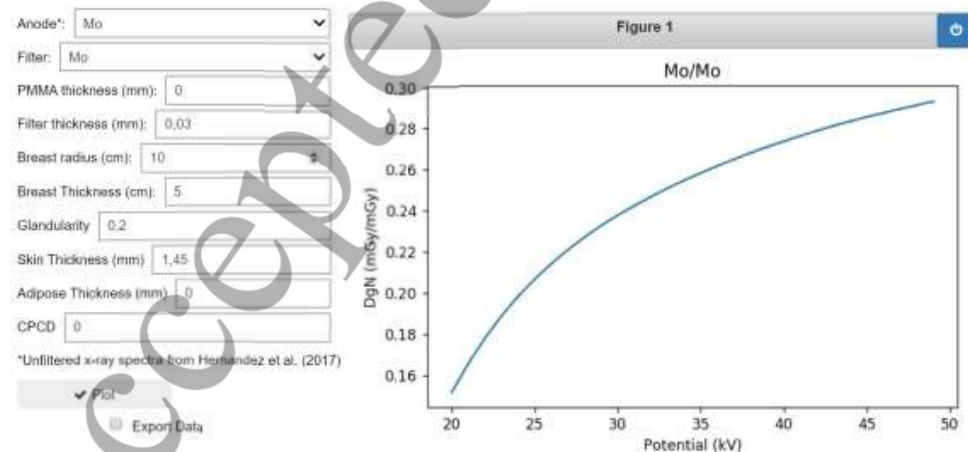
Figure 11. Example of implementation of the ANN to calculate *DgN* values for the user using a Jupyter script.

4. Discussion

According to the results, the ANN showed an overall good performance over the predicted values to calculate *MGD*, K_{air} and consequently, *DgN* values. However, there are still the presence of outliers, with errors in the order of 3(1)%. Nevertheless, these values are observed for very low energies and have a small significance over a polyenergetic spectrum implemented in mammography. It is worth to mention that the minimal energy studied in this work is 8.25 keV, which is a threshold for a conventional mammography spectrum where the probabilities become significant. For a Mo/Mo 28 kV and W/Rh 22 kV x-ray spectra, the cumulative probability for energies below 8.25 keV is negligible, being in the order of 0.3% and 0.15%, respectively. If there is an interest to study an alternative spectrum with less filtration, this effect can be more relevant. From our studies, for an extreme case of an unfiltered spectra, errors in the order of 5% were observed (results not included). Training the ANN algorithms with energies below 8 keV could be difficult due to the drastic reduction of the *MGD* values, as consequence of the low number of photons that can reach the homogeneous tissue without being absorbed by the skin, air or the compression plate. Besides the photon energy of the spectrum, the breast thickness has a large influence in *DgN* values (section 3.4) due to the depth dose curves (Cunha *et al* 2010), and the acquisition geometry (the reference of K_{air} changes with breast thickness).

A significant database size (over 200,000 values) was necessary to train the ANN to result in an acceptable performance, which could be a disadvantage for small datasets, when compared to other common employed techniques for *DgN* estimations, like parametric equations. However, when the number of parameters is sufficiently large, the ANN could be an automated alternative over the other techniques, since their use would be extremely complex or impractical. Additionally, most previous works focus on a specific breast model (e.g. a constant skin thickness, or breast radius) (Wu *et al* 1991, Boone 1999, Dance 1990), while the ANN method allowed the inclusion of more parameters. This characteristic could be an advantage considering recent studies of more complex and realistic breast models for dosimetric calculations (Sechopoulos *et al* 2016, Hernandez *et al* 2015, Sechopoulos *et al* 2012).

Therefore, this setup allows the study of different parameters combinations and their influence over the *DgN*. Once trained, the ANN can be easily implemented in different frameworks to calculate *DgN* values for the final users, as shown in section 3.6. The script shown in this section was intended to cover the most common parameters and their value range employed in breast dosimetry, and consequently is limited to these options and parameters range. The data augmentation with gaussian noise guaranteed a penalization proportional to the MC uncertainty, allowing a more generalized model. However, if the uncertainties are extremely small, the addition of the noise becomes irrelevant.

The input ANN parameters were selected from those commonly considered in *DgN* calculations: breast thickness, composition and beam quality. Additionally, the skin and adipose tissue thicknesses were included, considering their influence over the *DgN* as pointed out in previous studies (Sarno *et al* 2017a, Huang *et al* 2008, Massera and Tomal 2018). This work also implemented the breast radius, although its influence is less noticeable than other parameters. The air kerma acquisition geometry, which can also influence the *DgN* final values was included by varying the compression plate and ionization chamber distance, and the results are in agreement with published results (Dance *et al* 2009). Considering the breast characteristics and the geometry parameters, the ANN implementation allows the conversion between different acquisition protocols without performing new MC simulations. For example, it is possible to calculate in this setup the ratio between the *DgN* using a breast with 5 mm adipose shield layer and a compression plate in contact

17

with the chamber and a 4 mm skin or 1.45 mm skin and the compression plate not in contact with the chamber. This could be helpful in an experimental measurement, where the phantom has very specific characteristics, and a comparison with other models is needed. With few modifications, the ANN approach could be extended to link with current adopted dosimetry protocols and new ones that are currently in development (AAPM Task Group No. 282 - Development of a new universal breast dosimetry method) (Sechopoulos *et al* 2016).

This work focused on a homogeneous breast model, which is not recommended for patient-specific applications. Several works applied machine learning for breast imaging techniques in anthropomorphic models or real images (Lee and Nishikawa 2018, Caballo *et al* 2018a), including tissue segmentation tasks and to increase the model resolution (Caballo *et al* 2018b). Thus, the ANN could be employed in the future for the estimation of *DgN* coefficients in anthropomorphic phantoms. A major difficult is to acquire a relatively large dataset for training and validation. However, with the recent advances in computer generated realistic phantoms and the increasing in simulation performance this could be possible.

5. Conclusions

This work shows that artificial neural networks can be employed in *DgN* regressions trained via MC generated data. The ANN successfully learned the complex pattern involved between *DgN* and the different input parameters, being an efficient method to convert *DgN* values between different acquisition protocols. The ANN could be an alternative or a complementation to other techniques, such as tables, parametric equations and polynomial fits for *DgN* estimation. Moreover, the inclusion of new parameters in the future studies is straightforward using the ANN approach discussed in this work. The database, the trained ANN and the training scripts are available in the following repository: https://github.com/rtmass/ANNDgN for those interested. The scripts can be used to generate *DgN* values for traditional mammography spectra, for digital breast tomosynthesis and also for contrast-enhanced mammography. Future works could consider the heel effect and other parameters that can influence the *DgN* values to extend the ANN parameter space, besides to study of ANN to estimate *DgN* values for anthropomorphic breast phantoms.

Acknowledgements

Appendix

A.1 Additional information regarding the ANN parameters

This appendix gives more details about the ANN parameters cited in Table 3.

Table A1. ANN parameters definition employed in this work. More information can be found in the documentation of Scikit-learn (Pedregosa *et al* 2011) and Keras (Chollet and Others 2015).

Parameter Name	Explanation
Number of Neurons	The number of neurons in each hidden layer
Number of Hidden Layers	Number of layers that are between the input and output layer.
Activation Function	The type of the function (*f(x)*) that will be implemented in the neurons. In this case, hyperbolic tangent (*Tanh*) or rectified linear unit (*RELU*).
Feature Scaler	Specifies how the feature values will be scaled. *MinNorm*: the values are normalized and scaled between 0 and 1. *Standard*: Similar to *MinNorm*, but the standard deviation of the labels is also modified.
Label Scaler	Specifies how the label values will be scaled. It works similar to Feature Scaler.
Loss Function	Specifies which metric will be used to quantify the loss in the training. In this case, the Mean Absolute Percentage Error (*MAPE*) and Mean Squared Error (*MSE*).
Optimizer	The algorithm that is used in the training process of the ANN. In this case, *Lbfgs* or *ADAM*.
Learning Rate	This parameter determines how fast the training converges. High learning rates tends to faster trainings, but with the risk of not correctly converging.
Decay	The reduction of the learning rate after each batch.
Activity Regularizer	Parameter that introduces a penalty in the ANN to avoid overfitting and helping in generalization. In this case, the *L2* method is used.
Batch Size	The number of samples presented in each interaction during the training process.
Max Epochs	The maximum number of repetitions of the training data.
Tolerance	Value that is considered acceptable to stop the training process.
Max Iteration	Maximum number of interactions.

A.2 Training performance as function of ANN hyperparameters

This appendix presents some hyperparameters of the ANN and their relationship with the training performance.

Figure A.2.1 shows the Training Loss as function of the epoch number for different ANN topologies for (a) *MGD* and (b) K_{air}. The improvement factor achieved by increasing the complexity of ANN reaches a plateau for ANN with more than the number of neurons and hidden layers shown in figure A.2.1.

Figure A.2.2 shows the training loss as function of the epoch number for different activation functions for (a) *MGD* and (b) K_{air}. This case in particular shows that the best activation function varies with the application. While for *MGD* the *RELU* and *Sigmoid* functions had an overall good performance, for K_{air} hyperbolic tangent was the optimal one.

Figure A.2.3 shows the training loss as function of the epoch number for (a) *MGD* and (b) K_{air}, computed for different Learning rate and *L2* penalty factor, respectively. Higher learning rates produce a faster convergence, but it does not guarantee a good fitting. On the other hand, low

learning rates require a large number of epochs. The *L2* penalty factor plays an important role during training to prevent overfitting, as seen in (b). However, this value must be adequate with the application, if inappropriate, it prevents am optimal convergence.
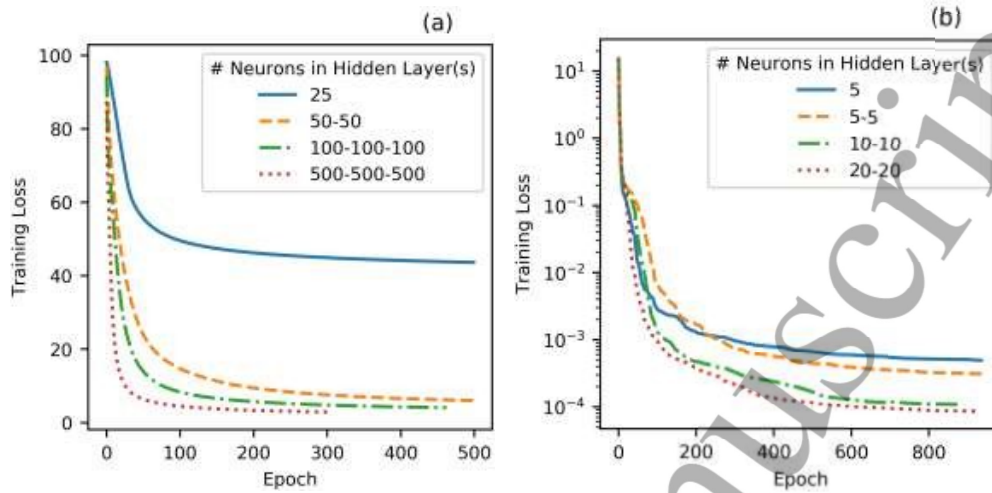
Figure A.2.1. Performance of the ANN as function of the epoch number measured by the training loss, for different number of hidden layers and the number of neurons on each layer for (a) *MGD* and (b) K_{air}. The notation follows the standard: X-Y-Z, meaning 3 hidden layers with X neurons on the first one, Y on the second and Z on the third.

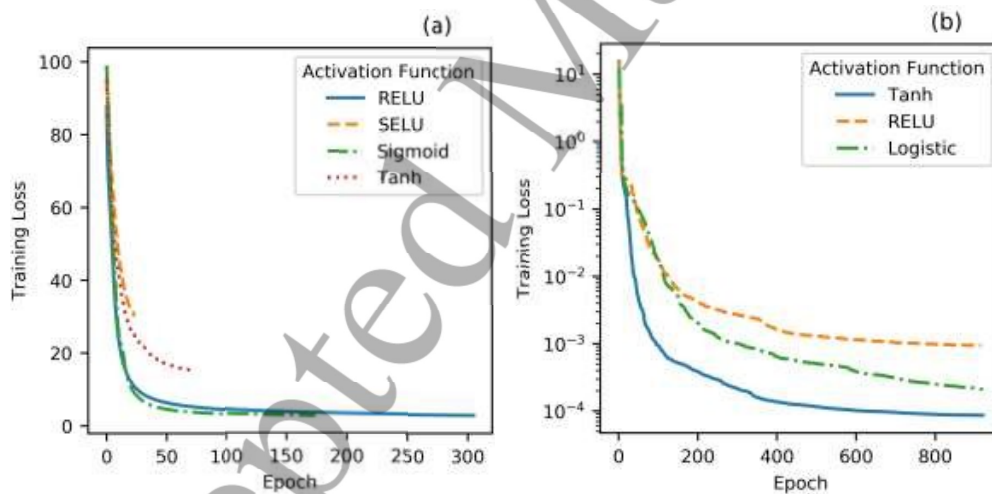**Figure A.2.2**. Performance of the ANN as function of the activation function for (a) *MGD* and (b) K_{air}.
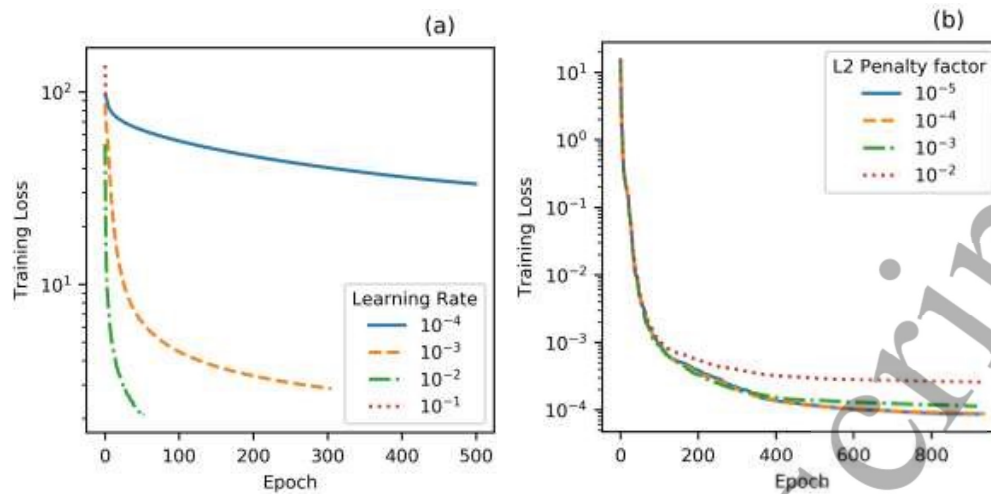
Figure A.2.3. Performance of the: (a) *MGD* ANN as function of the epoch number measured by the training loss, for different learning rate values; and (b) K_{air} ANN as function of the epoch number measured by the training loss, for different *L2* penalty factors.

References

Abadi M, Agarwal A, Barham P, Brevdo E, Chen Z, Citro C, Corrado G S, Davis A, Dean J, Devin M, Ghemawat S, Goodfellow I, Harp A, Irving G, Isard M, Jia Y, Jozefowicz R, Kaiser L, Kudlur M, Levenberg J, Mane D, Monga R, Moore S, Murray D, Olah C, Schuster M, Shlens J, Steiner B, Sutskever I, Talwar K, Tucker P, Vanhoucke V, Vasudevan V, Viegas F, Vinyals O, Warden P, Wattenberg M, Wicke M, Yu Y and Zheng X 2016 TensorFlow: Large-Scale Machine Learning on Heterogeneous Distributed Systems Online: http://arxiv.org/abs/1603.04467

Badal A and Sempau J 2006 A package of Linux scripts for the parallelization of Monte Carlo simulations *Comput. Phys. Commun.* **175** 440–50 Online: https://www.sciencedirect.com/science/article/pii/S001046550600230X

Berger M J, Hubbell J H, Seltzer S M, Chang J, Coursey J S, Sukumar R, Zucker D S and Olsen K 2010 Tables of X-Ray Mass XCOM: Photon Cross Sections Database. National Institute of Standards and Technology (NIST) Online: https://www.nist.gov/pml/x-ray-mass-attenuation-coefficients

Boone J M 1999 Glandular Breast Dose for Monoenergetic and High-Energy X-ray Beams: Monte Carlo Assessment *Radiology* **213** 23–37 Online: http://www.ncbi.nlm.nih.gov/pubmed/10540637

Boone J M 2002 Normalized glandular dose (DgN) coefficients for arbitrary x-ray spectra in mammography: Computer-fit values of Monte Carlo derived data *Med. Phys.* **29** 869–75 Online: http://www.ncbi.nlm.nih.gov/pubmed/12033583

Caballo M, Boone J M, Mann R and Sechopoulos I 2018a An unsupervised automatic segmentation algorithm for breast tissue classification of dedicated breast computed tomography images *Med. Phys.* **45** 2542–59 Online: http://doi.wiley.com/10.1002/mp.12920

Caballo M, Fedon C, Brombal L, Mann R M, Longo R and Sechopoulos I 2018b Development of 3D patient-based super-resolution digital breast phantoms using machine learning *Phys. Med. Biol.* Online: http://iopscience.iop.org/article/10.1088/1361-6560/aae78d

Chollet F and Others 2015 Keras Online: https://keras.io

Cunha D M, Tomal A and Poletti M E 2010 Evaluation of scatter-to-primary ratio, grid performance and normalized average glandular dose in mammography by Monte Carlo simulation including interference and energy broadening effects *Phys. Med. Biol.* **55** 4335–59 Online: http://stacks.iop.org/0031-9155/55/i=15/a=010?key=crossref.69e6ab10310c5dba5b142a95f9a7d1ca

Dance D R 1990 Monte Carlo calculation of conversion factors for the estimation of mean glandular breast

dose. *Phys. Med. Biol.* **35** 1211–9 Online: http://www.ncbi.nlm.nih.gov/pubmed/2236205

Dance D R and Sechopoulos I 2016 Dosimetry in x-ray-based breast imaging *Phys. Med. Biol.* **61** R271–304 Online: http://www.ncbi.nlm.nih.gov/pubmed/27617767

Dance D R, Skinner C L and Alm Carlsson G 1999 Breast dosimetry *Appl. Radiat. Isot.* **50** 185–203 Online: http://www.sciencedirect.com/science/article/pii/S0969804398000475?via%3Dihub

Dance D R, Skinner C L, Young K C, Beckett J R and Kotre C J 2000 Additional factors for the estimation of mean glandular breast dose using the UK mammography dosimetry protocol. *Phys. Med. Biol.* **45** 3225–40 Online: http://www.ncbi.nlm.nih.gov/pubmed/11098900

Dance D R, Young K C and van Engen R E 2009 Further factors for the estimation of mean glandular dose using the United Kingdom, European and IAEA breast dosimetry protocols *Phys. Med. Biol.* **54** 4361–72 Online: http://www.ncbi.nlm.nih.gov/pubmed/19550001

Erguzel T T, Tekin H O, Manici T, Altunsoy E E and Tarhan N 2018 Comparison of multiple linear regression analysis and artificial neural network approaches in the estimation of monte carlo mean glandular dose calculations of mammography *Dig. J. Nanomater. Biostructures* **13** 163–76

Hammerstein R G, Miller D W, White D R, Masterson M E, Woodard H Q and Laughlin J S 1979 Absorbed Radiation Dose in Mammography *Radiology* **130** 485–91 Online: http://www.ncbi.nlm.nih.gov/pubmed/760167

Hernandez A M, Seibert J A and Boone J M 2015 Breast dose in mammography is about 30% lower when realistic heterogeneous glandular distributions are considered *Med. Phys.* **42** 6337–48 Online: http://doi.wiley.com/10.1118/1.4931966

Hernandez A M, Seibert J A, Nosratieh A and Boone J M 2017 Generation and analysis of clinically relevant breast imaging x-ray spectra *Med. Phys.* **44** 2148–60 Online: http://doi.wiley.com/10.1002/mp.12222

Huang S-Y, Boone J M, Yang K, Kwan A L C and Packard N J 2008 The effect of skin thickness determined using breast CT on mammographic dosimetry *Med. Phys.* **35** 1199–206 Online: http://www.ncbi.nlm.nih.gov/pubmed/18491511

Kluyver T, Ragan-kelley B, Pérez F, Granger B, Bussonnier M, Frederic J, Kelley K, Hamrick J, Grout J, Corlay S, Ivanov P, Avila D, Abdalla S and Willing C 2016 Jupyter Notebooks—a publishing format for reproducible computational workflows *Positioning and Power in Academic Publishing: Players, Agents and Agendas* ed F Loizides and B Scmidt (IOS Press) pp 87–90 Online: https://eprints.soton.ac.uk/403913/

LeCun Y 1988 A theoretical framework for Back-Propagation *Proc. 1988 Connect. Model. Summer Sch.*

Lee J and Nishikawa R M 2018 Automated mammographic breast density estimation using a fully convolutional network *Med. Phys.* **45** 1178–90 Online: http://doi.wiley.com/10.1002/mp.12763

Litjens G, Kooi T, Bejnordi B E, Setio A A A, Ciompi F, Ghafoorian M, van der Laak J A W M, van Ginneken B and Sánchez C I 2017 A survey on deep learning in medical image analysis *Med. Image Anal.* **42** 60–88 Online: https://www.sciencedirect.com/science/article/pii/S1361841517301135

Ma X, Wei J, Zhou C, Helvie M A, Chan H-P, Hadjiiski L M and Lu Y 2019 Automated Pectoral Muscle Identification on MLO-view Mammograms: Comparison of Deep Neural Network to Conventional Computer Vision *Med. Phys.* Online: http://doi.wiley.com/10.1002/mp.13451

Massera R T and Tomal A 2018 Skin models and their impact on mean glandular dose in mammography *Phys. Medica* **51**

Murtagh F 1991 Multilayer perceptrons for classification and regression *Neurocomputing* **2** 183–97

Nosratieh A, Hernandez A, Shen S Z, Yaffe M J, Seibert J A and Boone J M 2015 Mean glandular dose coefficients (D(g)N) for x-ray spectra used in contemporary breast imaging systems. *Phys. Med. Biol.* **60** 7179–90 Online: http://www.ncbi.nlm.nih.gov/pubmed/26348995

Pedregosa F, Varoquaux G, Gramfort A, Michel V, Thirion B, Grisel O, Blondel M, Prettenhofer P, Weiss R, Dubourg V, Vanderplas J, Passos A, Cournapeau D, Brucher M, Perrot M and Duchesnay É 2011 Scikit-learn: Machine Learning in Python *J. Mach. Learn. Res.* **12** 2825–30 Online: http://jmlr.csail.mit.edu/papers/v12/pedregosa11a.html

Salvat F 2015 PENELOPE-2014: A Code System for Monte Carlo Simulation of Electron and Photon

Transport Online: https://www.oecd-nea.org/tools/abstract/detail/nea-1525

Samala R K, Chan H-P, Hadjiiski L M, Helvie M A, Cha K and Richter C 2017 Multi-task transfer learning deep convolutional neural network: application to computer-aided diagnosis of breast cancer on mammograms *Phys. Med. Biol.* **62** 8894 Online: http://iopscience.iop.org/article/10.1088/1361-6560/aa93d4

Sarno A, Mettivier G, Di Lillo F and Russo P 2017a A Monte Carlo study of monoenergetic and polyenergetic normalized glandular dose (DgN) coefficients in mammography *Phys. Med. Biol.* **62** 306–25 Online: http://stacks.iop.org/0031-9155/62/i=1/a=306?key=crossref.ff01f67cef7dc341833304c2b3e09bab

Sarno A, Mettivier G and Russo P 2017b Air kerma calculation in Monte Carlo simulations for deriving normalized glandular dose coefficients in mammography *Phys. Med. Biol.* **62** N337–49 Online: http://stacks.iop.org/0031-9155/62/i=14/a=N337?key=crossref.06eb191ff947c7acfe600fb45a298662

Sarno A, Tucciariello R M, Mettivier G, di Franco F and Russo P 2019 Monte Carlo calculation of monoenergetic and polyenergetic DgN coefficients for mean glandular dose estimates in mammography using a homogeneous breast model *Phys. Med. Biol.* **64** 125012 Online: https://iopscience.iop.org/article/10.1088/1361-6560/ab253f

Sechopoulos I, Ali E S M, Badal A, Badano A, Boone J M, Kyprianou I S, Mainegra-Hing E, McMillan K L, McNitt-Gray M F, Rogers D W O, Samei E and Turner A C 2015 Monte Carlo reference data sets for imaging research: Executive summary of the report of AAPM Research Committee Task Group 195 *Med. Phys.* **42** 5679–91 Online: http://doi.wiley.com/10.1118/1.4928676

Sechopoulos I, Bliznakova K, Qin X, Fei B and Feng S S J 2012 Characterization of the homogeneous tissue mixture approximation in breast imaging dosimetry *Med. Phys.* **39** 5050–9 Online: http://doi.wiley.com/10.1118/1.4737025

Sechopoulos I, Boone J M, Dance D R, Glick S J, Hulme K W and Seibert J A 2016 AAPM Committee - Task Group No. 282 - Development of a new universal breast dosimetry method (TG282) Online: https://www.aapm.org/org/structure/?committee_code=TG282

Sechopoulos I and Mann R M 2020 Stand-alone artificial intelligence - The future of breast cancer screening? *The Breast* **49** 254–60 Online: https://linkinghub.elsevier.com/retrieve/pii/S0960977619312214

Sechopoulos I, Rogers D W O, Bazalova-Carter M, Bolch W E, Heath E C, McNitt-Gray M F, Sempau J and Williamson J F 2018 RECORDS: improved Reporting of montE CarlO RaDiation transport Studies: Report of the AAPM Research Committee Task Group 268 *Med. Phys.* **45** e1–5 Online: http://doi.wiley.com/10.1002/mp.12702

Sempau J, Badal A and Brualla L 2011 A PENELOPE -based system for the automated Monte Carlo simulation of clinacs and voxelized geometries-application to far-from-axis fields *Med. Phys.* **38** 5887–95 Online: http://www.ncbi.nlm.nih.gov/pubmed/22047353

Sobol W T and Wu X 1997 Parametrization of mammography normalized average glandular dose tables *Med. Phys.* **24** 547–54 Online: http://doi.wiley.com/10.1118/1.597937

Wilkinson L and Heggie J C P 2000 Glandular breast dose: potential errors Radiology (electronic letter in response to: Boone J M 1999 Glandular breast dose for monoenergetic and high-energy x-ray beams: Monte Carlo assessment *Radiology* **213** 23–37

Wu X, Barnes G T and Tucker D M 1991 Spectral dependence of glandular tissue dose in screen-film mammography. *Radiology* **179** 143–8 Online: http://www.ncbi.nlm.nih.gov/pubmed/2006265

Wu X, Gingold E L, Barnes G T and Tucker D M 1994 Normalized average glandular dose in molybdenum target-rhodium filter and rhodium target-rhodium filter mammography. *Radiology* **193** 83–9 Online: http://www.ncbi.nlm.nih.gov/pubmed/8090926

Chapter 4

Breast glandularity and MGD assessment with DL

Breast glandularity and mean glandular dose assessment using a deep learning framework: virtual patients study

Rodrigo T. Massera, Alessandra Tomal*

Institute of Physics "Gleb Wataghin", University of Campinas, Campinas, Brazil

Abstract

Breast dosimetry in mammography is an important aspect of radioprotection since women are exposed periodically to ionizing radiation due to breast cancer screening programs. Mean glandular dose (MGD) is the standard quantity employed for the establishment of dose reference levels in retrospective population studies. However, MGD calculations requires breast glandularity estimation. This work proposes a deep learning framework for volume glandular fraction (VGF) estimations based on mammography images, which in turn are converted to glandularity values for MGD calculations. For this, 208 virtual breast phantoms were generated and compressed computationally. The mammography images were obtained with Monte Carlo simulations (MC-GPU code) and a ray-tracing algorithm was employed for labeling the training data. The architectures of the neural networks are based on the XNet and multilayer perceptron, adapted for each task. The network predictions were compared with the ground truth using the coefficient of determination (r^2). The results have shown a good agreement for inner breast segmentation (r^2=0.999), breast volume prediction (r^2=0.982) and VGF prediction (r^2=0.935). Moreover, the DgN coefficients using the predicted VGF for the virtual population differ on average 1.3% from the ground truth values. Afterwards with the obtained DgN coefficients, the MGD values were estimated from exposure factors extracted from the DICOM header of a clinical cohort, with median(75 percentile) values of 1.91(2.45) mGy. Therefore, we successfully implemented a framework for VGF and MGD calculations for virtual breast phantoms.

Keywords: Mammography, Mean Glandular Dose, breast glandularity, deep learning

1. Introduction

Digital mammography is an imaging technique recommended in several countries for breast cancer screening, being associated with a reduction in mortality rate and successful treatment of breast cancer [1]. Mean glandular dose (MGD) is currently the adopted

---

quantity used for dosimetry in mammography, since glandular tissue is the most prone to radiation-induced mutations. Historically, MGD values have been estimated considering simplified breast models [2], which are not, however, representative of mean population glandular tissue content and distribution [3], and can results in significant differences [4, 5].

With the development of new breast imaging techniques (i.e. digital breast tomosynthesis, DBT, and breast-CT), the quantity and vertical location of glandular tissue within the breast could be better evaluated to generate heterogeneous breast models [6–13]. Breast-CT provides more accurate breast models, since it allows to characterize in details the 3D distribution of the breast tissues [14] and could be used for patient-specif dose estimation. However, this technique is not available worldwide and it is limited to a small cohorts or number of images. Thus, breast models based on breast-CT images are not viable to cover the large populations variability where this technique is not implemented yet. Although the vertical location of glandular tissue within the breast is necessary for patient-specific dose estimation, homogeneous models based on more realistic and specific breast characteristics (i.e. dimensions and composition) could be used to obtain a more accurate radiation dose estimates. This allows to establish more accurate Dose Reference Levels [15] for large populations compared to a model that adopts the same glandularity for the entire population. In addition, the large number of images from mammography screening acquired each year around the world could be an important data source for the development of population-based breast models.

For a more accurate evaluation of MGD in a large population-based screening mammography, it is desirable to use an estimator to predict the breast glandular content from the images for each patient breast. Quantitative assessment of breast density (BD) based on mammography images has been largely performed using automated or semi-automated imaging systems, such as Cumulus (University of Toronto, Canada), Volpara (Matakina Technology Ltd, New Zealand), Quantra (Hologic Inc., Bedford, MA) and LIBRA (University of Pennsylvania USA), among others. Most of them are commercially available and used for clinical applications. Although the accuracy and robustness of these systems has been extensively explored and they have excellent or moderate reliability for repeated breast density measures [16, 17], the results are validated against other 3D breast imaging modalities results or using physical breast phantoms. However, such validations can be challenging since the ground truth from real patient images are always unknown and the target breast density are indirectly estimated from 3D imaging techniques, resulting in uncertainties due to tissue segmentation. Moreover, when physical breast phantoms (simplified or anthropomorphic) are used, a limitation of availability and variability between them in terms of materials, costs and infrastructure appears. There is also the distinction between breast density based on area and the volumetric breast density (VBD), where the latter considers the variation of the breast thickness during compression and enables an estimation of the breast composition[18].

Recently, also deep learning techniques have been employed for breast density assessments in mammography [19–23]. Although with promising results, a significant number of labeled data is required to train these models, which are usually acquired via other breast density algorithms or categorized by radiologists. On top of the difficulty to obtain the train-

ing data, the labeled results acquired indirectly do not represent the ground truth values, but predictions (which could carry potential errors and biases). Therefore, another method to acquire labeled data to train deep learning models would be useful. Considering this scenario, a virtual clinical study could generate the necessary data, where the ground truth is known in order to train deep learning models. Additionally, an independently trained deep learning model freely available could be a comparative/complementary result to other VBD algorithms.

This work presents the development of a deep learning framework for calculating the breast volume and the volume glandular fraction (VGF, consequently the VBD) from simulated mammography images obtained with anthropomorphic virtual phantoms. In this preliminary study, we show the feasibility and performance of training three neural networks, one for each specific task (segmentation, height prediction and relative glandular height prediction) with a labeling system based on a ray-tracing algorithm in order to obtain the breast glandularity. Afterwards, in an application topic, the MGD is estimated for the virtual breast phantoms using a homogeneous model approximation with the predicted glandularity and exposure parameters based on a clinical cohort.

2. Materials and Methods

The methodology used in this study is summarized in Fig. 1. Specific details related to each step of the flowchart are described in the following sections.
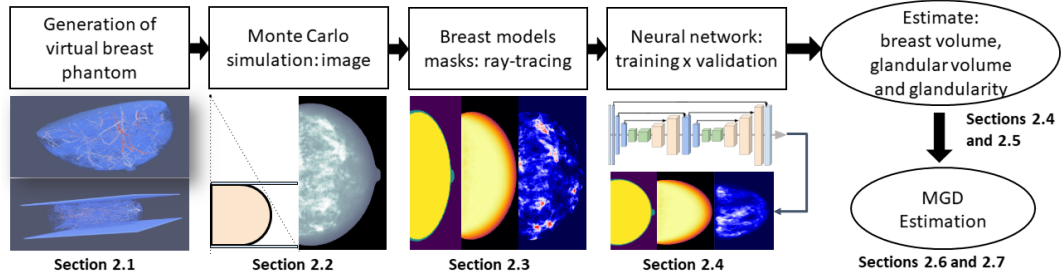
Figure 1: Flowchart of the whole pipeline of this study to calculate the breast glandularity and mean glandular dose based on virtual patients.

2.1. Computational breast phantoms

Anthropomorphic 3D breast phantoms were generated with the BreastPhantom software [24], based in two steps. First, the input parameters were selected in order to generate breasts with different sizes, shapes and glandular content, based on breast-CT data, to address the variability present in the population [6, 9, 25]. The phantoms consisted of 0.25 mm cubic voxels, and a 1.5 mm skin thickness was considered [26]. The virtual breasts are composed of skin, adipose, glandular, blood (for arteries), muscle and connective tissues. Second, the breast was compressed (BreastCompress program)[27] with a finite-element software (FEBio v. 2.9)[28] and cropped to remove uncompressed tissues, mainly

muscle (BreastCrop program)[27]. The whole process for generating each phantom took less than 30 minutes (depending on the breast thickness) using a standard computer (Ryzen 2700 3.2 GHz, 8 cores 16 threads, 16 GB RAM). A Python (v.3) script was written to automate the process to generate a total of 208 phantoms, whose characteristics are summarized in Table 1.

Table 1: Characteristics of the breast phantoms. The radius is calculated by approximating the breast as a semicylinder. The values are expressed as median(25 – 75 percentiles).

♯Phantoms	Thickness (cm)	Volume (cm^3)	Radius (cm)	VGF
208	5.8(4.6-6.8)	420(325-580)	6.7(5.9-7.9)	0.23 (0.13-0.51)

2.2. Data generation: Monte Carlo simulations

The image acquisition for a mammography cranio-caudal (CC) examination was simulated with the MC-GPU Monte Carlo code [29]. This code was chosen because it was already used successfully in a virtual clinical trial for mammography studies [30, 31]. Moreover, the code runs on graphical processing units (GPUs), which offers high performance to simulate the image acquisition in a reasonable time, considering the available hardware.

The simulated geometry consists of a point source, the compression plate (2.75 mm thick of polycarbonate), the support plate (2 mm of carbon fiber) and the compressed breast. The effects of a linear grid, whose grid parameters were based on Cunha et al. [32], were accounted using the transmission factors calculated using the algorithm proposed by Day and Dance [33]. An amorphous-selenium detector (200 μm thick), comprised of 1024×832 pixels, is located, respectively, 70 cm and 2.5 cm below the x-ray source and the bottom of the breast. The number of pixels was chosen based on real mammography detectors [34] with a 4×4 binning. The detector and the compression/support plates have an area equal to 29×24 cm^2, while the x-ray field irradiated an area of approximately 27.6×17.3 cm^2 of the detector (sufficient to irradiate all the surface of the breast phantoms). The detector is an ideal energy integrating device, with parameters set to default: electronic signal of 5200 electrons (mean), Swank factor of 0.99 and detector gain (W) equals to 50 eV per detected charge. Therefore, the signal is given in electrons/cm^2, and no dynamic range scaling was performed. After the image is generated, a mask is applied to modify the pixel intensity values to compensate for inhomogeneities introduced by the x-ray beam divergence geometry (i.e. inverse square law and angle of incidence). No further processing was applied, thus the images are equivalent as "for processing".

The number of photon histories varied between approximately 10^{11} and 10^{12} with a speed of 10^8 histories/s on a Tesla P100 (NVIDIA, USA) GPU. The corresponding average and standard deviation of the incident air kerma values, including all cases, were 1.5 and 0.7 mGy, respectively.

The absorption energy for photons is 1 keV, while the electrons are locally absorbed [35]. The photon cross sections were calculated using PENELOPE (v. 2018) [36]. The composition of breast tissues (adipose, glandular and skin) were obtained from Hammerstein et al. [37], while for all other breast tissues were obtained from Woodard and White [38]. The

x-ray spectra were generated using the TASMICS software for a tungsten target [39]. Table 2 shows the filter material and tube potential for the x-ray spectra used for each breast thickness interval, considering tungsten as the anode material. In some cases (when the breast thickness is near the limit for an interval), the tube potential selected was 1 kV above or below from those displayed from Table 2 in order to evaluate possible variations from the automatic exposure control (AEC).

Table 2: X-ray spectra used for image simulation as a function of the compressed breast thickness range.

Thickness range (mm)	Filter material	Tube potential (kV)
20-25		25
25-35		26
35-45		27
45-50	Rhodium	28
50-55		29
55-60		30
60-65		31
65-70		30
70-80		32
80-85	Silver	33
85-90		34

2.3. Breast models masks: segmentation, relative height and relative glandular height

The breast phantoms segmentation to separate different tissues was performed by a simplified ray-tracing algorithm (a generalist and complete ray-tracing algorithm implementation is explained in the reference [40]). First, for each material, a numerical matrix (M_i) filled with zeros is defined in the same place as the x-ray detector with each matrix element representing the detector pixels. Afterwards, for each pixel, a dummy particle is generated and travels backwards, in the direction of the x-ray source (in this case a point source). For each step "s" traveled by the particle (defined by the user), the algorithm checks the current voxel material and adds one to the counter. After the mapping is finished for all matrix elements, the counts are returned for the material. This process is repeated for all materials, thus several matrices are generated ($M_i...M_N$). The value s was empirically determined to be equal to the voxel side length.

After this process is performed and with the M_N matrices, three masks were build in order to train the neural networks. Each mask belongs to a specific task, explained in the following.

The first mask (task I) classified the image in three regions: (i) background, (ii) skin contour plus nipple and (iii) inner tissues. For this purpose, the following criteria were used: (i) is defined as the elements of the matrices that did not contain any breast tissues; (ii) the matrices elements that contain nipple or a certain threshold of skin content (this value was determined as the minimum fraction to form a continuous contour around the breast); (iii) the elements that did not fit the criteria (i) or (ii) were selected as region (iii) using the flood fill technique inside the contour formed by (ii). A binary erosion technique [41] was used to remove isolated pixels from (ii) that could be present inside (iii).

The second mask (task II) describes the relative breast height (h) for each pixel located in the inner breast (obtained from the first mask). It is calculated by summing all the matrices elements in depth and normalizing them by the compressed breast thickness. Due to the beam divergence, the relative height was corrected to yield values between 0 and 1. It was noticed that during the breast compression routine, small air gaps were present between the breast and the compression or support plates (generally less than 3% the compressed breast thickness), shifting the maximum height in some regions.

The third mask (task III) quantifies the relative glandular height (g) of each projected pixel (i.e. the ratio between the height of glandular tissue and total height on the breast). For this specific case, the mask is divided in patches of 4×4 pixels, and the average glandular height is calculated for each patch.

The inner volume of the breast (Vol) (without skin and nipple) was estimated from masks I and II, as:

$$Vol = \left(\frac{\mathrm{SDD} - \mathrm{AG} - t/2}{\mathrm{SDD}} \right)^2 \times \sum_{i=0}^{i=N} m_i \times h_i \times (t - 2 \times \mathrm{ST}) \times A \tag{1}$$

where SDD is the source-to-detector distance, AG is the distance between the bottom of the breast and the detector, t is the compressed breast thickness, N the number of patches, m_i is the ith element of mask I (the value is 1 for inner breast, 0 otherwise), h_i the relative height from mask II for the element i, ST is the skin thickness and A the pixel area. This approximation considers that the projected breast image corresponds to the area at half of the breast thickness.

The volume glandular fraction (VGF, i.e. ratio between the glandular volume and the total volume, excluding skin) [6] was estimated by combining masks I, II and III, by performing a sum over the 4×4 patches

$$VGF = \frac{\sum_{i=0}^{i=N} \bar{A}_i \times \bar{h}_i \times g_i}{\sum_{i=0}^{i=N} \bar{A}_i \times (\bar{h}_i - h_s)} \tag{2}$$

where N the number of patches, $\bar{A}_i$ is the relative area of the patch belonging to the inner breast (from 0 to 1), g_i the glandular height (from 0 to 1), $\bar{h}_i$ the relative average height of the patch (with skin), h_s the relative skin thickness.

The calculated volumes were compared with the nominal volumes for 178 phantoms with average and maximum differences of 0.9% and 3.6%, respectively. We also studied the relation between the ground truth breast volume with and without skin, and found a linear behavior (r^2=0.999). These results are summarized in Appendix A.1. The calculated VGF using the masks were compared with the nominal values for 178 phantoms, showing differences up to 10% due the constant skin thickness approximation. A third order polynomial fit was adjusted to convert mask VGF to ground truth VGF to remove potential bias with this approximation, as explained in Appendix A.1. All VGF results further on have this correction applied.

6

2.4. Neural networks: deep learning framework

A total of three neural networks architectures were employed, one for each segmentation task (I to III) described in section 2.3. The first two are based on an adapted version of XNet [42], a convolutional neural network architecture previously used for x-ray imaging classification. From now in this work, the terms network and neural network are used interchangeably. The network implementation was made in Python (v. 3.6.9) using the PyTorch framework (v. 1.6.0) [43], while the training was performed on a NVIDIA GTX 1060 (6 GB of VRAM, CUDA v. 11.0). The network hyperparameters, if not explicitly mentioned, were obtained empirically by testing exhaustively the values that yielded better training and validation results. 178 phantoms were used for training and validation (80%:20% proportion), while 30 phantoms were selected for testing.

Fig. 2 depicts the configuration used for the skin segmentation and tissue height projection (masks I and II, respectively). The channel sizes and layers types are indicated with the concatenation operations (which skips certain layers indicated by the arrows). In this work, a transpose convolution layer substitutes a linear upsampling operation in the original architecture. The input layer for task I is the image (1024×832 pixels), normalized by the pixels from (487-537, 25-75), corresponding to a fixed small region near the breast phantoms center. For task II, the input is the same from task I, but only regions segmented as inner breast are selected (the other values are zeroed). The output layer differs between tasks: for task I is a three channel image, with the probabilities for skin, inner breast and background, while for task II is a one channel image with the relative local height (the output layer is a sigmoidal function which limits the values from 0 to 1). Due to memory constraints, a batch of size 1 was used during training and consequently, the batch norm layers were removed from the original architecture. For both networks the ReLU activation function was used, and a weight decay (L2 penalization) of 5×10^{-5}.
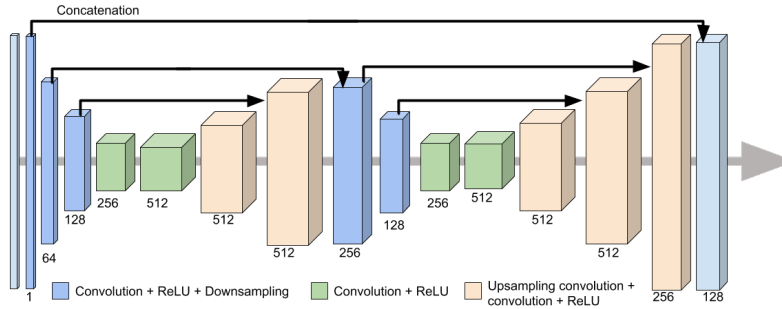
Figure 2: XNet [42] adapted architecture implemented in tissues segmentation and height quantification tasks. Each box corresponds to a layer, and the number below represents the number of channels.

For task III, an ensemble of five multi-layer perceptrons was adopted. The network consists of two fully connected layers of 200 neurons each and a linear output, as shown in Fig. 3. The procedure adopted started from the original image, where a box is drawn around the inner breast tissue segmented from mask I. Afterwards, this box is divided in images

7

patches of 4×4 pixels. The pixel values are normalized by the number of incident photons. In total, 11 features are included: the x-ray spectra (a label varying between 0 to 9), spectrum HVL (in millimeters of aluminum) and mean energy (in keV), the breast thickness (in mm), the average relative local height, the distance between the patch and the mask's center of mass, the area covered by the breast patch on image detector, the average and standard deviation pixel intensity, and two first order statistics (kurtosis and skewnes)[41]. All the features are normalized between 0 and 1. The network predicts the relative glandular height (i.e. the product of the glandular height by the relative local height, $g \times h$) in that image patch, and the output values were manually limited between 0 to 1 (values predicted outside this range were rounded to the nearest acceptable value). For stability purposes, we only considered patches that have an area 100% covered by breast.

Table 3 summarizes the networks used in this work. To account for uncertainties derived from the relative height predicted by task II, we implemented a five-fold cross validation scheme (i.e. the training data is divided in 5 non-overlapping parts). Then, five networks were trained in which 4 parts are for training and one is for validation (each network has a distinct training combination validation part). For each batch interaction during training, the relative heights (h) were multiplied by a factor sampled with a normal distribution $\mathcal{N}(C, \sigma = 0.05)$, where C is specific for each each network: 0.90, 0.95, 1.00, 1.05, 1.10. The final predicted relative glandular height is calculated by averaging the output from the five networks and the variation is calculated by the standard deviation. The ReLU activation function was used, and a weight decay (L2 penalization) of 10^{-4}.
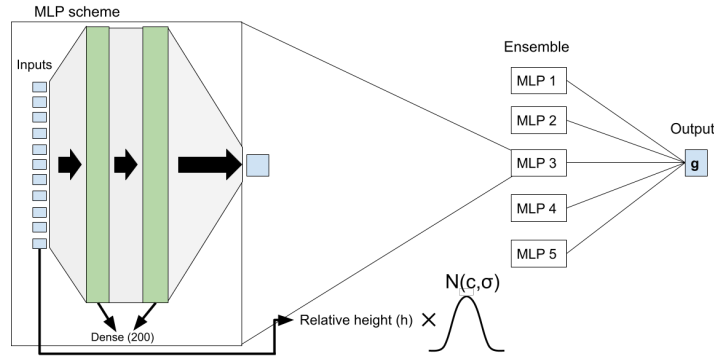
Figure 3: Illustration of glandular fraction estimation and the implemented architecture, which consists of five trained multi-layer, followed up by two fully connected layers (dense).

During the training of the network for task I, the skin and inner breast had a weight of 6 and 3, respectively, to compensate imbalanced dataset distributions. Moreover, the training data was augmented for tasks I and II, by flipping the image over the horizontal axis and translating the image by a random number between 0 and 50 in upwards and downwards directions, this procedure is applied for each epoch. The performance of the network from task I, besides the loss function used during training, is also benchmarked by comparing the inner breast and skin areas to the ground truth for validation and test samples. The task II is

Table 3: Summary of the networks used in this work.

Task	Architecture	Input	Output	Loss function
I - Skin segmentation	Fig. 2	Mammography image, pixels binned 4×4. Pixels normalized by the pixels from a fixed region, with the average pixel value subtracted and divided by the standard deviation	A tensor with three channels with probabilities for background, skin and inner breast.	Cross entropy
II - Relative height	Fig. 2	Mammography image, pixels binned 4×4. Pixels normalized by the pixels at the center of the breast.	Matrix with the relative breast height by pixel (h, values between 0 and 1).	Mean squared error
III - Relative glandular height	Fig. 3	11 features. Pixels normalized by number of histories.	Relative glandular height (glandular height times relative height, $g{\times}h$).	Mean squared error

benchmarked by comparing the ground truth breast phantom volume to the predicted breast volume (excluding skin) calculated from Eq. 1. The task III performance was benchmarked by comparing the predicted (Eq. 2) and the ground truth VGF values.

For the training and validation parts, the networks are evaluated separately (i.e. compared to each mask), while for the test step, the full framework is implemented and compared to the VGF expected values. The coefficient of determination (r^2)[44] is calculated when comparing the ground truth (T) and the predicted values by the networks (P) by adjusting a linear equation: $P = a \times T + b$, and forcing a=1 and b=0. The best linear fit was also adjusted by determining a and setting $b = 0$. The absolute differences (Δ) and the relative differences (Δ_r) are calculated as:

$$\Delta = P - T, \qquad \Delta_r(\%) = 100 \times (P - T)/T \tag{3}$$

In this work, the result representing the output of the networks, or those calculated from these outputs will be defined as "predicted".

Further information regarding comparison of our predicted VGF values and breast density values estimated with LIBRA tool for a small phantom dataset is available in the Supplementary material[45].

2.5. Estimation of glandularity

After the volume glandular fraction (VGF) of the breast was estimated, the breast glandularity (G) (i.e. the percentage by mass of glandular tissue in the breast, excluding skin) was calculated as:

$$G = 100 \times \frac{VGF \times \rho_g}{(1 - VGF) \times \rho_a + VGF \times \rho_g} \qquad (\%) \tag{4}$$

where ρ_a and ρ_g are the densities of adipose and glandular tissues (0.93 g/cm^3 and 1.04 g/cm^3), respectively [37]. In our approximation, tissues that were neither glandular nor skin were classified as adipose tissue.

2.6. Dosimetry and dose levels in mammography

The mean glandular dose (MGD) for the breast phantoms was estimated as:

$$MGD = DgN \times K_{\text{air}} \tag{5}$$

where K_{air} is the incident air kerma, and DgN is the normalized glandular dose (a conversion coefficient) [2].

The DgN values were obtained using neural networks from our previous work [46] based on the following input parameters: x-ray beam (anode, filter, tube potential and HVL), breast radius and thickness, glandularity, skin thickness and compression-plate ionization chamber distance. Summarizing the process, the parameters were fed through an ensemble of multi-layer perceptrons (MLP) as it performed the regression operations and returned the DgN for each case.

The x-ray beam parameters were obtained from the input files used to generated the images (Table 2). The breast thickness is known, while the radius is calculated by approximating the breast as a semicylinder (the radius value is limited from 6 cm to 12 cm). The glandularity was obtained from Eq. 4 and the skin model was set to 1.5 mm skin. The compression-plate ionization chamber distance is equal to 40 cm (the maximum allowed distance). The reported DgN values follow the homogeneous adipose-glandular tissue distribution. More details are contained in the original paper [46].

2.7. Clinical case selection

This study employed data from a retrospective analysis of patient mammography images, acquired on routinely collected anonymous data, ethical-board approved (CAAE: 47878315. 2.0000.5404). All mammograms were acquired using AEC with the Selenia Dimensions system (Hologic, Danbury, CT, USA) which is installed at the Institute of Radiology (InRad) in the Faculty of Medicine, University of São Paulo. The data was filtered to only consider CC images. A total of 2134 clinical images were used. The HVL values in the DICOM header were matched from those used in the DgN calculations by adding 3 mm additional filtration of PMMA. The K_{air} is extracted from the DICOM header, which is believed to be a good approximation from measured values obtained with an ionization chamber [47]. We also extracted the MGD values reported by the Organ Doses tag for further comparisons.

The following procedure was adopted. For each phantom in this study, we filtered the DICOM headers that present the same x-ray spectra and the compressed breast thickness (with 2 mm tolerance). Afterwards, we established K_{air} intervals based on percentiles 10%, 25%, 50%, 75% and 90%, which were selected based on the breast phantom glandularity (respective intervals: $G \leq 5\%$, $5\% < G \leq 15\%$, $15\% < G \leq 25\%$, $25\% < G \leq 40\%$, $G > 40\%$), as shown in Fig. 4. Finally, K_{air} values returned for each case and the MGD was estimated from Eq. 5. From the 208 original virtual phantoms, the MGD was estimated for 132 cases, the others 76 failed due to insufficient patient data for comparison.

3. Results

3.1. Breast segmentation training and validation

The training and validation loss values as a function of the interaction number for the three networks: image segmentation, relative height and relative glandular height predictions
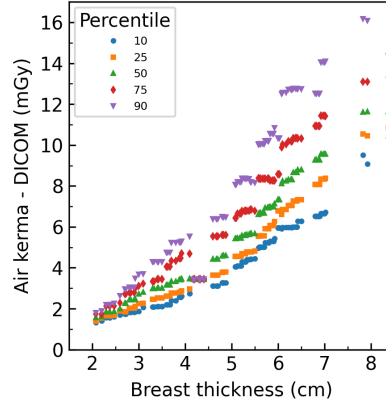
Figure 4: Incident air kerma values as function of breast thickness reported in the DICOM header and the respective percentile.

are shown in Figs. 5(a), (c), and (e), respectively. Figs. 5(b), (d), and (f) show the learning rate as a function of the interaction number (in the same order as described above). As expected, the training and validation losses decrease with the learning rate, until a plateau is reached, triggering the early training stop. The validation values are more stable because they represent the average validation values for all cases on each epoch (calculated when the training iterated over all the training samples), besides they are similar to the training trend (calculated using a moving average).

The skin and inner breast segmented relative areas (ground truth×predicted) for the validation and test images are shown in Fig. 6(a) and 6(b), respectively. In this case, to facilitate the comparison, the results were normalized by the maximum value on each ground truth sample. The area marked for skin plus nipple is approximately two orders of magnitude lower than the inner breast area (respectively $7.0{\times}10^3$ pixels versus $2.5{\times}10^5$, on average), thus a higher fluctuation is observed between the mask and the predicted values. For both validation and test, the predicted skin+nipple areas are usually higher than the ground truth, as seen by the angular coefficients a values (1.20 and 1.08, respectively) and r^2 (-0.638 and 0.284, respectively). This behavior is further explained in Fig. 7. An excellent agreement is observed regarding the inner breast area for both validation and test cases ($r^2 >0.999$ for both), with an average relative error below 1%.

The image segmentation performed for the four randomly selected breast models from the test data are exemplified in Fig. 7. For each case, the original simulated mammography image is compared with the ground truth mask and prediction. An interesting behavior observed is that the skin contour for the ground truth masks is not smooth, which contrasts with the predicted segmentation where the contours are smoothed out and continuous. Although the nipple is correctly identified in the four images, in some cases, we observe an over-classification inwards the breast. The validation and training results (images not shown here) also present a few cases where the nipple is only partially identified, and the other region is classified as inner breast tissue. The smoothing and the over-classification could

11
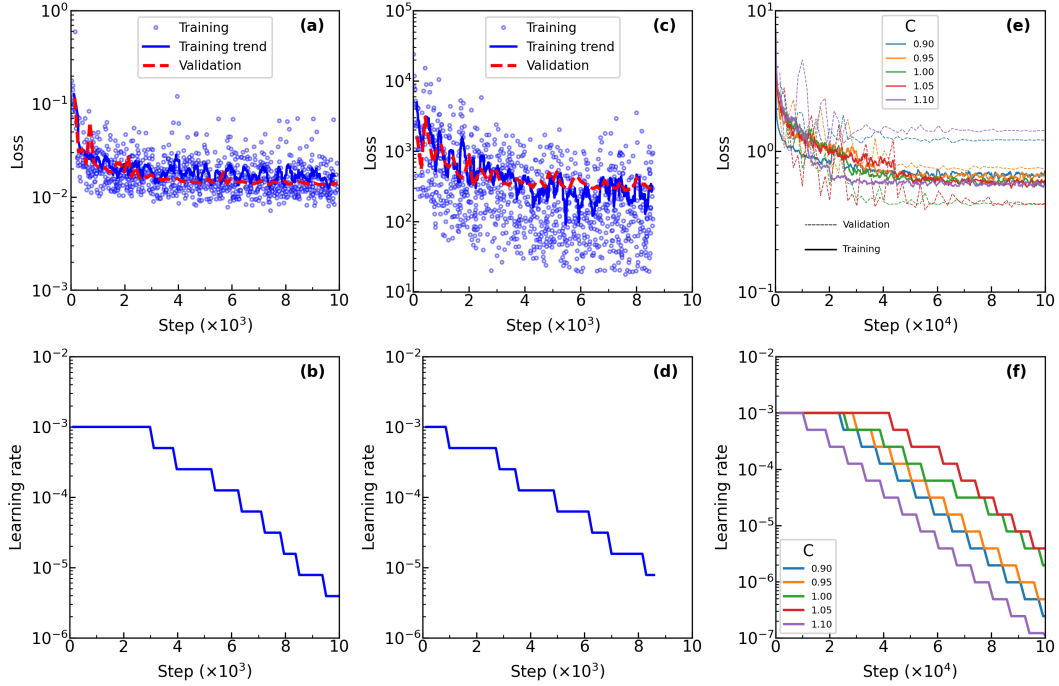
Figure 5: Training/validation results for: (a)/(b) breast segmentation; (c)/(d) relative height; (e)/(f) relative glandular height. A total of 60, 70 and 60 epochs are shown for (a), (c), (e), respectively. The step number is obtained by multiplying the value in the x-axis with the offset number indicated on each graph. C is the offset factor for each network of the ensemble for task III regarding the noise sampling for the relative height (Fig.s (e) and (f)).

be an explanation of the skin + nipple area discrepancies showed in Fig. 6 and consequently low r^2 values. Nevertheless, for our application, due to the inner breast area being orders of magnitude higher than the skin + nipple region, the impact of this effect on the other results can be neglected.

The relative height prediction for the four selected breast phantoms (the same cases from Fig. 7) are shown in Fig. 8. The vertical and horizontal profile views are also compared. Cases (a) and (b) illustrate standard acquisitions with full breast compression and a smooth variation in the glandular distribution across the breast, where an excellent agreement between the mask and the predicted relative height map is observed. The cases (c) and (d) correspond to unusual virtual phantoms to assess the performance of the network. For the case (c), when a drastic variation of glandular content is present within a large region of the breast, the network interprets as a variation of the relative thickness, as shown by the discontinuity around the 0.8 relative x-axis location. The case (d) shows an example of the breast not being properly compressed, where the relative horizontal height drops smoothly as function of the pixel coordinates. For all selected cases, the nipple artifact discussed in Fig. 7 is present in the images, since the breast was previously segmented with the first network.
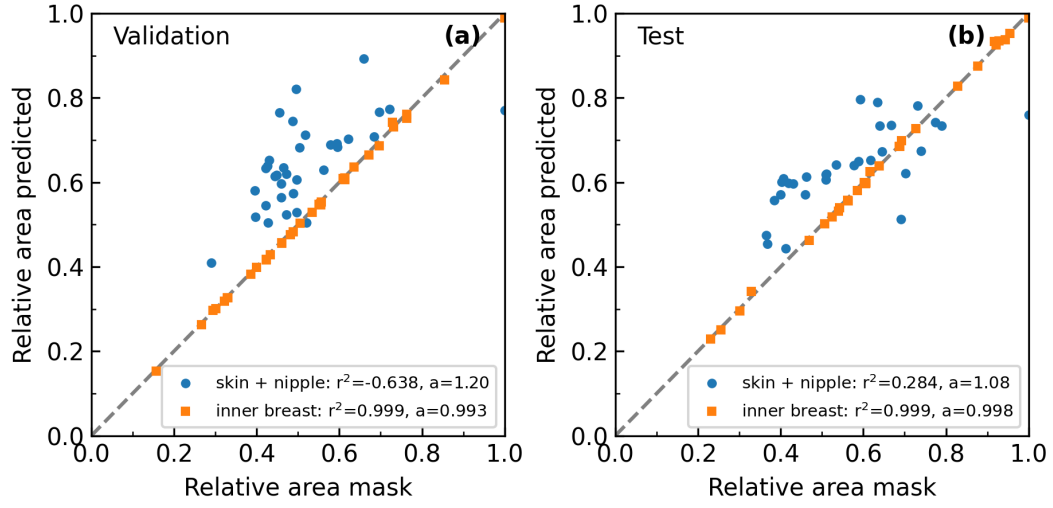
Figure 6: (a) Validation and (b) test results for the image segmentation task. The areas are normalized by the maximum values for each region: (a) 13204 pixels for skin + nipple, 483592 pixels for inner breast; and (b) 13114 pixels for skin + nipple, 391670 pixels for inner breast. In both (a) and (b), the identity line is represented by the dashed gray line.
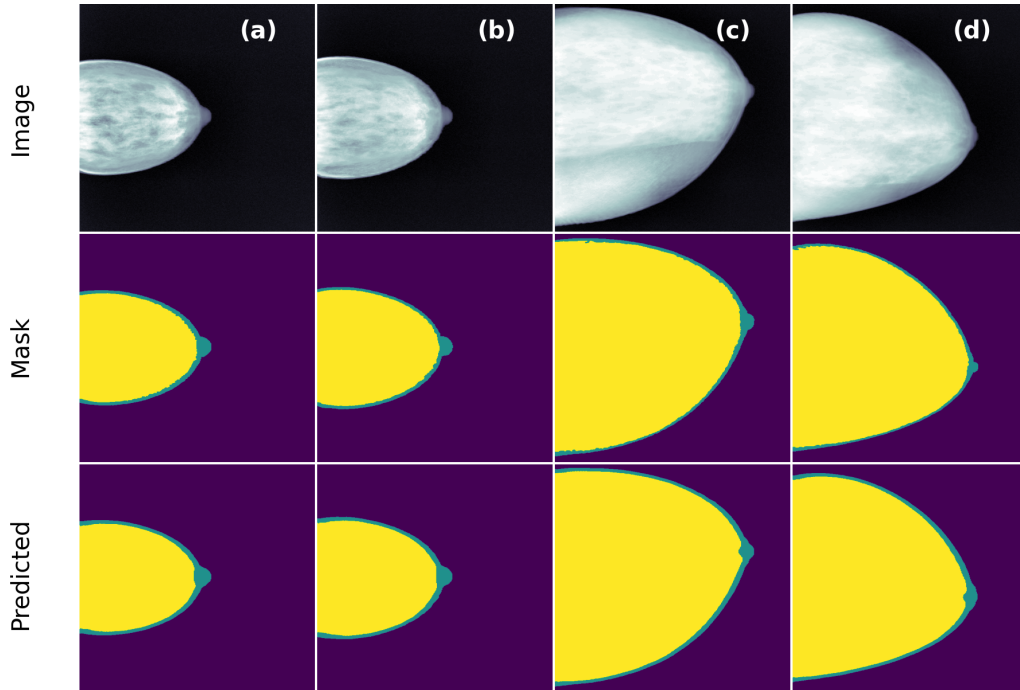
Figure 7: Four randomly selected cases (with labels from (a) to (d)) illustrating the image segmentation process for the test sample.

13
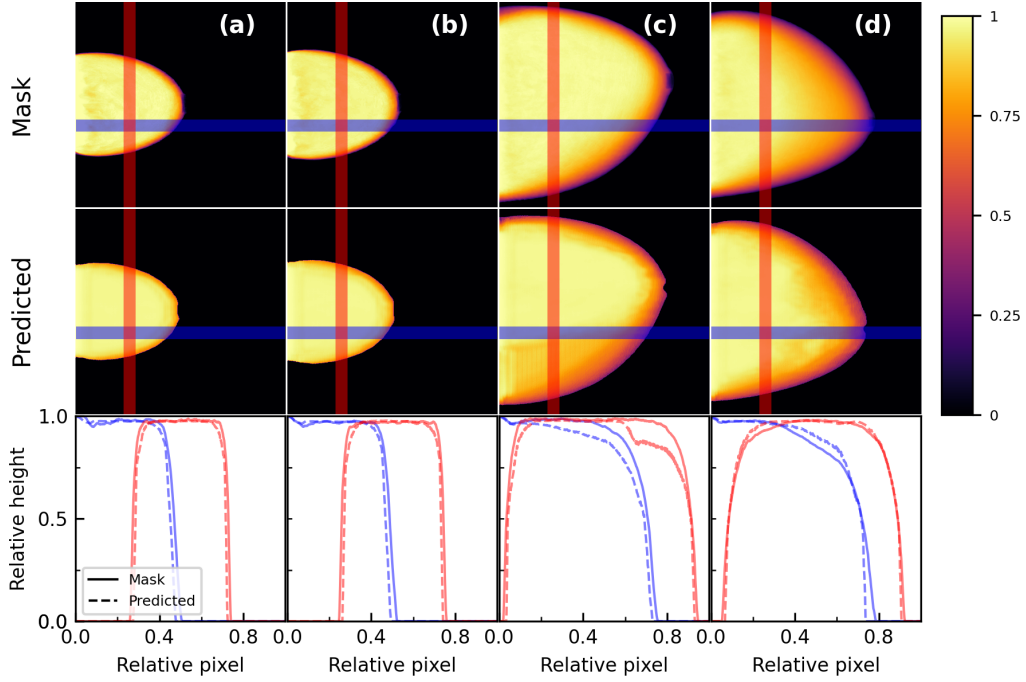
Figure 8: Relative height prediction from the cases showed in Fig. 7. The blue and red patches represent cross sections in the horizontal and vertical directions. The respective profile views are displayed in the third row.

The breast volume obtained with the relative height predicted maps versus the ground truth is shown in Fig. 9(a). Both validation and test results presented a good agreement with the ground truth volumes ($r^2 > 0.994$ and 0.982, respectively). The relative differences (Δ_r) between the predicted and ground truth values are displayed in Fig. 9(b). The dashed red line and the shaded area represent, respectively, the average relative difference and one standard deviation for test cases. The average relative difference and standard deviation are in the order of 4% for both validation and test data. The predicted breast volume is systematically underestimated for very thinner breasts (thickness near 2 cm and volumes below 250 cm^3) due to the approximation of the skin layer being constant (1.5 mm thick).

Fig. 10(a) shows the relative glandular height prediction compared to the ground truth for the validation data, with the identity as the dashed gray line. The results of relative glandular height present a good agreement, with a r^2=0.986. The differences Δ are quantified in Fig. 10(b), with an absolute average difference of 0.02 in the relative glandular height.

The ground truth relative glandular height, the patches calculated with the 4×4 binning mask and the network predictions for four test breasts are shown in Fig. 11. A good overall agreement was observed between the predicted and ground truth values for cases (a), (b) and (d). The incorrect height prediction showed in Fig. 8(c) causes the network to predict a slightly higher glandular height than the ground truth in case (c).

With the three networks trained, we implemented the full pipeline to estimate the volume
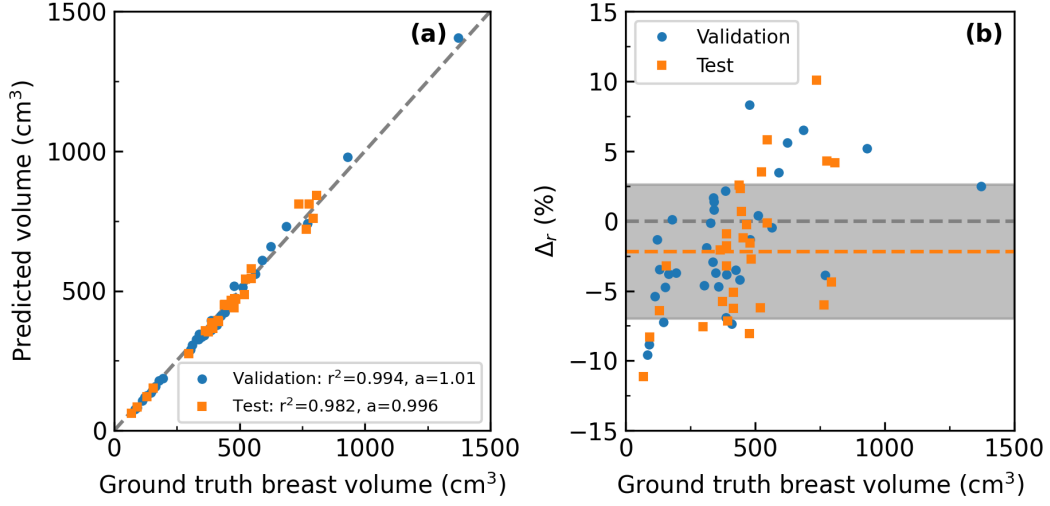
Figure 9: (a) Validation and test results for volume predicted compared to the ground truth volumes derived from breast phantoms. The identity line is represented by the dashed gray line. (b) Relative differences Δ_r between the values. The dashed red line and the shaded area indicate, respectively, the average relative difference for the test cases and one standard deviation.
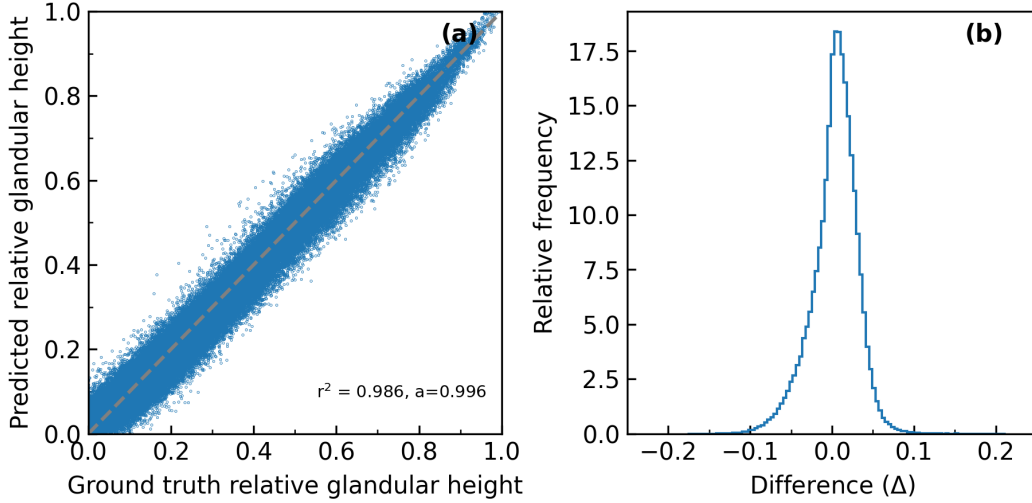
Figure 10: (a) Validation results for relative glandular height prediction compared to the ground truth values from the masks. The identity line is represented by the dashed gray line. (b) Distribution of the differences Δ between prediction and the ground truth values.

glandular fraction (VGF) for the test data. For sake of completeness, we also predicted the VGF for the phantoms that were used for training since the full pipeline was not used beforehand. The results shown in Fig. 12(a) indicates a good correlation between the ground truth VGF and the predicted values, with r^2 coefficients of 0.959 and 0.935 for training and
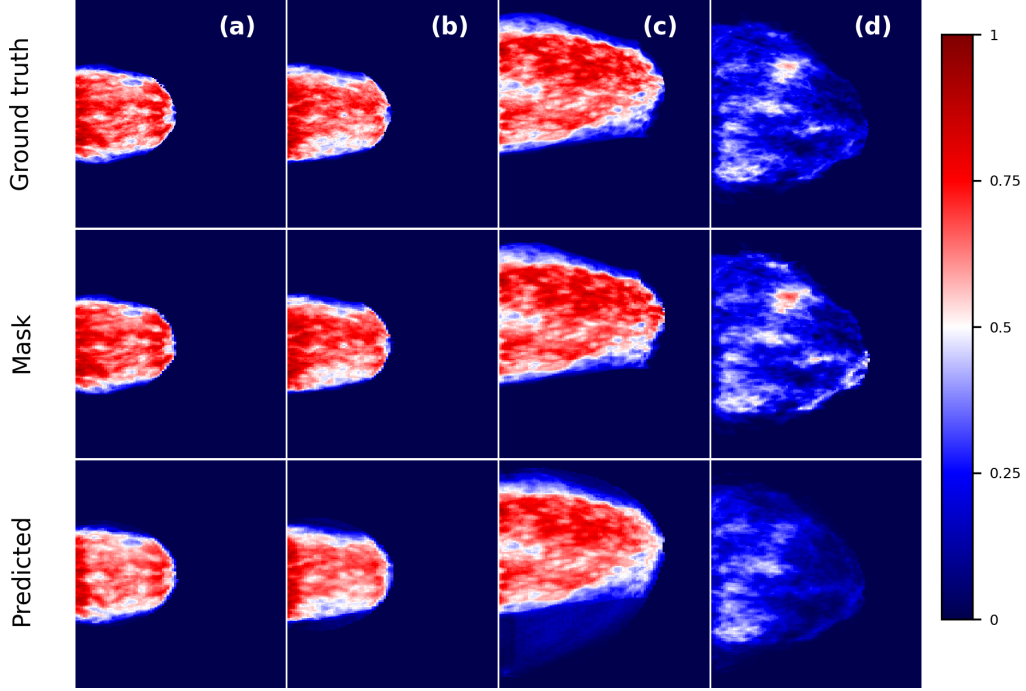
Figure 11: Relative glandular height prediction from the cases shown in Fig. 7. The predicted patches are assembled to match the original mask shape.

test data, respectively. The average absolute differences Δ (standard deviation) for training and test data are 0.03(4) and 0.04(5), respectively, as illustrated in Fig. 12(b). It is important to notice that the distribution of VGF, in a real population, is more concentrated towards low values, and values higher than 0.5 represent the minority of cases [3].

3.2. Breast dosimetry

The DgN conversion coefficients were estimated for all 208 phantoms after the glandularity values were calculated based on the VGF obtained with the ground truth and the ones predicted with the network. The DgN coefficients obtained with fixed glandularity given by the median glandularity of all phantoms (approximately 23%) were also calculated. Fig. 13(a) shows the relative DgN differences calculated from the predicted glandularity and those using the median glandularity compared to the ground truth. It is observed that using a fixed glandularity for the entire population introduces a systematic error that, in general, overestimates the DgN coefficients calculated compared the ground truth glandularity, on average 8.5%. Meanwhile, the DgN coefficients obtained with the glandularity calculated with the pipeline resulted in an average error of 1.3% compared to the ground truth.

Fig. 13(b) shows the predicted MGD distribution for 132 test phantoms calculated using the pipeline, as described in section 2.6, and the incident air kerma extracted from the DICOM header for clinical cases. For sake of completeness, we also included values estimated with a 4 mm skin thickness (model used for organ dose by the Hologic system [48]) and
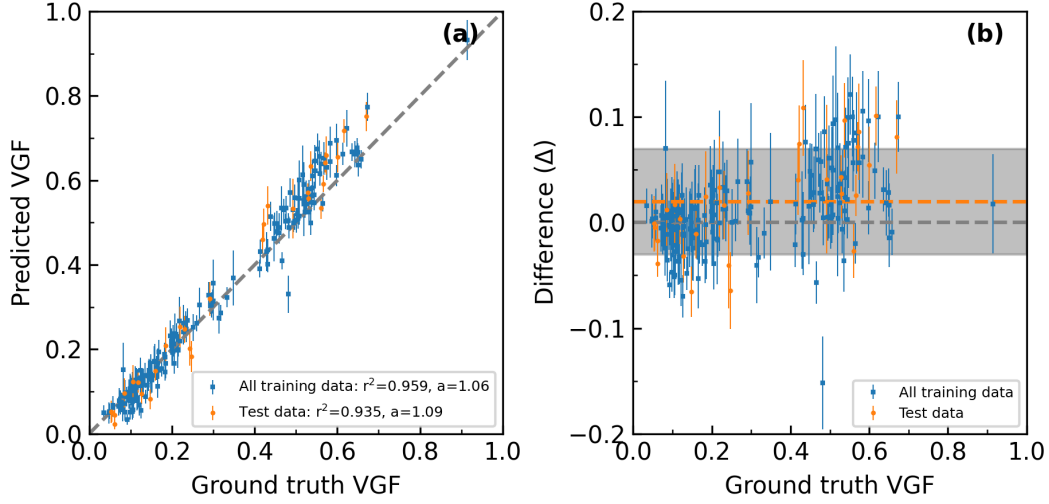
Figure 12: (a) Reconstructed volume glandular fraction (VGF) for the training and test data as function of the ground truth extracted from the breast phantoms. (b) Differences between predicted and the ground truth values. The shaded area indicates one standard deviation for test data. Bars: standard deviation of the ensemble prediction.

50% glandularity for the test phantoms (Estimated) and the Organ Dose reported in the DICOM header for the entire clinical dataset. Simulated cases that did not presented a real counterpart were ignored in this process. The median(75 percentile) MGD values are 1.91(2.45) mGy, while the estimated and DICOM values are 1.60(2.10) mGy and 1.62(2.00) mGy, respectively. From those distributions, the dose reference levels could be extracted based on the 75 percentile values.

The predicted MGD as a function of the breast thickness is shown in Fig. 14(a). The apparent discontinuity for breasts thickness closer to 4 cm is due to the combination of variations on average breast compositions and incident air kerma values used in this work, considering the glandularity percentiles. Fig. 14(b) compares the MGD between the predicted and DICOM values for three breast thickness groups. The trend of increasing the MGD for thicker breasts becomes evident. It is observed a significant variation for each interval, represented by the bars (one standard deviation). This behavior can be explained because a 2 cm interval width is considered, covering a range of MGD values, also there is a variation of glandularity within the patients for each interval. Nevertheless, the average MGD predicted values for each interval are higher than the respective Organ Dose DICOM values for all thickness range, due to the dosimetry models employed in each case.

4. Discussion

The segmentation of mammography images including edge detection and nipple removal was previously implemented by other authors using different algorithms [49, 50]. In our implementation, the ground truth masks were created by establishing threshold values (only for
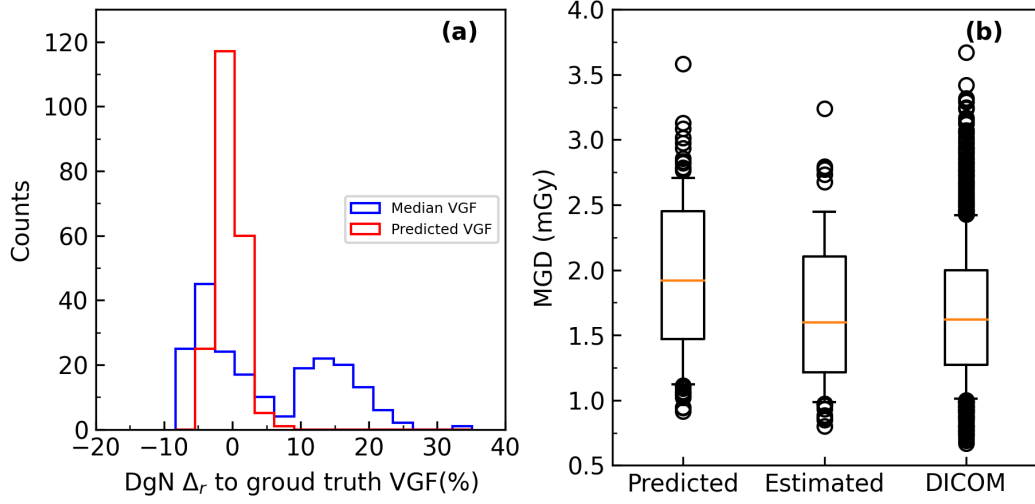
Figure 13: (a) DgN relative differences for all 208 breasts calculated from the predicted glandularity and those using the median glandularity of the population, compared to the ground truth. (b) Boxplot of MGD distribution for three cases: (i) predicted by the network with 1.5 mm skin, (ii) estimated using 4 mm skin and 50% glandularity (iii) extracted from the DICOM header. Centerline: median, lower and upper box limits: 25 and 75 percentiles, whiskers: 10 and 90 percentiles, circles: outliers.
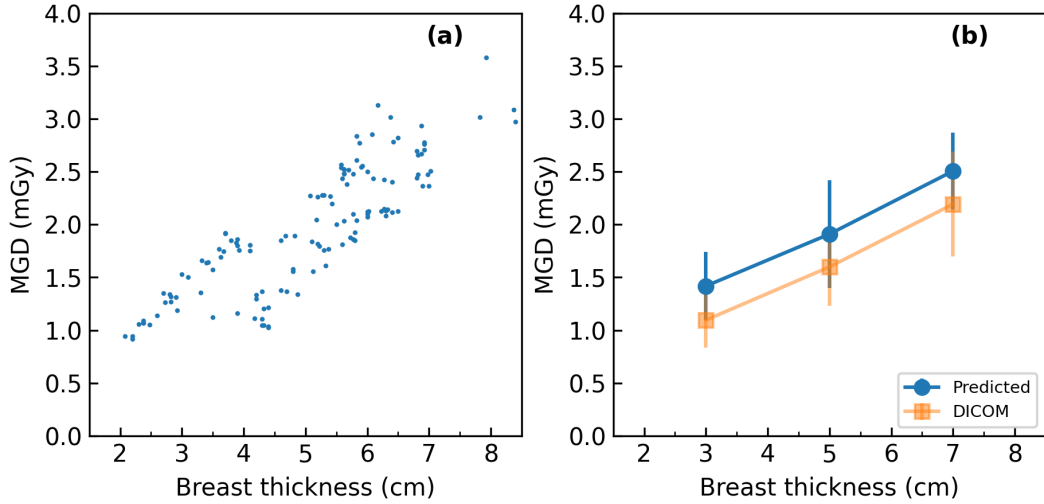
Figure 14: (a) MGD dose distribution from Fig. 13(b) as function of breast thickness. (b) Predicted MGD and Organ Dose from DICOM header trends as function of breast thickness for three intervals, bars indicate one standard deviation.

task I) for the projected skin and nipple, which resulted in some skin and nipple boundaries to be not smooth and in some regions presenting slight discontinuities. This pattern could explain the discrepancies between the ground truth skin plus nipple areas and the predicted

areas by the network. However, for the application proposed in this work, an excellent agreement was found between the ground truth inner breast areas and the predicted ones. The performance of breast segmentation can still be improved since in a few cases, regions of the nipple were incorrectly classified as inner breast. Moreover, the breasts are imaged in a CC view, thus the pectoral muscle is not present and consequently, the inclusion of medium lateral oblique projections would require the additional segmentation of muscle tissue [51]. Since the exact shape of the breast cannot be reconstructed from a single 2D image, a model that approximates the breast with a 1.5 mm skin layer was adopted. This approximation according to our comparisons, induced systematic errors specially for thinner breasts that were compensated with correction factors using a polynomial fit. From the results, it was showed that the overall prediction performance is better for firmly compressed breasts and with phantoms with a more homogeneous glandular distribution, as those achieved in high quality clinical mammography images for real patients. Although the relative glandular height maps presented a lower resolution than a native mammography image, it did not interfere significantly on the overall VGF predictions. The highest errors were observed for unusual cases where the compression was partially incomplete or the phantoms presented an extremely heterogeneous glandular tissue distribution. We are studying, for future versions, to include the compression force as an input parameter to address some of these issues, since the correct measure of breast thickness is an important factor for an accurate breast density estimations [52]. We successfully trained a network to predict the relative glandular height within the breast, which showed a good performance for the validation and test samples. An interesting aspect observed in this work was the limitation of the technique when tissues different from glandular and adipose are present in the phantoms. The predicted values tend to overestimates the glandular height since these other tissues have higher attenuation coefficients than adipose tissue and more similar to glandular tissue. The framework is purposely divided in three parts to facilitate future implementations that requires one specific task. Although this work focused primarily on images generated from Monte Carlo simulations, preliminary tests (not included) showed that the deep learning algorithm performed equally under different quantum noise levels. For a relative dose varying from 0.1 to 10 times the original dose, the predicted VGD varied less than 0.01 for a nominal 0.12 VGF. Moreover, the MC code tries to simulate a real mammography image, as previously stated in other works [30, 31]. A future work is planned to apply this algorithm for real mammography breast images.

From the volume glandular fraction values predicted by our framework, it was possible to calculate the glandularity and finally the DgN factors using neural networks previously trained [46] for the 208 virtual breast phantoms generated in this work. We found 1.3% of difference, on average, between the DgN values from the predicted glandularity and the ground truth DgN, with a maximum below 8%. We also compared the case where the median glandularity (23%) of the phantoms is considered, which resulted on average error of 8.5%, and a maximum error of 35%. Naturally, these errors are propagated to the MGD calculations and could induce bias on the dose reference levels. In terms of radioprotection, it is desirable to minimize potential biases and errors for the dose estimation. With incidente air kerma values extracted from DICOM mammography images, we estimated the

19

MGD for 132 phantoms and found a median(75 percentile) values of 1.89(2.44) mGy. On the other hand, by employing a traditional model of 4 mm thick skin used for Organ Dose estimation by the Hologic system [48] and 50% (constant) glandularity, the reported values are 1.60(2.10) mGy, which are closer to the Organ Dose tag values 1.62(2.00) mGy. This highlights the importance of knowing which model is being considered for the MGD estimations when comparing dose levels, since some models could result in systematically higher or lower doses than others [8]. It is important to notice that the model used for calculating the MGD value reported by the Organ Dose tag within the DICOM header can vary between manufactures [48].

The results presented in this work are based on anthropomorphic virtual phantoms and Monte Carlo simulations, thus they are based on the characteristics of the virtual breasts generated by the software and the limitations of the simulations. It offers the advantage of knowing the ground truth values and, to easily label the training data, which is a good environment for testing the concept of the deep learning proposed in this work. However, it is still an approximation and does not reflect completely a clinical situation, requiring further studies and refinements before applying for clinical cases. Therefore, this approach of determining the breast density with deep-learning models trained on virtual phantoms shows promising preliminary results and it could be a complementary method over the existing ones, since it uses a different methodology of determining breast density with virtual breast phantoms, and not relying on physical models developed by other algorithms. Additionally, the framework could be adapted for other tasks and improved over time, with different neural network architectures or expanding the training dataset. Since the images were generated from virtual patients, there is the advantage of openly sharing and distributing the database and the algorithm.

5. Conclusions

In this work we introduce a deep learning framework to estimate VGF values from 208 virtual breast phantoms, with promising preliminary results. From the predicted VGF values, the DgN coefficients were calculated by using another neural network. Afterwards, the mean glandular dose values are obtained from air kerma extracted from DICOM header for a clinical cohort. This approach enables to establish dose reference levels more accurately for a given population than using an average glandularity model. This framework could be adapted for other applications (e.g. image processing and segmentation) by employing transfer learning techniques, especially in cases where the training dataset is small. Moreover, future studies can explore this implementation for real mammography units and clinical images, and compare the results with other glandularity estimation algorithms. Finally, application for deriving patient-specific doses need different approaches, since the vertical location of glandular tissue cannot be determined by using single view mammography images. The database and the deep learning algorithm used in this study are freely available by request to the corresponding author atomal@ifi.unicamp.br.

Acknowledgments

References

[1] Sardanelli F, Aase HS, Álvarez M, Azavedo E, Baarslag HJ, Balleyguier C, et al. Position paper on screening for breast cancer by the European Society of Breast Imaging (EUSOBI) and 30 national breast radiology bodies from Austria, Belgium, Bosnia and Herzegovina, Bulgaria, Croatia, Czech Republic, Denmark, Estonia, Finland, France, G. Eur Radiol 2017;27(7):2737–43. doi:`10.1007/s00330-016-4612-z`.

[2] Dance DR, Sechopoulos I. Dosimetry in x-ray-based breast imaging. Phys Med Biol 2016;61(19):R271–304. doi:`10.1088/0031-9155/61/19/R271`.

[3] Yaffe MJ, Boone JM, Packard N, Alonzo-Proulx O, Huang SY, Peressotti CL, et al. The myth of the 50-50 breast. Med Phys 2009;36(12):5437–43. doi:`10.1118/1.3250863`.

[4] Hernandez AM, Seibert JA, Boone JM. Breast dose in mammography is about 30% lower when realistic heterogeneous glandular distributions are considered. Med Phys 2015;42(11):6337–48. doi:`10.1118/1.4931966`.

[5] Sechopoulos I, Bliznakova K, Qin X, Fei B, Feng SSJ. Characterization of the homogeneous tissue mixture approximation in breast imaging dosimetry. Med Phys 2012;39(8):5050–9. doi:`10.1118/1.4737025`.

[6] Huang SY, Boone JM, Yang K, Packard NJ, McKenney SE, Prionas ND, et al. The characterization of breast anatomical metrics using dedicated breast CT. Med Phys 2011;38(4):2180–91. doi:`10.1118/1.3567147`.

[7] Caballo M, Boone JM, Mann R, Sechopoulos I. An unsupervised automatic segmentation algorithm for breast tissue classification of dedicated breast computed tomography images. Med Phys 2018;45(6):2542–59. doi:`10.1002/mp.12920`.

[8] Sarno A, Mettivier G, Di Lillo F, Bliznakova K, Sechopoulos I, Russo P. Homogeneous vs. patient specific breast models for Monte Carlo evaluation of mean glandular dose in mammography. Phys Med 2018;51:56 – 63. doi:`https://doi.org/10.1016/j.ejmp.2018.04.392`.

[9] Arana Peña LM, Fedon C, Garcia E, Diaz O, Longo R, Dance DR, et al. Monte Carlo dose evaluation of different fibroglandular tissue distribution in breast imaging. In: Van Ongeval C, Marshall N, Bosmans H, editors. 15th International Workshop on Breast Imaging (IWBI2020); vol. 11513. SPIE; 2020, p. 76. doi:`10.1117/12.2564278`.

[10] Geeraert N. Quantitative evaluation of fibroglandular tissue for estimation of tissue differentiated absorbed energy in breast tomosynthesis. Ph.D. thesis; Télécom ParisTech/TSI; 2014.

[11] Teuwen J, Moriakov N, Fedon C, Caballo M, Reiser I, Bakic P, et al. Deep learning reconstruction of digital breast tomosynthesis images for accurate breast density and patient-specific radiation dose estimation. Tech. Rep.; Accessed November 27, 2020. `arXiv:2006.06508v1`.

[12] di Franco F, Sarno A, Mettivier G, Hernandez AM, Bliznakova K, Boone JM, et al. GEANT4 Monte Carlo simulations for virtual clinical trials in breast X-ray imaging: Proof of concept. Phys Med 2020;74:133–42. doi:`https://doi.org/10.1016/j.ejmp.2020.05.007`.

[13] Fedon C, Caballo M, García E, Diaz O, Boone JM, Dance DR, et al. Fibroglandular tissue distribution in the breast during mammography and tomosynthesis based on breast ct data: A patient-based characterization of the breast parenchyma. Med Phys 2021;n/a(n/a). doi:`https://doi.org/10.1002/mp.14716`.

[14] Sechopoulos I, Boone JM, Dance D, van Engen R, Russo P, Young KC. Mammography dose estimates do not reflect any specific patient's breast dose. Eur J Radiol 2020;131. doi:`10.1016/j.ejrad.2020.109216`.

[15] Power G, Manley M, Baldelli P, Keavey E, Phelan N. Breast thickness based DRLs in screening mammography. Phys Med 2019;67:203. doi:`10.1016/j.ejmp.2019.09.204`.

[16] Alonzo-Proulx O, Mawdsley GE, Patrie JT, Yaffe MJ, Harvey JA. Reliability of automated breast density measurements. Radiology 2015;275(2):366–76. doi:`10.1148/radiol.15141686`.

[17] Ekpo EU, Hogg P, Highnam R, McEntee MF. Breast composition: Measurement and clinical use. Radiography 2015;21(4):324–333. doi:`{10.1016/j.radi.2015.06.006}`.

[18] Ng KH, Lau S. Vision 20/20: Mammographic breast density and its clinical applications. Med Phys 2015;42(12):7059–77. doi:`https://doi.org/10.1118/1.4935141`.

[19] Lee J, Nishikawa RM. Automated mammographic breast density estimation using a fully convolutional network. Med Phys 2018;45(3):1178–90. doi:`10.1002/mp.12763`.

[20] Lizzi F, Laruina F, Oliva P, Retico A, Fantacci ME. Residual convolutional neural networks to automatically extract significant breast density features. In: Vento M, Percannella G, editors. Computer Analysis of Images and Patterns (CAIP 2019); vol. 1089. 2019, p. 28–35.

[21] Ionescu GV, Fergie M, Berks M, Harkness EF, Hulleman J, Brentnall AR, et al. Prediction of reader estimates of mammographic density using convolutional neural networks. J Med Imag 2019;6(03):1. doi:`10.1117/1.jmi.6.3.031405`.

[22] Warren LM, Harris P, Gomes S, Trumble M, Halling-Brown MD, Dance DR, et al. Deep learning to calculate breast density from processed mammography images. In: Van Ongeval C, Marshall N, Bosmans H, editors. 15th International Workshop on Breast Imaging (IWBI2020); vol. 11513. SPIE; 2020, p. 24. doi:`10.1117/12.2561278`.

[23] Maghsoudi OH, Gastounioti A, Scott C, Pantalone L, Wu FF, Cohen EA, et al. Deep-libra: Artificial intelligence method for robust quantification of breast density with independent validation in breast cancer risk assessment. 2020. `arXiv:2011.08001`.

[24] Graff CG. A new, open-source, multi-modality digital breast phantom. In: Kontos D, Flohr TG, Lo JY, editors. Medical Imaging 2016: Physics of Medical Imaging; vol. 9783. SPIE; 2016, p. 978309. doi:`10.1117/12.2216312`.

[25] Hernandez AM, Becker AE, Boone JM. Updated breast CT dose coefficients (DgN CT) using patient-derived breast shapes and heterogeneous fibroglandular distributions. Med Phys 2019;46(3):1455–66. doi:`10.1002/mp.13391`.

[26] Huang SY, Boone JM, Yang K, Kwan ALC, Packard NJ. The effect of skin thickness determined using breast CT on mammographic dosimetry. Med Phys 2008;35(4):1199–206. doi:`10.1118/1.2841938`.

[27] Sharma D, Graff CG, Badal A, Zeng R, Sawant P, Sengupta A, et al. Technical Note: In silico imaging tools from the VICTRE clinical trial. Med Phys 2019;46(9):3924–8. doi:`10.1002/mp.13674`.

[28] Maas SA, Ellis BJ, Ateshian GA, Weiss JA. FEBio: Finite elements for biomechanics. J Biomech Eng 2012;134(1). doi:`10.1115/1.4005694`.

[29] Badal A, Badano A. Accelerating Monte Carlo simulations of photon transport in a voxelized geometry using a massively parallel graphics processing unit. Med Phys 2009;36(11):4878–80. doi:`10.1118/1.3231824`.

[30] Badano A, Graff CG, Badal A, Sharma D, Zeng R, Samuelson FW, et al. Evaluation of Digital Breast Tomosynthesis as Replacement of Full-Field Digital Mammography Using an In Silico Imaging Trial. JAMA Network Open 2018;1(7):e185474. doi:`10.1001/jamanetworkopen.2018.5474`.

[31] Badal A, Sharma D, Graff CG, Zeng R, Badano A. Mammography and breast tomosynthesis simulator for virtual clinical trials. Comput Phys Commun 2020;In press:107779. doi:`10.1016/j.cpc.2020.107779`.

[32] Cunha DM, Tomal A, Poletti ME. Evaluation of scatter-to-primary ratio, grid performance and normalized average glandular dose in mammography by Monte Carlo simulation including interference and energy broadening effects. Phys Med Biol 2010;55(15):4335–59. doi:`10.1088/0031-9155/55/15/010`.

[33] Day GJ, Dance DR. X-ray transmission formula for antiscatter grids. Phys Med Biol 1983;28(12):1429–

33. doi:`10.1088/0031-9155/28/12/008`.

[34] Bick U, Diekmann F. Digital Mammography. Medical Radiology; Berlin, Heidelberg: Springer Berlin Heidelberg; 2010. doi:`10.1007/978-3-540-78450-0`.

[35] Sechopoulos I, Ali ESM, Badal A, Badano A, Boone JM, Kyprianou IS, et al. Monte Carlo reference data sets for imaging research: Executive summary of the report of AAPM Research Committee Task Group 195. Med Phys 2015;42(10):5679–91. doi:`10.1118/1.4928676`.

[36] Salvat F. PENELOPE-2018: A Code System for Monte Carlo Simulations of Electron and Photon Transport. Issy-les-Mounlineaux, OECD/NEA; 2019.

[37] Hammerstein RG, Miller DW, White DR, Masterson ME, Woodard HQ, Laughlin JS. Absorbed Radiation Dose in Mammography. Radiology 1979;130(2):485–91. doi:`10.1148/130.2.485`.

[38] Woodard HQ, White DR. The composition of body tissues. Brit J Radiol 1986;59(708):1209–18. doi:`10.1259/0007-1285-59-708-1209`.

[39] Hernandez AM, Seibert JA, Nosratieh A, Boone JM. Generation and analysis of clinically relevant breast imaging x-ray spectra. Med Phys 2017;44(6):2148–60. doi:`10.1002/mp.12222`.

[40] Amanatides J, Woo A. A Fast Voxel Traversal Algorithm for Ray Tracing. Eurographics 1987;doi:`10.1.1.42.3443`.

[41] Virtanen P, Gommers R, Oliphant TE, Haberland M, Reddy T, Cournapeau D, et al. SciPy 1.0: Fundamental Algorithms for Scientific Computing in Python. Nat Methods 2020;17:261–72. doi:`10.1038/s41592-019-0686-2`.

[42] Bullock J, Cuesta-Lázaro C, Quera-Bofarull A. XNet: a convolutional neural network (CNN) implementation for medical x-ray image segmentation suitable for small datasets. In: Gimi B, Krol A, editors. Medical Imaging 2019: Biomedical Applications in Molecular, Structural, and Functional Imaging; vol. 10953. International Society for Optics and Photonics; SPIE; 2019, p. 453 –63. doi:`10.1117/12.2512451`.

[43] Paszke A, Gross S, Massa F, Lerer A, Bradbury J, Chanan G, et al. Pytorch: An imperative style, high-performance deep learning library. In: Wallach H, Larochelle H, Beygelzimer A, d'Alché-Buc F, Fox E, Garnett R, editors. Advances in Neural Information Processing Systems 32. Curran Associates, Inc.; 2019, p. 8024–35.

[44] Pedregosa F, Varoquaux G, Gramfort A, Michel V, Thirion B, Grisel O, et al. Scikit-learn: Machine learning in Python. J Mach Learn Res 2011;12:2825–30.

[45] Keller BM, Nathan DL, Wang Y, Zheng Y, Gee JC, Conant EF, et al. Estimation of breast percent density in raw and processed full field digital mammography images via adaptive fuzzy c-means clustering and support vector machine segmentation. Med Phys 2012;39(8):4903–17. doi:`10.1118/1.4736530`.

[46] Trevisan Massera R, Tomal A. Estimation of glandular dose in mammography based on artificial neural networks. Phys Med Biol 2020;65(9):095009. doi:`10.1088/1361-6560/ab7a6d`.

[47] Gennaro G, Bigolaro S, Hill ML, Stramare R, Caumo F. Accuracy of mammography dosimetry in the era of the European Directive 2013/59/Euratom transposition. Eur J Radiol 2020;127:108986. doi:`10.1016/j.ejrad.2020.108986`.

[48] Suleiman ME, Brennan PC, McEntee MF. Mean glandular dose in digital mammography: a dose calculation method comparison. J Med Imag 2017;4(1):13502. doi:`10.1117/1.JMI.4.1.013502`.

[49] Tzikopoulos SD, Mavroforakis ME, Georgiou HV, Dimitropoulos N, Theodoridis S. A fully automated scheme for mammographic segmentation and classification based on breast density and asymmetry. Comput Meth Prog Bio 2011;102(1):47–63. doi:`10.1016/J.CMPB.2010.11.016`.

[50] Feng SSJ, Patel B, Sechopoulos I. Objective models of compressed breast shapes undergoing mammography. Med Phys 2013;40(3):031902. doi:`10.1118/1.4789579`.

[51] Ma X, Wei J, Zhou C, Helvie MA, Chan HP, Hadjiiski LM, et al. Automated pectoral muscle identification on MLO-view mammograms: Comparison of deep neural network to conventional computer vision. Med Phys 2019;46(5):2103–14.

[52] Tyson AH, Mawdsley GE, Yaffe MJ. Measurement of compressed breast thickness by optical stereoscopic photogrammetry. Med Phys 2009;36(2):569–76. doi:`10.1118/1.3065066`.

Appendix A. Appendix

Appendix A.1. Calibration for breast volume and VGF

Fig. A.15(a) shows the ground truth breast volume compared to the mask volume calculated from Eq. (1), while Fig. A.15(b) compares the breast volumes with and without skin. Fig. A.16(a) shows the relation between the ground truth VGF calculated directly from the phantoms and the reconstructed VGF using the masks calculated from Eq. (2). Fig. A.16(b) quantifies the ratio between the the ground truth and the reconstructed VGF obtained from the masks as function of breast thickness. The results are for the training sample (179 phantoms).
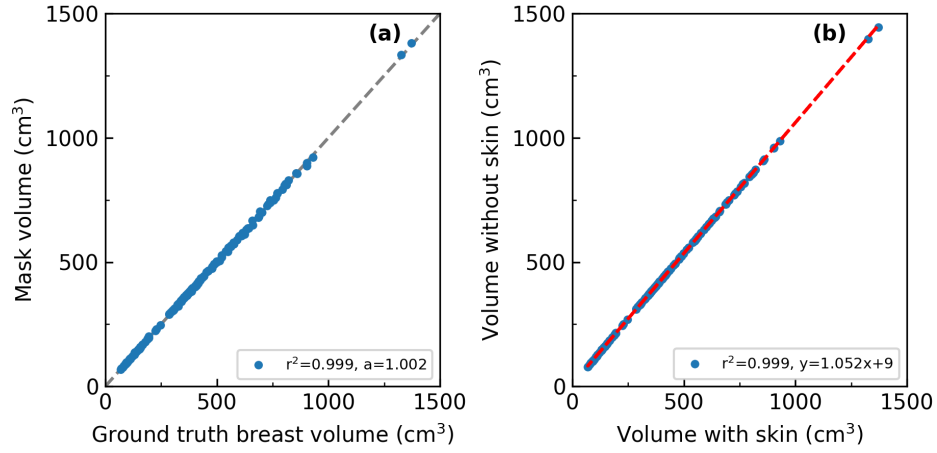
Figure A.15: Comparison between: (a) the ground truth breast volume and the ones calculated using the height mask, and (b) the ground truth breast volumes with and without skin.
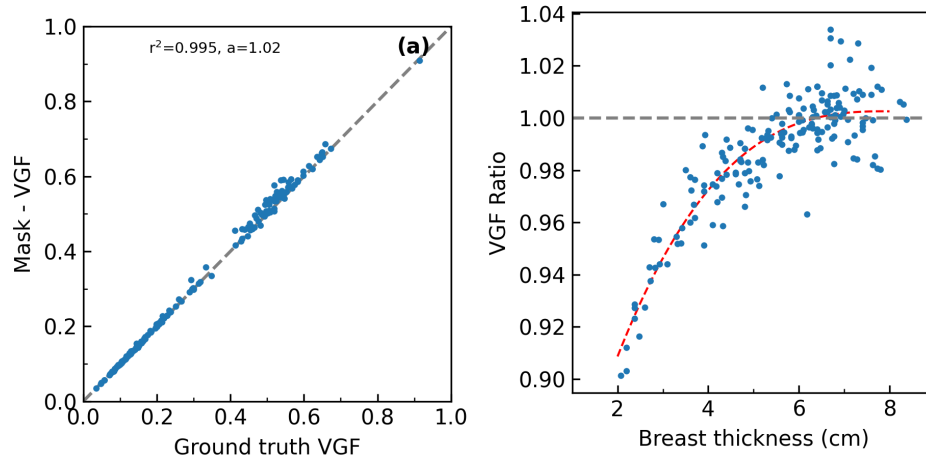
Figure A.16: (a) Comparison between the ground truth VGF and the one calculated using the relative glandular height mask. (b) Ratio between the ground truth and the mask VGF (rVGF) as function of breast thickness (t, in cm), fitted with a third order polynomial (dashed line).
$rVGF = 3.51 \times 10^{-4} \times t^3 - 8.96 \times 10^{-3} \times t^2 + 7.58 \times 10^{-2} \times t + 0.79$.

Chapter 5

Breast dosimetry and phase space files

Technical Note: MC-GPU breast dosimetry validations with other Monte Carlo codes and Phase Space File implementation

Rodrigo T. Massera[1,2], Rowan M. Thomson[2], Alessandra Tomal[1]

1: Instituto de Física "Gleb Wataghin", Universidade Estadual de Campinas, Campinas, São Paulo, 13083-859, Brazil
2: Carleton Laboratory for Radiotherapy Physics, Department of Physics, Carleton University, Ottawa, Ontario, K1S 5B6, Canada

Author to whom correspondence should be addressed. email: atomal@ifi.unicamp.br

Abstract

Purpose: To validate the MC-GPU Monte Carlo code for dosimetric studies in x-ray breast imaging modalities: mammography, digital breast tomosynthesis, contrast enhanced digital mammography and breast-CT. Moreover, to implement and validate a phase space file generation routine.

Methods: The MC-GPU code (v. 1.5 DBT) was modified in order to generate phase space files and to be compatible with PENELOPE v. 2018 derived cross section database. Simulations were performed with homogeneous and anthropomorphic breast phantoms for different breast imaging techniques. The glandular dose was computed for each case and compared with results from the PENELOPE (v. 2014) + penEasy (v. 2015) and egs_brachy (EGSnrc) Monte Carlo codes. Afterwards, several phase space files were generated with MC-GPU and the scored photon spectra were compared between the codes. The phase space files generated in MC-GPU were used in PENELOPE and EGSnrc to calculate the glandular dose, and compared with the original dose scored in MC-GPU.

Results: MC-GPU showed good agreement with the other codes when calculating the glandular dose distribution for mammography, mean glandular dose for digital breast tomosynthesis, and normalized glandular dose for breast-CT. The latter case showed average/maximum relative differences of 2.3%/27%, respectively, compared to other literature works, with the larger differences observed at low energies (around 10 keV). The recorded photon spectra entering a voxel were similar (within statistical uncertainties) between the three Monte Carlo codes. Finally, the reconstructed glandular dose in a voxel from a phase space file differs by less than 0.65%, with an average of 0.18% to 0.22% between the different MC codes, agreement within approximately 2σ statistical uncertainties. In some scenarios, the simulations performed in MC-GPU were from 20 up to 40 times faster than those performed by PENELOPE.

Conclusions: The results indicate that MC-GPU code is suitable for breast dosimetric studies for different x-ray breast imaging modalities, with the advantage of a high performance derived from GPUs. The phase space file implementation was validated and is compatible with the IAEA standard, allowing multiscale Monte Carlo simulations with a combination of CPU and GPU codes.

Key words: Monte Carlo; dosimetry; breast imaging; GPU

I. Introduction

Monte Carlo (MC) simulations are a powerful tool employed for glandular dose assessments for x-ray breast imaging.[1–5] With advances in computational power and promising imaging techniques for studying breast anatomy, there is a growing interest in performing advanced dose evaluations in mammography and other related x-ray imaging techniques,[6–8] such as mean glandular dose calculations and 3D dose distribution in anthropomorphic breast phantoms. The increase in complexity, mainly from the realistic breast models, and a high number of simulations (from hundreds to thousands possible combinations between parameters and models) requires considerable hardware resources and computational power. One option is to take advantage of central processing unit (CPU) parallelism capabilities and distribute the necessary MC calculations over a large number of CPUs. Another option, depending of the application, is to implement Graphical Processing Units (GPUs) to perform the calculations instead the traditional CPUs. With this approach, a single GPU could match the performance of several CPUs, as previously shown with the MC-GPU code,[9] thus allowing complex simulations with reduced hardware resources. However, this MC code only simulates photon transport.[9] MC-GPU has already been employed for simulating some applications involving low-energy (x-ray) beams, e.g. breast imaging studies and virtual clinical trials[10,11] and coherent x-ray scattering[12] by adapting the code to include molecular interference.[13] Original and modified MC-GPU codes were also validated for applications in interventional radiology and cardiology.[14,15] MC-GPU was also adapted for patient specific CT dose calculations.[16] In addition, traditional CPU Monte Carlo codes were adapted to GPU, e.g. Geant4[17] and EGSnrc.[18] A GPU Monte Carlo code was also developed for DNA damage simulations due to ionizing radiation.[19,20] These examples demonstrate the capabilities of GPU MC codes and their possible applications. Nevertheless, to our knowledge, a framework for multiscale dose calculations in mammography x-ray imaging using a combination of GPU and CPU MC codes was not yet implemented.

MC-GPU has been used for breast imaging studies with a focus on image quality (due to its performance advantages), however, there has not been a detailed comparison between MC-GPU and other MC codes with a focus in breast dosimetry. This would be useful, especially with the current developments in anthropomorphic phantoms for breast dosimetry, and could support migration from CPU MC codes to GPU ones. With recent interest in

other x-ray breast imaging modalities besides mammography, an efficient and validated MC code capable of performing dosimetry studies in different modalities would be of interest.

With MC-GPU, the simulations are limited to macroscopic scales, where the geometric components (*e.g.*, voxels) are several times the electron range, and only photon transport is modeled. This approximation is acceptable, for example, to estimate the mean glandular dose and 3D dose distributions (e.g., in mm-scale voxels).[21,22] On the other hand, a more detailed approach for dosimetric analysis in x-ray breast imaging involves multiple length scales, including cell populations,[23] for which electron transport must be considered.

One possible approach for these multiscale simulations is to segment the simulation into different steps. First, the GPU code could simulate photon transport in the macroscopic geometry (*e.g.* in a virtual patient model) and then record the phase space information for particles entering a smaller region. Next, a CPU code could be used to simulate coupled electron-photon transport within the smaller volume with more detailed microscopic model. With this concept, MC-GPU could be employed in a multiscale framework for x-ray breast imaging dosimetry.

The present work focuses on developments that are relevant for application of MC-GPU for breast dosimetry and is divided in two main parts: the first one describes a detailed validation with MC-GPU for breast dosimetry considering different imaging modalities: mammography, digital breast tomosynthesis (DBT) and breast-CT. Meanwhile, the second part consists of an implementation and validation of the phase space file generation algorithm which includes the previous cited imaging modalities plus contrast-enhanced digital mammography (CEDM).

II. Methods

The MC-GPU (v. 1.5 VICTRE-DBT)[24] code was employed with some modifications. This code uses the interaction scoring method. The cross section database was updated from PENELOPE 2006 to the newer version 2018.[25] For comparison purposes, two other codes were used: the previously modified and validated[26] PENELOPE[25] (v. 2014) + penEasy[27] (v. 2015); and egs_brachy,[28] an application of EGSnrc. For PENELOPE 2014, the default cross section database was implemented (which is similar to the 2018 version) and the in-

teraction scoring was used, while for EGSnrc the mcdf-XCOM photon cross section with the PENELOPE energy absorption coefficients were used (calculated using PENELOPE routines) with tracklength scoring. The statistical uncertainties were estimated using the history-by-history method, which updates the uncertainty counters at the end of each primary particle history (more details in Refs.[29, 30]).

Electron transport was not modeled. The photon energy cutoff was set to 1 keV. Information regarding the material compositions and the respective references are contained in Table 1.

The simulations using PENELOPE were performed in a Ryzen 1700x (AMD, USA) and Core i7 7700 (Intel, USA), while for MC-GPU the simulations were performed in a GeForce GTX 1060 (NVIDIA, USA).

II.A.   Dosimetry validations

This section covers the dosimetry validation for different breast imaging modalities and breast models. Subsection II.A.1. includes the digital breast tomosynthesis (DBT) and breast-CT validations for homogeneous breast models, while subsection II.A.2. describes the validation for mammography using heterogeneous breast models. Table 2 summarizes the general parameters employed in the simulations explained further.

II.A.1.   Dosimetry validations for homogeneous breast models

The DBT dosimetry validation consisted of two steps. First, a modified version of PENE-LOPE/penEasy MC code for breast dosimetry was validated against the report of Task Group 223[34] (results of this step are available in the Supplementary Materials). Second, we compared the modified PENELOPE code results with MC-GPU using a geometry adapted from Task Group 223. The MC-GPU geometry consisted of voxelized rectilinear geometries, which are the only geometries that may be simulated within this code, with 0.5 mm resolution. The adapted geometry is described as a 66 cm source-to-detector distance, and a 26×14 cm^2 x-ray field at the detector entrance (Table 2). The support and compression

plates (2 mm thick, PMMA) were also included. In MC-GPU and PENELOPE, the breast was modeled as a randomly sampled adipose-glandular distribution. For both codes, the inner breast is surrounded by a 1.5 mm skin thickness, and the breast has a semi-cylindrical shape (8 cm radius) to address a cracioncaudal (CC) view. The skin is absent in the region where the breast would be in contact with the chest wall. Three breast thickness/glandularity combinations were evaluated: 2 cm/100%; 5 cm/50%; 8 cm/1%, whose selection was based on the extreme values usually employed in dose validation studies.[3,34] The following spectra, obtained from TASMICS,[35] were used: W/Rh 23 kV; W/Rh 28 kV; W/Rh 35 kV for 2 cm, 5 cm and 8 cm breast thicknesses, respectively. The detector-center of rotation distance was set to 0 cm, and the mean glandular dose (MGD, i.e. the sum of the energy deposited in glandular voxels by their total mass) was compared between MC-GPU and PENELOPE codes from a 0° to 30° tube rotation angle (5° step). The 0° DBT projection presents a similar acquisition geometry of a mammography examination, thus a specific mammography validation for the homogeneous model was not included. The total number of primary photons were in the order of 10^8 for PENELOPE and 10^9 for MC-GPU. We validated MC-GPU with PENELOPE and not with TG223 directly due to the difficulty to convert the geometry to voxels.

For the breast-CT validations, the setup was based on the work of Sarno et al.[4] The breast was modeled as a cylinder with a radius/height of: 4 cm/4 cm; 6 cm/9 cm; 9 cm/18 cm, including a 1.5 mm skin layer and the patient chest (a block of muscle tissue, while the original work uses water). For the original work and PENELOPE, the breast was modeled as a homogeneous mixture of adipose-glandular tissues. Meanwhile, for MC-GPU, the geometry consisted of voxelized rectilinear geometries, and the breast model was voxelized with a randomly sampled adipose-glandular distribution. The glandularity varied from 0.1% to 100%. The MGD for the heterogeneous model was calculated by summing the energy deposited in glandular voxels divided by their total mass. Meanwhile, the MGD for the homogeneous models was obtained by applying a weighting factor $(G)^{3,4}$ to the imparted energy in the homogeneous mixture then dividing by the mass of glandular tissue. Afterwards, the breast was replaced by rectangular box of air ($3 \times 1.8 \times 1.1$ cm^3) simulating an ionization chamber (at the isocenter) and the air kerma (K_{air}) was scored inside this region. Finally, the Normalized Glandular Dose (DgN_{CT}) was calculated by the ratio: MGD/K_{air}. Therefore, the DgN was compared between the reference work and PENELOPE/MC-GPU results for mo-

noenergetic photons from 10 to 80 keV (5 keV steps). The total number of primary photons was on the order of 10^8. Figure 1 illustrates the geometry implemented in the simulations for dosimetry validations in this section.

The comparisons with EGSnrc were not included within these tests because the implementation and validation of the code adaptation to perform DBT and breast-CT simulations were beyond the scope of this work.

II.A.2.   Dose distribution comparison for anthropomorphic breast models

To quantify the dose distribution within the breast, a voxelized anthropomorphic breast phantom was generated using the BreastPhantom software[36] (0.5 mm resolution, 20% glandularity), and computationally compressed using the BreastCompress software (with FEBiO[37]) to 5 cm thick. The breast was irradiated with a W/Rh 28 kV spectrum with a geometry similar to Report-195 (Case III)[21] (as described in Table 2, column *Mammography*). Afterwards, the dose in all breast voxels (comprising different materials) was compared between the codes MC-GPU, PENELOPE and EGSnrc to verify the agreement between them, including the dose distribution. The dose was normalized by the number of histories (i.e. the number of primary photons that were generated in the source, collimated within the detector field). The total number of primary photons was on the order of 10^{10}. The relative dose difference in a voxel (Δ) was calculated as follows:

$$\Delta = 100 \times \frac{Dg_{ii} - Dg_i}{Dg_i} \qquad \%, \tag{1}$$

where subscripts refer to MC-GPU (i) and PENELOPE or EGSnrc (ii).

II.B.   Phase Space File

A tracking algorithm was adapted from PENELOPE for MC-GPU (named "Voxel_intercept") to identify photons that cross the boundaries of a given voxel from the outside. The ray tracing routine for quadric geometries was implemented to check if the photon intercepts one of the six cube faces. If more than one plane is crossed, the plane closest to the starting point is selected, then the routine stores the partial state variables in memory (energy, position coordinates and direction of movement). After each angular step of the x-ray tube rotation, the information stored in the GPU memory

is dumped to disk in a temporary binary file. When the simulation is finished, a software program (PSFConverter), which was written from an adapted code from penEasy 2019, is called to convert the raw binary file to a format compatible with the IAEA standard.[38] Data for each particle (position, direction, energy) are stored in 29 bytes. In order to verify if the framework is set up correctly, three tests described in the following sections were performed.

II.B.1.   Energy distribution comparison

The simulation of the anthropomorphic phantom (section II.A.2.) was adapted to record the energy of photons that entered in a specific voxel near the middle of the breast (simulation description in Table 2). Two spectra were employed (from TASMICS): W/Rh 28 kV and W/Cu 49 kV, to represent mammography and CEDM modalities, respectively. The functions to score the energy spectrum of photons were enabled in PENELOPE and EGSnrc. For MC-GPU, the information was retrieved by the generated phase space file. Finally, the photon energy spectra recorded by the three codes were compared.

In addition, the anthropomorphic phantom was downsampled to 2 mm voxels and two phase space files were generated: one in MC-GPU and other in PENELOPE for the mammography spectrum. Afterwards, the distribution of the particles' position and direction contained in the phase space files were compared.

II.B.2.   Glandular dose reconstruction

MC-GPU was used to simulate irradiation of the anthropomorphic breast phantom in four scenarios: (i) mammography; (ii) DBT; (iii) CEDM; (iv) breast-CT (uncompressed breast). For each setup, five phase space files were recorded in glandular voxels using MC-GPU. Afterwards, the phase space file was loaded in PENELOPE and EGSnrc where the geometry consisted of a single glandular voxel, and it was irradiated in order to score the dose. Therefore, the reconstructed doses from the phase space files in PENELOPE and EGSnrc were compared to the MC-GPU reported doses.

For all modalities, the number of simulated histories in MC-GPU was fine-tuned to yield a mean glandular dose of 4 mGy. For mammography and CEDM, the spectrum was the same as the previous section, while for the breast-CT simulation, the selected spectrum

was W/Al 49 kV.[39] The number of projections was 120, with a constant number of histories (fixed mAs per scan). For DBT, the selected spectrum was W/Al 31 kV, with 31 projections.

II.B.3. Practical example

As an example of application of the phase space file implementation, a simplified case of multiscale MC simulation was studied and the results of a full simulation performed in PENELOPE was compared to a simulation with MC-GPU plus PENELOPE (using the phase space file approach).

For this, the geometry for the mammography case described in Table 2 was implemented. The inner breast tissue was modified to include only adipose tissue (to facilitate the implementation), except in one region at the middle of the breast (a cube of 2 mm sides) where the material was set to glandular tissue. In this glandular region, the energy cutoffs for electrons and photons were set to 50 eV to enable a detailed simulation. In addition, the cube was sectioned in small sub regions of 10 μm side voxels, and the specific energy (energy imparted divided by mass) distribution was scored. In PENELOPE, this simulation was performed in a single step. For MC-GPU, the macroscopic simulation was performed and a phase space file was generated to describe the particles entering in the glandular voxel. Afterwards, the phase space file was loaded in PENELOPE and a detailed simulation was carried out to score the specific energy distribution in the cube subregions, i.e., ($10 \times 10 \times 10$ μm^3). Only subregions more than 50 μm from the edge of the glandular voxel were considered for the analysis to ensure that electron transport is accurately modeled. A total of 3.2×10^{11} primary photons were simulated.

III.   Results

III.A.   Digital Breast Tomosynthesis and Breast-CT

Figure 2(a) compares the relative MGD values for the DBT between PENELOPE and MC-GPU for three breast thicknesses with distinct glandular proportions. An excellent agreement was found between the codes with differences smaller than 0.25% (statistical uncertainties below 0.14%, 1σ), except for the 8 cm breast with projection angles 25° and 30°, where

the differences were 0.9% and 3.0%, respectively. This difference could be explained by the variations on the beam collimation algorithm for the DBT mode among the codes, more specifically, the projected x-ray field fluence at the surface of thicker breasts for high angles of incidence. Figure 2(b) shows a good agreement between the MC codes and also with the work of Sarno et al.,[4] with linear fits close to an ideal line, and an average relative difference of 2.3%. However, it is important to notice that for low energies (around 10 keV) where the DgN_{CT} is below 0.05, some differences between MC-GPU and Sarno et al. were up to 27%. This could be explained by the different cross sections used in the codes, the air kerma acquisition geometry and the randomized-sampling of glandular voxels inside the heterogeneous breast phantom. However, those low energies have a negligible impact in the dose when integrating over a breast-CT spectrum. For PENELOPE and MC-GPU, the average and maximum DgN_{CT} relative differences were 0.87% and 12.6%, respectively.

Regarding performance, for illustration, MC-GPU and PENELOPE (Ryzen 1700X, using only 1 core) presented a simulation speed of 1.76×10^7 and 1.44×10^5 histories/s, respectively for a breast-CT simulation of 50 keV monoenergetic photons and a large breast (50% glandular tissue). The ratio between the simulation speed achieved for MC-GPU and PENELOPE codes goes from approximately 242 at 10 keV down to 121 at 80 keV.

III.B. Dose distribution

The relative difference between the breast dose distribution in voxels for PENELOPE and EGSnrc compared to MC-GPU are shown in Figure 3(a). The differences resemble a normal distribution, without an apparent offset (i.e. centered near zero), which is consistent with the statistical uncertainty of the values. The uncertainty obtained with PENELOPE were higher compared to the other codes due to the longer computation times (smaller number of available processors). Nevertheless, the majority of the differences are contained within the -1 to 1% interval. The glandular dose as function of the breast depth is shown in Figure 3(b). An excellent agreement was found between the codes, with differences smaller than 0.35%. The voxel with maximum dose (excluding air and the plates) was the same for all three codes, which is located at the top of the breast, with differences lower than 0.4% between the dose values.

III.C.   Phase Space File: Photon energy spectrum

In order to validate the algorithm implemented in MC-GPU to generate the phase space files, the recorded spectrum of photons entering in a voxel was compared with the PENELOPE and EGSnrc MC codes. The results are shown in Figure 4 where it can be observed that the relative probability is similar between the codes within the estimated statistical uncertainty for both x-ray spectra. The bins below 10 keV were omitted due to the relative low probability and, consequently, the low impact in the results. The average relative differences for W/Rh 28 kV (10 keV threshold) and W/Cu 49 kV (20 keV threshold) between MC-GPU and PENELOPE/EGSnrc were lower than 2.5%.

III.D.   Phase Space File: Glandular Dose reconstruction

The glandular dose values obtained in MC-GPU (full simulation) compared to those obtained within PENELOPE and EGSnrc (phase space files) are shown in Table 3 with their respective statistical uncertainties. The average Δ between MC-GPU and PENELOPE/EGSnrc was 0.22%/0.18%, with maximum Δ values of 0.63%/0.43%. Considering that 1σ statistical uncertainty is approximately 0.3% for both PENELOPE and EGSnrc, and 0.004% for MC-GPU, the glandular dose values computed using phase space files (PENELOPE, EGSnrc) are in good agreement with those from full simulation (MC-GPU).

III.E.   Practical example

Figure 5 compares the results from the multiscale simulation using PENELOPE and the phase space file using MC-GPU plus PENELOPE method proposed in this work, showing an excellent agreement. The PENELOPE simulation took approximately 65.4 hours (Ryzen 1700X, using 8 cores) to finish. Meanwhile, the whole process of MC-GPU generating the phase space file then simulating in PENELOPE took approximately 3.2 hours, a speed-up of approximately 20 times. The time spent in file manipulations was on the order of seconds, 6% of the time in the PENELOPE simulation and the rest in MC-GPU. It is important to notice that by turning on the additional phase space files calculations in MC-GPU, the performance was slowed by approximately 30%. The generated phase space file size was approximately 450 megabytes, which resulted in a negligible impact on the performance of

the calculations ($\approx$ hours) due to disk read/write operations ($\approx$ seconds).

IV. Discussion

MC-GPU simulates photon transport through matter with physics models based on PENE-LOPE,[9] with minor modifications. As seen in the results, there is a good overall agreement between MC-GPU and the other considered MC codes. Moreover, a comparison with EGSnrc and the work of Sarno et al.[4] (which used a program based on GEANT4) was also included. In the latter case, high discrepancies were observed at very low energies, but could be explained by the differences in the cross sections of the codes and minor modifications in the geometry. In breast imaging simulations, it is often assumed that the electrons are locally deposited[4,21] due to mm-to-cm length scales of simulated objects, significantly larger than the short range of electrons at low energies (from 0.05 μm at 1 keV to 144 μm at 100 keV, CSDA in liquid water). Thus, MC-GPU may be used for efficient dosimetric simulations, enabling a large number of simulations with limited compute cluster resources. A generalized comparison of simulation speeds shows that using MC-GPU in a GeForce GTX 1060 (NVIDIA, USA) had a performance 40 times greater than PENELOPE in a Core i7 7700 (Intel, USA) processor (using all cores). Although limited (since we are comparing CPU to GPU), these results at least show the performance improvements that could be achieved when desktops (with a limited number of CPUs) are used in MC simulations. The need to optimize simulation efficiency becomes important especially with recent studies focusing in complex breast models,[6–8,10,39] where a high computation power is needed. The MC-GPU code also supports the use of a search tree in the tracking algorithm which greatly reduces the amount of memory to store high-resolution phantoms. This is highly efficient compared to the parallelism implemented in some MC simulations where the jobs do not share memory and the same breast phantom must be loaded for every job.

The phase space file functionality implemented in MC-GPU was developed to support future multiscale studies of breast dosimetry,[23] where the macroscopic scale would be simulated in MC-GPU and the microscopic scale in a different code with electron transport, such as PENELOPE or EGSnrc. The effects of potentially missed secondary photons, in this application, is small[22] and can be disregarded since low energy photons are used for x-ray imaging of the breast, associated with low atomic number of breast tissues.

Moreover, this routine could be adapted for other purposes, such as simulating energy deposition in a detector. There is a trade off between the simulation speed and the number of particles being scored. The user should optimize between the size of the scoring region and the total number of particles entering the region for efficiency and in order to limit the size of the phase space file considering the overhead time to write and load them. It is important to notice that MC-GPU does not simulate electrons and does not have routines to calculate fluorescence effects in the materials. Since the effective atomic number of breast tissues is relatively low, the probability of fluorescence is negligible. However, this might be needed in other applications. Another interesting feature implemented in the phase space file generating algorithm is the option to not kill particles that enter the volume of interest. This is particularly useful for the application discussed in this work of recreating a dose in a voxel because it ensures that backscatter photons are included.

Preliminary tests (not included in this work) show that for a mammography simulation and a voxel in the middle of the breast, 2% and 0.5% of photons are missed if photons are killed when they enter the volume of interest for voxels with 2 mm and 0.5 mm side length, respectively.

For the practical example (Section III.E.), the average dose in adipose tissue was 0.54 mGy, almost on the same order of magnitude found in real mammography imaging. Thus, it is expected that the size of the phase space files in this type of multiscale studies would be in the worst case scenario of a few gigabytes, which is still viable with most current hardware available.

V.   Conclusion

Recent studies of breast dosimetry employ complex breast models with realistic features, presenting considerable demands on computing power. The present article demonstrates that MC-GPU is suitable for carrying out accurate MC dosimetric evaluations for different x-ray breast imaging modalities. Moreover, the option to record phase space files in specific regions of the geometry has been successfully implemented. This development will enable future studies of energy deposition on different scales by also employing an MC code that models coupled electron-photon transport, e.g., the relation between dose in

macroscopic models and the specific energy imparted in cells. In theory, any code that allows the IAEA phase space file format is compatible to work with the files generated with MC-GPU. The authors will release the modified MC-GPU code in a digital repository (https://github.com/rtmass/MCGPU-PSF). Future studies could expand these applications to other x-ray imaging techniques besides the breast and other low x-ray energies applications.

Conflicts of interest

The authors have no conflicts of interest.

Acknowledgments

Data availability

The modifications implemented in MC-GPU for this study are available in a digital repository (https://github.com/rtmass/MCGPU-PSF). Specific data are available on reasonable request from the correspondence author.

References

[1] D. R. Dance, Monte Carlo calculation of conversion factors for the estimation of mean glandular breast dose, Physics in Medicine and Biology **35**, 1211–9 (1990).

[2] X. Wu, G. T. Barnes, and D. M. Tucker, Spectral dependence of glandular tissue dose in screen-film mammography, Radiology **179**, 143–148 (1991).

[3] J. M. Boone, Glandular breast dose for monoenergetic and high-energy x-ray beams: Monte Carlo assessment, Radiology **213**, 23–37 (1999).

[4] A. Sarno, G. Mettivier, R. M. Tucciariello, K. Bliznakova, J. M. Boone, I. Sechopoulos, F. Di Lillo, and P. Russo, Monte Carlo evaluation of glandular dose in cone-beam X-ray computed tomography dedicated to the breast: Homogeneous and heterogeneous breast models, Physica Medica **51**, 99–107 (2018).

[5] D. R. Dance and I. Sechopoulos, Dosimetry in x-ray-based breast imaging, Physics in Medicine and Biology **61**, R271–R304 (2016).

[6] F. di Franco, A. Sarno, G. Mettivier, A. M. Hernandez, K. Bliznakova, J. M. Boone, and P. Russo, GEANT4 Monte Carlo simulations for virtual clinical trials in breast X-ray imaging: Proof of concept, Physica Medica **74**, 133–142 (2020).

[7] A. M. Hernandez, J. A. Seibert, and J. M. Boone, Breast dose in mammography is about 30% lower when realistic heterogeneous glandular distributions are considered, Medical Physics **42**, 6337–6348 (2015).

[8] A. M. Hernandez, A. E. Becker, and J. M. Boone, Updated breast CT dose coefficients (DgN CT) using patient-derived breast shapes and heterogeneous fibroglandular distributions, Medical Physics **46**, 1455–1466 (2019).

[9] A. Badal and A. Badano, Accelerating Monte Carlo simulations of photon transport in a voxelized geometry using a massively parallel graphics processing unit, Medical Physics **36**, 4878–4880 (2009).

[10] A. Badano, C. G. Graff, A. Badal, D. Sharma, R. Zeng, F. W. Samuelson, S. J. Glick, and K. J. Myers, Evaluation of Digital Breast Tomosynthesis as replacement of full-field digital mammography using an in silico imaging trial, JAMA Network Open **1**, e185474 (2018).

[11] A. Badal, D. Sharma, C. G. Graff, R. Zeng, and A. Badano, Mammography and breast tomosynthesis simulator for virtual clinical trials, Computer Physics Communications **261**, 107779 (2020).

[12]   B. Ghammraoui and A. Badal, Monte Carlo simulation of novel breast imaging modalities based on coherent x-ray scattering, Physics in Medicine and Biology **59**, 3501–3516 (2014).

[13]   B. Ghammraoui, R. Peng, I. Suarez, C. Bettolo, and A. Badal, Including the effect of molecular interference in the coherent x-ray scattering modeling in MC-GPU and PENELOPE for the study of novel breast imaging modalities, in *Medical Imaging 2014: Physics of Medical Imaging*, edited by B. R. Whiting and C. Hoeschen, volume 9033, page 90334N, SPIE, 2014.

[14]   D. Fernández Bosman, V. García Balcaza, C. Delgado, S. Principi, M. A. Duch, and M. Ginjaume, Validation of the MC-GPU Monte Carlo code against the PENELOPE/penEasy code system and benchmarking against experimental conditions for typical radiation qualities and setups in interventional radiology and cardiology, Physica Medica **82**, 64–71 (2021).

[15]   V. García Balcaza, A. Camp, A. Badal, M. Andersson, A. Almen, M. Ginjaume, and M. Duch, Fast Monte Carlo codes for occupational dosimetry in interventional radiology, Physica Medica **85**, 166–174.

[16]   S. Sharma, A. Kapadia, W. Fu, E. Abadi, W. P. Segars, and E. Samei, A real-time Monte Carlo tool for individualized dose estimations in clinical CT, Physics in Medicine & Biology **64**, 215020 (2019).

[17]   J. Bert, H. Perez-Ponce, Z. E. Bitar, S. Jan, Y. Boursier, D. Vintache, A. Bonissent, C. Morel, D. Brasse, and D. Visvikis, Geant4-based Monte Carlo simulations on GPU for medical applications, Physics in Medicine and Biology **58**, 5593–5611 (2013), Publisher: IOP Publishing.

[18]   J. Lippuner and I. A. Elbakri, A GPU implementation of EGSnrc's Monte Carlo photon transport for imaging applications, Physics in Medicine and Biology **56**, 7145–7162 (2011).

[19]   M.-Y. Tsai, Z. Tian, N. Qin, C. Yan, Y. Lai, S.-H. Hung, Y. Chi, and X. Jia, A new open-source GPU-based microscopic Monte Carlo simulation tool for the calculations of DNA damages caused by ionizing radiation - Part I: Core algorithm and validation, Medical Physics **47**, 1958–1970 (2020).

[20]   Y. Lai, M.-Y. Tsai, Z. Tian, N. Qin, C. Yan, S.-H. Hung, Y. Chi, and X. Jia, A new open-source GPU-based microscopic Monte Carlo simulation tool for the calculations of DNA damages caused by ionizing radiation - Part II: sensitivity and uncertainty analysis, Medical Physics **47**, 1971–1982 (2020).

[21]   I. Sechopoulos, E. S. M. Ali, A. Badal, A. Badano, J. M. Boone, I. S. Kyprianou, E. Mainegra-Hing, K. L. McMillan, M. F. McNitt-Gray, D. W. O. Rogers, E. Samei, and

A. C. Turner, Monte Carlo reference data sets for imaging research: Executive summary of the report of AAPM Research Committee Task Group 195, Medical Physics **42**, 5679–5691 (2015).

[22] A. Sarno, G. Mettivier, F. Di Lillo, and P. Russo, A Monte Carlo study of monoenergetic and polyenergetic normalized glandular dose (DgN) coefficients in mammography, Physics in Medicine and Biology **62**, 306–325 (2017).

[23] P. A. K. Oliver and R. M. Thomson, Investigating energy deposition in glandular tissues for mammography using multiscale Monte Carlo simulations, Medical Physics **46**, 1426–1436 (2019).

[24] A. Badal, D. Sharma, C. G. Graff, R. Zeng, and A. Badano, Mammography and breast tomosynthesis simulator for virtual clinical trials, Computer Physics Communications **261**, 107779 (2021).

[25] F. Salvat, PENELOPE-2018: A code system for Monte Carlo simulations of electron and photon transport, 2019.

[26] R. Massera and A. Tomal, Skin models and their impact on mean glandular dose in mammography, Physica Medica **51**, 38–47 (2018).

[27] J. Sempau, A. Badal, and L. Brualla, A PENELOPE -based system for the automated Monte Carlo simulation of clinacs and voxelized geometries-application to far-from-axis fields, Medical Physics **38**, 5887–5895 (2011).

[28] M. J. P. Chamberland, R. E. P. Taylor, D. W. O. Rogers, and R. M. Thomson, egs_brachy: a versatile and fast Monte Carlo code for brachytherapy, Physics in Medicine and Biology **61**, 8214–8231 (2016).

[29] J. Sempau, A. Sánchez-Reyes, F. Salvat, H. O. b. Tahar, S. B. Jiang, and J. M. Fernández-Varea, Monte Carlo simulation of electron beams from an accelerator head using PENELOPE, Physics in Medicine and Biology **46**, 1163–1186 (2001).

[30] B. R. B. Walters, I. Kawrakow, and D. W. O. Rogers, History by history statistical estimators in the BEAM code system, Medical Physics **29**, 2745–2752 (2002).

[31] R. G. Hammerstein, D. W. Miller, D. R. White, M. E. Masterson, H. Q. Woodard, and J. S. Laughlin, Absorbed radiation dose in mammography, Radiology **130**, 485–491 (1979).

[32] H. Q. Woodard and D. R. White, The composition of body tissues, The British Journal of Radiology **59**, 1209–1218 (1986).

[33] M. Berger, J. Hubbell, S. Seltzer, J. Chang, J. Coursey, R. Sukumar, D. Zucker, and K. Olsen, XCOM: Photon Cross Section Database. National Institute of Standards and Technology (NIST), (2010).

[34] I. Sechopoulos, J. M. Sabol, J. Berglund, W. E. Bolch, L. Brateman, E. Christodoulou, M. Flynn, W. Geiser, M. Goodsitt, A. Kyle Jones, J. Y. Lo, A. D. A. Maidment, K. Nishino, A. Nosratieh, B. Ren, W. Paul Segars, and M. Von Tiedemann, Radiation dosimetry in digital breast tomosynthesis: Report of AAPM Tomosynthesis Subcommittee Task Group 223, Medical Physics **41**, 091501 (2014).

[35] A. M. Hernandez, J. A. Seibert, A. Nosratieh, and J. M. Boone, Generation and analysis of clinically relevant breast imaging x-ray spectra, Medical Physics **44**, 2148–2160 (2017).

[36] C. G. Graff, A new, open-source, multi-modality digital breast phantom, in *Medical Imaging 2016: Physics of Medical Imaging*, edited by D. Kontos, T. G. Flohr, and J. Y. Lo, volume 9783, page 978309, SPIE, 2016.

[37] S. A. Maas, B. J. Ellis, G. A. Ateshian, and J. A. Weiss, FEBio: Finite elements for biomechanics, Journal of Biomechanical Engineering **134** (2012).

[38] R. Capote, R. Jeraj, C. M. Ma, D. W. O. Rogers, F. Sanchez-Doblado, J. Sempau, J. Seuntjens, and J. V. Siebers, Phase-space database for external beam radiotherapy Summary report of a consultants' meeting, Technical report, International Atomic Energy Agency (IAEA), 2006.

[39] I. Sechopoulos, K. Bliznakova, X. Qin, B. Fei, and S. S. J. Feng, Characterization of the homogeneous tissue mixture approximation in breast imaging dosimetry, Medical Physics **39**, 5050–5059 (2012).

VI.   Figures
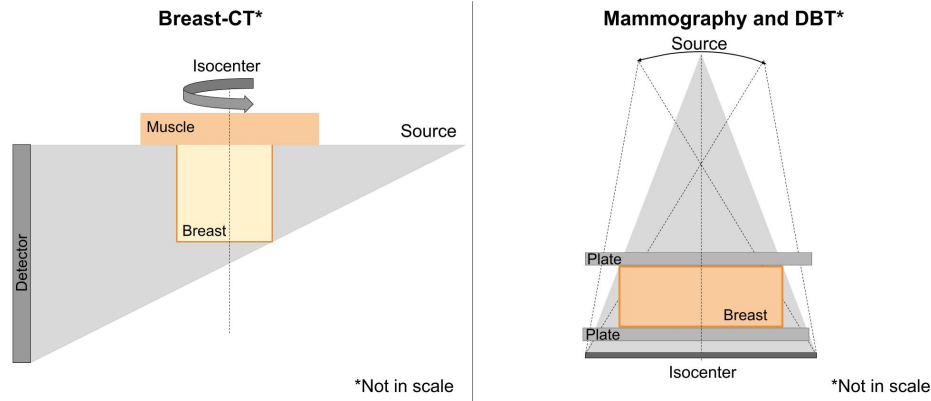
Figure 1: Schematic of the geometries used in section II.A.1. for the dosimetry validations. Figures not in scale.
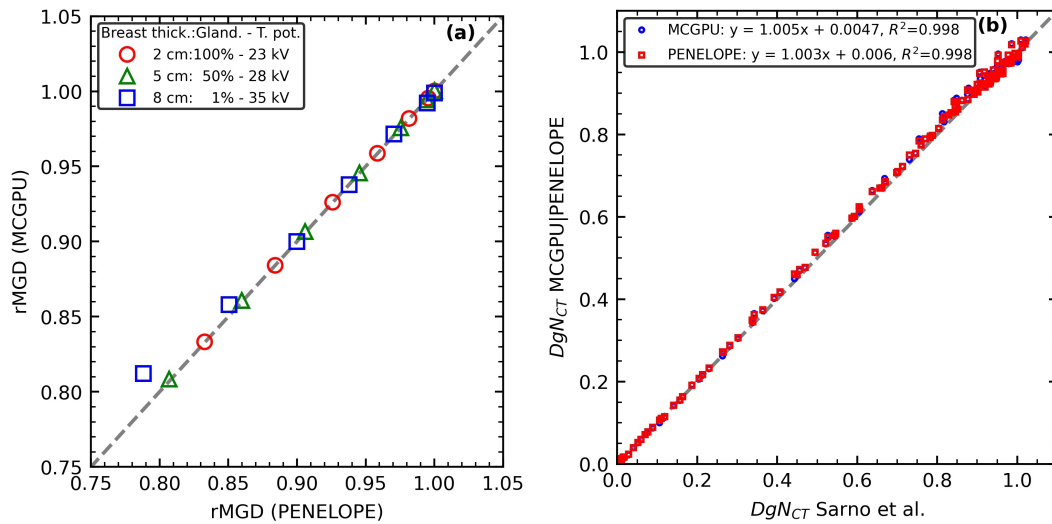
Figure 2: (a) Comparison between the relative MGD (rMGD) values for MC-GPU and PENELOPE for DBT for different breast thicknesses, glandularities and tube potentials. The results were normalized by the PENELOPE 0° projection MGD value for each breast thickness to obtain the rMGD values. Coefficient of variation: 0.25% (2σ). (b) Comparison between DgN_{CT} values for MC-GPU, PENELOPE and Sarno et al.[4] for photon energies between 10 keV and 80 keV. The linear fit quantifies agreement between them, coefficient of variation: 0.7% (2σ). For both cases, the dashed lines indicate a perfect agreement.
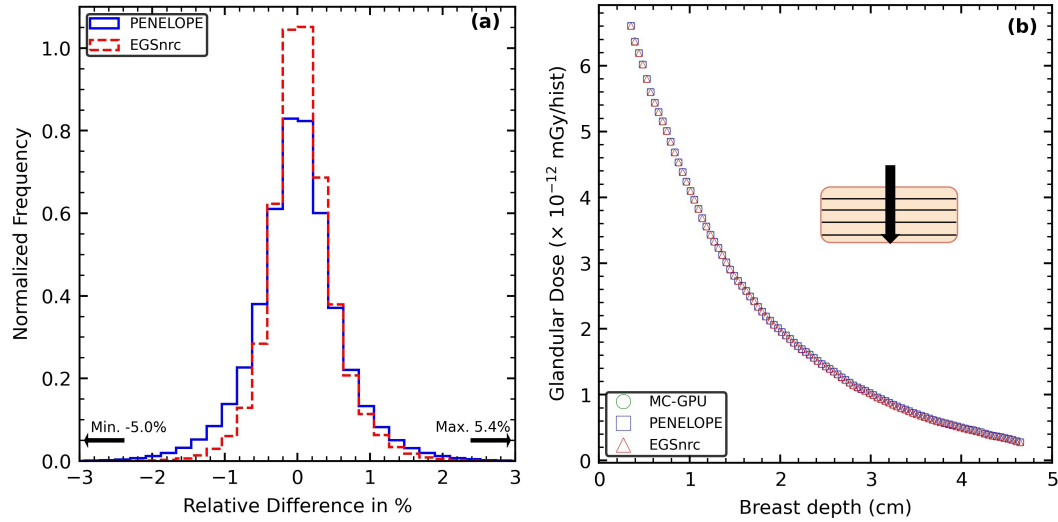
Figure 3: (a) Relative difference between MC-GPU and PENELOPE/EGSnrc for the breast dose voxels. The arrows indicate the minimum and maximum values. Maximum coefficient of variation: 2%. (b) Glandular dose as function of the breast depth for different MC codes. Each point represents the average value for all glandular voxels in a particular depth. The reference plane is exemplified by the insert. Imaging modality: Mammography.
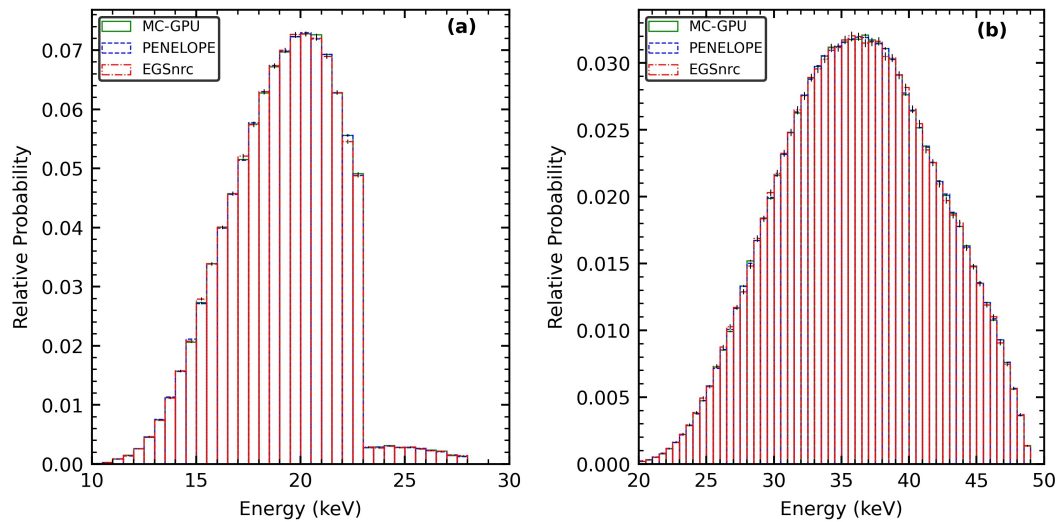
Figure 4: Spectra of photons entering in a glandular voxel inside the breast recorded in different MC codes. The simulations were performed with the following spectra: (a) W/Rh 28 kV and (b) W/Cu 49 kV.
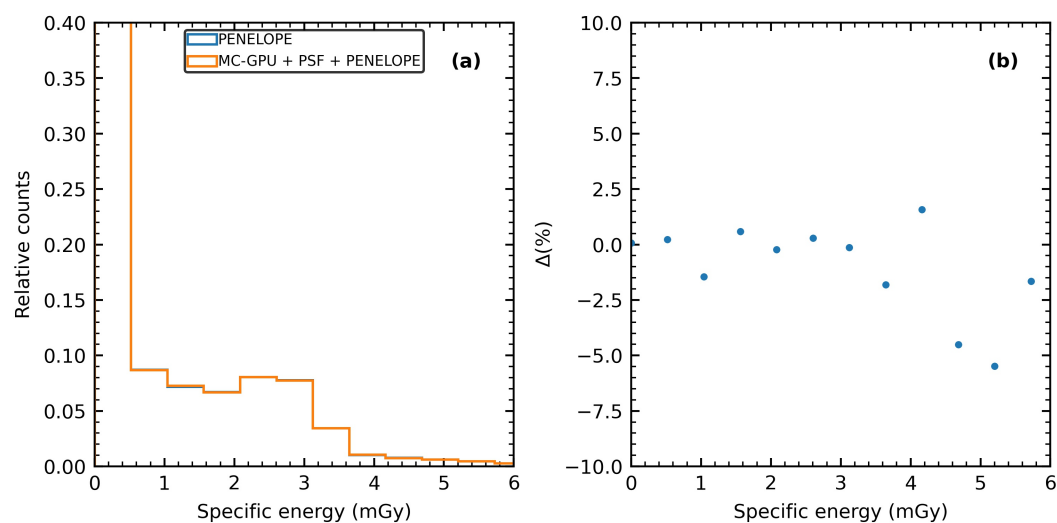
Figure 5: (a) Specific energy distribution obtained in a full simulation within PENELOPE and using the phase space file approach (MC-GPU + PSF + PENELOPE). (b) Relative differences (Δ) between both approaches for each bin. Values of specific energy higher than 6 mGy where excluded due to their low probabilities.

VII.   Tables

Table 1: Elemental composition (in mass percent composition) of the materials employed in the simulations with their respective reference.

Material	Density (g/cm^3)	H	C	N	O	Others
Adipose[31]	0.93	11.2	61.9	1.7	25.1	P(0.025),S(0.025),K(0.025),Ca(0.025)
Glandular[31]	1.04	10.2	18.4	3.2	67.7	P(0.125),S(0.125),K(0.125),Ca(0.125)
Skin[31]	1.09	9.8	17.8	5.0	66.7	P(0.175),S(0.175),K(0.175),Ca(0.175)
Connective[32]	1.12	9.4	20.7	6.2	62.2	Na(0.2),S(0.6),Cl(0.3)
Blood (ICRP)[33]	1.06	10.187	10.002	2.964	75.941	Na(0.185),Mg(0.004),Si(0.003), P(0.035),S(0.185),Cl(0.278),K(0.163), Ca(0.006),Fe(0.046),Zn(0.001)
Muscle (ICRP)[33]	1.04	10.064	10.783	2.768	75.477	Na(0.075),Mg(0.019),P(0.180),S(0.241), Cl(0.079),K(0.302),Ca(0.003), Fe(0.004),Zn(0.005)
PMMA[33]	1.19	8.054	59.985	-	31.961	-

Table 2: Overview of simulations for dosimetric validations: breast geometric descriptors (shape, radius, thickness) and glandularity, source parameters (x-ray spectra, field size, source-detector/isocenter distances), and scored quantities for each simulated modality, as well as the publication motivating the simulation.

	Simulated modality		
Parameter	DBT	Breast-CT	Mammography
Breast shape	Semicylinder	Cylinder	Semicylinder
Breast radius	8 cm	4, 6, 9 cm	≈ 10 cm
Breast thickness (height)	2, 5, 8 cm	4, 9, 18 cm	5 cm
Glandularity	1, 50, 100%	0.1, 50, 100%	20%
Field size	26×14 cm^2	40×30 cm^2	26×14 cm^2
Source detector distance	66 cm	92.3 cm	66 cm
Source isocenter distance	66 cm	65 cm	-
X-ray spectra	W/Rh: 23, 28, 35 kV	Mono: 10 – 80 keV	W/Rh: 28 kV
Scored quantity	MGD	DgN$_{CT}$	DD*
Adapted geometry from	TG-195,[21] TG-223[34]	Sarno et al.[4]	TG-195[21]

*DD: dose distribution.

Table 3: Dose in five distinct glandular voxels (ROI) obtained directly with MC-GPU, and reconstructed from phase space files for EGSnrc and PENELOPE. Values in mGy. The statistical uncertainty (in mGy) is indicated by the values in parentheses.

ROI	MC-GPU	PENELOPE	EGSnrc
		Mammography	
1	3.4230(1)	3.424(9)	3.416(9)
2	3.7656(1)	3.769(9)	3.760(9)
3	3.3138(1)	3.302(9)	3.296(9)
4	3.3027(1)	3.295(9)	3.280(9)
5	3.2874(1)	3.299(9)	3.296(9)
		DBT	
1	3.4508(1)	3.442(9)	3.442(9)
2	3.6832(1)	3.661(9)	3.661(9)
3	3.3716(1)	3.362(9)	3.362(9)
4	3.4411(1)	3.433(9)	3.433(9)
5	3.4237(1)	3.409(9)	3.409(9)
		CEDM	
1	4.4531(2)	4.46(1)	4.46(1)
2	4.1154(1)	4.13(1)	4.13(1)
3	4.1303(1)	4.15(1)	4.15(1)
4	4.2368(1)	4.26(1)	4.25(1)
5	4.3637(2)	4.36(1)	4.36(1)
		Breast-CT	
1	3.4240(1)	3.44(1)	3.43(1)
2	3.7656(1)	3.78(1)	3.76(1)
3	3.3138(1)	3.311(8)	3.31(1)
4	3.3027(1)	3.30(1)	3.32(1)
5	3.2874(1)	3.308(9)	3.29(1)

Chapter 6

Multiscale breast dosimetry part I

Original article title: Multiscale Monte Carlo Simulations for dosimetry in X-ray breast imaging: Part I - Macroscopic scales.
Authors: Rodrigo T. Massera, Alessandra Tomal, Rowan M. Thomson.
Published in: To be submitted.
Note: This is a work in progress. Small modifications could be present compared to the submitted version.

Multiscale Monte Carlo simulations for dosimetry in x-ray breast imaging: Part I - Macroscopic scales

Rodrigo T. Massera[a,1,2], Alessandra Tomal[b,1], Rowan M. Thomson[c,2]

email: a) rtmassera@gmail.com b) atomal@ifi.unicamp.br c) rthomson@physics.carleton.ca

1: Instituto de Física "Gleb Wataghin", Universidade Estadual de Campinas, Campinas, São Paulo, Brazil
2: Carleton Laboratory for Radiotherapy Physics, Department of Physics, Carleton University, Ottawa, Ontario, K1S 5B6, Canada

Abstract

Background: X-ray breast imaging modalities are commonly employed for breast cancer detection, from screening programs to diagnosis. Thus, dosimetry studies are important for quality control and risk estimations since ionizing radiation is used.

Purpose: To perform multiscale dosimetry assessments for different breast imaging modalities and for a variety of breast sizes and compositions. The first part of our study is focused on macroscopic scales (millimeters).

Methods: Nine anthropomorphic breast phantoms with a voxel size of 0.5 mm were computationally generated, representing three breast sizes with three distinct volume glandular fraction for each size. Four breast imaging modalities were studied: digital mammography, contrast enhanced digital mammography (CEDM), digital breast tomosynthesis (DBT) and breast-CT (BCT). Additionally, the impact over tissue elemental compositions were compared between two databases. Monte Carlo simulations were performed with the MC-GPU for all cases to obtain the 3D glandular dose distribution. For all cases, the mean glandular dose (MGD) was fixed at 4 mGy.

Results: The glandular dose distribution within the breast is more uniform for the CEDM and BCT compared to mammography and DBT. For large breasts, the ratio between the minimum/maximum glandular dose to MGD is 0.12/4.02 for mammography and 0.53/1.77 for BCT, while for a small breast the minimum/maximum ratios are 0.35/1.98, respectively. The elemental tissue composition of skin, adipose and glandular tissue have a significant impact over the MGD, with variations up to 30% compared to the baseline. On the other hand, the inclusion of tissues other than glandular and adipose within the breast does not change significantly the MGD (differences below 2%).

Conclusions: The glandular dose distribution varies significantly between breast imaging modalities for a constant MGD. The elemental tissue compositions impacts significantly the MGD values, being a source of systematic uncertainties in Monte Carlo simulations and, consequently, in breast dosimetry.

Key words: Digital Mammography, Digital Breast Tomosynthesis (DBT), Breast CT, Contrast imaging, Radiation dosimetry, Monte Carlo

I. Introduction

X-rays have been employed in breast imaging for decades[1] and play an important role in screening and early diagnosis of breast cancer among women.[2] Several techniques have been developed with different acquisition geometries and technologies. Among them, digital mammography is currently the standard technique for breast cancer screening with several studies pointing to its benefits in detecting breast cancer at early stages and saving's lives.[3,4] Recent studies indicate that digital breast tomosynthesis (DBT), which provides a pseudo 3D image of the breast, could also be employed in screening,[5–7] with the advantage of partially overcoming tissue overlap of 2D mammography images.[8] Contrast enhanced digital mammography (CEDM) is an advanced breast imaging technique with the potential to be used in screening for women with high risk of developing breast cancer:[9] a contrast-agent (iodine) is injected into the breast to increase the contrast between tissues and x-ray beams of higher energy are employed.[10] Dedicated breast computed tomography (BCT) is an imaging modality capable of producing real three-dimensional breast tissue information, thus yielding a superior contrast compared to projection radiography[11,12] and providing anatomical breast information.[13]

Given that the breast is a highly radiosensitive organ[14] and the above-cited imaging modalities expose the breast to ionizing radiation, screening benefits must outweigh risks. For risk assessment, dosimetric studies play an important role in quality control and protocol optimization,[15] thus aiding to determine pros and cons for each technique. Furthermore, screening programs mean women are exposed to radiation multiple times during their lifetimes, further increasing the concern of radiation-induced cancers.[16] The standard dosimetric quantity in x-ray breast imaging is the mean glandular dose (MGD), which is usually studied by Monte Carlo (MC) simulations.[15] Several works addressed the MGD or DgN (Normalized Glandular Dose, i. e. the MGD divided by the incident air kerma) for the following techniques: mammography;[17–25] CEDM,[23,26] DBT,[24,27–29] and BCT.[11,24,30–32] Moreover, it was shown that the glandular distribution inside the breast could impact MGD estimates and that the traditional assumption of homogeneously-distributed gland results in overestimation of MGD by 30% for mammography[22,33] and 4% for BCT[33] compared to heterogeneous distributions.

The MGD provides the average ratio of the energy imparted in glandular tissue by

its mass, and consequently does not inform about the dose distribution within the breast. For the low energy x-rays usually employed in some breast imaging modalities and system geometries, the exponential attenuation of the photons through matter could contribute for a more heterogeneous glandular dose distribution. For example, Sechopoulos et al.[34] showed that the doses at the entrance of the breast are four times higher than the average dose in mammography, while this effect is less noticeable in high energy beams such as those used in BCT.[33,34] Therefore, the dose distribution inside the breast could provide additional information of the dose ranges deposited in glandular tissue. Additionally, the behavior of energy deposition at microscopic length scales (in cells) could bring new insights in breast dosimetry, since damage to the DNA can induce mutations and consequently radio-induced carcinogenesis.[35] In this scope, Oliver and Thomson[36] investigated the energy deposition in glandular tissue from microscopic to macroscopic length scales for mammography varying the x-ray spectra, the compressed breast thickness, the glandular content distribution within the breast, cell configurations and cell sizes. The authors reported that the glandular dose distribution varies between 0.1 and 4 times the MGD, the specific energy in cell nuclei could be approximately 30% higher than the respective scored voxel glandular dose, and is dependent on the cell composition and nucleus size. Although the aforementioned works studied breast dosimetry for different x-ray imaging techniques and even from microscopic to macroscopic scales, to our knowledge, no study yet comprehensively considered different breast x-ray imaging techniques for detailed 3D dosimetric studies in multiple length scales. In light with these findings, an extension to other breast imaging modalities would help understand the influence of the diverse parameters presented in distinct contemporary breast imaging modalities, such as the beam energy, the geometry of the irradiation and the breast shape to the overall dose distributions.

The scope of this study is to perform multiscale Monte Carlo simulations to study the breast dosimetry for different imaging modalities: mammography, DBT, CEDM and BCT and to compare the results between them in microscopic and macroscopic length scales. The work is divided in two parts: in the first one, addressed here, the macroscopic length scales are studied. In the second one, the study is focused on microscopic length scales and the energy deposited in cells (nucleus and cytoplasm).

II.   Methods

II.A.   Monte Carlo code

The macroscopic length scale Monte Carlo simulations were performed in a modified version of MC-GPU (v. 1.5b)[37,38] which was validated for breast dosimetry studies in our previous work.[39] Table 1 describes general Monte Carlo parameters implemented in this work, while more specific ones are described in the following sections.

Table 1: General parameters regarding the Monte Carlo simulations performed in this work following TG-268 guidelines.[40]

Checklist item	Description
(5) Hardware	The simulations were performed in two GPUs: GeForce GTX 1060 and GTX Titan (NVIDIA, USA) both with 6 GB of VRAM. The simulation speeds were in the order of 5×10^7 histories/s and took from 5 to 17 hours.
(7) Materials	The elemental compositions of the materials, if not explicitly indicated, are taken from NIST.[41]
(9) Crosss sections	The cross sections values were obtained from PENELOPE (v. 2018, default settings).
(10) Transport Parameters	Photon energy cutoff: 1 keV. The code does not simulate electrons, thus those generated by photon interactions were locally absorbed.
(12,13,14) Scoring	The dose deposited in voxels was scored and its value is normalized by the number of primary particles (photons) that were generated in the source. The statistical uncertainty was estimated via the history-by-history method. The number of generated primary particles was in the order of 10^{12}.

II.B.   Breast Phantoms

The breast models used in the simulations were generated by the BreastPhantom software[42] and compressed (when applicable) via a finite element algorithm.[43] The skin thickness is 1.5 mm.[44,45] The breast tissues are assigned as: skin, glandular, adipose, connective or blood.[42] The breast sizes and volume glandular fraction (VGF)[13] were based on values provided by Hernandez et al.,[32] while the compressed thickness were approximately fitted by the linear relation with breast diameter by Boone et al.[46] Since, in our work, the breast phantoms are composed by tissues other than glandular and adipose, the formula to calculate the VGF was modified accordingly to include other tissues as VGF$= N_{\text{gland}}/N_{\text{total}}$, where N_{gland} is the

number of voxels assigned as glandular tissue and N_{total} the total number of voxels of the whole breast, excluding skin. Table 2 describes the main characteristics of the breast models used in this work.

Table 2: Parameters of the breast phantoms generated and used in this work.

Size	Total volume (cm^3)	Breast diameter (cm)	Compressed thickness (cm)	VGF (%) Low	Medium	High
Small	299	9.7	2	9.9	19.6	30.5
Medium	653	12.0	4	5.8	9.6	17.0
Large	1193	15.0	6	2.1	4.0	7.7

In order to verify the impact of the elemental composition of breast tissues in dosimetry, two databases were used for skin, glandular and adipose tissues: Hammerstein et al.[47] and Woodard and White.[48] Since the tables from those works provide the average and a typical range of elemental proportions for each tissue, we developed an analytic model to search for the elemental combinations which minimizes and maximizes the dose in glandular tissue (i.e. the mean glandular dose), which is explained in details in Appendix A. Table 3 summarizes the combinations of tissues compositions used in this work, while the detailed description of the elemental compositions is presented in Appendix B.

Table 3: Breast tissue combinations studied in this work and their respective nomenclature.

	Hammerstein et al.[47] (H) Skin	Adipose	Glandular	Woodard and White[48] (WW) Skin	Adipose	Glandular
Target Glandular Dose						
Low	H	H_1	H_1	W_3	W_1	W_1
Average	H	H_2	H_2	W_2	W_2	W_2
High	H	H_3	H_3	W_1	W_3	W_3

Note: for Woodard and White[48] the notation representing each elemental composition matches those in the original work, while the notation numbers for Hammerstein et al.[47] were included in this work to maintain the same notation pattern, thus were not present in the original work. The skin for Hammerstein et al.[47] was the same for all tests.

II.C. Breast imaging modalities: simulation geometries

For each breast imaging modality, a distinct geometry was implemented in the simulations, this includes the source position, x-ray field size and, when applied, the source rotation. In addition, the geometry contains the breast phantom, and the support and compression

plates (PMMA, $26 \times 14 \times 0.2$ cm^3) for mammography, CEDM and DBT. The detector, the antiscatter grid and the patient chest were not included in the simulations. Table 4 describes the geometry parameters designed for the breast imaging modalities studied in this work. The geometry structures (i.e. breast phantom, support and compression plates) are made of rectilinear cubic voxels of 0.5 mm sides. The world is vacuum, except the regions near the breast were the material was set to air. For CEDM, the iodine application was not simulated during the dose estimation.

Table 4: Information about the geometry employed in the simulations for each modality.

Parameters	Simulated modality			
	Mammography	DBT	CEDM	BCT
Source-detector distance (cm)	66	66	66	92.3
X-ray field size (cm^2)	26×14	26×14	26×14	40×30
Compression plate-detector gap (cm)	1.1	1.8	1.1	N/A
Detector-center of rotation distance (cm)	N/A	0	N/A	27.3
Number of projections	1	31	1	300
Projection angle range (^{o})	N/A	-30 to 30	N/A	0 to 360

An isotropic point source was modeled and the heel effect was not considered. Table 5 describes the spectrum employed for each modality and breast size. The x-ray spectra were calculated by the TASMICS (M-T and BCT) programs.[49]

Table 5: Anode/filter and tube potential combinations for each breast size and imaging modality. The filter thickness is also included.

Breast Size	Modality			
	Mammography	DBT	CEDM	BCT
Small	W/Rh 22 kV	W/Al 26 kV	W/Cu 45 kV	W/Al 49 kV
Medium	W/Rh 28 kV	W/Al 29 kV	W/Cu 47 kV	W/Al 49 kV
Large	W/Rh 30 kV	W/Al 33 kV	W/Cu 49 kV	W/Al 49 kV
Filter thickness	0.05 mm	0.7 mm	0.3 mm	1.5 mm

II.D. Glandular dose assessment

MC-GPU provides the voxel and material doses contained in the geometry. In this study, we focused in the dose corresponding to glandular voxels, which is the tissue of interest for breast dosimetry.[15] The MGD was obtained by the energy imparted in all voxels of glandular

tissue by the mass of glandular tissue in the breast, and is obtained via the output file at the end of the simulation. For all cases, the number of primary photons was fine-tuned to yield a MGD of 4 mGy, small variations were observed (less than 0.5% differences) and were corrected by normalizing the number of histories and the results to match exactly the nominal value. The relative standard deviation for the glandular dose scored in voxels was below 0.1% for all simulations. The MGD ratio between two cases (a and b) is defined as:

$$MGD_{ratio} = \frac{MGD_a}{N_a} \times \left(\frac{MGD_b}{N_b} \right)^{-1} \tag{1}$$

Where N is the number of histories for a or b. Since in this work, the MGD was fixed at 4 mGy for all simulations, the expression can be simplified as: $MGD_{ratio} = N_b/N_a$.

Three conditions are studied: (i) The first assessment consists of the glandular dose distribution (GDD) compared to different modalities, for each breast size and VGF. In this case, the glandular, adipose and skin have the compositions of $H_{Average}$ by default (see Appendix B for details). This totaled in 36 simulations. (ii) The second test compared the impact of the tissue compositions over the MGD. For this, only the medium VGF is considered. Therefore, a total of 72 simulations were performed. (iii) The third test compared the influence of the blood, connective and muscle tissues over the MGD. These tissues were changed to adipose and the dose distribution was compared between the original model. In this test, the comparison was selected for mammography and BCT, and medium/large breast sizes with $H_{Average}$ composition.

III. Results

III.A. Glandular dose distribution across modalities

Figure 1 illustrates the glandular dose distribution for the same MGD within the breast for two breast imaging modalities (mammography and BCT) obtained by MC simulation. The higher energy employed in BCT and the rotating source, related to the irradiation geometry, result in a more homogeneous dose across the breast in contrast to mammography.

The glandular dose distributions is shown in Figure 2 for different breast sizes and imag-
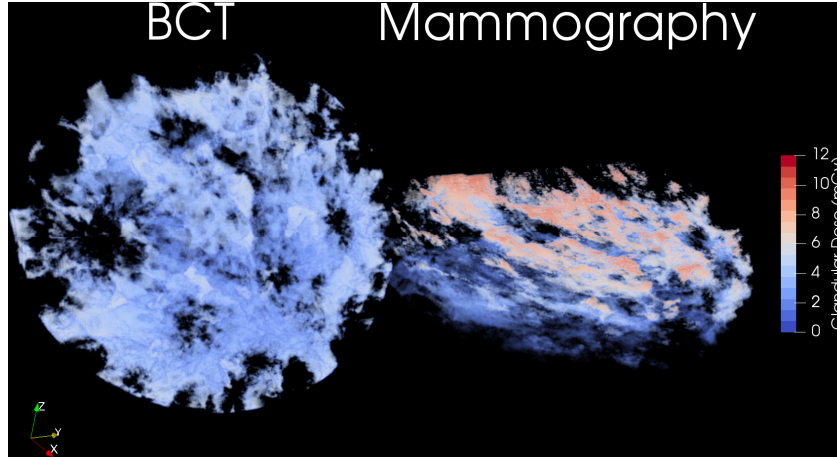
Figure 1: Glandular dose distribution for two breast imaging modalities: BCT and Mammography, the other tissues are transparent. Medium sized breast with average VGF. MGD is 4 mGy.

ing modalities. We observe that a higher variability between the dose values is observed for mammography and DBT compared to CEDM and BCT due to the higher energy spectra employed in the latter modalities. The CEDM presented a narrower dose distribution compared to BCT for small and medium breasts, this could be the effect of the smaller breast thickness due to compression. Additionally, the variability is also related to the breast size: the dose intervals (between minimum and maximum) increases with breast size (in increasing breast size order: Figures 2 (a), (b) and (c)). This behavior could be explained by the exponential attenuation of low energy photons, which have a higher probability of depositing energy at the entrance of the breast, while deeper tissues present less probability of being irradiated.

Table 6 summarizes the glandular dose values for the median, 1 and 99 percentiles, minimum and maximum, considering all glandular voxels. The table comprises the results obtained for all imaging modalities, breast sizes and compositions. In order to keep a clear view in the comparison, the results were normalized by the MGD which corresponds to 4 mGy. An interesting aspect is that the median is slightly below the MGD for mammography and DBT, which indicates that more than half of the voxels received less than the MGD. The minimum and maximum dose values drastically changes between breast sizes. While for small breasts the glandular dose varies from 0.35 to 2.24 times the MGD, large breasts present variations from 0.12 to 4.02 times the MGD. Comparing these values, a non symmetric behavior is observed. The VGF affects the range of glandular dose values: fatty breasts have

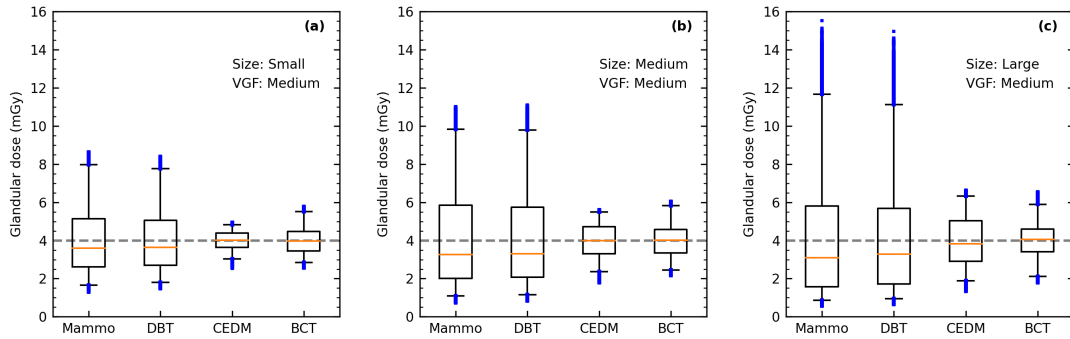III.A.   Glandular dose distribution across modalities

Figure 2: Boxplot of the glandular dose distribution among voxels for different imaging modalities and breast sizes: (a) small, (b) medium and (c) large. Dashed line MGD (4 mGy), centerline: median. Box lower and upper edges: first and third quartiles, respectively. Whiskers: 1-99% intervals, blue dots: outliers. Breast tissue compositions: $H_{Average}$.

a narrower distribution compared to dense breasts. This is due to the attenuation coefficient of glandular tissue being higher than the fat tissue.

III.B.   Glandular dose and the tissues elemental compositions

The impact of the elemental compositions of the breast tissues following the combinations described in Table 3 is shown in Figure 3. To facilitate the comparison, the results for the different imaging modalities were condensed by taking the average and standard deviations. The MGD ratio was calculated using equation 1 setting $H_{Average}$ as b, and the compared case as a. (RMT: I'm confused here. Are MGD values taken in the ratio with different numbers of histories (not the number of histories in ratios?) Also, not all simulations are tuned to obtain 4 mGy, right (so that you can show that the different compositions yield different doses corresponding to different cross sections)? Did I miss something in the methods? RTM: in this case, all MGD are 4 mGy for all compositions, I included an equation in the methodology) The results shows that only the H_{High} combinations yielded significantly higher MGD than the $H_{Average}$ (up to 1.09(2)). Meanwhile, the WW_{Low} and $WW_{Average}$ compositions presented lower MGD values (down to 0.68(3)) and the WW_{High} compositions resulted in practically identical values (from 1.00(1) to 1.01(1)). H_{Low} values were similar to $WW_{Average}$, and this was expected due to the more similar densities and elemental compositions of the breast tissues.

Table 6: Glandular dose distribution values for different imaging modalities and breast models, considering all glandular voxels. All values are normalized by the MGD (4 mGy). The 1% and 99% correspond to the respective percentile intervals while Min. and Max. are the minimum and maximum values, respectively.

| Size	VGF	Modality	Ratio to MGD				
			Median	1%	99%	Min.	Max.
Small	Low	Mammography	0.96	0.45	1.83	0.35	1.98
		DBT	0.96	0.49	1.79	0.40	1.94
		CEDM	1.01	0.76	1.18	0.64	1.21
		BCT	0.99	0.69	1.36	0.63	1.42
	Medium	Mammography	0.90	0.41	1.99	0.32	2.16
		DBT	0.91	0.45	1.94	0.36	2.10
		CEDM	1.00	0.76	1.20	0.64	1.24
		BCT	0.99	0.71	1.38	0.64	1.45
	High	Mammography	0.92	0.41	2.02	0.29	2.24
		DBT	0.92	0.45	1.96	0.33	2.18
		CEDM	1.01	0.76	1.20	0.61	1.23
		BCT	0.99	0.69	1.37	0.65	1.54
Medium	Low	Mammography	0.86	0.28	2.32	0.17	2.68
		DBT	0.86	0.30	2.32	0.20	2.72
		CEDM	1.01	0.58	1.34	0.44	1.40
		BCT	1.00	0.66	1.42	0.56	1.49
	Medium	Mammography	0.82	0.27	2.46	0.18	2.76
		DBT	0.82	0.29	2.45	0.20	2.77
		CEDM	1.00	0.59	1.37	0.44	1.40
		BCT	1.00	0.61	1.46	0.54	1.51
	High	Mammography	0.76	0.26	2.65	0.16	3.21
		DBT	0.77	0.28	2.62	0.20	3.23
		CEDM	0.98	0.59	1.40	0.42	1.46
		BCT	0.98	0.66	1.48	0.56	1.59
Large	Low	Mammography	0.73	0.22	3.13	0.14	3.69
		DBT	0.74	0.24	3.03	0.16	3.62
		CEDM	0.97	0.49	1.58	0.33	1.64
		BCT	0.99	0.56	1.57	0.49	1.69
	Medium	Mammography	0.78	0.21	2.91	0.14	3.88
		DBT	0.82	0.24	2.78	0.16	3.74
		CEDM	0.96	0.47	1.58	0.33	1.66
		BCT	1.01	0.53	1.47	0.44	1.64
	High	Mammography	0.65	0.21	3.31	0.12	4.02
		DBT	0.69	0.24	3.17	0.15	3.89
		CEDM	0.93	0.50	1.63	0.35	1.70
		BCT	0.99	0.53	1.58	0.46	1.77
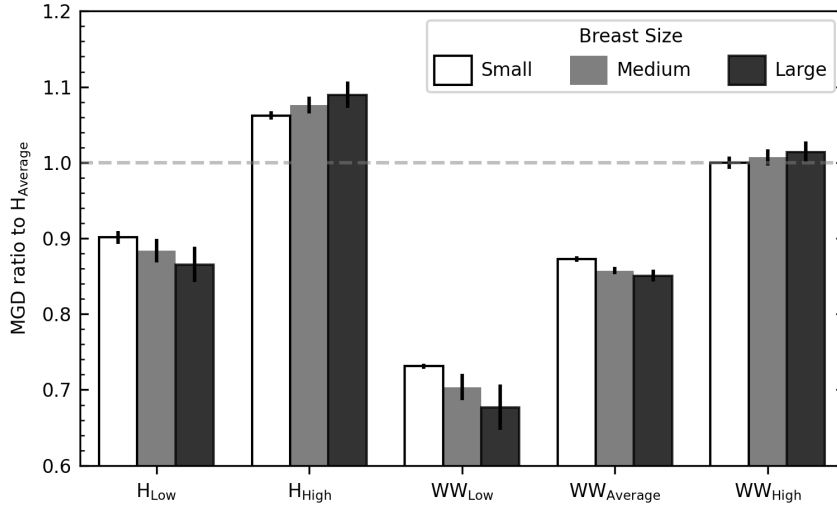
Figure 3: MGD comparison between the different elemental compositions for distinct breast sizes averaged across all imaging modalities. Values normalized by $H_{Average}$. Error bars: standard deviation calculated from the MGD across all imaging modalities. In this case, only the medium VGF is considered for all breast sizes.

The impact of the elemental composition on the dose distribution is shown in Figure 4. The MGD was set to 4 mGy, and the glandular voxel doses are compared between $H_{Average}$ and the other compositions. The cases (a) BCT for a small breast and (b) mammography for a large breast cases were selected to illustrate the extremes, where more energetic x-ray beam ensures lower differences for (a) and a low energy x-ray beam produces higher differences for (b). The others breast sizes and imaging modalities, not included here, have a pattern in between (a) and (b). In general, distributions are narrower for small breasts and high energy beams (such as CEDM and BCT). Meanwhile, a double-peaked distribution is observed for larger breasts and low energy beams (mammography and DBT). In addition, the H_{Low} and WW_{Low} compositions deviated more than the other studied compositions. The highest discrepancies for the glandular dose distribution are in the order of 20%.

III.C. Glandular dose and the tissue assignment

The glandular dose was compared between the breast models containing only three type of tissues (adipose, glandular and skin) and a more complex model (which also includes muscle, blood and connective tissues). The relative differences in the glandular dose distribution is shown in Figure 5 for (a) medium and (b) large breasts. The more energetic beam employed
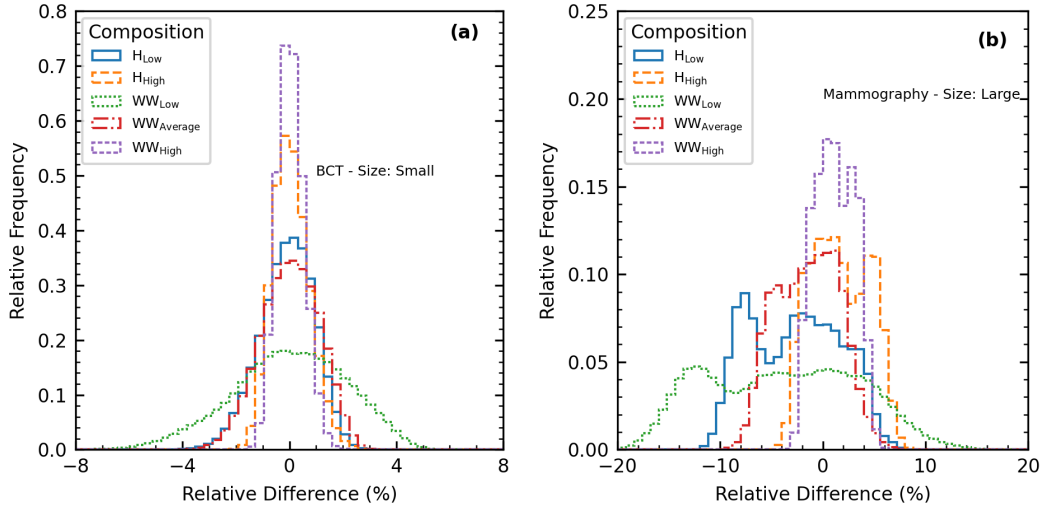
Figure 4: Glandular dose relative differences between $H_{Average}$ and other elemental compositions for different breast sizes/imaging modalities: (a) small/BCT and (b) large/mammography. MGD is 4 mGy.

in BCT produced a single peaked distribution centered near 0 for both breast sizes, while the mammography distributions (with a lower energy beam) presented two peaks with a larger value distribution. This is expected since the elemental composition of the tissues has more impact at lower energies than at higher energies (same behavior as shown in Figure 4). When the MGD is corrected for a constant number of simulated histories, and considered for each imaging modality and breast sizes as in Figure 5, the MGD is consistently lower for the three tissue breast model from 1.4% to 1.7% compared to the more complex breast model (other combinations were not included).

IV. Discussion

The MGD is a well established dosimetric quantity for breast imaging and is employed in a variety of studies: from quality control, to model comparison and risk assessment.[15,50] However, as its name suggests, it provides an average estimation of the glandular dose within the breast and consequently it does not consider the spacial variations.

In this work, for mammography, the glandular dose varied from 0.35 to 1.98 the MGD for small breasts, from 0.12 to 4.02 the MGD for the large breast. For BCT, the variations were less sensitive to breast sizes, going from 0.63 to 1.54 the MGD for small breasts and
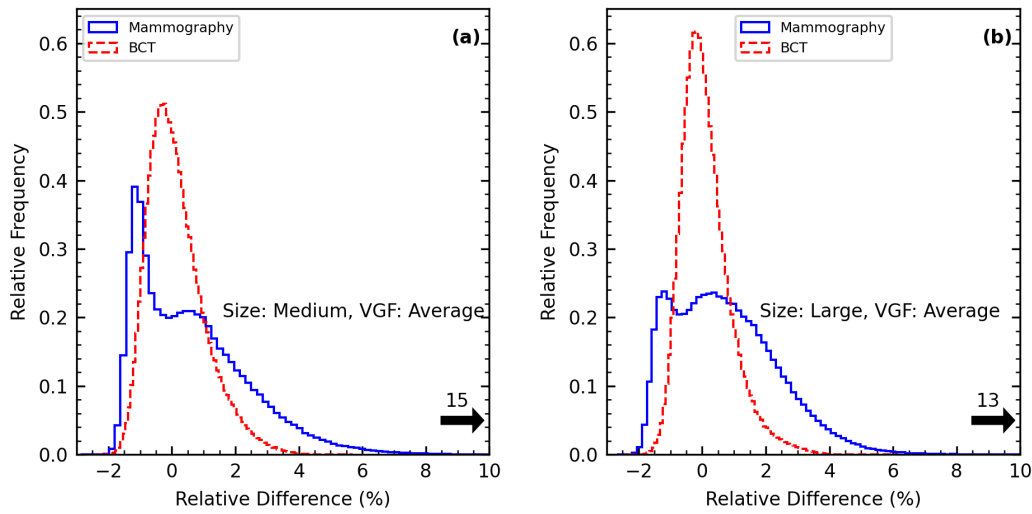
Figure 5: Relative differences of glandular dose in voxels between standard breast phantom and the one replaced with adipose tissues when the MGD is set to 4 mGy. (a) Medium breast and (b) large breast. The arrow indicates the maximum difference value. Composition: $H_{Average}$.

0.44 to 1.77 for larger ones. We also included the 1% to 99% intervals because a large dose variation is present in a small voxel subset. For example, excluding 2% of the voxels, the dose variation for large breast in mammography dropped to 0.21 to 3.31 times the MGD. We also found that the median of the glandular dose distributions is lower than the MGD for mammography and DBT, specially for large breasts. In the extreme case (mammography, large breast and high VGF) the median was 0.65 times the MGD, which indicates that a significant number of voxels are receiving less than the average dose.

The elemental composition of breast tissues has a significant impact in the dosimetry results, which was expected comparing the respective attenuation coefficients between the materials.[15] The MGD obtained with the $H_{Average}$ composition (traditionally employed in dosimetric studies) was higher than the other studied compositions, except the H_{High}/WW_{High} cases. In addition, the results with WW_{High} were in closer agreement with $H_{Average}$ compared to H_{High}. The MGD between the different elemental compositions varied approximately between 0.7 to 1.1 the $H_{Average}$. The breast imaging modalities and breast sizes affected the MGD ratio in a few percent without modifying the overall dose underestimation or overestimation for different elemental compositions. The $H_{Average}$ provides a conservative estimation of the dose, i. e. the maximum MGD underestimation is in the order of 10% while in the other cases the values are lower (reaching 30% less dose at WW_{Low}). This behavior may

be explained by the variations of the elemental composition of each tissue in the databases, mainly the differences between Carbon and Oxygen. The glandular dose distribution varied between the breast tissue composition databases when the MGD was set to 4 mGy for all combinations. For small breasts and high energy beams (BCT), the differences were less than 8%, while for large breasts and low energy modalities (mammography) the differences reached 20%. H_{Low} and WW_{Low} compositions yielded the highest discrepancies compared to $H_{Average}$, this could be explained, as explained for the MGD ratio, by the combination of the tissues elemental compositions, more specifically the variations of O and C, and densities for WW.

The traditional three-tissue breast model (skin, adipose and glandular) yielded a systematic higher MGD in the order of 1.4% to 1.7% compared to the breast model including other tissues, due to the additional tissues having a higher density than the adipose tissue. The impact of the three-tissue breast model approximation over the MGD is less pronounced than the impact of the MGD due to the other variations and uncertainties presented earlier (such as the breast tissue elemental compositions). However, it is important to notice that the results were obtained with computer-generated phantoms, and a comparison with models built from real patient data is necessary.

The exponential attenuation of photons trough the breast, which is more evident at low energies such as those employed in mammography ($\approx$ 20 keV), in addition with the geometry of a fixed beam source, makes the dose distribution significantly heterogeneous in this imaging modality. This behavior was studied by Boone et al.,[11] when they compared the dose profiles between mammography and BCT. For the latter, a more homogeneous dose was observed. Oliver and Thomson[36] found that the glandular dose distribution within the breast varies from approximately from 0.1 to 4 times the MGD in a mammography simulation. Sechopoulos et al.[33] also found variations in the same order for mammography, and from 0.5 to 1.5 times the MGD for BCT. The results shown in this work are in an excellent agreement compared to those in literature. In addition, the disposition of the glandular tissue within the breast affects the glandular dose distribution, and consequently the mean glandular dose.[22] Due to the uncertainty of the effects of ionizing radiation to biological tissues at very low doses, it is difficult to determine if a more homogeneous dose within the breast (from CEDM and BCT) is less harmful than more heterogeneous ones (from mammography and DBT).[11] However, studying the dosimetry at multiscale levels

could help to better understand the energy deposition at cell scales[36] and its relation at macroscopic scales. The second part of our study explores this subject.

In this work we studied a limited number of breast sizes and compositions, thus the values could vary significantly for a female breast population, specially for very large breasts not explored in this work. Moreover, the breast dose at this study is maintained the same for all breast sizes and modalities, which is reasonable for relative comparisons. However, in clinical practice, the doses will vary significantly between modalities, breast characteristics and equipment from different vendors. The results of this work show the uncertainty of the glandular dose distribution within the breast due to the elemental composition of breast tissues, which in turn vary between databases and could be explored in future works to include new elemental composition databases of breast tissues. Furthermore, the influence of the iodine and the glandular dose in multiple length scales could be quantified, since in our work this effect was neglected.

V.   Conclusion

The glandular dose distributions was assessed at macroscopic scales for a variety of breast sizes and compositions. These distributions of glandular dose vary significantly within the breast, specially for low energy x-ray beams such as mammography and DBT. The tissue elemental compositions of glandular, adipose and skin affect directly the MGD and the glandular dose distributions. The three tissue breast model approximation had a minor impact on the MGD for the computer-generated breast models used in this study. The second part of our work compares the relation between the dose at macroscopic and microscopic scales in order to better understand how the dose variations will affect the energy depositions in a cellular level.

Acknowledgments

A Analytic model description

To select the tissues compositions of the breast within the databases, a simplified analytic model based on Ref.[51] was implemented to estimate the mean glandular dose. The geometry consists of a parallel beam of monoenergetic x-rays incident on a 5 cm semi-cylinder, 20% glandular breast with 1.5 mm skin thickness. In our case, the contribution of scattered x-rays were neglected. An optimization routine was used to determine which elemental compositions for skin, adipose and glandular tissue would minimize or maximize the mean glandular dose. The calculations were done interactively until the results converged (usually 80 interactions were necessary). The optimization constraints for Hammerstein[47] database were based on the elemental composition values range for the elements Oxygen and Carbon for glandular and adipose tissues. For the Woodard and White[48] database, there are three different elemental compositions for adipose, glandular and skin tissues. The combinations between the three tissues were tested exhaustively until they yielded the minimum and maximum MGD values.

B Elemental Compositions

This appendix describes the elemental composition for every material used in this work.

Table 7: Adipose elemental composition (by weight) employed in the simulations with their respective reference.

Reference	Density (g/cm^3)	H	C	N	O	Others
H$_1$[47]	0.93	11.2	51.3	1.7	35.7	P(0.025),S(0.025),K(0.025),Ca(0.025)
H$_2$[47]	0.93	11.2	61.9	1.7	25.1	P(0.025),S(0.025),K(0.025),Ca(0.025)
H$_3$[47]	0.93	11.2	68.1	1.7	18.9	P(0.025),S(0.025),K(0.025),Ca(0.025)
W$_1$[48]	0.97	11.2	51.7	1.3	35.5	Na(0.1),S(0.1),Cl(0.1)
W$_2$[48]	0.95	11.4	59.8	0.7	27.8	Na(0.1),S(0.1),Cl(0.1)
W$_3$[48]	0.93	11.6	68.1	0.2	19.8	Na(0.1),S(0.1),Cl(0.1)

Table 8: Glandular elemental composition (by weight) employed in the simulations with their respective reference.

Reference	Density (g/cm^3)	H	C	N	O	Others
H$_1$[47]	1.04	10.2	30.5	3.2	55.6	P(0.125),S(0.125),K(0.125),Ca(0.125)
H$_2$[47]	1.04	10.2	18.4	3.2	67.7	P(0.125),S(0.125),K(0.125),Ca(0.125)
H$_3$[47]	1.04	10.2	10.8	3.2	75.3	P(0.125),S(0.125),K(0.125),Ca(0.125)
W$_1$[48]	0.99	10.9	50.6	2.3	35.8	Na(0.1),S(0.1),Cl(0.1)
W$_2$[48]	1.02	10.6	33.2	3.0	52.7	Na(0.1),S(0.2),Cl(0.1)
W$_3$[48]	1.06	10.2	15.8	3.7	69.8	Na(0.1),S(0.2),Cl(0.1)

Table 9: Skin elemental composition (by weight) employed in the simulations with their respective reference.

Reference	Density (g/cm^3)	H	C	N	O	Others
H[47]	1.09	9.8	17.8	5.0	66.7	P(0.175),S(0.175),K(0.175),Ca(0.175)
W$_1$[48]	1.09	10.0	25.0	4.6	59.4	Na(0.2),P(0.1),S(0.3),Cl(0.3),K(0.1)
W$_2$[48]	1.09	10.0	20.4	4.2	64.5	Na(0.2),P(0.1),S(0.2),Cl(0.3),K(0.1)
W$_3$[48]	1.09	10.1	15.8	3.7	69.5	Na(0.2),P(0.1),S(0.2),Cl(0.3),K(0.1)

Table 10: Elemental composition (by weight) of the remaining materials employed in the simulations with their respective reference.

Material	Density (g/cm^3)	H	C	N	O	Others
Air (dry)[41]	0.001205	-	0.0124	75.5267	23.1781	Ar(1.2827)
PMMA[41]	1.19	8.054	59.985	-	31.961	-
Blood (ICRP)[41]	1.06	10.187	10.002	2.964	75.9414	Na(0.185),Mg(0.004),Si(0.003), P(0.035),S(0.185),Cl(0.278), K(0.163),Ca(0.006),Fe(0.046), Zn(0.001)
Connective[48]	1.12	10.064	10.783	2.768	75.477	Na(0.2),S(0.6),Cl(0.3)
Muscle (ICRP)[41]	1.04	10.064	10.783	2.768	75.477	Na(0.075),Mg(0.019),P(0.18), S(0.241),Cl(0.079),K(0.302), Ca(0.003),Fe(0.004),Zn(0.005)

Multiscale breast dosimetry: part I   page 19

References

[1]   R. H. Gold, L. W. Bassett, and B. E. Widoff, Highlights from the history of mammography., Radiographics: a review publication of the Radiological Society of North America, Inc (1990).

[2]   European Society of Radiology, *Screening & Beyond: Medical Imaging in the Detection, Diagnoses and Management of Breast Diseases*, ESR, Vienna, 2016.

[3]   M. G. Marmot, D. G. Altman, D. A. Cameron, J. A. Dewar, S. G. Thompson, and M. Wilcox, The benefits and harms of breast cancer screening: An independent review, British Journal of Cancer (2013).

[4]   F. Sardanelli et al., Position paper on screening for breast cancer by the European Society of Breast Imaging (EUSOBI) and 30 national breast radiology bodies from Austria, Belgium, Bosnia and Herzegovina, Bulgaria, Croatia, Czech Republic, Denmark, Estonia, Finland, France, G, European Radiology **27**, 2737–2743 (2017).

[5]   P. Skaane, A. I. Bandos, R. Gullien, E. B. Eben, U. Ekseth, U. Haakenaasen, M. Izadi, I. N. Jebsen, G. Jahr, M. Krager, L. T. Niklason, S. Hofvind, and D. Gur, Comparison of digital mammography alone and digital mammography plus tomosynthesis in a populationbased screening program, Radiology (2013).

[6]   P. Skaane, A. I. Bandos, R. Gullien, E. B. Eben, U. Ekseth, U. Haakenaasen, M. Izadi, I. N. Jebsen, G. Jahr, M. Krager, and S. Hofvind, Prospective trial comparing full-field digital mammography (FFDM) versus combined FFDM and tomosynthesis in a population-based screening programme using independent double reading with arbitration, European Radiology (2013).

[7]   D. Bernardi, P. Macaskill, M. Pellegrini, M. Valentini, C. Fantò, L. Ostillio, P. Tuttobene, A. Luparia, and N. Houssami, Breast cancer screening with tomosynthesis (3D mammography) with acquired or synthetic 2D mammography compared with 2D mammography alone (STORM-2): a population-based prospective study, The Lancet Oncology **17**, 1105–1113 (2016).

[8]   H. R. Peppard, B. E. Nicholson, C. M. Rochman, J. K. Merchant, R. C. Mayo, and J. A. Harvey, Digital breast tomosynthesis in the diagnostic setting: Indications and clinical applications, Radiographics **35**, 975–990 (2015).

[9]   J. S. Sung, L. Lebron, D. Keating, D. D'Alessio, C. E. Comstock, C. H. Lee, M. C. Pike, M. Ayhan, C. S. Moskowitz, E. A. Morris, and M. S. Jochelson, Performance of dual-energy contrast-enhanced digital mammography for screening women at increased risk of breast cancer, Radiology **293**, 81–88 (2019).

10   C. Dromain, C. Balleyguier, G. Adler, J. R. Garbay, and S. Delaloge, Contrast-enhanced digital mammography, European Journal of Radiology **69**, 34–42 (2009).

11   J. M. Boone, T. R. Nelson, K. K. Lindfors, and J. A. Seibert, Dedicated breast CT: Radiation dose and image quality evaluation, Radiology **221**, 657–667 (2001).

12   A. Sarno, G. Mettivier, and P. Russo, Dedicated breast computed tomography: Basic aspects, Medical Physics **42**, 2786–2804 (2015).

13   S. Y. Huang, J. M. Boone, K. Yang, N. J. Packard, S. E. McKenney, N. D. Prionas, K. K. Lindfors, and M. J. Yaffe, The characterization of breast anatomical metrics using dedicated breast CT, Medical Physics **38**, 2180–2191 (2011).

14   The 2007 Recommendations of the International Commission on Radiological Protection. ICRP publication 103, Annals of the ICRP (2007).

15   Dosimetry in x-ray-based breast imaging, Physics in Medicine and Biology **61**, R271–R304 (2016).

16   M. J. Yaffe and J. G. Mainprize, Risk of radiation-induced breast cancer from mammographic screening, Radiology **258**, 98–105 (2011).

17   X. Wu, G. T. Barnes, and D. M. Tucker, Spectral dependence of glandular tissue dose in screen-film mammography., Radiology **179**, 143–148 (1991).

18   X. Wu, E. L. Gingold, G. T. Barnes, and D. M. Tucker, Normalized average glandular dose in molybdenum target-rhodium filter and rhodium target-rhodium filter mammography., Radiology **193**, 83–89 (1994).

19   D. R. Dance, Monte Carlo calculation of conversion factors for the estimation of mean glandular breast dose, Physics in Medicine and Biology **35**, 1211–9 (1990).

20   D. R. Dance, K. C. Young, and R. E. van Engen, Further factors for the estimation of mean glandular dose using the United Kingdom, European and IAEA breast dosimetry protocols, Physics in Medicine and Biology **54**, 4361–4372 (2009).

21   M. E. Myronakis, M. Zvelebil, and D. G. Darambara, Normalized mean glandular dose computation from mammography using GATE: a validation study, Physics in Medicine and Biology **58**, 2247–2265 (2013).

22   A. M. Hernandez, J. A. Seibert, and J. M. Boone, Breast dose in mammography is about 30% lower when realistic heterogeneous glandular distributions are considered, Medical Physics **42**, 6337–6348 (2015).

23   A. Nosratieh, A. Hernandez, S. Z. Shen, M. J. Yaffe, J. A. Seibert, and J. M. Boone, Mean glandular dose coefficients (D(g)N) for x-ray spectra used in contemporary breast imaging systems., Physics in Medicine and Biology **60**, 7179–90 (2015).

[24] A. Sarno, G. Mettivier, F. Di Lillo, R. Tucciariello, K. Bliznakova, and P. Russo, Normalized glandular dose coefficients in mammography, digital breast tomosynthesis and dedicated breast CT, **55**, 142–148.

[25] A. Sarno, R. M. Tucciariello, G. Mettivier, F. di Franco, and P. Russo, Monte Carlo calculation of monoenergetic and polyenergetic DgN coefficients for mean glandular dose estimates in mammography using a homogeneous breast model, Physics in Medicine and Biology **64**, 125012 (2019).

[26] E. Tzamicha, E. Yakoumakis, I. Tsalafoutas, A. Dimitriadis, E. Georgiou, V. Tsapaki, and A. Chalazonitis, Dual-energy contrast-enhanced digital mammography: Glandular dose estimation using a Monte Carlo code and voxel phantom, Physica Medica: European Journal of Medical Physics **31**, 785–791, Publisher: Elsevier.

[27] I. Sechopoulos, S. Suryanarayanan, S. Vedantham, C. D'Orsi, and A. Karellas, Computation of the glandular radiation dose in digital tomosynthesis of the breast, Medical Physics **34**, 221–232 (2006).

[28] A. K. W. Ma, D. G. Darambara, A. Stewart, S. Gunn, and E. Bullard, Mean glandular dose estimation using MCNPX for a digital breast tomosynthesis system with tungsten/aluminum and tungsten/aluminum+silver x-ray anode-filter combinations, Medical Physics **35**, 5278–5289 (2008).

[29] D. R. Dance, K. C. Young, and R. E. van Engen, Estimation of mean glandular dose for breast tomosynthesis: factors for use with the UK, European and IAEA breast dosimetry protocols, Physics in Medicine and Biology **56**, 453–471 (2011).

[30] S. C. Thacker and S. J. Glick, Normalized glandular dose (DgN) coefficients for flat-panel CT breast imaging, Physics in Medicine and Biology **49**, 5433–5444 (2004).

[31] A. M. Hernandez and J. M. Boone, Average glandular dose coefficients for pendant-geometry breast CT using realistic breast phantoms, Medical Physics **44**, 5096–5105 (2017).

[32] A. M. Hernandez, A. E. Becker, and J. M. Boone, Updated breast CT dose coefficients (DgN CT) using patient-derived breast shapes and heterogeneous fibroglandular distributions, Medical Physics **46**, 1455–1466 (2019).

[33] I. Sechopoulos, K. Bliznakova, X. Qin, B. Fei, and S. S. J. Feng, Characterization of the homogeneous tissue mixture approximation in breast imaging dosimetry, Medical Physics **39**, 5050–5059 (2012).

[34] I. Sechopoulos, S. S. J. Feng, and C. J. D'Orsi, Dosimetric characterization of a dedicated breast computed tomography clinical prototype, Medical Physics **37**, 4110–4120 (2010).

[35] A. Brahme et al., Volume 7 - Radiation Biology and Radiation Safety, in *Comprehensive Biomedical Physics*, Elsevier, 2014.

[36] P. A. K. Oliver and R. M. Thomson, Investigating energy deposition in glandular tissues for mammography using multiscale Monte Carlo simulations, Medical Physics **46**, 1426–1436 (2019).

[37] A. Badal and A. Badano, Accelerating Monte Carlo simulations of photon transport in a voxelized geometry using a massively parallel graphics processing unit, Medical Physics **36**, 4878–4880 (2009).

[38] A. Badano, A. Badal, S. Glick, C. G. Graff, F. Samuelson, D. Sharma, and R. Zeng, In silico imaging clinical trials for regulatory evaluation: Initial considerations for VICTRE, a demonstration study, in *Medical Imaging 2017: Physics of Medical Imaging*, edited by T. G. Flohr, J. Y. Lo, and T. Gilat Schmidt, volume 10132, page 1013220, SPIE, 2017.

[39] R. T. Massera, R. M. Thomson, and A. Tomal, Technical note: MC-GPU breast dosimetry validations with other Monte Carlo codes and phase space file implementation, Medical Physics **49**, 244–253 (2022).

[40] I. Sechopoulos, D. W. O. Rogers, M. Bazalova-Carter, W. E. Bolch, E. C. Heath, M. F. McNitt-Gray, J. Sempau, and J. F. Williamson, RECORDS: improved Reporting of montE CarlO RaDiation transport Studies: Report of the AAPM Research Committee Task Group 268, Medical Physics **45**, e1–e5 (2018).

[41] M. Berger, J. Hubbell, S. Seltzer, J. Chang, J. Coursey, R. Sukumar, D. Zucker, and K. Olsen, Tables of X-Ray Mass XCOM: Photon Cross Sections Database. National Institute of Standards and Technology (NIST), (2010).

[42] C. G. Graff, A new, open-source, multi-modality digital breast phantom, in *Medical Imaging 2016: Physics of Medical Imaging*, edited by D. Kontos, T. G. Flohr, and J. Y. Lo, volume 9783, page 978309, SPIE, 2016.

[43] D. Sharma, C. G. Graff, A. Badal, R. Zeng, P. Sawant, A. Sengupta, E. Dahal, and A. Badano, Technical Note: In silico imaging tools from the VICTRE clinical trial, Medical Physics **46**, 3924–3928 (2019).

[44] S.-Y. Huang, J. M. Boone, K. Yang, A. L. C. Kwan, and N. J. Packard, The effect of skin thickness determined using breast CT on mammographic dosimetry, Medical Physics **35**, 1199–1206 (2008).

[45] L. Shi, S. Vedantham, A. Karellas, and A. M. O'Connell, Technical Note: Skin thickness measurements using high-resolution flat-panel cone-beam dedicated breast CTa), Medical Physics **40**, 031913 (2013).

46   J. M. Boone, A. L. C. Kwan, J. A. Seibert, N. Shah, K. K. Lindfors, and T. R. Nelson, Technique factors and their relationship to radiation dose in pendant geometry breast CT, Medical Physics **32**, 3767–3776 (2005).

47   R. G. Hammerstein, D. W. Miller, D. R. White, M. E. Masterson, H. Q. Woodard, and J. S. Laughlin, Absorbed radiation dose in mammography, Radiology **130**, 485–491 (1979).

48   H. Q. Woodard and D. R. White, The composition of body tissues, The British Journal of Radiology **59**, 1209–1218 (1986).

49   A. M. Hernandez, J. A. Seibert, A. Nosratieh, and J. M. Boone, Generation and analysis of clinically relevant breast imaging x-ray spectra, Medical Physics **44**, 2148–2160 (2017).

50   A. Sarno, G. Mettivier, F. Di Lillo, and P. Russo, A Monte Carlo study of monoenergetic and polyenergetic normalized glandular dose (DgN) coefficients in mammography, Physics in Medicine and Biology **62**, 306–325 (2017).

51   A. Tomal, M. Poletti, and L. Caldas, Evaluation of subject contrast and normalized average glandular dose by semi-analytical models, **68**, 755–759.

Chapter 7

Multiscale breast dosimetry part II

Original article title: Multiscale Monte Carlo Simulations for dosimetry in X-ray breast imaging: Part II - Microscopic scales.

Authors: Rodrigo T. Massera, Alessandra Tomal, Rowan M. Thomson.

Published in: To be submitted.

Note: This is a work in progress. Small modifications could be present compared to the submitted version.

Multiscale Monte Carlo Simulations for dosimetry in X-ray breast imaging: Part II - Microscopic scales

Rodrigo T. Massera[a,1,2], Alessandra Tomal[b,1], Rowan M. Thomson[c,2]

email: a) rtmassera@gmail.com b) atomal@ifi.unicamp.br c) rthomson@physics.carleton.ca

1: Instituto de Física "Gleb Wataghin", Universidade Estadual de Campinas, Campinas, São Paulo, Brazil

2: Carleton Laboratory for Radiotherapy Physics, Department of Physics, Carleton University, Ottawa, Ontario, K1S 5B6, Canada

Abstract

Background: Although the benefits of breast screening and early diagnosis are known for breast cancer, the effects and risks of low radiation doses from the exams to the cells in the breast is still an ongoing topic of study.

Purpose: To study the specific energy distribution in cytoplasm and nuclei of cells corresponding to glandular tissue for different x-ray breast imaging modalities.

Methods: A cubic lattice (500 μm length side) containing 4064 spherical cells was irradiated with photons loaded from phase space files with varying glandular voxel doses (D_g). The specific energy distribution ($f(z, D_g)$) was scored for nucleus and cytoplasm using the PENELOPE (v. 2018) + penEasy (v. 2020) Monte Carlo (MC) code. The phase space files, generated in a previous work, were obtained from Monte Carlo (MC) simulations in a voxelized anthropomorphic phantom corresponding to glandular voxels for different breast imaging modalities, including mammography, digital breast tomosynthesis (DBT), contrast enhanced digital mammography (CEDM) and breast-CT (BCT).

Results: In general, the average specific energy in nuclei is higher than the respective glandular dose scored in the same region, up to approximately 10%. The $f(z, D_g)$ for nucleus and cytoplasm is directly related to the glandular dose in the voxel (D_g), with a weak dependence on the spacial location. For similar D_g values, $f(z, D_g)$ in nuclei is slightly different between Mammography/DBT and CEDM/BCT, indicated that the distinct x-ray spectra plays a significant role in $f(z, D_g)$. In addition, it was observed that the specific energy distribution in glandular tissue $f(z)$ also varies between the modalities.

Conclusions: Microdosimetry studies are complementary to the traditional macroscopic breast dosimetry based on the mean glandular dose (MGD). For the same MGD, the specific energy distribution in glandular tissue varies between breast imaging modalities, indicating that this effect could be considered when studying the risks of exposing the breast to ionizing radiation.

Key words: breast dosimetry; multi-scale Monte Carlo simulations; microdosimetry.

I. Introduction

The exposure of breast cells to low doses of ionizing radiation resulting from diagnostic mammography is a topic of interest for risk assessments.[1] This includes its effects on cell growth and survival, and DNA damage.[2] Despite clear evidences indicating that mammography screening is beneficial in decreasing breast cancer mortality and is recommended mainly for women between 50 to 69 years (with some variations between countries),[3,4] the available microdosimetry data at low doses employed in diagnostic breast imaging is still limited and more studies are necessary to access the long term effects.[5] The benefits of early detection should overcome the risks of radio-induced breast cancer,[6] and this relation is considered to determine the recommended starting age of breast cancer screening.[7,8] Therefore, dosimetry studies are important for understanding the dose deposited in biological tissues of interest (i.e. glandular tissue), and to especially define the dose levels found in radiodiagnostics examinations, allowing to assess the associated risks at low doses.

Besides digital mammography, other x-ray breast imaging modalities are currently employed for breast cancer detection, such as digital breast tomosynthesis (DBT), contrast enhanced mammography (CEDM) and dedicated breast breast CT (BCT). Each x-ray breast imaging modality has its particular geometry and x-ray spectrum energy,[9–11] which could provide different breast dose profiles as discussed in Part I of our work.[12] Moreover, it is still unclear the real impact of these factors and the dose at cellular level. Thus, multiscale studies could contribute to better understand the relation between mean glandular dose (MGD), glandular dose distribution (GDD) and energy deposited in cells between different breast imaging modalities.

Since the energy deposition in matter due to x-rays is derived from a stochastic phenomena, it is expected that the behavior observed at macroscopic scales would be different from the microscopic scales, especially when the characteristic size of the region of interest is of the same order of the electrons track length. Thus, different dosimetry quantities are defined for each regimen. While the absorbed dose, i.e. energy imparted per unit mass, is a commonly quantity used for dosimetry at macroscopic scales, its counterpart for miscroscopic scales is defined as specific energy (z). However, single values of z carry little information, and what is usually studied is the distribution of z ($f(z)$) for a large sample population (from hundreds to thousands of cells).[13] In addition, $f(z)$ and the macroscopic absorbed

69 dose values are related, and as previously discussed in Part I, the dose distribution within

70 the breast can vary significantly depending of the x-ray imaging modalities.

71 Although breast dosimetry at macroscopic scales is a extensively researched topic that

72 span decades,[14] multiscale breast dosimetry is still a recent topic and, to our knowledge, no

73 work compared microscopic dosimetry between different x-ray breast imaging modalities. In

74 addition, considering the distinct glandular dose distribution inside the breast discussed in

75 Part I, a new methodology is necessary to effectively compare the specific energy distribution

76 in cells for mammography, DBT, CEDM and BCT.

77 The first part of our work was focused in the glandular dose at macroscopic scales within

78 the breast, including MGD and the glandular dose distribution in sub-millimeter voxels. This

79 second part addresses the specific energy distribution at microscopic scales (i.e. cells) and

80 its relation with macroscopic dosimetry quantities employed in x-ray breast imaging.

81 II.   Methodology

82 II.A.   Monte Carlo code and general parameters

83 The macroscopic simulations are explained in details in part I of this study.[12] Here, only

84 a brief summary is provided regarding the parameters and geometries. In part I, a total

85 of nine anthropomorphic breast phantoms were generated. The glandular dose distribution

86 $(h(D_g))$ was studied considering a variety of breast imaging modalities and breast sizes.

87 However, for the microscopic studies only the medium sized breast with average glandular

88 content was considered, with the following characteristics: 635 cm^3 of total volume, 12 cm

89 diameter near the chest wall, 4 cm compressed breast thickness (when applied) and a volume

90 glandular fraction of 9.6%. The following modalities were studied for this phantom size (with

91 the respective x-ray spectrum): digital mammography (W/Rh 28 kV), DBT (W/Al 29 kV),

92 CEDM (W/Cu 47 kV) and BCT (W/Al 49 kV). The MGD was fixed at 4 mGy for all cases.

93 From a previous modification[15] in the MC-GPU (v. 1.5)[16] code, we generated phase

94 space files in glandular voxels for a variety of x-ray breast imaging modalities sampled from

95 $h(D_g)$. The phase space files contains the information for each photon that enters the

96 selected voxel volume (energy, direction and position). Afterwards, these files were loaded

97 in PENELOPE (v. 2018) with penEasy (v. 2020) as the steering code in order to perform

98 detailed simulations. Table 1 summarizes the parameters employed in this work.

Table 1: General parameters regarding the Monte Carlo simulations performed in this work following TG-268 guidelines.[17]

Checklist item	Description
(5) Hardware	The simulations were performed in two CPU models: Ryzen 1700X and Ryzen 2700 (AMD, USA). The simulation speeds were in the order of 3×10^4 histories/s and lasted 10 minutes.
(7) Materials	The elemental compositions of breast tissues were extracted from Hammerstein et al.[18] and Woodard and White.[19] The cytoplasm and nuclei compositions were based on Oliver and Thomson[20]
(9) Crosss sections	The cross sections values were obtained from PENELOPE (v. 2018, default settings).
(10) Transport Parameters	Photon energy and electron cutoff: 50 eV. The detailed simulation parameters were selected: $C_{1,2}$=0.0, $W_{CC,CR}$=50, DSMAX=10^{-5} cm.
(12,13,14) Scoring	The dose in glandular voxel is scored along with the specific energy distributions for cell cytoplasm and nucleus compartments.

99 II.B. Simulation geometry

100 Figure 1 illustrates the implemented steps for Part I and Part II, respectively. The simulated

101 geometry in this work consists of a cube of glandular tissue measuring 500 µm on each side.

102 Inside and centered it is located another cube of $306 \times 306 \times 306$ voxels (each voxel has 1 µm

103 in length). This volume between the cubes is a "buffer" zone to compensate for electrons

104 that could be generated from photon-interactions and escape the innermost cube. The vox-

105 elized cube hosts a lattice geometry of cells as described in Ref.,[21] this ensures that the cells

106 are tightly packed within the geometrical volume. Each cell is composed of two concentric

107 voxelized spheres of radii equals to 9 and 6 µm representing cytoplasm and nucleus, respec-

108 tively.[22] The gap between cells in the lattice is fixed at 2 µm yielding 4064 cells, and a cell

109 number density of 1.42×10^8 cells/cm^3. The glandular tissue density and composition was

110 extracted from Refs.,[18,19] while for the nucleus and cytoplasm were obtained from Oliver and

111 Thomson[20] (case "g"). The extracellular matrix (ECM) material composition and density

112 were set to be equivalent as glandular tissue considering a homogeneous mixture of nucleus,

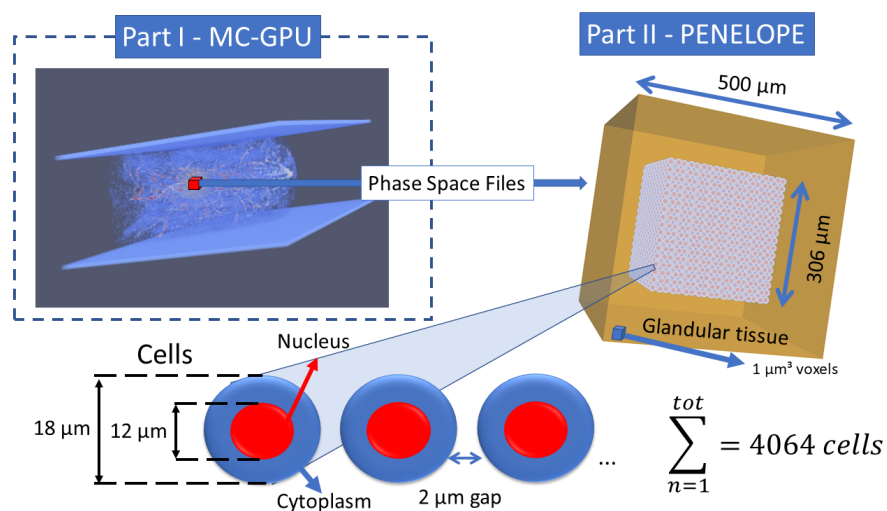113 cytoplasm and ECM inside the innermost cube.

Figure 1: Schematics showing the two parts of our study and the corresponding employed Monte Carlo codes with an inset describing the geometry of the microscopic simulations.
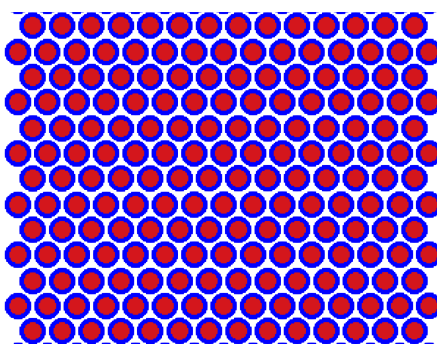

Figure 2: Cross section of the lattice showing one layer of voxelized cells.

II.B.   Simulation geometry

II.C.   Scored quantities

The geometry detailed in section II.B. was irradiated with photons loaded from phase space files, and the energy imparted in each voxel was scored, along with the energy imparted in the buffer zone. The dose in the simulated region (D_{mix}), consisting of mixture of cells (cytoplasm and nucleus) and glandular tissue, which compose the buffer zone, is defined as:

$$D_{mix} = \frac{\varepsilon_{\text{buffer}} + \varepsilon_{\text{cyto}} + \varepsilon_{\text{nucl}}}{m_{\text{buffer}} + m_{\text{cyto}} + m_{\text{nucl}}} \tag{1}$$

where ε is the imparted energy in each material and m their respective mass. The D_{mix} was compared with the respective dose in macroscopic glandular voxel (D_g) for a given phase space file.

The specific energy (z) was calculated for nucleus (z_{nucl}) and cytoplasm (z_{cyto}) by summing the imparted energy in the voxels corresponding to each cell structure and dividing by the respective mass; this procedure was repeated for all cells. With z calculated for all cells, the specific energy distribution $f(z, D_g)$ was obtained. To facilitate the comparison between different $f(z, D_g)$ the following convention was implemented. The range between $z = 0$ and $z = z_{max}$ is divided in 100 bins with the same width and the relative frequency is compared for each interval, hence most of the comparisons were illustrate as histograms. Moreover, the fraction of structures (nucleus or cytoplasm) that did not register any deposited energy ($z = 0$) was defined as $f(z = 0, D_g)$ and calculated as:

$$f(z = 0, D_g) = \frac{N_{z=0}}{N_{tot}} \tag{2}$$

Where $N_{z=0}$ is the number of structures with zero specific energy and N_{tot} the total number of scored structures (in this work this number is fixed as 4064).

II.D.   Comparison between different $f(z, D_g)$

Each phase space file is characterized by its macroscopic glandular voxel dose (D_g), the spatial location within the breast and the original imaging modality. We compared the behavior of $f(z, D_g)$ under three conditions:

  i.   Similar D_g values but different breast imaging modalities.

140   ii.   Distinct D_g values for the same breast imaging modality.

141   iii. Similar D_g values for the same breast imaging modality but at different spatial locations

142   within the breast.

143   The D_g from the phase space files studied in this work varied between approximately

144   1.6 mGy to 8.6 mGy, and the number of primary photons are in the order of 10^6 to 10^7

145   particles.

II.E.   Assessment of specific energy distribution in glandular tissue

147   The specific energy distribution $f(z, D_g)$ depends upon the macroscopic voxel glandular dose,

148   which in turn, follows a distribution $h(D_g)$ for the entire breast. Therefore, we could define

149   a distribution of specific energy taking into account $h(D_g)$. This could be particularly useful

150   when comparing different breast imaging modalities that results in distinct $h(D_g)$. For the

151   following evaluation, we approximate that for a given D_g and an specific imaging modality,

152   the macroscopic voxel spacial location within the breast does not influence the behavior of

153    $f(z, D_g)$, which was studied in the previous section, case ii. Moreover, we assume that the

154   distribution of cells is constant for all glandular voxels.

155   For a given glandular dose distribution $h(D_g)$ within the breast, we can define a specific

156   energy distribution $f(z)$ for the entire glandular tissue inside the breast as:

$$f(z) = \left[\int h(D_g) \, \mathrm{d}D_g \right]^{-1} \int f(z, D_g) h(D_g) \, \mathrm{d}D_g \tag{3}$$

158   where the integration is over D_g. Since the glandular dose is scored in voxels, we approximate

159   as a discrete distribution ($\mathrm{d}D_g$ becomes ΔD_g), and assuming $h(D_g)$ is already normalized:

$$f(z) \approx \sum_{D_g min}^{D_g max} f(z, D_g) h(D_g) \Delta D_g \tag{4}$$

161   Unfortunately, it is impractical to sum over all glandular voxels within the breast, thus

162    $h(D_g)$ was sampled at fixed points. To determine the D_g values, the cumulative distribution

163   function of $h(D_g)$ was calculated ($H(D_g)$). Afterwards, $H(D_g)$ was divided at 10 fixed

164   intervals (percentiles) from 5% to 95% (10% step) and the respective values of D_g were

165 selected (see appendix A for more details). In other words, the product $h(D_g)\Delta D_g$ is constant
166 and equals to 0.1. Finally:

$$167 \quad f(z) \approx \frac{1}{10} \sum_{i=1}^{10} f(z, D_g|_{p=10i-5\%}) \tag{5}$$

168 where p is the respective percentile. The computed $f(z)$ distributions were compared between
169 the imaging modalities studied in this work. The average $(\bar{z})$ and standard deviation (σ)
170 were also calculated and compared for all specific energy distribution for the entire glandular
171 tissue $(f(z))$.

172 III.   Results

173 III.A.   Relation between dosimetry quantities

174 The relation between different dosimetry quantities is shown in Figure 3 for two x-ray breast
175 imaging modalities. It is observed that D_g, D_{mix} and $\bar{z}_{nucl}$ follows an upward trend as
176 function of the D_g percentile. However, this trend is more accentuated in mammography
177 (Figure 3a) than CEDM (Figure 3b) due to the different x-ray spectra employed in each
178 case. Since more energetic x-rays are used in CEDM, the glandular dose distribution within
179 the breast tends to be more homogeneous compared to mammography. Another feature is
180 that D_{mix} is systematically lower than D_g (from approximately 1% to 3%), which could be
181 explained by the escaping electrons released through photon interaction within the buffer
182 zone and the different materials present in the mixture. The same behavior is present for
183 $\bar{z}_{nucl}$, where D_{mix} is systematically lower from approximately 4% to 13%. It is important
184 to notice that the material for the nucleus is denser than the glandular tissue, which could
185 also contribute for this behavior. The ratio $\bar{z}_{nucl}/\sigma$ presents the lowest and highest values
186 in mammography, varying from 0.79 to 2.00 when $D_g = 1.3$ mGy and $D_g = 8.6$ mGy,
187 respectively. Meanwhile, for CEDM, $\bar{z}_{nucl}/\sigma$ ranges from 1.09 to 1.54 when $D_g = 2.6$ mGy
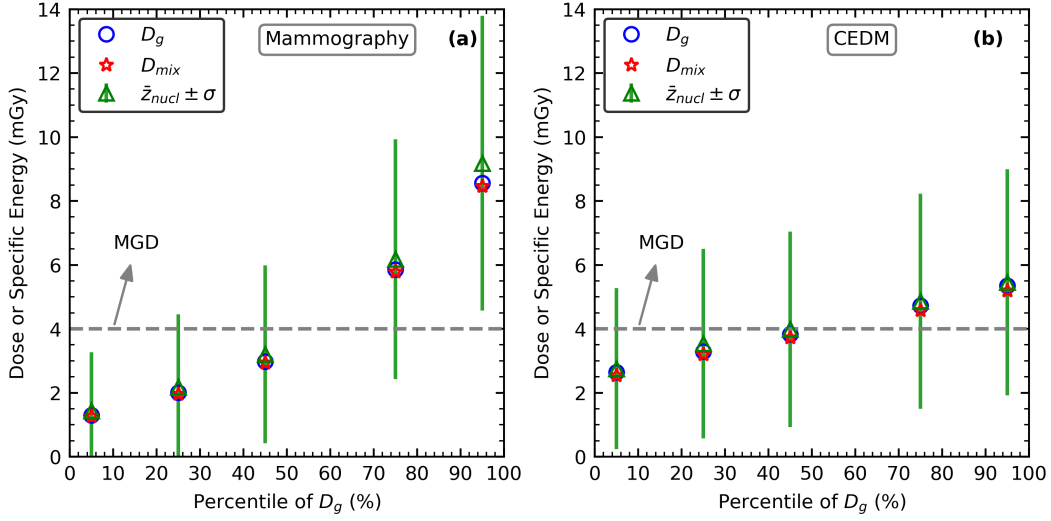188 and $D_g = 5.3$ mGy, respectively.

Figure 3: Comparison between MGD, glandular voxel dose, and specific energy for: (a) mammography and (b) CEDM.

III.B. Comparison of $f(z, D_g)$ under distinct conditions

Figure 4 shows the specific energy distribution for (a) nucleus and (b) cytoplasm under different D_g values. For both cell structures, $f(z, D_g)$ shifts to higher specific energies as D_g increases. The values of $f(z = 0)$ decreases with increasing D_g for both nucleus and cytoplasm, i.e. the probability of no event depositing energy in the cells is becomes lower when the total dose in the lattice is high. Interestingly, this dependency between $f(z = 0)$ and D_g is distinct between the cell structures, which is expected since the volume of cytoplasm is bigger than the volume of nucleus, and the shapes are different among the structures. This difference in size between structures also explains why $f_{cyto}(z, D_g)$ is narrower than $f_{nucl}(z, D_g)$.

Figure 5 compares specific energy distributions between different locations in the breast when the nominal voxel dose value is fixed. $f(z, D_g)$ is practically spatially independent for a same value of D_g (approximately 4 mGy), with $\bar{z}_{nucl}/\sigma$ ranging from 1.33 to 1.36 (less than 2.3%). In addition, $f(z = 0)$ varies from 4.6% to 5.2% for nucleus and is 0% for cytoplasm.
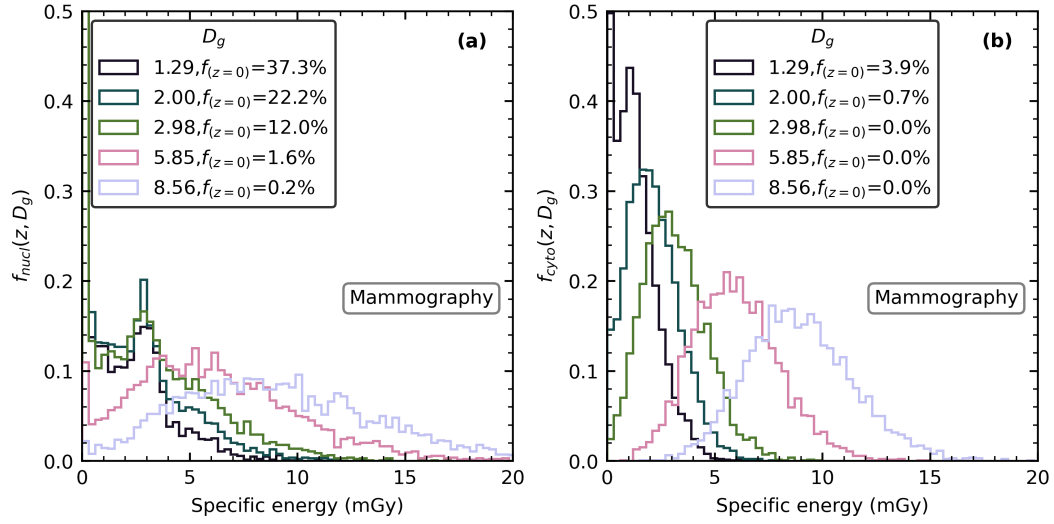
Figure 4: Specific energy distribution as function of the glandular dose in a voxel for (a): nucleus and (b): cytoplasm.
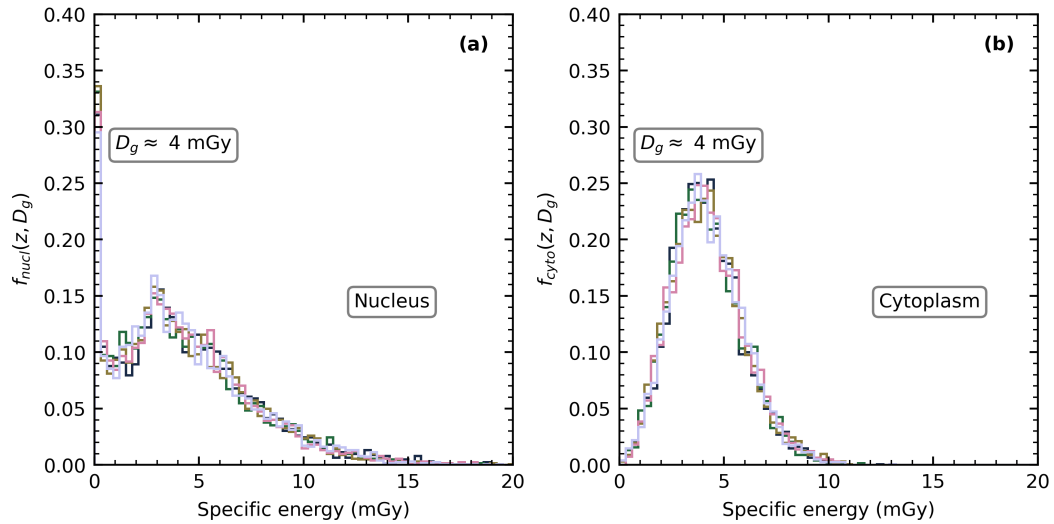

Figure 5: Specific energy distribution in glandular tissue with similar D_g values (approximately 4 mGy) under different spatial locations, (a): nucleus and (b): cytoplasm. Modality: DBT.

III.B.   Comparison of $f(z, D_g)$ under distinct conditions

203   The comparison between $f_z(z, D_g)$ for nucleus and cytoplasm, with similar D_g values

204 and considering all the imaging modalities in this study is shown in Figures 6 (a) and (b),

205 respectively. While $f_{cyto}(z, D_g)$ presents minor variations between modalities, $f_{nucl}(z, D_g)$

206 differs at low z values, specially when a low energy spectrum is employed (mammography

207 and DBT) in contrast to high energy spectrum (CEDM/BCT). In addition, $f(z = 0)$ for

208 the nuclei varies between the imaging modalities, ranging from 3.3% for CEDM to 7.4% for
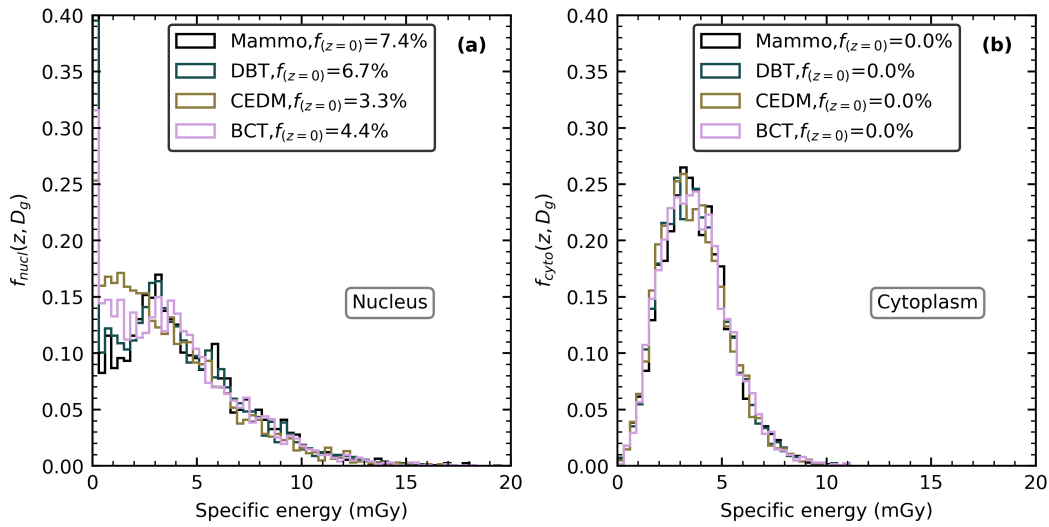
209 mammography.

Figure 6: Specific energy distribution in glandular tissue with similar D_g values for distinct imaging modalities, (a): nucleus and (b): cytoplasm. D_g range: 3.4 to 3.5 mGy.

III.C.   Specific energy distribution in glandular tissue

211 The specific energy distributions obtained in glandular tissue for different imaging modalities

212 is illustrated in Figure 7(a) and Figure 7(b), for nucleus and cytoplasm, respectively. For both

213 graphs there is a clear distinction between the distributions for (i) mammography/DBCT

214 and (ii) CEDM/BCT cases. The lower energy spectrum from (i) yields a more heterogeneous

215 distribution compared to (ii). The peak at a specific energy of approximately 3 mGy observed

216 in Figure 7(a) for mammography and DBT is equivalent to the dose deposited in a single

217 photoelectric interaction considering the average energy of the spectrum.
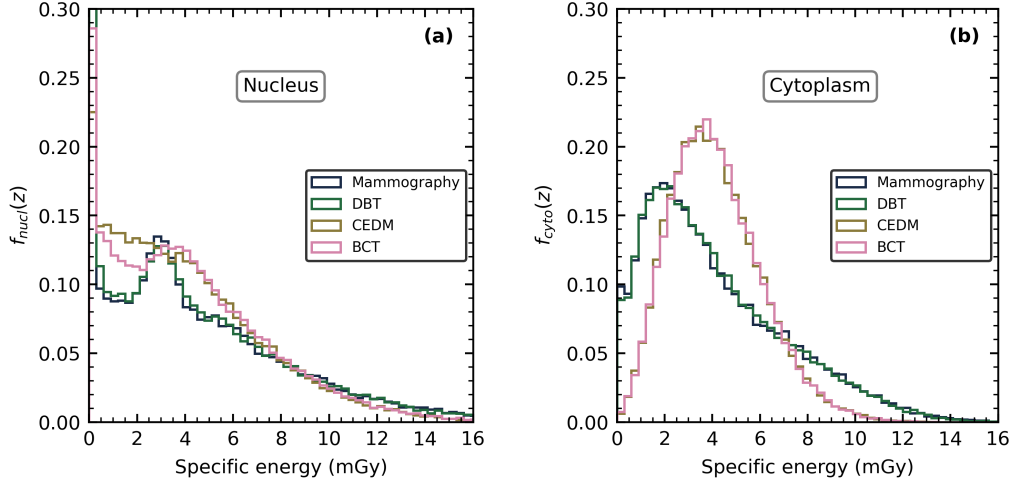
Figure 7: Specific energy distribution in glandular tissue ($f(z)$) for different modalities, (a): nucleus and (b): cytoplasm.

Table 2 quantifies $\bar{z}$, σ_z and $f(z = 0)$ from the data displayed in Figure 7(a) and (b). $\bar{z}$ is systematically higher compared to the MGD for all cases, with slightly higher values for nucleus in contrast to cytoplasm. On the other hand, the values of σ_z are lower for cytoplasm compared to nucleus, which is a behavior already mentioned when the distributions of $f_{cyto}(z)$ and $f_{nucl}(z)$ were compared. The fraction of nucleus without energy deposition ($f(z = 0)$) ranges from 0.03 for CEDM to 0.13 for mammography. Almost all (>0.99) cells' cytoplasm presented a nonzero specific energy for all modalities, indicating that the size of the cellular structure is an important factor to determine the shape of $f(z)$ and consequently, the fraction of structures that absorbs the energy deposited from secondary particles.

Table 2: Average ($\bar{z}$) and standard deviation (σ_z) calculated from the specific energy distribution in glandular tissue for nucleus and cytoplasm considering different imaging modalities.

Modality	Nucleus			Cytoplasm		
	$\bar{z}$	σ_z	$f(z = 0)$	$\bar{z}$	σ_z	$f(z = 0)$
Mammo	4.30	4.03	0.13	4.17	2.97	0.01
DBT	4.29	3.99	0.12	4.16	2.93	0.01
CEDM	4.16	3.23	0.03	4.14	1.93	0.00
BCT	4.23	3.31	0.04	4.15	1.91	0.00

IV. Discussion

The MGD is one of the main quantities studied in breast dosimetry.[14] However, as discussed in part I of our work, the same value of MGD could be obtained with different glandular dose distributions within the breast, since it considers the average energy imparted in glandular tissue. In addition, in some modalities the breast is compressed (mammography, DBT, CEDM) or pendant (BCT),[11] and this could also influence how the dose is distributed in glandular tissue. Now, in part II, we studied how the different glandular dose distributions could impact the microdosimetry quantities, and consequently, link the relations between MGD, glandular dose distribution and specific energy distributions.

Oliver and Thomson[22] showed that, for digital mammography, the average specific energy in cells' nuclei at a specific location in the breast is higher than the glandular dose in the same region. Our results are in agreement with these findings, and the same behavior is present for all imaging modalities studied in this work, suggesting that the nucleus elemental composition plays an important role on the observed specific energy distributions. However, while Oliver and Thomson[22] findings showed an increase on the average specific energy deposition in the order of 30% compared to the glandular dose, our results were lower, in the order of 10%. Several factors could contribute for this difference, including the elemental composition of breast tissues, the cells distribution and size. It is important to notice that the focus of our work was to study the specific energy distribution for different imaging modalities, and consequently only one configuration of the cells' geometry was considered. However, since we implemented a two-step simulation with phase space files, only the simulations considering the microscopic part with different cells' configurations would be necessary to access the effects of cell parameters over the specific energy distributions. Future works could take advantage of this setup, requiring significant less computational time to study different microscopic configurations.

A distinct behavior was found for $f_z(z, D_g)$ between nucleus and cytoplasm. In general, $f_{cyto}(z, D_g)$ presented a lower dispersion compared to $f_{nucl}(z, D_g)$. Additionally, $f(z = 0)$ is systematically higher for the nuclei in contrast to cytoplasm. This is due to the difference in shape and volume, the cytoplasm is more than two times bigger than the nuclei, thus, the probability of an interaction occurring in cytoplasm is higher. For similar values of D_g, $f_z(z, D_g)$ is almost the same inside the breast, independent of the spacial location. On

the other hand, the similar values of D_g but with different modalities yielded in distinct $f_{nucl}(z, D_g)$. The range of the secondary electrons released by the photon interactions at the average energy of each spectrum, calculated with PENELOPE, for the nucleus varied from 7 µm and 24 µm for mammography and CEDM, respectively. For mammography and DBT, the range of the secondary electrons is smaller than the size of the nucleus (diameter of 12 µm), while for CEDM and DBCT the secondary electrons have a range larger than the cell size, this directly impacts the shape of $f_z(z, D_g)$.

Unfortunately is difficult to compare the specific energy distribution in glandular tissue considering the glandular dose distribution for the entire breast, due to the number of required simulations to account for all regions. To circumvent this, we proposed to select specific samples, 10 in total, based on the percentiles of D_g, and afterwards combine the results to approximately estimate the behavior for the entire breast. Using this methodology, it was possible to compare $f(z)$ under different modalities in a reasonable simulation time. Albeit the average specific energy is almost equal for cytoplasm across the different modalities, the standard deviation is lower for BCT/CEDM compared to Mammography/DBT. Meanwhile, both the average and standard deviation are distinct between BCT/CEDM, and Mammography/DBT for nucleus, being higher for the latter. Under the 10 sampling approximation, 12%/13% of the nuclei registered no energy deposition events for Mammography/DBT, compared to 3%/4% for BCT/CEDM, indicating that for more energetic spectrum, the specific energy distribution is more homogeneous although more nuclei suffer energy deposition events.

The multiscale simulations for breast dosimetry could be employed along with other breast models with a complex glandular tissue distributions .[23–25] In this case, the differences between realistic (heterogeneous) and simplified (homogeneous) models could be extended beyond the MGD to encompass also the glandular dose distribution and the specific energy distribution. The methodology that was used in this work (equation 3) can, in theory, be adapted for any breast model with the advantage that, while the macroscopic simulations are necessary to map the $h(D_g)$ distributions, the distributions of $f(z, D_g)$ can be reused from previous microscopic simulations.

V.   Conclusion

In this work, we studied breast dosimetry at microscopic scales with Monte Carlo simulations under different x-ray breast imaging techniques. The behavior of the specific energy distribution depends upon the macroscopic glandular dose distribution, which in turn, varies with the x-ray spectra. Thus, multiscale Monte Carlo simulations could bring additional information besides the MGD, specially when comparing different imaging modalities and the distinct glandular dose distributions. Future works could extend these results exploring more detailed cell models to study the DNA damage in cells. In addition, the contribution of different cells' configurations to the specific energy distributions could be studied and their relation with the x-ray breast imaging modalities. The effect of the contrast agent, used in CEDM, in the specific energy distribution for cells could also be investigated in the future.

Acknowledgments

A   Determining the number of $f(z, D_g)$ sampling points

This section describes the methodology used for determining the necessary number of sampled points of $f(z, D_g)$ from $H(D_g)$ for a good convergence of $f(z)$. The following procedure was performed for the mammography modality, since it provides the widest distribution of D_g between minimum and maximum values. The simulations for the specific energy deposited in nuclei were obtained with a parallel beam and a fixed mammography x-ray spectrum

314 (W/Rh 28 kV), the number of primary photons was fine-tuned to yield a particular value of

315 D_{mix} (which is similar to D_g according to our previous results). The selected values of D_g

316 followed the procedure described in section II.E. but instead the 10 fixed points the number

317 varied between 1 to 64.

318   Figure 8 shows the specific energy distribution in glandular tissue in nucleus for a variety

319 of sampled D_g values. The behavior of the distribution converges specially after N>8, with

320 an average relative difference (in module) below 10% compared to N=64, indicating that

321 N=10 is an acceptable approximation is this case to study $f(z)$ in glandular tissue.
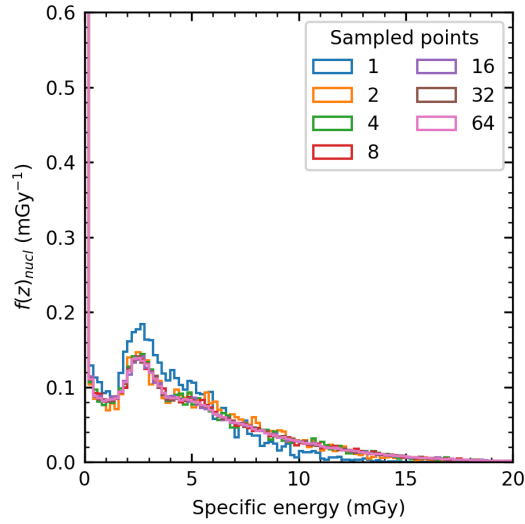

Figure 8: Specific energy distribution for different D_g sampled points.

References

[1] G. J. Heyes, A. J. Mill, and M. W. Charles, Mammography - oncogenecity at low doses, Journal of Radiological Protection **29**, A123–A132 (2009).

[2] L. Pereira, M. T. Ferreira, A. G. F. Lima, C. Salata, S. C. Ferreira-Machado, I. Lima, V. Morandi, and L. A. Magalhães, Biological effects induced by doses of mammographic screening, Physica Medica **87**, 90–98 (2021).

[3] F. Sardanelli et al., Position paper on screening for breast cancer by the European Society of Breast Imaging (EUSOBI) and 30 national breast radiology bodies from Austria, Belgium, Bosnia and Herzegovina, Bulgaria, Croatia, Czech Republic, Denmark, Estonia, Finland, France, G, European Radiology **27**, 2737–2743 (2017).

[4] Instituto Nacional de Câncer José Alencar Gomes da Silva, *Guidelines for the early detection of breast cancer in Brazil (in portuguese)*, INCA, 2015.

[5] J. Depuydt, T. Viaene, P. Blondeel, N. Roche, R. Van den Broecke, H. Thierens, and A. Vral, DNA double strand breaks induced by low dose mammography X-rays in breast tissue: A pilot study., Oncol Lett **16**, 3394–3400 (2018).

[6] E. Pauwels, N. Foray, and M. Bourguignon, Breast cancer induced by x-ray mammography screening? A review based on recent understanding of low-dose radiobiology, Medical Principles and Practice **25**, 101–109 (2016).

[7] M. J. Yaffe and J. G. Mainprize, Risk of radiation-induced breast cancer from mammographic screening, Radiology **258**, 98–105 (2011).

[8] A. Berrington de González and G. Reeves, Mammographic screening before age 50 years in the UK: comparison of the radiation risks with the mortality benefits, British Journal of Cancer **93**, 590–596 (2005).

[9] C. Dromain, C. Balleyguier, G. Adler, J. R. Garbay, and S. Delaloge, Contrast-enhanced digital mammography, European Journal of Radiology **69**, 34–42 (2009).

[10] I. Sechopoulos, A review of breast tomosynthesis. Part I. The image acquisition process, Medical Physics **40**, 014301 (2013).

[11] A. Sarno, G. Mettivier, and P. Russo, Dedicated breast computed tomography: Basic aspects, Medical Physics **42**, 2786–2804 (2015).

[12] R. T. Massera, A. Tomal, and R. M. Thomson, Multiscale Monte Carlo simulations for dosimetry in x-ray breast imaging: Part I - Macroscopic scales, To be submitted .

[13] P. A. Oliver and R. M. Thomson, Investigating energy deposition within cell populations using Monte Carlo simulations, Physics in Medicine and Biology **63**, 155018 (2018).

14   D. R. Dance and I. Sechopoulos, Dosimetry in x-ray-based breast imaging, Physics in Medicine and Biology **61**, R271–R304 (2016).

15   R. T. Massera, R. M. Thomson, and A. Tomal, Technical note: MC-GPU breast dosimetry validations with other Monte Carlo codes and phase space file implementation, Medical Physics **49**, 244–253 (2022).

16   A. Badal and A. Badano, Accelerating Monte Carlo simulations of photon transport in a voxelized geometry using a massively parallel graphics processing unit, Medical Physics **36**, 4878–4880 (2009).

17   I. Sechopoulos, D. W. O. Rogers, M. Bazalova-Carter, W. E. Bolch, E. C. Heath, M. F. McNitt-Gray, J. Sempau, and J. F. Williamson, RECORDS: improved Reporting of montE CarlO RaDiation transport Studies: Report of the AAPM Research Committee Task Group 268, Medical Physics **45**, e1–e5 (2018).

18   R. G. Hammerstein, D. W. Miller, D. R. White, M. E. Masterson, H. Q. Woodard, and J. S. Laughlin, Absorbed radiation dose in mammography, Radiology **130**, 485–491 (1979).

19   H. Q. Woodard and D. R. White, The composition of body tissues, The British Journal of Radiology **59**, 1209–1218 (1986).

20   P. A. Oliver and R. M. Thomson, A Monte Carlo study of macroscopic and microscopic dose descriptors for kilovoltage cellular dosimetry, Physics in Medicine and Biology **62**, 1417–1437 (2017).

21   M. P. Martinov and R. M. Thomson, Technical Note: Taking EGSnrc to new lows: Development of egs++ lattice geometry and testing with microscopic geometries, Medical Physics **47**, 3225–3232 (2020).

22   P. A. K. Oliver and R. M. Thomson, Investigating energy deposition in glandular tissues for mammography using multiscale Monte Carlo simulations, Medical Physics **46**, 1426–1436 (2019).

23   A. M. Hernandez, J. A. Seibert, and J. M. Boone, Breast dose in mammography is about 30heterogeneous glandular distributions are considered, Medical Physics **42**, 6337–6348 (2015).

24   R. Tucciariello, P. Barca, D. Sarto, R. Lamastra, G. Mettivier, A. Retico, P. Russo, A. Sarno, A. Traino, and M. Fantacci, Voxelized Breast Phantoms for Dosimetry in Mammography, in *Proceedings of the 14th International Joint Conference on Biomedical Engineering Systems and Technologies - Volume 3: BIOINFORMATICS,*, pages 154–161, INSTICC, SciTePress, 2021.

[25] C. Fedon, M. Caballo, E. García, O. Diaz, J. M. Boone, D. R. Dance, and I. Sechopoulos, Fibroglandular tissue distribution in the breast during mammography and tomosynthesis based on breast CT data: A patient-based characterization of the breast parenchyma, Medical physics **48**, 1436–1447 (2021).

Chapter 8

General discussions

This chapter provides a general discussion of the results obtained in Chapters 2, 3, 4,5, 6, 7 and their potential impact in breast dosimetry. In addition, the current limitations and possible improvements are also discussed for each topic.

8.1 Monte Carlo simulations and cross section impact in breast dosimetry

Monte Carlo simulations are being used for breast dosimetry studies since the 1980 years, with different free and open source MC codes available [24, 25, 66]. In general, the user should tailor the general parameters of the simulations for the desired application. These parameters include, among many, the number of particles that are simulated, which impacts the statistical uncertainties of the results, and the minimum particle energy for absorption. More advanced parameters include the physics modeling of the particle interactions, and the cross section databases. Detailed physics modeling could produce more accurate results at the expense of longer computational times. Meanwhile, the cross section database dictates the probabilities of each type of interaction occurring for each chemical element as a function of the energy. Therefore, different cross sections could yield distinct dose values. In chapter 2, it was studied the differences between two cross section databases for the photoelectric effect related to breast dosimetry in mammography.

Before version 2014, PENELOPE employed the photoelectric cross sections from EPDL97 database that did not incorporate the normalization screening correction (unnormalized). Starting from version 2014, PENELOPE uses by default the EPDL97 database with the normalization screening correction (renormalized). Since the photoelectric effect is the predominant type of interaction regarding energy deposition in the energy range for x-rays employed in mammography, the differences between cross sections directly impact the energy deposited in the breast. Indeed, the comparisons contained in chapter 2 showed that differences up to 2.5% are present for DgN values between the two databases for a conventional mammography

spectrum. In addition, the differences were more evident for the glandular depth dose distributions, with differences ranging from 1% to 4%. Although small, these differences could be significant considering the recommendations from TRS 457, where a maximum uncertainty of 7% is desirable when comparing dose results [36, 67].

Future studies are required to determine which cross section yields results closer to experimental measurements. However, it is challenging to obtain experimental results with the necessary low uncertainties to differentiate both cross sections. Nevertheless, the systematic uncertainty discussed in this chapter is important for comparison between MC codes, where the relative statistical uncertainties are usually below this threshold of a few percent, and this systematic uncertainty could become apparent. If more MC codes start adopting these renormalized cross sections, differences are expected with the validations with previous works that used the unnormalized cross section. For example, the report of AAPM Task Group 195 [68] that presents instructions for validations of MC codes, including a mammography and DBT case, contains results using the PENELOPE 2006 version, and other MC codes which adopt the unnormalized cross sections. New users that are performing simulations with recent versions of PENELOPE will obtain different results from those contained in the report, and chapter 2 could point to the causes and the order of magnitude of the systematic uncertainty.

8.2   Machine learning and deep learning in breast dosimetry

Undoubtedly, artificial intelligence (AI) presence in medical physics research has become more common in recent years. Deep learning has allowed the use of AI in complex tasks regarding medical imaging, including lesion detection, image segmentation and artificial image generation. X-ray breast imaging is one of the fields that has benefited with this recent surge in AI applications. Chapters 3 and 4 present applications of AI in breast dosimetry.

The use of artificial neural networks for the calculation of conversion coefficients (DgN), based on homogeneous breast models, in breast dosimetry is shown in chapter 3. This method is advantageous when a significant number of parameters are considered during the simulations, including the x-ray energy, breast size and composition and the geometry of acquisition of air kerma. Traditional methods of representing values of DgN, such as parametric equations or tables poses a limitation of the number of parameters that could be considered in the simulations, because the parameter space increases rapidly and the necessary amount of tables or equations could make these approaches impractical. On the other hand, neural networks are capable of learning complex patterns and intrinsic relations between the data. The median error, using the neural network ensembles, for MGD and K_{air} was below 0.25% for the test data. Still, some outliers were present with maximum errors up to 3%. Despite their good performance, the use of neural networks require additional steps for a correct setup and use, mainly installing the required packages and running the code. These steps are not required in a more conventional approach, such as tables and parametric equations. A graphical user interface was

developed and is publicly available to assist the deployment and use of the neural networks developed in this work. The limitations of using artificial intelligence in such tasks is the large number of data for correct training, validation and testing. In addition, the selection of the best models is time consuming and requires an additional effort. Nevertheless, neural networks is a promising new method of sharing DgN values besides tables and parametric equations.

Machine learning frameworks, including deep learning, were successfully implemented for breast density estimation from mammography images [62, 63, 69]. However, it is challenging to obtain the labeled data in sufficient numbers to train the algorithms to a desirable level of performance. Chapter 4 explored the concept of employing computer generated anthropomorphic breast phantoms to overcome this limitation, with mammography images generated using MC simulation. The proposed framework consisted of a combination of two XNets (a variation of Unet) and an ensemble of multi-layer perceptrons. Each network was responsible for a different task, from image segmentation, relative breast height and relative glandular height prediction, respectively. This structure was selected because, in preliminary tests, the performance achieved by separating each task was better, when compared to a single network. However, this finding could be dependent on the size of the dataset (original of 208 images), and further tests are necessary for larger datasets with more diverse breast phantom models. The framework showed promising results for the volume glandular fraction (VGF) prediction, with an average absolute difference of 0.04(5) for the test data. Applied to dosimetry, the glandularity calculated using the deep learning framework provided conversion coefficients closer than a constant glandular value (median of the population), with average differences of 1.3% and 8.5% to the ground truth. It is important to note that these DgN values are for population references only, and do not reflect patient specific information because the assumption of the homogeneous breast model is employed for dose calculations [55]. In the future, the framework could be expanded to accept images from the MLO projection instead of only accepting the CC projection, and the information of both views could be combined to provide more reliable breast density estimations. In addition, currently this framework is not accepting real mammography images, thus more studies are necessary for validation and testing before the application for clinical mammography images.

8.3 Multiscale Monte Carlo simulations for breast dosimetry

MC-GPU was validated with other MC codes, and the implementation of phase space files could be useful for multiscale simulations, as detailed in chapter 5. Since the computation speed in MC simulations usually scales with the processing power, computer clusters are employed for complex simulations that would require an unfeasible time to finish in a personal computer. However, a high optimized MC designed for GPUs (e.g. MC-GPU) allows some complex simulations to be performed with fewer hardware resources. The results have shown that MC-GPU using a single GPU was almost 30 times faster when compared with

PENELOPE using a CPU for breast dosimetry simulations. However, MC-GPU does not simulate electrons, and this could be a limitation if the dose at small scales is needed because the approximation of locally energy deposition is no longer accurate. To overcome this limitation, we proposed the use of phase space files that are generated in MC-GPU, and then loaded in another general purpose MC code (i.e. PENELOPE) to simulate a small region in space with finer details, including electron transport. However, this approach is limited for certain conditions, for example scoring the photons entering in a voxel of a breast model, because generating phase space files requires storage in memory and is a costly process in terms of performance if the files are too big. The validations performed comparing splitting the simulations in MC-GPU and PENELOPE using phase space files with only PENELOPE showed an excellent agreement with differences smaller than 0.7%, but with the advantage of being approximately 20 times faster.

The developments and validations made in chapter 5 were applied for multiscale MC simulations for x-ray breast imaging contained in chapters 6 and 7. The differences between the dosimetry quantities at distinct length scales is evident when comparing the results for the MGD, the glandular dose distribution and the specific energy distribution in cells. While maintaining the same MGD value for all the imaging modalities, the glandular dose range in voxels varied considerably. For a medium size breast, the minimum and maximum glandular dose values were approximately 0.2 to 3 times the MGD. Meanwhile, for BCT these values were approximately 0.5 and 1.5, respectively. The x-ray beam energy and the geometry of acquisition are important for the behavior of the dose distribution within the breast. The elemental tissue composition and density of breast tissues, mainly glandular, adipose and skin, is a source of uncertainty in breast dosimetry. Comparing two databases that define the composition of breast tissues, differences up to 30% in the MGD observed. This systematic uncertainty due to the composition of breast tissues should also be considered when studying dose levels in breast dosimetry, along with the systematic uncertainty of the cross sections discussed in section 8.1.

At cellular length scales (in the order of micrometers), the specific energy distribution between nucleus and cytoplasm is mainly dependent on the glandular dose scored in the respective voxel. Voxels with the same glandular dose but at different spatial locations provided similar specific energy distributions. However, the specific energy distribution for nuclei is slightly different between mammography and DBT compared to CEDM and DBCT when similar dose levels are compared. This is mainly due to the x-ray beam energy and the range of the secondary particles. The spectra employed in mammography and DBT are less energetic than CEDM and DBCT, thus, on average, the electrons travel a shorter distance within the cells before transferring their kinetic energy, and consequently, this impacts the shape of the specific energy distribution.

The multiscale MC simulations provide additional information regarding breast dosimetry and the relation between the macroscopic and microscopic quantities. The relation between dose and risk is still uncertain at the dose levels found in diagnostic imaging. However,

the findings contained in chapters 6 and 7 provide at least a generalization of the specific energy distributions and dose values for different x-ray imaging modalities of the breast. Further experimental studies could pursue the assessment of the damage to the cells, particularly DNA, with the dose values found in our study.

Chapter 9

Final conclusions and future perspectives

In this work, a comprehensive study was performed in breast dosimetry using MC simulations. Since breast dosimetry is a complex field with a plethora of parameters involved, only certain aspects could be detailed explored. A special attention was given to the parameters that could be selected in the simulations to assess their effect over the dosimetry data. In addition, it was explored the possibility of using MC generated data and machine learning algorithms for breast dosimetry.

The cross section databases used in the MC simulations can interfere significantly in dosimetry results, based on different simplifications on the physics description. Thus, the choice of the databases is a factor that must be considered when comparing results from MC simulations for breast dosimetry, and the systematic uncertainty derived from these approximations should be take into account for risk assessments.

ML proved to be a useful tool for breast dosimetry, from determining the normalized glandular dose in a homogeneous breast, to prediction of the glandularity of virtual phantoms in simulated mammography images. Neural networks could successfully predict DgN values, for homogeneous breast models, with neural networks trained using MC results. In addition, DL combined with data from MC simulations and computer generated phantoms proved to be a powerful combination for breast density estimation. A natural step for the future is to implement the DL framework for real mammography images, and to extend into the MLO projection.

Although the mean glandular dose is the common factor between them in breast dosimetry, each type of exam presents its particularities, from the geometry of the system to the x-ray beam. Those particularities reflect how the glandular dose is distributed over the breast and, consequently, impact the specific energy distribution in cells. Multiscate dosimetry studies could possibly help future works to investigate the implications of the cell damage due to x-ray breast imaging under different modalities. To overcome the computer-intensive requirements of multiscale MC simulations, the combination of different MC codes, tailored for macroscopic and microscopic simulations, using phase space files, could be viable option. A future topic of study would be to consider the energy interaction process at DNA scales, adding another step into the multiscale simulations.

Bibliography

1. Stewart, B. & Wild, C. *World Cancer Report 2014* ISBN: 978-92-832-0429-9 (International Agency for Research on Cancer, 2014).

2. Sung, H. *et al.* Global Cancer Statistics 2020: GLOBOCAN Estimates of Incidence and Mortality Worldwide for 36 Cancers in 185 Countries. *CA: A Cancer Journal for Clinicians* **71,** 209–249 (2021).

3. *Breast cancer in Brazil: synthesis of information* (in portuguese) (INCA, Rio de Janeiro, 2019).

4. World Health Organization. *Guide to cancer early diagnosis* Section: 48 p. ISBN: 978-92-4-151194-0 (World Health Organization, Geneva, 2017).

5. Sardanelli, F. *et al.* Position paper on screening for breast cancer by the European Society of Breast Imaging (EUSOBI) and 30 national breast radiology bodies from Austria, Belgium, Bosnia and Herzegovina, Bulgaria, Croatia, Czech Republic, Denmark, Estonia, Finland, France, G. **27,** 2737–2743 (2017).

6. Sardanelli, F., Helbich, T. H. & European Society of Breast Imaging (EUSOBI). Mammography: EUSOBI recommendations for women's information. *Insights into imaging* **3,** 7–10 (2012).

7. *Diretrizes para a Detecção Precoce do Câncer de Mama no Brasil* (INCA, Rio de Janeiro, 2015).

8. Bick, U. & Diekmann, F. *Digital Mammography* (eds Bick, U. & Diekmann, F.) 216. ISBN: 978-3-540-78449-4 (Springer Berlin Heidelberg, Berlin, Heidelberg, 2010).

9. Holland, K. *et al.* Influence of breast compression pressure on the performance of population-based mammography screening. *Breast Cancer Research* **19,** 126–126 (2017).

10. Zhou, A., Yin, Y., White, G. L. & Davidson, R. A new solution for radiation transmission in anti-scatter grids. *Biomedical Physics & Engineering Express* **2,** 055011. ISSN: 2057-1976 (2016).

11. Checka, C. M., Chun, J. E., Schnabel, F. R., Lee, J. & Toth, H. The Relationship of Mammographic Density and Age: Implications for Breast Cancer Screening. *American Journal of Roentgenology* **198,** W292–W295 (2012).

12. Sechopoulos, I. A review of breast tomosynthesis. Part I. The image acquisition process. *Medical Physics* **40,** 014301 (2013).

13. Badano, A. *et al.* Evaluation of Digital Breast Tomosynthesis as Replacement of Full-Field Digital Mammography Using an In Silico Imaging Trial. *JAMA Network Open* **1,** e185474–e185474 (2018).

14. Taourel, P. Breast Cancer Screening with Digital Breast Tomosynthesis: The Initial Benefits Continue Over Time. *Radiology* **295,** 540–541 (2020).

15. Dromain, C., Balleyguier, C., Adler, G., Garbay, J. R. & Delaloge, S. Contrast-enhanced digital mammography. *European Journal of Radiology* **69,** 34–42 (2009).

16. Sung, J. S. *et al.* Performance of Dual-Energy Contrast-enhanced Digital Mammography for Screening Women at Increased Risk of Breast Cancer. *Radiology* **293,** 81–88 (2019).

17. O'Connell, A. M., Karellas, A. & Vedantham, S. The Potential Role of Dedicated 3D Breast CT as a Diagnostic Tool: Review and Early Clinical Examples. *The Breast Journal* **20,** 592–605 (2014).

18. Yaffe, M. J. *et al.* The myth of the 50-50 breast. *Medical Physics* **36,** 5437–5443 (2009).

19. Huang, S.-Y. *et al.* The characterization of breast anatomical metrics using dedicated breast CT. *Medical Physics* **38,** 2180–2191 (2011).

20. Huang, S.-Y., Boone, J. M., Yang, K., Kwan, A. L. C. & Packard, N. J. The effect of skin thickness determined using breast CT on mammographic dosimetry. *Medical Physics* **35,** 1199–1206 (2008).

21. Shi, L., Vedantham, S., Karellas, A. & O'Connell, A. M. Technical Note: Skin thickness measurements using high-resolution flat-panel cone-beam dedicated breast CT). *Medical Physics* **40,** 031913 (2013).

22. Caballo, M., Michielsen, K., Fedon, C. & Sechopoulos, I. Towards 4D dedicated breast CT perfusion imaging of cancer: development and validation of computer simulated images. *Physics in Medicine & Biology* **64,** 245004 (2019).

23. Kalos, M. & Whitlock, P. *Monte Carlo Methods* Second edition. (Wiley, 2008).

24. Salvat, F. *PENELOPE-2018: A Code System for Monte Carlo Simulations of Electron and Photon Transport* (Issy-les-Mounlineaux, OECD/NEA, 2019).

25. Allison, J. *et al.* Recent developments in Geant4. *Nuclear Instruments and Methods in Physics Research Section A* **835,** 186–225 (2016).

26. Boone, J. M. Glandular breast dose for monoenergetic and high-energy X-ray beams: Monte Carlo assessment. *Radiology* **213,** 23–37 (1999).

27. Boone, J. M. Normalized glandular dose (DgN) coefficients for arbitrary x-ray spectra in mammography: Computer-fit values of Monte Carlo derived data. *Medical Physics* **29,** 869–875 (2002).

28. Sechopoulos, I., Suryanarayanan, S., Vedantham, S., D'Orsi, C. & Karellas, A. Computation of the glandular radiation dose in digital tomosynthesis of the breast. *Medical Physics* **34,** 221–232 (2006).

29. Wu, X., Barnes, G. T. & Tucker, D. M. Spectral dependence of glandular tissue dose in screen-film mammography. *Radiology* **179,** 143–148 (1991).

30. Dance, D. R. Monte-Carlo calculation of conversion factors for the estimation of mean glandular breast dose. *Physics in Medicine & Biology,* 1211–1220 (1990).

31. Delis, H., Spyrou, G., Costaridou, L., Tzanakos, G. & Panayiotakis, G. Suitability of new anode materials in mammography: Dose and subject contrast considerations using Monte Carlo simulation. *Medical Physics* **33,** 4221–4235 (2006).

32. Badal, A., Sharma, D., Graff, C. G., Zeng, R. & Badano, A. Mammography and breast tomosynthesis simulator for virtual clinical trials. *Computer Physics Communications* **261,** 107779 (2021).

33. Mettivier, G. *et al. Virtual clinical trials in 3D and 2D breast imaging with digital phantoms derived from clinical breast CT scans* in *Medical Imaging 2020: Physics of Medical Imaging* (eds Bosmans, H. & Chen, G.-H.) **11312** (SPIE, 2020), 191.

34. The 2007 Recommendations of the International Commission on Radiological Protection. ICRP publication 103. *Annals of the ICRP* (2007).

35. Yaffe, M. J. & Mainprize, J. G. Risk of Radiation-induced Breast Cancer from Mammographic Screening. *Radiology* **258,** 98–105 (2011).

36. Dance, D. R. & Sechopoulos, I. Dosimetry in x-ray-based breast imaging. *Physics in Medicine & Biology* **61,** R271–R304 (2016).

37. Dance, D. R., Young, K. C. & Van Engen, R. E. Further factors for the estimation of mean glandular dose using the United Kingdom, European and IAEA breast dosimetry protocols. *Physics in Medicine & Biology* **54,** 4361–4372 (2009).

38. Nosratieh, A. *et al.* Mean glandular dose coefficients (D(g)N) for x-ray spectra used in contemporary breast imaging systems. *Physics in Medicine & Biology* **60,** 7179–90 (2015).

39. Sechopoulos, I., Bliznakova, K., Qin, X., Fei, B. & Feng, S. S. J. Characterization of the homogeneous tissue mixture approximation in breast imaging dosimetry. *Medical Physics* **39,** 5050–5059 (2012).

40. Hernandez, A. M., Seibert, J. A. & Boone, J. M. Breast dose in mammography is about 30% lower when realistic heterogeneous glandular distributions are considered. *Medical Physics* **42,** 6337–6348 (2015).

41. Tucciariello, R. *et al. Voxelized Breast Phantoms for Dosimetry in Mammography* in *Proceedings of the 14th International Joint Conference on Biomedical Engineering Systems and Technologies - Volume 3: BIOINFORMATICS,* (SciTePress, 2021), 154–161.

42. Fedon, C. *et al.* Fibroglandular tissue distribution in the breast during mammography and tomosynthesis based on breast CT data: A patient-based characterization of the breast parenchyma. *Medical Physics* **48,** 1436–1447.

43. Graff, C. G. *A new, open-source, multi-modality digital breast phantom* in *Medical Imaging 2016: Physics of Medical Imaging* (eds Kontos, D., Flohr, T. G. & Lo, J. Y.) **9783** (SPIE, 2016), 978309.

44. Boone, J. M., Nelson, T. R., Lindfors, K. K. & Seibert, J. A. Dedicated Breast CT: Radiation Dose and Image Quality Evaluation. *Radiology* **221,** 657–667 (2001).

45. Sechopoulos, I., Feng, S. S. J. & D'Orsi, C. J. Dosimetric characterization of a dedicated breast computed tomography clinical prototype. *Medical Physics* **37,** 4110–4120 (2010).

46. Oliver, P. A. K. & Thomson, R. M. Investigating energy deposition in glandular tissues for mammography using multiscale Monte Carlo simulations. *Medical Physics* **46,** 1426–1436 (2019).

47. Pereira, L. *et al.* Biological effects induced by doses of mammographic screening. *Physica Medica* **87,** 90–98.

48. Goodfellow, I., Bengio, Y. & Courville, A. *Deep Learning* Acessed in 24-01-2022, `http://www.deeplearningbook.org` (MIT Press, 2016).

49. Manco, L. *et al.* Basic of machine learning and deep learning in imaging for medical physicists. *Physica Medica* **83,** 194–205 (2021).

50. Castiglioni, I. *et al.* AI applications to medical images: From machine learning to deep learning. *Physica Medica* **83,** 9–24 (2021).

51. Rajkomar, A., Dean, J. & Kohane, I. Machine Learning in Medicine. *New England Journal of Medicine* **380,** 1347–1358 (2019).

52. A survey on deep learning in medical image analysis. *Medical Image Analysis* **42,** 60–88 (2017).

53. Nousiainen, K., Mäkelä, T., Piilonen, A. & Peltonen, J. I. Automating chest radiograph imaging quality control. *Physica Medica* **83,** 138–145 (2021).

54. Capobianco, E. High-dimensional role of AI and machine learning in cancer research. *British Journal of Cancer.* ISSN: 1532-1827 (2022).

55. Sechopoulos, I. *et al.* Mammography dose estimates do not reflect any specific patient's breast dose. *European Journal of Radiology* **131** (2020).

56. Alyafi, B., Diaz, O., Vilanova, J. C., Del Riego, J. & Marti, R. *Quality analysis of DCGAN-generated mammography lesions* tech. rep. (2019). arXiv: `1911.12850v1`.

57. Caballo, M. *et al.* Development of 3D patient-based super-resolution digital breast phantoms using machine learning. *Physics in Medicine & Biology* **63,** 225017 (2018).

58. T. Kretz, K. -R. Müller, T. Schaeffter & C. Elster. Mammography Image Quality Assurance Using Deep Learning. *IEEE Transactions on Biomedical Engineering* **67,** 3317–3326 (2020).

59. Su, T. *et al.* DIR-DBTnet: Deep iterative reconstruction network for three-dimensional digital breast tomosynthesis imaging. *Medical Physics* **48,** 2289–2300 (2021).

60. Johansson, H. *et al.* Breast-density measurement using photon-counting spectral mammography. *Medical Physics* **44,** 3579–3593 (2017).

61. Ng, K.-H. & Lau, S. Vision 20/20: Mammographic breast density and its clinical applications. *Medical Physics* **42,** 7059–7077 (2015).

62. Keller, B. M. *et al.* Estimation of breast percent density in raw and processed full field digital mammography images via adaptive fuzzy c-means clustering and support vector machine segmentation. *Medical Physics* **39,** 4903–4917 (2012).

63. Warren, L. M. *et al. Deep learning to calculate breast density from processed mammography images* in *15th International Workshop on Breast Imaging (IWBI2020)* **11513** (SPIE, 2020), 24.

64. Teuwen, J. *et al.* Deep learning reconstruction of digital breast tomosynthesis images for accurate breast density and patient-specific radiation dose estimation. *Medical Image Analysis,* 102061 (2021).

65. Sechopoulos, I. *et al. AAPM Committee - Task Group No. 282 - Development of a new universal breast dosimetry method (TG282)* 2016. `https://www.aapm.org/org/structure/?committee_code=TG282` (2022).

66. Kawrakow, I., Mainegra-Hing, E., Rogers, D. W. O., Tessier, F. & Walters, B. R. B. The EGSnrc code system: Monte Carlo simulation of electron and photon transport, Technical Report PIRS-701. *National Research Council Canada.* `http://nrc-cnrc.github.io/EGSnrc/doc/pirs701-egsnrc.pdf` (2017).

67. IAEA. *Dosimetry in Diagnostic Radiology: An International Code of Practice Reports Series No. 457* (IAEA, Vienna, 2007).

68. Sechopoulos, I. *et al.* Monte Carlo reference data sets for imaging research: Executive summary of the report of AAPM Research Committee Task Group 195. *Medical Physics* **42,** 5679–5691 (2015).

69. Maghsoudi, O. H. *et al.* *Deep-LIBRA: Artificial intelligence method for robust quantification of breast density with independent validation in breast cancer risk assessment* 2020. arXiv: `2011.08001 [eess.IV]`.

Appendix A

Ethics committee approval

UNICAMP - CAMPUS CAMPINAS

PARECER CONSUBSTANCIADO DO CEP

DADOS DA EMENDA

Título da Pesquisa: Avaliação da densidade volumétrica mamária em mulheres brasileiras baseada em imagens mamográficas

Pesquisador: Alessandra Tomal

Área Temática:

Versão: 3

CAAE: 47878315.2.0000.5404

Instituição Proponente: Instituto de Física "Gleb Wataghin"

Patrocinador Principal: Financiamento Próprio

DADOS DO PARECER

Número do Parecer: 2.809.100

Apresentação do Projeto:

Introdução- O câncer de mama é o tipo de câncer mais comum entre as mulheres e o maior responsável por óbitos nesta população. De acordo com o Instituto Nacional do Câncer, a cada ano no Brasil são diagnosticados em torno de 50.000 novos casos da doença. O diagnóstico precoce é a forma mais eficaz de reduzir a mortalidade pela doença, aumentando a sobrevida dos pacientes. Atualmente, a mamografia é a técnica mais utilizada para esse detecção e diagnósticodo câncer de mama, sendo amplamente aplicada em programas de rastreamento. Apesar disso, a taxa de falso negativos em mamografia é aproximadamente 20 -30%. Diversos estudos da literatura têm mostrado que um dos fatores associados com menores sensibilidade e especificidade da mamografia é a densidade da mama, definida como o volume da mama ocupado pelo tecido fibroglandular. Além disso, estudos a respeito da composição de tecidos mamários têm mostrado que além de afetar a sensibilidade da mamografia, a densidade da mama é um fator de risco para o câncer de mama. O risco relativo da doença associado com a alta densidade mamária é apenas menor que os associados com a idade e a mutação do gene BRAC. Apesar disso, o mecanismo exato que relaciona o risco de câncer com a densidade da mama ainda não são totalmente conhecidos. Desta forma, a análise quantitativa da densidade mamária pode ter um papel essencial na predição do risco do câncer de mama em uma população. Tradicionalmente, a avaliação da densidade mamária é baseada na imagem mamográfica e realizada visualmente pelo médico radiologista, sendo baseado em diversos protocolos de classificação. Os mais populares são Breast

UNICAMP - CAMPUS CAMPINAS
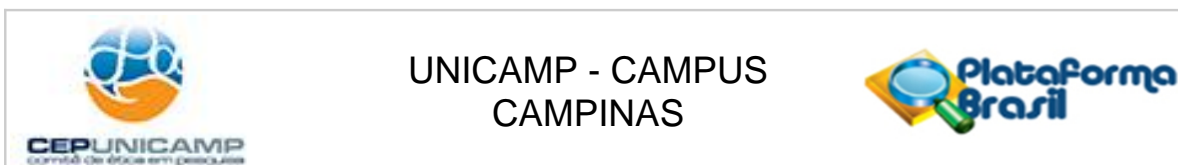
Continuação do Parecer: 2.809.100

Imaging Reporting and Data System (BI-RADS), Boyd's six category classification, e Tabar. Esse tipo de avaliação é subjetiva e depende do treinamento e experiência do radiologista, de forma que pode estar sujeita a erros de interpretação. Uma avaliação mais precisa da densidade da mama poderia ser realizada de forma quantitativa. Com esse objetivo, diversos métodos semiautomáticos computacionais têm sido desenvolvidos, principalmente após o desenvolvimento da mamografia digital. A densidade mamária têm sido estudada em diferentes populações baseada na avaliação da imagem mamográfica digital sem processamento (raw data) e também usando dados de aquisição das imagens (potencial do tubo, mAs e espessura da mama comprimida). A densidade mamária têm sido estudada em mulheres de diferentes grupos étnicos, tais como Chinesas, Malasianas, Indianas, Americanas, Australianas e Alemãs. Estes estudos têm mostrado diferenças na proporção de tecido glandular presente na mama entre diferentes grupos étnicos, principalmente entre as mulheres mais jovens. De acordo com o conhecimento dos pesquisadores, não existe nenhum estudo que quantifique a densidade mamária de mulheres brasileiras através do exame mamográfico. Em sumário, a determinação da densidade mama representa um estudo fundamental tanto para avaliação da sensibilidade de detecção do exame mamográfico quanto para a estimativa do risco do câncer de mama. Neste contexto, a densidade mamária pode ser utilizada para melhorar a predição individualizada do câncer de mama e fornecer métodos mais eficazes e de menor custo para o rastreamento desta doença dos que os disponíveis atualmente. A longo prazo, o conhecimento da densidade mamária de uma população e de sua correlação com fatores como idade, espessura da mama e diagnóstico, pode auxiliar a compreensão da base biológica que relaciona a alta densidade mamária com o risco de câncer de mama.   Hipótese: Avaliar se existe correlação entre a densidade mamária determinada através das imagens mamográficas e a idade da paciente, espessura e área da mama. Metodologia Proposta: Nesta proposta pretende-se adotar uma abordagem experimental para estudar a densidade volumétrica das mamas de mulheres brasileiras baseado nas imagens mamográficas adquiridas nos programas de rastreamento. O trabalho será dividido em três etapas: (i) primeiramente serão adquiridas imagens de objetos simuladores de diferentes composições para validação do método; (ii) depois serão avaliados as imagens de mamas de pacientes de forma quantitativa visando determinar a densidade mamária e a área de contato entre a mama e o suporte do receptor de imagem;(iii) por fim, a densidade mamária será correlacionada com diversos parâmetros extraídos do cabeçalho DICOM das imagens (idade, dose, técnica de exposição). Critério de Inclusão: Imagens mamográficas de pacientes que realizaram esse tipo de exame e estão armazenadas na base de dados do sistema PACS do INRAD HCUSP e ICESP.

UNICAMP - CAMPUS CAMPINAS
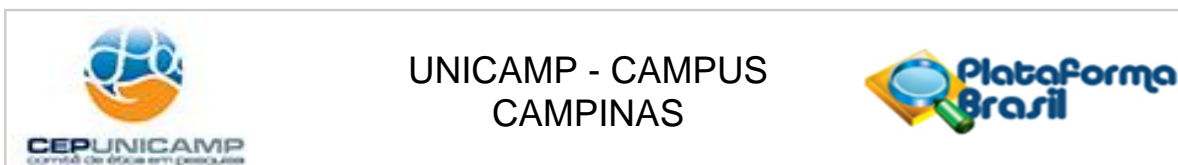
Continuação do Parecer: 2.809.100

Objetivo da Pesquisa:

Objetivo Primário: A meta central deste trabalho é estudar, de forma quantitativa, a glandularidade de mamas em mulheres brasileiras a partir de imagens mamográficas de 50000 pacientes. Inicialmente, a metodologia será testada parem imagens de objetos simuladores (phantoms) com diferentes glandularidades, e em seguida serão avaliadas as imagens adquiridas na projeção crânio-caudal. Objetivo Secundário: 1 - Levantar o perfil de densidades de mama (glandularidade) de mulheres brasileiras, e estudar sua correlação com outros parâmetros das participantes, tais como idade e espessura da mama. 2 - Efetuar análise estatística automatizada, correlacionando informações adquiridas no cabeçalho DICOM das imagens clínicas, para auxílio ao controle de qualidade dos sistemas avaliados. 3 - Elaborar relatórios técnicos destinados ao desenvolvimento de um padrão de qualidade das imagens com doses de radiação otimizadas.

Avaliação dos Riscos e Benefícios:

Mantidos em relação ao projeto original.

Comentários e Considerações sobre a Pesquisa:

Esta versão é uma emenda ao protocolo aprovado em 18/11/2015 via parecer nº 1327787 do CEP do HC/USP. Apresenta a seguinte justificativa: "Inclusão de três novos membros na equipe do projeto (alunos de iniciação científica e pós-graduação). Inclusão das etapas de análise estatística dos dados e estimativa da dose na mama baseada nos dados das imagens." Novos membros: GABRIEL SARON- Aluno de graduação em Física Médica na Unicamp, RODRIGO TREVISAN MASSERA -Aluno de doutorado em Física da UNICAMP e THAIS DAMASIO QUADROS- Aluna de graduação em Física Médica na Unicamp.

Considerações sobre os Termos de apresentação obrigatória:

Foram considerados para a elaboração deste parecer os seguintes documentos: "PB_INFORMAÇÕES_BÁSICAS_1131108_E2.pdf", "AlessandraDensidadeFIM.pdf" e "emenda.pdf".

Recomendações:

Não há.

Conclusões ou Pendências e Lista de Inadequações:

A solicitação de emenda foi apresentada e justificada de forma adequada.

Considerações Finais a critério do CEP:

- O participante da pesquisa deve receber uma via do Termo de Consentimento Livre e Esclarecido, na íntegra, por ele assinado (quando aplicável).

Endereço: Rua Tessália Vieira de Camargo, 126
Bairro: Barão Geraldo **CEP:** 13.083-887
UF: SP **Município:** CAMPINAS
Telefone: (19)3521-8936 **Fax:** (19)3521-7187 **E-mail:** cep@fcm.unicamp.br

UNICAMP - CAMPUS CAMPINAS

Continuação do Parecer: 2.809.100

- O participante da pesquisa tem a liberdade de recusar-se a participar ou de retirar seu consentimento em qualquer fase da pesquisa, sem penalização alguma e sem prejuízo ao seu cuidado (quando aplicável).

- O pesquisador deve desenvolver a pesquisa conforme delineada no protocolo aprovado. Se o pesquisador considerar a descontinuação do estudo, esta deve ser justificada e somente ser realizada após análise das razões da descontinuidade pelo CEP que o aprovou. O pesquisador deve aguardar o parecer do CEP quanto à descontinuação, exceto quando perceber risco ou dano não previsto ao participante ou quando constatar a superioridade de uma estratégia diagnóstica ou terapêutica oferecida a um dos grupos da pesquisa, isto é, somente em caso de necessidade de ação imediata com intuito de proteger os participantes.

- O CEP deve ser informado de todos os efeitos adversos ou fatos relevantes que alterem o curso normal do estudo. É papel do pesquisador assegurar medidas imediatas adequadas frente a evento adverso grave ocorrido (mesmo que tenha sido em outro centro) e enviar notificação ao CEP e à Agência Nacional de Vigilância Sanitária – ANVISA – junto com seu posicionamento.

- Eventuais modificações ou emendas ao protocolo devem ser apresentadas ao CEP de forma clara e sucinta, identificando a parte do protocolo a ser modificada e suas justificativas e aguardando a aprovação do CEP para continuidade da pesquisa. Em caso de projetos do Grupo I ou II apresentados anteriormente à ANVISA, o pesquisador ou patrocinador deve enviá-las também à mesma, junto com o parecer aprovatório do CEP, para serem juntadas ao protocolo inicial.

- Relatórios parciais e final devem ser apresentados ao CEP, inicialmente seis meses após a data deste parecer de aprovação e ao término do estudo.

-Lembramos que segundo a Resolução 466/2012 , item XI.2 letra e, "cabe ao pesquisador apresentar dados solicitados pelo CEP ou pela CONEP a qualquer momento".

-O pesquisador deve manter os dados da pesquisa em arquivo, físico ou digital, sob sua guarda e responsabilidade, por um período de 5 anos após o término da pesquisa.

UNICAMP - CAMPUS
CAMPINAS

Continuação do Parecer: 2.809.100

Este parecer foi elaborado baseado nos documentos abaixo relacionados:

Tipo Documento	Arquivo	Postagem	Autor	Situação
Informações Básicas do Projeto	PB_INFORMAÇÕES_BÁSICAS_1131108_E2.pdf	15/07/2018 15:12:07		Aceito
Projeto Detalhado / Brochura Investigador	AlessandraDensidadeFIM.pdf	15/07/2018 15:11:45	Alessandra Tomal	Aceito
Outros	emenda.pdf	15/07/2018 15:10:02	Alessandra Tomal	Aceito
Declaração de Instituição e Infraestrutura	inrad.pdf	16/09/2015 14:30:48	Alessandra Tomal	Aceito
Folha de Rosto	Scan0134.pdf	04/08/2015 08:47:27		Aceito
Declaração de Instituição e Infraestrutura	Carta de anuência.pdf	31/07/2015 08:23:15		Aceito

Situação do Parecer:
Aprovado

Necessita Apreciação da CONEP:
Não

CAMPINAS, 09 de Agosto de 2018

Assinado por:
Renata Maria dos Santos Celeghini
(Coordenador)

Endereço: Rua Tessália Vieira de Camargo, 126
Bairro: Barão Geraldo   **CEP:** 13.083-887
UF: SP   **Município:** CAMPINAS
Telefone: (19)3521-8936   **Fax:** (19)3521-7187   **E-mail:** cep@fcm.unicamp.br

UNICAMP - CAMPUS CAMPINAS

PARECER CONSUBSTANCIADO DO CEP

DADOS DA EMENDA

Título da Pesquisa: Avaliação da densidade volumétrica mamária em mulheres brasileiras baseada em imagens mamográficas

Pesquisador: Alessandra Tomal

Área Temática:

Versão: 5

CAAE: 47878315.2.0000.5404

Instituição Proponente: Instituto de Física "Gleb Wataghin"

Patrocinador Principal: Financiamento Próprio

DADOS DO PARECER

Número do Parecer: 4.752.335

Apresentação do Projeto:

Trata-se da apresentação de uma Emenda ao projeto CAAE 47878315.2.0000.5404.

Objetivo da Pesquisa:

Apresentar uma Emenda.

Avaliação dos Riscos e Benefícios:

Os riscos e benefícios não foram alterados em relação ao projeto original.

Comentários e Considerações sobre a Pesquisa:

Esta versão é uma emenda ao protocolo aprovado em 18/11/2015 via parecer nº 1327787 do CEP do HC/USP. Apresenta a seguinte justificativa: "Venho através desta justificar a emenda no projeto "Avaliação da densidade volumétrica mamária em mulheres brasileiras baseada em imagens mamográficas" com número CAAE 47878315.2.0000.5404. Essa emenda baseia-se na inclusão de dois novos membros na equipe do projeto (um aluno de iniciação científica e um pesquisador) e atrasos na coleta das imagens devido à pandemia de COVID-19. Além disso, durante a análise das imagens observamos variações nos resultados do software utilizado para quantificação da densidade mamária, como por exemplo variações nos valores obtidos usando em imagens adquiridas usando diferentes equipamentos e para mulheres que realizaram mais de um exame. Dessa forma, com base nesses achados e em estudos publicados recentemente na literatura desde a aprovação do presente projeto, consideramos necessário fazer a inclusão da etapa de

Endereço: Rua Tessália Vieira de Camargo, 126
Bairro: Barão Geraldo **CEP:** 13.083-887
UF: SP **Município:** CAMPINAS
Telefone: (19)3521-8936 **Fax:** (19)3521-7187 **E-mail:** cep@fcm.unicamp.br

Página 01 de 05

UNICAMP - CAMPUS
CAMPINAS

Continuação do Parecer: 4.752.335

comparação entre dados de densidade mamária extraídos das imagens mamográficas usando diferentes softwares disponíveis comercialmente ou frameworks baseados em deep learning, uma área de pesquisa que teve um amplo desenvolvimento nos últimos anos e altamente promissora para imagens médicas, visando alcançar uma melhor precisão e confiança nos resultados. Os nomes dos novos membros estão destacados na tabela da equipe do Projeto de Pesquisa apresentado, bem como a metodologia apresentada foi descrita mais detalhadamente para incluir a descrição dos diferentes softwares de análise." A pesquisadora anexou uma carta em relação à pendência com a seguinte informação: "Em resposta às pendências da emenda no projeto "Avaliação da densidade volumétrica mamária em mulheres brasileiras baseada em imagens mamográficas" com número CAAE 47878315.2.0000.5404 submetida ao CEP-UNICAMP, as seguintes correções foram realizadas: 1. A lista de todos os pesquisadores que fazem parte do projeto foi incluída na capa do projeto detalhado. 2. Os pesquisadores Eric Francisco Scolastici e Mariana Yuamoto que constam no projeto detalhado foram incluídos no item "equipe de pesquisa" do Formulário de Informações Básicas da Plataforma Brasil. 3. O pesquisador Dr Prof Kwan–Hoong Ng é professor da University of Malaya, na Malásia. Pelo fato do pesquisador ser estrangeiro, justifico que não conseguimos realizar a sua inserção dele na Equipe de Pesquisa do Formulário de Informações Básicas da Plataforma Brasil. Apesar disso, ressalto que o Dr. Ng fará parte da Equipe do projeto e seu nome foi incluído na capa e na descrição da equipe do projeto detalhado."

Considerações sobre os Termos de apresentação obrigatória:
Para a elaboração deste parecer foram analisados os seguintes documentos: "PB_INFORMAÇÕES_BÁSICAS_1740891_E3.pdf", "carta_resposta_pendencias.pdf" e "Projeto.pdf".
Recomendações:
A Comissão Nacional de Ética em Pesquisa (Conep), do Conselho Nacional de Saúde (CNS) orienta a adoção das diretrizes do Ministério da Saúde (MS) decorrentes da pandemia causada pelo Coronavírus SARS-CoV-2 (Covid-19), com o objetivo de minimizar os potenciais riscos à saúde e a integridade dos participantes de pesquisas e pesquisadores.
De acordo com carta circular da CONEP intitulada "ORIENTAÇÕES PARA CONDUÇÃO DE PESQUISAS E ATIVIDADE DOS CEP DURANTE A PANDEMIA PROVOCADA PELO CORONAVÍRUS SARS-COV-2 (COVID-19)" publicada em 09/05/2020, referente ao item II. "Orientações para Pesquisadores":
- Aconselha-se a adoção de medidas para a prevenção e gerenciamento de todas as atividades de pesquisa, garantindo-se as ações primordiais à saúde, minimizando prejuízos e potenciais riscos, além de prover cuidado e preservar a integridade e assistência dos participantes e da equipe de pesquisa.

UNICAMP - CAMPUS CAMPINAS

Continuação do Parecer: 4.752.335

- Em observância às dificuldades operacionais decorrentes de todas as medidas impostas pela pandemia do SARS-CoV-2 (COVID- 19), é necessário zelar pelo melhor interesse do participante da pesquisa, mantendo-o informado sobre as modificações do protocolo de pesquisa que possam afetá-lo, principalmente se houver ajuste na condução do estudo, cronograma ou plano de trabalho.

- Caso sejam necessários a suspensão, interrupção ou o cancelamento da pesquisa, em decorrência dos riscos imprevisíveis aos participantes da pesquisa, por causas diretas ou indiretas, caberá aos investigadores a submissão de notificação para apreciação do Sistema CEP/Conep.

- Nos casos de ensaios clínicos, é permitida, excepcionalmente, a tramitação de emendas concomitantes à implementação de modificações/alterações no protocolo de pesquisa, visando à segurança do participante da pesquisa, assim como dos demais envolvidos no contexto da pesquisa, evitando-se, ainda, quando aplicável, a interrupção no tratamento dos participantes da pesquisa. Eventualmente, na necessidade de modificar o Termo de Consentimento Livre e Esclarecido (TCLE), o pesquisador deverá proceder com o novo consentimento, o mais breve possível.

Conclusões ou Pendências e Lista de Inadequações:

Emenda aprovada.

Considerações Finais a critério do CEP:

- O participante da pesquisa deve receber uma via do Termo de Consentimento Livre e Esclarecido, na íntegra, por ele assinado (quando aplicável). - O participante da pesquisa tem a liberdade de recusar-se a participar ou de retirar seu consentimento em qualquer fase da pesquisa, sem penalização alguma e sem prejuízo ao seu cuidado (quando aplicável). - O pesquisador deve desenvolver a pesquisa conforme delineada no protocolo aprovado. Se o pesquisador considerar a descontinuação do estudo, esta deve ser justificada e somente ser realizada após análise das razões da descontinuidade pelo CEP que o aprovou. O pesquisador deve aguardar o parecer do CEP quanto à descontinuação, exceto quando perceber risco ou dano não previsto ao participante ou quando constatar a superioridade de uma estratégia diagnóstica ou terapêutica oferecida a um dos grupos da pesquisa, isto é, somente em caso de necessidade de ação imediata com intuito de proteger os participantes. - O CEP deve ser informado de todos os efeitos adversos ou fatos

Endereço: Rua Tessália Vieira de Camargo, 126	
Bairro: Barão Geraldo	**CEP:** 13.083-887
UF: SP **Município:** CAMPINAS	
Telefone: (19)3521-8936 **Fax:** (19)3521-7187	**E-mail:** cep@fcm.unicamp.br

UNICAMP - CAMPUS
CAMPINAS

Continuação do Parecer: 4.752.335

relevantes que alterem o curso normal do estudo. É papel do pesquisador assegurar medidas imediatas adequadas frente a evento adverso grave ocorrido (mesmo que tenha sido em outro centro) e enviar notificação ao CEP e à Agência Nacional de Vigilância Sanitária – ANVISA – junto com seu posicionamento. - Eventuais modificações ou emendas ao protocolo devem ser apresentadas ao CEP de forma clara e sucinta, identificando a parte do protocolo a ser modificada e suas justificativas e aguardando a aprovação do CEP para continuidade da pesquisa. Em caso de projetos do Grupo I ou II apresentados anteriormente à ANVISA, o pesquisador ou patrocinador deve enviá-las também à mesma, junto com o parecer aprovatório do CEP, para serem juntadas ao protocolo inicial. - Relatórios parciais e final devem ser apresentados ao CEP, inicialmente seis meses após a data deste parecer de aprovação e ao término do estudo. -Lembramos que segundo a Resolução 466/2012 , item XI.2 letra e, "cabe ao pesquisador apresentar dados solicitados pelo CEP ou pela CONEP a qualquer momento". -O pesquisador deve manter os dados da pesquisa em arquivo, físico ou digital, sob sua guarda e responsabilidade, por um período de 5 anos após o término da pesquisa.

Este parecer foi elaborado baseado nos documentos abaixo relacionados:

Tipo Documento	Arquivo	Postagem	Autor	Situação
Informações Básicas do Projeto	PB_INFORMAÇÕES_BÁSICAS_1740891_E3.pdf	27/05/2021 15:04:02		Aceito
Outros	carta_resposta_pendencias.pdf	27/05/2021 15:02:57	Alessandra Tomal	Aceito
Projeto Detalhado / Brochura Investigador	Projeto.pdf	27/05/2021 15:02:16	Alessandra Tomal	Aceito
Outros	Material_complementar.pdf	30/04/2021 13:49:54	Alessandra Tomal	Aceito
Outros	Carta.pdf	30/04/2021 13:49:24	Alessandra Tomal	Aceito
Declaração de Instituição e Infraestrutura	inrad.pdf	16/09/2015 14:30:48	Alessandra Tomal	Aceito
Folha de Rosto	Scan0134.pdf	04/08/2015 08:47:27		Aceito
Declaração de Instituição e Infraestrutura	Carta de anuência.pdf	31/07/2015 08:23:15		Aceito

UNICAMP - CAMPUS
CAMPINAS

Continuação do Parecer: 4.752.335

Situação do Parecer:
Aprovado

Necessita Apreciação da CONEP:
Não

CAMPINAS, 02 de Junho de 2021

_____

Assinado por:
Renata Maria dos Santos Celeghini
(Coordenador(a))

Endereço: Rua Tessália Vieira de Camargo, 126
Bairro: Barão Geraldo   **CEP:** 13.083-887
UF: SP   **Município:** CAMPINAS
Telefone: (19)3521-8936   **Fax:** (19)3521-7187   **E-mail:** cep@fcm.unicamp.br

Appendix B

Permission to use articles in thesis

B.1 Permission I

For articles published in Physics in Medicine & Biology, contained in Chapters 2 and 3.

This text was retrieved from the link: `https://publishingsupport.iopscience.iop.org/current-policy-author-rights-policy-for-subscription-articles-for-which-the-copyright-form-was-submitted-on-or-after-26-april-2016/` in 02/12/2021.

B.2 Permission II

For the article published in Physica Medica, contained in Chapter 4.

Breast glandularity and mean glandular dose assessment using a deep learning framework: Virtual patients study

Author: Rodrigo T. Massera, Alessandra Tomal
Publication: Physica Medica
Publisher: Elsevier
Date: March 2021

© 2021 Associazione Italiana di Fisica Medica. Published by Elsevier Ltd. All rights reserved.

Journal Author Rights

Please note that, as the author of this Elsevier article, you retain the right to include it in a thesis or dissertation, provided it is not published commercially. Permission is not required, but please ensure that you reference the journal as the original source. For more information on this and on your other retained rights, please visit: https://www.elsevier.com/about/our-business/policies/copyright#Author-rights

BACK   CLOSE WINDOW

B.3 Permission III

For the articles submitted or published in Medical Physics, contained in Chapters 5, 6, 7.

Medical Physics
Copyright

If your paper is accepted, the author identified as the formal corresponding author for the paper will receive an email prompting them to login into Author Services; where via the Wiley Author Licensing Service (WALS) they will be able to complete the license agreeement on behalf of all authors on the paper.

For authors signing the non-standard copyright transfer agreement (CTA).

If the OnlineOpen option is not selected the corresponding author will be presented with the MP SUB to sign. The terms and conditions of the MP SUB can be previewed here. Please do not complete this PDF until you are prompted to login into Author Services as described above.

Note to Contributors on Deposit of Accepted Version

Authors are permitted to self-archive the peer reviewed (but not final) version of the Contribution on the Contributor's personal website, in the Contributor's company/institutional repository or archive, and in certain not for profit subject-based repositories such as PubMed Central as listed at the following website: http://olabout.wiley.com/WileyCDA/Section/id-820227.html, subject to an embargo period of 12 months for scientific, technical and medical (STM) journals and 24 months for social science and humanities (SSH) journals following publication of the final Contribution. There are seperate arrrangements with certain funding agencies governing reuse of this version as set forth at the following website: http://www.wiley.com/go/funderstatement. The Contributor may not update the accepted version or replace it with the published Contribution.

This text was retrieved from the link: `https://medphys.msubmit.net/cgi-bin/main.plex?form_type=do_cat&file_nm=medphys_specific_info.html` in 02/12/2021.